

Diamonds On The Inside:

Imaging Nanodiamonds With Hyperpolarized MRI

FACULTY OF SCIENCE

SCHOOL OF PHYSICS

David E. J. Waddington

A thesis submitted in fulfillment of the requirements for the
degree of Doctor of Philosophy

2018

Abstract

Nontoxic nanodiamonds (NDs) have proven useful as a vector for therapeutic drug delivery to cancers and as optical bioprobes of subcellular processes. Despite their potential clinical relevance, an effective means of noninvasively imaging NDs *in vivo* is still lacking. Recent developments in hyperpolarized MRI leverage an over 10 000 times increase in the nuclear polarization of biomolecules, enabling new molecular imaging applications. This work explores hyperpolarization via intrinsic paramagnetic defects in nanodiamond. We present the results of MRI experiments that enable direct imaging of nanodiamond via hyperpolarized ^{13}C MRI and indirect imaging of nanodiamonds via Overhauser-enhanced MRI. The construction of custom hardware for these experiments is detailed and the path to future *in vivo* experiments outlined. As nanodiamond has been established as a biocompatible platform for drug delivery, our results will motivate further research into hyperpolarized MRI for tracking nanoparticles *in vivo*.

Acknowledgements

First, I want to express my gratitude to my supervisor David Reilly. Thank you for your support and guidance through the course of this work. David's ability to articulate and communicate a vision for the future is second to none. It is this vision, and David's passion for fundamental science, that laid the foundation for the work contained in this thesis—a translation of advances in quantum physics to biomedical applications.

Second, I want to acknowledge my other compatriots on the aptly named 'Team NMR' at the University of Sydney. Ewa Rej, thanks for trailblazing the NMR project and being there at the beginning of my PhD, when we were still figuring it all out. I learnt a lot from the courage you displayed when voyaging into the uncertainty of the scientific unknown and it is immensely satisfying to now share with you, the fruits of our labour. Torsten Gaebel, thank you for being the experienced and steady hand, always willing to help though my time at Sydney University. Your support was invaluable in working through the niggles of each new experimental setup. Your persistence certainly cracked many a problem after I had lost patience. Thomas Boele, thank you for bringing your fresh ideas, and energy, to the nanodiamond project and always being willing to lend a much appreciated hand as I strived to meet deadlines. I have enjoyed watching you develop confidence in your research abilities. I look forward to seeing the new heights to which I know you will take this work.

Of course, I had a second home in Boston for a significant portion of this PhD. Many thanks go to Matt Rosen for making me feel very welcome in his lab at the Martinos Center, and for his ongoing support ever since. Matt's curiosity and connection with his joyful inner child bring an enthusiasm for

science and discovery to those who work in his lab. This curiosity drove many a revealing scientific discussion during my time in Boston—often coinciding with our ritual of 3 pm pourover coffee. My stay in the USA was also much richer for having had the opportunity to work with Mathieu Sarracanie and Najat Salameh. À Mathieu et Najat, merci pour votre soutien sans cesse. Je me sentais comme chez moi dans le laboratoire à Boston. Je suis ravi de voir votre nouveau laboratoire à Bâle s'épanouir.

Thanks also go to Dick Marsh and Arnold Itkin for their hard work on delivering the MRI system from Boston to Sydney. That system made much of this work possible. I look forward to future boat trips on Boston Harbor together.

I drew on the wisdom of many a senior colleague in the course of this work. In particular, I am grateful to my co-supervisor Andrew Doherty for his continuing guidance over our many coffee catch ups, as he strove to ensure my PhD stayed on track. Thanks also go to Adam Micolich and Dane McCamey for their generous mentorship and support.

Experimental physics is not a cheap endeavour. I'm grateful to the funding bodies that supported this work both directly and indirectly—in particular, the Australian-American Fulbright Commission, the Australian Research Council and the US Department of Defense.

Thank you also to the other students, postdocs, academics, administrative staff and professional staff I had the honour of meeting and working with at the University of Sydney, the Martinos Center and beyond. There are many of these amazing people who helped me along the way. An extra thank you to each one of them that proof read this thesis.

To my friends, thank you for being there through the ups and the downs. I treasure the many resilience building trips we've shared over the last few years to crags, mountains, canyons, beaches and pubs far and wide.

To Mum, Alice, Shahe and all my family, I am extremely grateful for being born into such a loving bunch of people. Thank you for always being there for me.

And to Teresa, thank you for being my champion. You make me stronger every single day.

Authorship Attribution and Originality Statement

The material presented in Chapter 3 is adapted from the publication:

E. Rej, T. Gaebel, T. Boele, **D. E. J. Waddington** and D. J. Reilly, Hyperpolarized nanodiamond with long spin-relaxation times. *Nat. Commun.*, **6**, 9459 (2015).

The work in Chapter 4 is adapted from the preprint:

D. E. J. Waddington, T. Boele, E. Rej, D. R. McCamey, N. J. C. King, T. Gaebel and D. J. Reilly, Phase-Encoded Hyperpolarized Nanodiamond for Magnetic Resonance Imaging. *arXiv*, 1709.0185 (2017).

Material in Chapter 5 is adapted from the publication:

E. Rej, T. Gaebel, **D. E. J. Waddington** and D. J. Reilly, Hyperpolarized Nanodiamond Surfaces. *J. Am. Chem. Soc.*, **139**, 193-199 (2017).

The material in Chapter 6 is adapted from the publication:

D. E. J. Waddington, M. Sarracanie, H. Zhang, N. Salameh, D. R. Glenn, E. Rej, T. Gaebel, T. Boele, R. L. Walsworth, D. J. Reilly and M. S. Rosen, Nanodiamond enhanced MRI via *in situ* Hyperpolarization. *Nat. Commun.*, **8**, 15118 (2017).

The work in Chapter 7 related to rat head imaging is adapted from the manuscript: **D. E. J. Waddington**, M. Sarracanie, N. Salameh, F. Herisson, C. Ayata and M. S. Rosen, An Overhauser-enhanced MRI platform for dynamic free radical imaging *in vivo*, *NMR Biomed.*, **31**, e3896 (2018).

Appendix D contains material adapted from the publication:

M. Sarracanie, C. D. Lapierre, N. Salameh, **D. E. J. Waddington**, T. Witzel and M. S. Rosen, Low-Cost High-Performance MRI, *Sci. Rep.*, **5**,

15177 (2015).

The convention for these manuscripts is that authors are listed in order of contribution. Senior authors are listed in reverse order of contribution at the end of the author list.

In addition to the statements above, in cases where I am not the corresponding author of a published item, permission to include the published material has been granted by the corresponding author.

I certify that to the best of my knowledge, the content of this thesis is my own work, unless acknowledged otherwise. This thesis has not been submitted for any degree or other purposes. I certify that the intellectual content of this thesis is the product of my own work and that all the assistance received in preparing this thesis and sources have been acknowledged.

David E. J. Waddington

Signature

Date

As supervisor for the candidature upon which this thesis is based, I can confirm that the authorship attribution statements above are correct.

David J. Reilly

Signature

Date

Contents

Abstract	2
Acknowledgements	3
Authorship Attribution and Originality Statement	5
1 Introduction	12
2 Background	17
2.1 Theranostics and Nanoparticles in Biomedicine	17
2.1.1 Magnetic Resonance Imaging	18
2.1.2 Computed Tomography	22
2.1.3 Optical Fluorescence	23
2.1.4 Positron Emission Tomography	24
2.2 MRI Gets a Boost	26
2.2.1 Acquiring Signals in NMR and MRI	26
2.2.2 Thermal Spin Polarization in an External Magnetic Field	29
2.3 Hyperpolarization	32
2.3.1 The Overhauser Effect	33
2.3.2 The Solid Effect	34
2.3.3 Other DNP Mechanisms	35
2.4 Taking DNP to MRI	36
2.4.1 Overhauser-enhanced MRI	37
2.4.2 Dissolution-DNP	37
2.5 DNP MRI with Nanoparticles	38
2.5.1 Silicon	39
2.6 Diamond	40

2.6.1	NDs in Biomedicine	41
2.6.2	Diamond DNP	42
3	Hyperpolarized Nanodiamond with Long Spin-Relaxation Times	45
3.1	Abstract	45
3.2	Introduction	46
3.3	Results	48
3.3.1	ESR spectra and nuclear spin relaxation	48
3.3.2	Brute-force hyperpolarization	54
3.3.3	Hyperpolarization via the solid effect	54
3.3.4	Hyperpolarization in the presence of water	58
3.3.5	ND impurity selection and surface modification	60
3.4	Discussion	62
3.5	Methods	64
3.6	Feasibility of imaging with hyperpolarized nanodiamonds	66
4	Phase-Encoded Hyperpolarized Nanodiamond for MRI	70
4.1	Abstract	70
4.2	Introduction	71
4.3	Intrinsic Defects as a Source of Polarized Spins	72
4.4	Spin Relaxation and Spin Dephasing	73
4.5	MRI with Hyperpolarized Nanodiamond	78
4.6	Animal Imaging	80
4.7	Phase-Encoded Hyperpolarization	81
4.8	Discussion	85
4.9	Methods	86
4.10	Additional Results	90
4.10.1	Hyperpolarization Mechanism and Nanodiamond Characterization	90
4.10.2	RARE Imaging	93
4.10.3	Retaining Polarization with Magnetic Shielding	96
4.10.4	Effect of T_2 relaxation times on resolution.	100

4.10.5	^{13}C Enrichment	100
4.10.6	Stability of nanodiamond solutions	101
4.10.7	Conditions for adiabatic transfer	102
5	Hyperpolarized Nanodiamond Surfaces	103
5.1	Introduction	103
5.2	Results	105
5.2.1	Nanodiamond Surfaces	105
5.2.2	Nanodiamond as a Hyperpolarizing Agent	107
5.2.3	Hyperpolarization at the Nanodiamond Surface	115
5.3	Discussion and Conclusion	119
5.4	Methods	120
6	Nanodiamond-enhanced MRI via <i>in situ</i>	
	Hyperpolarization	123
6.1	Abstract	123
6.2	Introduction	124
6.3	Results	125
6.3.1	The Overhauser effect in nanodiamond solutions	125
6.3.2	Overhauser-enhanced MRI with Nanodiamond	132
6.4	Discussion	136
6.5	Methods	139
6.6	Additional Data and Information	141
6.6.1	Additional characterization of Nanodiamond Solutions and the Overhauser Effect	141
6.6.2	EPR Spectra of Nanodiamond Solutions	144
6.6.3	Calculation of the coupling factor	144
6.6.4	Impact of the nanophase on the Overhauser effect	147
6.6.5	Probes and Imaging	147
7	A Platform for <i>in vivo</i> Overhauser-enhanced MRI	150
7.1	Abstract	150
7.2	Introduction	151
7.3	Materials and Methods	152

7.3.1	OMRI Scanner	152
7.3.2	NMR Design	153
7.3.3	EPR Design	155
7.3.4	Overhauser-enhanced MRI	157
7.3.5	Animal Preparation	159
7.3.6	<i>In vivo</i> Overhauser-enhanced MRI	160
7.3.7	Specific absorbance rate	160
7.4	Results	160
7.4.1	EPR Resonator Design	160
7.4.2	Probe performance	163
7.4.3	<i>In vivo</i> Overhauser-enhanced MRI	166
7.4.4	Specific absorbance rate	168
7.5	Discussion - Rat brain imaging	170
7.6	Conclusion - Rat brain imaging	171
7.7	A Probe For Whole Body OMRI in a Rat Model	172
7.7.1	Body Probe Design	172
7.7.2	Imaging Performance of the Body Probe	173
7.7.3	Cretaceous OMRI	175
7.7.4	<i>In vivo</i> Whole Body OMRI	177
7.7.5	Conclusion - Whole body imaging	179
8	Conclusion	181
	Appendix A Apparatus for X-band Hyperpolarization	184
A.1	DNP Probe Design	184
A.2	Probe Performance	186
A.3	Conclusion	188
	Appendix B ^1H MRI of of Nanodiamond Solutions at 7 T	189
	Appendix C Spin-Relaxation In Ruby Microparticles	195
	Appendix D Coil Development for Ultra-low Field MRI	198
D.1	Coil Design	199

D.1.1	Noise in ULF MRI	199
D.1.2	Signal and SNR	200
D.1.3	Coil Geometry	200
D.1.4	Q-factor	201
D.2	Imaging Sequences at ULF	203
D.3	Human Imaging	203
D.4	Conclusion	203
References		206

Chapter 1

Introduction

The last decade has seen enormous growth in the applications of nanotechnology to medicine. Advances in the synthesis of nanoparticles, in particular, have driven the development of new tools for the isolation and treatment of disease. Of the many nanoparticles available, nontoxic diamond nanoparticles have attracted disproportionate attention in biomedicine, with their surfaces being readily functionalized for applications including tissue growth and the targeted delivery of chemotherapeutics. A popular dream for nanodiamond, is to extend its proven therapeutic potential to the realm of diagnostics, and use it to track the targeted delivery of drugs to disease sites. Recent demonstrations, tracking nanodiamonds in subcellular environments via fluorescent defects known as NV centers, have been promising. However, for nanodiamond to reach its full diagnostic potential, techniques must be developed to noninvasively image nanodiamonds in regions that are not optically accessible. In this thesis, we develop new modalities for nanodiamond imaging that are based on magnetic resonance imaging (MRI), the gold standard of noninvasive imaging in the clinic.

The cornerstone of MRI is nuclear magnetic resonance (NMR), the physical mechanism by which nuclei, with non-zero spin, absorb and re-emit electromagnetic radiation (EMR) in the presence of an external magnetic field. The frequency of this EMR corresponds to the energy difference between Zeeman split nuclear spin states. In a typical NMR experiment, inductive

techniques are used to measure nuclear magnetization via emitted EMR. MRI is an extension of NMR, where images are generated by application of magnetic field gradients that encode information on the spatial distribution of nuclear spins via the frequency and phase of the received EMR. NMR is reliant on thermal polarization of nuclear spins, given by a Boltzmann distribution, as the induced signals measured are proportional to the population differences between nuclear spin states. As the energy difference between nuclear spin states, ~ 100 neV at 1 T, is significantly smaller than the thermal energy available at room temperature, 26 meV, thermal spin polarization of nuclei is very small. This means that there is a small population difference between the number of nuclear spins aligned and anti-aligned with the magnetic field, for the spin-1/2 systems of interest in this thesis. This small population difference, of order 0.001 % or lower, has limited the application of conventional MRI to imaging of ^1H nuclei, as the very high (~ 80 M) abundance ^1H nuclei overcomes the limitations of low thermal polarization.

Nanodiamonds can in theory be directly imaged with conventional MRI via spin-1/2 ^{13}C nuclei in the diamond lattice. This approach, however, is impractical in biological environments due to the sensitivity limitations of conventional MRI and the relatively low numbers of 1.1% abundant ^{13}C nuclei in nanodiamonds. We begin this thesis by using dynamic nuclear polarization (DNP) techniques to enable nanodiamond imaging with ^{13}C MRI. These DNP techniques allow us to achieve nuclear hyperpolarization, a situation where nuclear spin polarization is far from thermal equilibrium, by transferring large electronic spin polarizations onto ^{13}C nuclei. As MRI sensitivity scales with nuclear polarization, using DNP to create large, non-equilibrium polarizations enables the imaging of low-abundance, low-sensitivity nuclei such as ^{13}C .

The production of non-equilibrium polarizations with DNP is analogous to generating population inversion in optical systems. Essential to the operation of lasers, the generation of population inversion requires a quantized system with at least three energy levels, between which exist a high energy transition that can be externally ‘pumped’ as well as an alternate relaxation pathway consisting of a ‘fast’ relaxation transition followed by a ‘slow’ re-

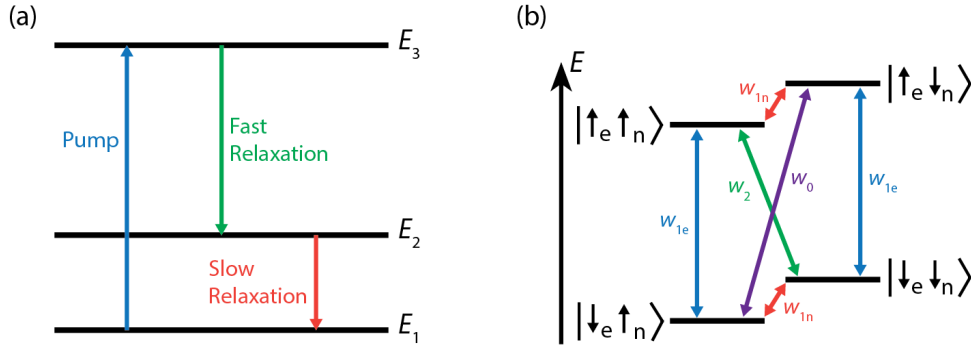


Figure 1.1: **Creating populations far from thermal equilibrium.** (a) Population inversion in three-level system. Boltzmann statistics dictate that, at thermal equilibrium, the number of particles in the E_1 state ($n(E_1)$) is greater than the number in the E_2 state ($n(E_2)$). However, if the relaxation $E_3 \rightarrow E_2$ (green) is significantly faster than $E_2 \rightarrow E_1$ (red) and the transition $E_1 \rightarrow E_3$ (blue) is pumped, a population inversion ($n(E_2) > n(E_1)$) can be achieved. (b) Energy level diagram of a coupled electron (e) and a spin-1/2 nucleus (n) in an external magnetic field. In the solid effect, if the w_1 (red) transition probability is sufficiently low, when w_2 transition (green) or w_0 transition (purple) is pumped, nuclei will accumulate in the $|\uparrow_n\rangle$ state or $|\downarrow_n\rangle$ state, respectively. In the Overhauser effect, if the w_1 (red) transition probability is sufficiently low, and if w_2 (green) $>$ w_0 (purple), when the electron paramagnetic resonance transition w_{1e} (blue) is pumped, a population inversion of nuclear spins will occur, with nuclei accumulating in the $|\downarrow_n\rangle$ state.

laxation transition (see schematic in Fig. 1.1(a)). When such a system is pumped, the slow relaxation pathway acts as a bottleneck, and members of the system accumulate at a higher energy state than the ground state, allowing the creation of a non-equilibrium population distribution.

To hyperpolarize nuclear spins with DNP, we use transitions between the four-level electron-nuclear spin system, shown in Fig. 1.1(b), that arises from the Zeeman splitting of a coupled spin-1/2 nucleus and spin-1/2 electron in a magnetic field. In Chapter 3, we use a DNP technique known as the solid effect to transfer spin polarization from intrinsic electronic defects in nanodiamond to nearby ^{13}C nuclear spins. Performing DNP at cryogenic temperatures and high magnetic fields gives large electron spin polarizations, hyperpolarizing the ^{13}C polarization by up to 10 000 times over room tem-

perature polarization. In implementing the solid effect, we pump either the w_0 or w_2 transition, with fast relaxation occurring via the w_{1e} transition. Crucial to the success of DNP in nanodiamond is the up-to-hours-long spin-lattice relaxation times of the ^{13}C nuclei in diamond, which means that the w_{1n} transition acts as a *very slow* relaxation transition. After attaining high ^{13}C polarizations in the core of the nanoparticles with DNP, the long spin-lattice relaxation time of ^{13}C nuclei in nanodiamond further allow transfer of the hyperpolarized nanodiamonds from the cryogenic DNP environment to an MRI scanner for subsequent imaging in a process known as dissolution-DNP. We present this implementation of nanodiamond imaging, a key result of this thesis, in Chapter 4.

After demonstrating ^{13}C imaging of nanodiamond, we turn our attention from nuclei in the core of nanodiamonds to nuclei at the nanodiamond surface. In doing so, we show in Chapter 5 that dangling electronic bonds at the nanodiamond surface can be used to hyperpolarize adsorbed ^1H nuclei via the solid effect at low magnetic field (~ 330 mT). We extend this result in Chapter 6, showing that at ultra low magnetic fields (6.5 mT) these same surface dangling bonds can be used to hyperpolarize ^1H nuclei in water solutions via the Overhauser effect. In this demonstration of the Overhauser effect we pump the w_{1e} transition in Fig. 1.1(b) and, as the w_2 rate is significantly faster than the w_0 rate, hyperpolarization of relatively long-lived ^1H nuclear spins near the nanodiamond surface occurs. We find that when we interleave pumping of the w_{1e} transition with conventional ^1H MRI, in a technique known as Overhauser-enhanced MRI, we can image nanodiamond in solution via a change in ^1H MRI signal. Given that our ultimate goal is the *in vivo* demonstration of nanodiamond imaging, we conclude our presentation of results in Chapter 7 with the demonstration of a homebuilt platform developed for *in vivo* imaging of a rat model with Overhauser-enhanced MRI.

This work traverses two key results, describing the first demonstrations of nanodiamond imaging via hyperpolarized ^{13}C MRI and nanodiamond imaging via Overhauser-enhanced MRI. Within this thesis, we detail the development of homebuilt hardware and custom techniques that have been necessary to enable hyperpolarized nanodiamond imaging. It is expected that the new

approaches to nanoparticle imaging we have developed in the course of this work will lead to new *in vivo* diagnostic applications of nanodiamond.

Chapter 2

Background

In this chapter, we begin by providing an overview of techniques used for nanoparticle imaging in biomedicine to put our goal, of enabling nanodiamond as a hyperpolarized MRI contrast agent, in context. We then explain the basics of hyperpolarized MRI, along with the current state of hyperpolarized nanoparticle imaging.

2.1 Theranostics and Nanoparticles in Biomedicine

The buzzword ‘theranostics’ has become popular to describe efforts that aim to combine diagnostic and therapeutic capabilities into a single agent [1]. Such a theranostic approach to medicine aims to improve treatment by providing personalized feedback on the efficacy of drug delivery to disease sites. Information on the efficacy of a given theranostic agent would allow subsequent medical decisions to be made on the response of the individual to treatment, with the goal of improved health outcomes.

Nanoparticles present themselves as excellent candidates to unite diagnostics and therapy. Their large surface areas allow for functionalization with high concentrations of therapeutic loads and imaging agents. Many nanoparticles also have intrinsic properties that grant them diagnostic imaging capabilities without surface functionalization. For diagnostic applications, it

is highly favorable if the nanoparticle itself is stable and nontoxic *in vivo*, although a polymer coating can often be used to stabilize the nanoparticle if necessary [2]. Further, to be effective theranostic agents, nanoparticles must have long blood circulation lifetimes, evading the body's immune system for long enough to allow targeted delivery of therapeutics. Evading immune clearance requires nanoparticles to be sized in a Goldilocks zone of 5-200 nm [3]. Below 5 nm, nanoparticles are rapidly cleared by the renal system (kidneys) and above 200 nm they are cleared by the reticuloendothelial system (white blood cells). For nanoparticles in this Goldilocks zone, circulation lifetimes can be further improved with neutral surface coatings and by avoiding functionalization with targeting ligands that trigger clearance by macrophages.

As might be expected, designing nanoparticles and surface functionalizations to fulfill the above criteria and effect drug delivery is inherently nontrivial [4, 5]. However, for the purpose of this thesis we allow such 'targeting' issues to remain a biochemistry problem and instead turn our focus to the problem of how to image nanoparticles once they have reached their destination of interest. Over the following few pages, I provide an overview of some leading techniques for noninvasive imaging of nanoparticles. As we shall see, there is no one 'magic bullet' for nanoparticle imaging, with each technique presenting at least one major limitation and as such, the differing techniques lend themselves to different theranostic applications. For detailed reviews on the plethora of nanoparticle imaging techniques being developed, the reader is encouraged to see References [6–11].

2.1.1 Magnetic Resonance Imaging

As the primary topic of this thesis, we begin the overview of nanoparticle imaging techniques with a high level view of what is possible with MRI. In Section 2.2, we will delve more deeply into the theory of NMR and how we can create new forms of MRI contrast with hyperpolarization.

Magnetic resonance imaging is the gold standard of noninvasive clinical imaging due to its high resolution, soft tissue contrast and depth of pene-

tration. Widely used for anatomical imaging, conventional MRI signals arise from the inductive detection of radio-frequency induced precession of ^1H nuclear spin. Whilst the MRI technique is intrinsically insensitive, detecting only 1 in 100 000 ^1H nuclei at 3 T (see Section 2.2.2), the *in vivo* concentration of detected aqueous ^1H nuclei is extremely high (~ 80 M), which results in high clinical sensitivity in practice.

Direct MRI of Nanoparticles

Extending the successes of clinical ^1H MRI to nanoparticle imaging has proven challenging, largely because the maximum safe concentration of nanoparticles *in vivo* is orders of magnitude smaller than the ^1H nuclei concentration [12]. In fact, it is the case in general that MRI sensitivity is the limiting factor when imaging spin-1/2 nuclei other than ^1H . Nonetheless, imaging of nanomaterials via alternate spin-1/2 nuclei is a subject of active research, a leading example of which is the tracking of high gyromagnetic ratio ^{19}F nuclei in perfluorocarbon nanoemulsions [13–15]. Such direct imaging of nanoparticles is favored for its background free signal, allowing unambiguous visualization of nanoparticle location in co-registered ^1H MRI scans, as is shown in the example in Fig. 2.1. High-resolution imaging of such perfluorocarbon nanoemulsions is still, however, limited by sensitivity. Direct imaging of other nanoparticles with MRI will require dramatic increases in sensitivity, something that can occur thanks to new hyperpolarization techniques that boost the size of MRI signals from nanoparticles by over a factor of 10 000 [16]. We will delve into such techniques in detail in Section 2.2.

Indirect MRI of Nanoparticles

The high sensitivity of ^1H imaging with clinical MRI has led to the development of techniques that indirectly detect nanoparticles through changes in the ^1H MRI signal. In this section, we describe T_1 , T_2 and PARACEST contrast mechanisms, which are the most popular mechanisms for generating ^1H contrast in nanoparticle theranostics.

Nanoparticles with magnetic cores, such as super-paramagnetic iron oxide

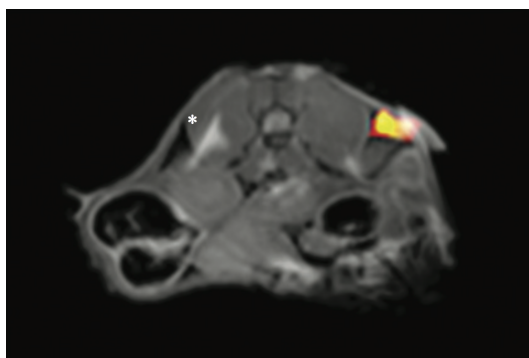


Figure 2.1: **Co-registered $^1\text{H}:$ ^{19}F MRI of glioma cells in a mouse flank.** The glioma cells are labeled with ^{19}F nanoemulsion and the ^{19}F signal plotted in colorscale, overlaying the ^1H anatomy scan in gray-scale. Reproduced with the permission of Macmillan Publishers Ltd from Ref. [15], copyright 2016.

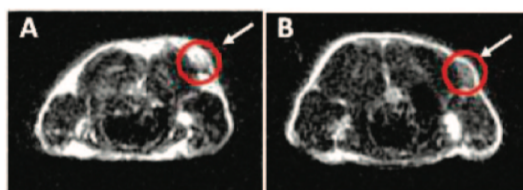


Figure 2.2: **MRI of implanted tumors in a mouse brain with T_2 contrast.** (a) Without SPIONs the tumor (red circle) appears bright. (b) With targeted SPIONs the tumor (red circle) appears dark. Reproduced with permission from Ref. [18]. Copyright 2008 ACS.

nanoparticles (SPIONs), create local variations in magnetic field on the microscopic level [3]. These field fluctuations result in fast dephasing (short T_2 or spin-spin relaxation time) of the spin precession of ^1H nuclei in the vicinity of nanoparticles and a corresponding reduction in the ^1H MRI signal, as shown in Fig. 2.2. Such T_2 contrast effects, have been used for imaging SPIONs for over 25 years [12], and are now often used for clinical diagnosis of cancers of the liver and spleen [3]. The key limitation of T_2 -contrast effects is that detecting the presence of nanoparticles via a reduction in signal intensity (negative contrast) is problematic in or near regions of low signal, typically requiring the acquisition of lengthy pre-/post-comparison images, during which various types of biological noise are introduced [17].

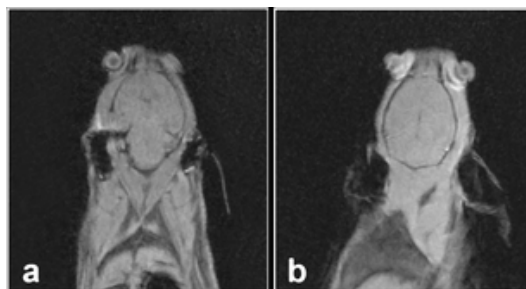


Figure 2.3: **MRI of Gd loaded nanoparticles in a mouse.** Images for the coronal orientation are shown without (a) and after (b) administration of targeted Gd loaded nanoparticles. The signal intensity in the brain is approximately 1.5 times higher after nanoparticle administration. Reproduced with permission from Ref. [24]. Copyright 2013 World Molecular Imaging Society.

Another approach, useful for imaging nanoparticles that are not intrinsically magnetic, is to incorporate a heavy metal ion with multiple unpaired electrons (traditionally Gd^{3+}) into the nanoparticle. Such nanoparticles can be synthesized by grafting gadolinium to the surface of the nanoparticle [19, 20] or by encapsulating gadolinium in the core of liposomal nanoparticles [21]. For these Gd-enhanced nanoparticles, the unpaired electrons on the metal ions shorten the time required for refreshment of the local ^1H MRI signal after radio-frequency perturbation (short T_1 or spin-lattice relaxation time) [22]. Over multiple acquisitions, the shorter signal refreshment time leads to a larger signal intensity in the presence of nanoparticles, as can be seen for the example in Fig. 2.3. Whilst the increase of signal intensity with T_1 imaging is preferred over the negative contrast of T_2 imaging, its reliance on detecting small changes against a large background ^1H signal, and concerns over the long term toxicity of gadolinium [23], are obstacles to increased use.

In response to these limitations an alternative technique known as Paramagnetic Chemical Exchange Saturation Transfer (PARACEST) is becoming popular for nanomaterial imaging [25, 26] because of the ability to turn nanoparticle contrast on and off. In this mechanism, exchangeable protons at the nanomaterial surface experience a chemical shift, allowing local quench-

ing of the ^1H magnetization by a frequency selective radio-frequency pulse. Whilst the contrast achieved when imaging nanomaterials with PARACEST is strongly dependent on the chemistry of proton exchange, it is likely that new theranostic applications of this young MRI technique will continue to emerge [27].

2.1.2 Computed Tomography

Computed Tomography (CT) is an imaging technology based on the absorption and scattering of high energy photons. CT reconstructs 3D images of the body's internal structure by using computational algorithms on information gathered by passing x-rays through the body at many different angles and detecting the x-ray intensity as it exits the body. As the x-ray beam travels through the body, it is primarily absorbed and scattered via the photoelectric effect and Compton scattering, respectively. As such, contrast in CT arises from differences in the electron density between materials, with materials of high atomic number (Z), displaying a higher CT signal.

The sensitivity of CT to materials with high Z has led to the development of nanoparticles synthesized from heavy elements as contrast agents for x-ray imaging [28,29]. However, due to the general toxicity of heavy elements, tracking of nanoparticles with CT has mainly been limited to a few types of high Z nanoparticles that are nontoxic, such as micelles with iodine in the core [30], barium nanoparticles [31], and gold nanoparticles [32]. The long circulation times and uptake by macrophages of these CT-imageable nanoparticles has made them popular for targeting of diseases such as atherosclerosis and cancer, an example of which is shown in Fig. 2.4 [6]. Whilst the poor soft tissue contrast of CT imaging is well known, new techniques, such as spectral CT, which measures the energy dependence of x-ray absorption to generate contrast, are rapidly overcoming contrast limitations with nanoparticle CT [33]. However, the fundamental sensitivity limits of the nanoparticle CT (estimated to be 5.9 mM for gold nanoparticles), and concerns over radiation doses in the long term, are barriers to more widespread use [28]. For further information on CT with nanoparticle contrast agents, see Refs. [28,29]

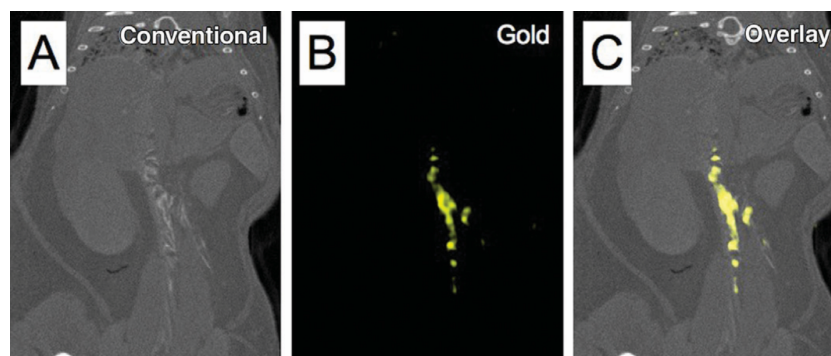


Figure 2.4: **CT imaging of the accumulation of gold nanoparticles in the arteries of atherosclerotic mice.** (a) Conventional CT images, showing anatomical structure and gold nanoparticles as a whiter region in the center of the image. (b) Spectral CT images, showing the location of gold nanoparticles. (c) Overlay of conventional CT and spectral CT images. Reproduced from Fig. 4 of Ref. [33] with permission from the RSNA.

for review articles.

2.1.3 Optical Fluorescence

Imaging of nanoparticles with biocompatible optical techniques has become popular for the high resolution, high sensitivity and richness of contrast that can be achieved [34]. Nanoparticles used with fluorescence techniques derive their fluorescence either intrinsically, as is the case for some quantum dots, or via fluorophore labeling. Optical tracking of such nanoparticles has been applied with great success in subcellular imaging applications, revealing new cellular processes related to interactions with nanomaterials [35,36]. Beyond subcellular imaging however, biomedical applications are limited by the penetration depth of light into soft tissue. To extend the biomedical applications of fluorescence imaging, targeted nanoparticles that fluoresce in the near infrared, where penetration depths are greater than visible light, have been developed [37]. Such nanoparticles have enabled successful imaging of tumors in preclinical studies, as shown in Fig. 2.5.¹ However, extending the

¹ACS AuthorsChoice license: This is an unofficial adaptation of a figure from an article that appeared in ACS Nano. ACS has not endorsed the content of this adaptation or the context of its use.

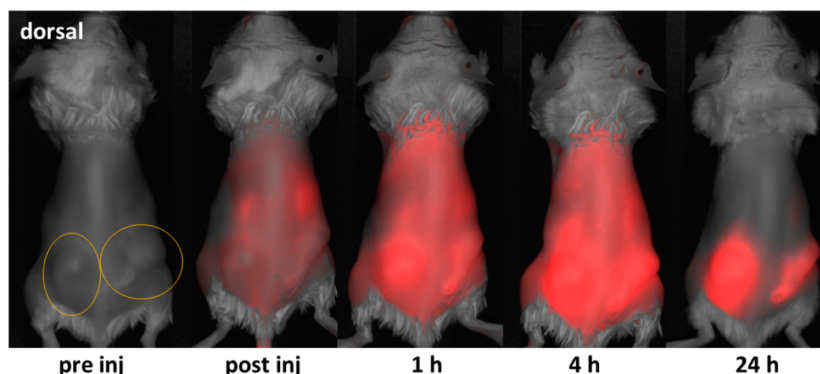


Figure 2.5: **Fluorescence imaging of quantum dots in a tumor bearing mouse at different time points.** Circles indicate tumor locations. Red color: quantum dot fluorescence. Reproduced from Ref. [37] under an ACS AuthorsChoice License.

success of these preclinical studies on small animals to human applications would appear impractical at present without invasive techniques or further improvement in penetration depth [38].

2.1.4 Positron Emission Tomography

Positron emission tomography (PET) is a medical imaging technique popular for functional studies due to its high sensitivity, being able to detect tagged molecules such as glucose at picomolar concentrations [39]. Images are generated with PET by the detection of gamma ray pairs that are emitted by positron-emitting radionuclides incorporated into tracer molecules. The high sensitivity of PET stems from the fact that each gamma emission event, which corresponds to decay of a single atom, can lead to a detectable signal [7]. Labeling of functionalized nanoparticles with radionuclides, such as ^{64}Cu and ^{89}Zr , have enabled PET imaging of diseases such as cancer [40]. The materials most popular as PET-nanoparticle tracers include polymers and dextrans [9]. Such PET nanoparticle probes can be tracked for up to tens of hours depending of the half life of the radionuclide used. Despite the high sensitivity of nanoparticle tracking with PET approaches, spatial resolution is still limited to a few mm by the fundamental resolution limits of PET [41].

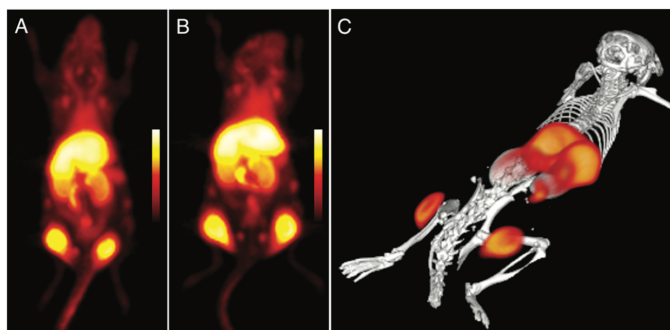


Figure 2.6: **PET imaging of ^{89}Zr -labeled dextran nanoparticles in mice bearing flank tumors.** (a,b) Two different mice with PET showing nanoparticle accumulation in tumors. (c) 3D rendering of the animal in a with PET-CT. Reproduced with permission from Ref. [46]. Copyright 2011 ACS.

One approach to overcoming these resolution limits is the development of hybrid nanoparticles that can be imaged with PET and a higher resolution imaging technique such as CT or MR [42, 43]. An example of this PET-CT approach to tumor imaging is shown in Fig. 2.6. We also note that whilst PET is a well established technique for imaging when there is a clinical need, its repeated use has been linked to significantly increased rates of cancer due to the radioactive nature of the modality [44]. For further details on the use of PET in nanoparticle tracking, the reader is directed towards the reviews found in Refs. [40, 45].

Other Modalities

A variety of other modalities for noninvasive *in vivo* nanoparticle imaging are also the subject of active research. Examples of such other modalities are ultrasound [47], photoacoustic imaging [48, 49], single-photon emission computed tomography [50], magnetic particle imaging [51, 52] and Raman imaging [53]. Whilst many of these approaches show promise, for now, they all suffer from limited penetration depth, limited sensitivity and/or a requirement to use ionizing radiation.

2.2 MRI Gets a Boost

Having established the strengths and weaknesses of various nanoparticle techniques we choose to focus now, and for the rest of this thesis, on nanoparticle imaging with MRI. But why MRI?

Of all the leading imaging techniques we described in detail, MRI is the only one to not be limited by penetration depth issues or concerns over the use of ionizing radiation. Indeed the key limitation of MRI is its sensitivity. However, recent developments in dynamic nuclear polarization (DNP) techniques are redefining the imaging sensitivity possible with MRI. Dropping the sensitivity limits of MRI creates opportunities for developing noninvasive, safe, high resolution forms of contrast.

So, why MRI? Because MRI's future just became *hyperpolarized*.

In this section we provide background to the sensitivity limitations of NMR and MRI. We then explain the physics behind hyperpolarization and explain how it can be used.

2.2.1 Acquiring Signals in NMR and MRI

Signal acquisition in NMR and MRI occurs via the inductive detection of the precessing magnetic moments of nuclear spins. We begin our discussion of signal detection by considering the precession of a magnetic moment in an external magnetic field [54].

When a magnetic moment $\vec{\mu}$, associated with the angular momentum of a particle, is placed in a static magnetic field \vec{B} , it experiences a torque $\vec{\tau}$ given by the cross product:

$$\vec{\tau} = \vec{\mu} \times \vec{B}. \quad (2.1)$$

Hence, if $\vec{\mu}$ and \vec{B} are not parallel, the particle will experience a torque and resulting change in angular momentum. This torque causes the magnetic moments of such particles to precess around the static magnetic field.

In NMR experiments, the magnetic moments of interest are associated with nuclei of non-zero, typically one-half, nuclear spin. When placed in

a magnetic field, these nuclei will, on average, align in parallel with the magnetic field on a timescale known as the spin-lattice relaxation time or T_1 . With excitation of the nuclei via a resonant radio frequency pulse, known as a $\pi/2$ pulse, the resulting nuclear magnetization can be rotated such that it is perpendicular to the magnetic field. After this $\pi/2$ pulse, the nuclear spins will precess around the static magnetic field at a characteristic frequency, known as the Larmor frequency, that is determined by the magnetic field strength and the type of nucleus.

As nuclear magnetization reorients during nuclear precession, it gives rise to a fluctuating magnetic field. If an open loop is placed around the nuclei, oriented perpendicular to the static magnetic field, these magnetic field fluctuations will induce a voltage across its ends due to Faraday's law. Such inductive detection techniques are the primary means of acquiring signals in NMR experiments, with the induced voltage directly proportional to the magnitude of the magnetic field fluctuations [55]. As the voltage induced in a pickup coil by a precessing nuclear spin is extremely small, large ensembles of nuclear spins must be measured in practice for a sufficient signal-to-noise ratio (SNR). After a $\pi/2$ pulse, the magnetization of the nuclear spin ensemble decays over a timescale known as the spin-spin relaxation time or T_2 . Hence, the detected signal is known as a free induction decay (FID), where T_2 is determined by the rate at which nuclear spins in the sample lose phase coherence.

Turning NMR signals into images with MRI requires the use of magnetic field gradients. We explain this by considering the example, shown in Fig. 2.7a, where two test tubes containing water are placed in a 7 T magnetic field with a linear magnetic field gradient applied in the direction of separation. If a $\pi/2$ pulse is applied to this system, the resulting NMR signal can be acquired (see Fig. 2.7b). Taking the Fourier transform of the NMR signal (see Fig. 2.7c) reveals that the NMR signal has frequency components at values corresponding to the Larmor frequencies of ^1H at the locations of test tubes containing water. In this way, a magnetic field gradient can be used to create one-dimensional spatial information from NMR signals. In practice, three-dimensional MRI images are acquired with sequences that

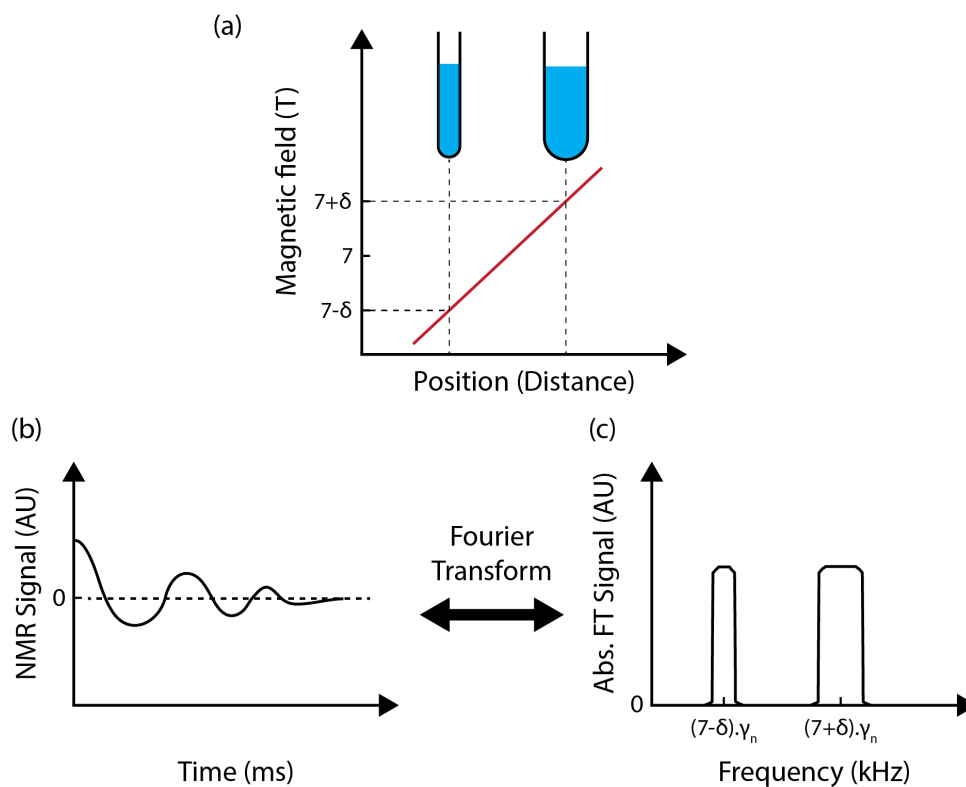


Figure 2.7: **Using magnetic field gradients to encode spatial information.** (a) Schematic of a linearly varying magnetic field in a 7 T MRI scanner. Two test tubes containing water, and hence, ^1H nuclear spins, are placed in the positions shown. (b) The NMR signal acquired, from the samples in a magnetic field gradient shown in a, after a $\pi/2$ pulse has been applied (c) Fourier transform of the NMR signal in b.

leverage multiple NMR pulses to dynamically control the orientation and phase properties of nuclear spins. Two additional magnetic field gradients, in mutually orthogonal directions to the first, are also used to encode further position information via a combination of phase and selective pulses that only excite partial volumes of the nuclear spins being imaged, see Reference [56] for further details.

Whilst MRI is highly effective at turning NMR signals into images, the use of frequency to encode position means that significantly larger frequency bandwidths are required for acquisition, reducing the comparative SNR of MRI. For acceptable image quality, conventional MRI requires the nuclear magnetization in each voxel to be the order of the magnetization of 10^{13} aligned ^1H nuclei [56]. However, as the magnetic moments of nuclear spins are rarely aligned by thermal polarization, we require much larger total numbers of spins to image with conventional MRI. We now calculate the extent of thermal polarization at conventional fields and temperatures as motivation for hyperpolarization techniques.

2.2.2 Thermal Spin Polarization in an External Magnetic Field

The allowed states of a spin-1/2 particle placed in a static magnetic field are quantized into an aligned, spin-up state $|\uparrow\rangle$ and an anti-aligned, spin-down state $|\downarrow\rangle$ due to the Zeeman effect. In conventional NMR, MRI and Electron Paramagnetic Resonance (EPR) experiments, ensembles of spin-1/2 particles are placed in magnetic fields up to 23 T in strength. Spins then distribute between the two states with the statistics of a Boltzmann distribution. This leads a net polarization P of the ensemble given by:

$$P = \frac{n_{|\uparrow\rangle} - n_{|\downarrow\rangle}}{n_{|\uparrow\rangle} + n_{|\downarrow\rangle}} \quad (2.2)$$

$$= \tanh \frac{\gamma \hbar B_0}{2k_B T}, \quad (2.3)$$

where $n_{|\uparrow\rangle}$ is number of nuclei in the aligned state, $n_{|\downarrow\rangle}$ is the number of nuclei in the anti-aligned state, γ is the nuclear gyromagnetic ratio, \hbar is the reduced Planck constant, B_0 is the magnitude of the external magnetic field, k_B the Boltzmann constant and T the temperature [54].

For a ^{13}C nucleus ($\gamma_{^{13}\text{C}} = 10.705 \text{ MHz/T}$), at 300 K and 3 T, thermal polarization equates to 0.0002% or 500 002 nuclei aligned with the field for every 500 000 nuclei aligned against the field. This means that, in our inductive detection of nuclear precession, we only see 2 nuclei out of every 1 000 000, as inductively detected signals from the rest of the spins cancel. Such low spin polarizations are the bane of NMR, especially for nuclei of lower abundance and gyromagnetic ratio than ^1H .

Electron spins have much higher gyromagnetic ratios than nuclei ($\gamma_e \sim 28 \text{ GHz/T}$), leading to spin polarizations that are orders of magnitude higher at the same magnetic fields and temperatures. For an electron at 300 K and 3 T, the thermal polarization is 0.7%, leading to a much higher number of observed spins in electron paramagnetic resonance (EPR) spectroscopy than in NMR spectroscopy and hence, the much higher sensitivity of EPR. Thermal polarization can also be further increased by lowering the temperature.

Transferring the high spin polarization of electron spins to coupled nuclear spins is at the heart of DNP and this thesis. In Fig. 2.8 we summarize the thermal polarization of electrons and nuclei at various field strengths and temperatures. In Chapters 3 and 4 we use the coupling between ^{13}C nuclei and electron spins at 4 K to hyperpolarize ^{13}C nuclei. Then we use the coupling between ^1H nuclei and electrons at room temperature to hyperpolarize ^1H nuclei at various field strengths (300-500 mT) in Chapter 5 and at 6.5 mT in Chapters 6 and 7.

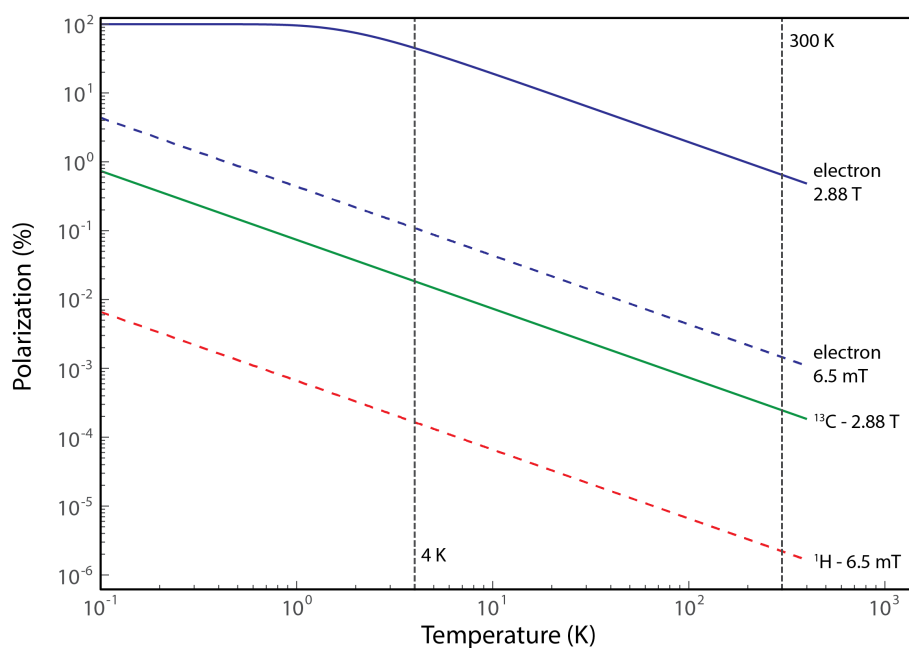


Figure 2.8: **Thermal polarization of electrons and nuclei in a static magnetic field as a function of temperature.** Polarization is shown for ^1H nuclei at 6.5 mT (red) and ^{13}C nuclei at 2.88 T (green) as well as for electrons at both these field strengths (blue).

2.3 Hyperpolarization

The term *hyperpolarization* describes any of a range of techniques that move a spin system to non-equilibrium polarizations that are larger than that found at equilibrium after thermal polarization. In the quest to boost NMR and MRI sensitivity, a range of hyperpolarization techniques have been developed, including the notable examples of:

- Spin-Exchange Optical Pumping (SEOP) - Small amounts of alkali metals are vaporized and atomic transitions are pumped with a laser, leading to near unity polarization of electron spins. This electronic spin polarization is then transferred to nuclear spins of noble gases such as ^3He and ^{129}Xe by atomic collisions in the gaseous phase [57].
- ParaHydrogen Induced Polarization (PHIP) - The proportion of the spin isomer parahydrogen in molecular hydrogen can be enriched from 25% at room temperature to 50% at 70 K with the use of an iron-oxide catalyst. Chemical reactions of hydrogen with, typically organic, molecules then allow transfer of spin polarization to nuclei such as ^{13}C . A newer PHIP technique called Signal Amplification by Reversible Exchange (SABRE) allows transfer of polarization to a substrate molecule without it chemically reacting with parahydrogen [58].
- Brute force hyperpolarization - Nuclear spins are cooled to extremely low temperatures and placed in very high magnetic fields, increasing their thermal polarization. The spin containing sample can then be rapidly warmed and transferred to a different strength magnetic field where it will remain in its hyperpolarized state for a characteristic time [59].
- Dynamic Nuclear Polarization (DNP) - The thermal spin polarization of an electron spin reservoir is transferred to a coupled nuclear spin reservoir by high frequency, typically microwave, electromagnetic radiation [60]. DNP processes can lead to a maximum enhancement of the nuclear spin polarization given by the relative size of the electron

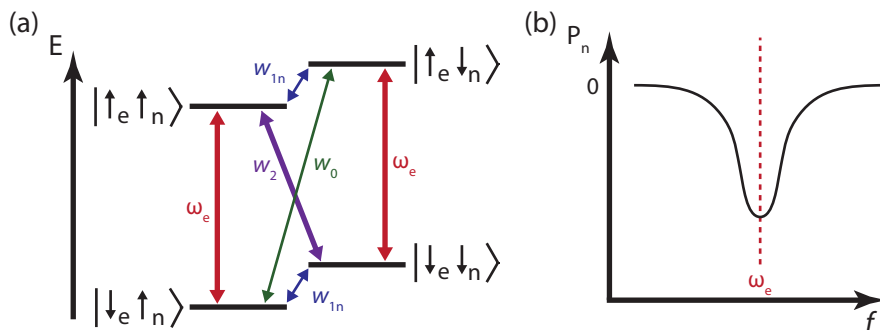


Figure 2.9: **The Overhauser Mechanism.** (a) The Zeeman split, four-level energy diagram of an electron-nucleus pair in a magnetic field. Double quantum w_2 , zero quantum w_0 and nuclear w_{1n} transition rates are shown. (b) Nuclear polarization versus the microwave pump frequency. When $w_2 > w_0$, negative nuclear polarization accumulates when the system is pumped at the electron spin resonance frequency (ω_e).

and nuclear gyromagnetic ratios (γ_e/γ_I). This factor gives a maximum enhancement of 660 for ^1H nuclei and 2,620 for ^{13}C nuclei.

In this thesis, we achieve hyperpolarization of diamond nanoparticles and ^1H via DNP techniques. Hence, we now explore mechanisms for performing DNP with a focus on the Overhauser effect and solid effect mechanisms that are of most importance in the results we present. For reviews and books on the topic of hyperpolarization see Refs [58, 60–64].

2.3.1 The Overhauser Effect

The Overhauser effect is a DNP technique that relies on cross-relaxation mechanisms between electron and nuclear spins to build up nuclear hyperpolarization when the electron spin transition is saturated [65]. Whilst originally demonstrated in metals [66, 67], the Overhauser effect has found its main applications in the hyperpolarization of nuclear spins in solution, where the necessary relaxation processes occur via time-dependent dipolar or scalar interactions [63].

The energy level diagram describing the Overhauser effect is shown in Fig. 2.9. When the system is pumped at the electron spin resonance frequency ω_e ,

the populations in $|\uparrow_e\rangle$ and $|\downarrow_e\rangle$ states are equalized. If the double-quantum transition rate w_2 is larger than the zero-quantum transition rate w_0 , as is the case in systems where cross-relaxation is mediated by dipolar coupling [68], and if the nuclear relaxation rate w_{1n} is sufficiently slow, then nuclear spins will become hyperpolarized in the $|\downarrow_n\rangle$ state.

Hyperpolarization via the Overhauser effect relies on the condition $\omega_e\tau < 1$, where τ is the correlation time of electron and nuclear spins. Hence, the Overhauser effect is typically performed at low magnetic fields ($B_0 < 500$ mT) where the electron spin resonance frequency is small enough for the inequality to hold [63,68].

2.3.2 The Solid Effect

The solid effect is a two-spin DNP process in which polarization transfer between electron and nuclear spins occurs via driven flip-flip or flip-flop transitions [60]. The energy level diagram describing the solid effect is shown in Fig. 2.10(a). In the solid effect, a microwave field is used to directly drive the transitions shown at energies of $\omega_e - \omega_n$ or $\omega_e + \omega_n$, simultaneously flipping both an electron and a nuclear spin. Such combined spin flips are known as ‘forbidden transitions’ as they cannot occur through strictly first order processes. However, mixing of the base states via the time independent spatial hyperfine interaction in solids means that these processes become weakly allowed via second order transitions [62]. Hence, when the microwave drive field is sufficiently large and the nuclear spin-relaxation rate is sufficiently slow, positive or negative nuclear hyperpolarization can be created, as shown in Fig. 2.10(b). After a flip-flop or flip-flip transition is pumped, the electron spin, which has a very short spin-lattice relaxation time T_{1e} , is rapidly reinitialized via the ω_{1e} transitions shown. This rapid relaxation allows the same electron spin to be used for hyperpolarization of many nuclei. The non-equilibrium spin polarization can then also spread to other nuclei in a solid via nuclear spin diffusion, allowing hyperpolarization of nuclei that are not coupled to electrons.

The solid effect requires the inhomogeneous electron linewidth Δ_e and

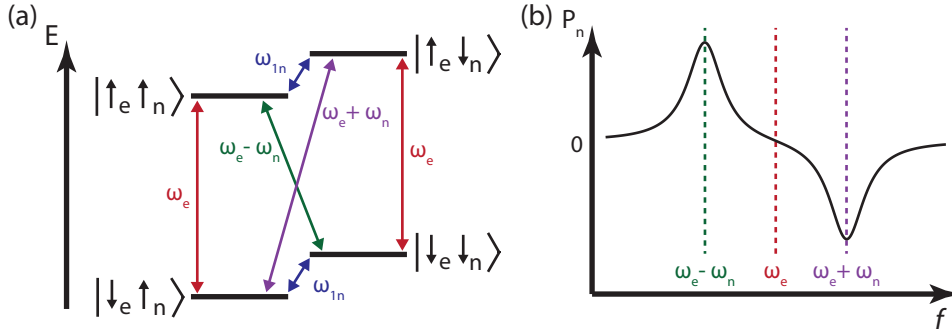


Figure 2.10: **The Solid Effect.** (a) The Zeeman split, four-level energy diagram of an electron-nucleus pair in a magnetic field. Driving forbidden transitions at $\omega_e - \omega_n$ or $\omega_e + \omega_n$ simultaneously flips nuclear spins. (b) Nuclear polarization versus saturation frequency. Positive hyperpolarization of nuclear spin occurs when driving at $\omega_e - \omega_n$ and negative hyperpolarization occurs when driving at $\omega_e + \omega_n$.

the homogeneous electron linewidth δ_e to be smaller than the nuclear Larmor frequency ω_n . For spin-1/2 nuclei in solids, these conditions are typically satisfied at low temperature when electrons with long spin lifetimes are present [62]. If the conditions are not satisfied, simultaneous saturation of both transitions can occur, leading to reduced enhancements in a process known as the differential solid effect.

2.3.3 Other DNP Mechanisms

The Overhauser effect and the solid effect are of most interest for the hyperpolarization that is described in this thesis. DNP can also be achieved by a variety of other mechanisms, including:

- *Cross effect* - The cross-effect is a three-spin DNP mechanism in which two dipolar coupled electron spins and one nuclear spin simultaneously flip when driven with a resonant microwave field. For this process to occur, the electron linewidth must be inhomogeneously broadened such that the Larmor frequencies can satisfy the condition: $\omega_n = \omega_{e1} - \omega_{e2}$, and the electron linewidth satisfies the condition: $\Delta_e > \omega_n > \delta_e$ [63].
- *Thermal mixing* - Thermal mixing is similar to the cross effect but

occurs when the electron linewidth is homogeneously broadened such that $\omega_n < \delta_e$. In this situation, the electron-nuclear system can be thought of as three interacting spin baths: the electron dipolar system, the electron Zeeman system and the nuclear Zeeman system. Off resonance saturation of the electron spin resonance creates a polarization gradient across the electron dipolar system, which then cools the spin baths in contact with it, leading to nuclear hyperpolarization [69].

- *Pulsed DNP* - A range of DNP techniques based on coherent microwave pulses, rather than cw mechanisms, also exist. Such techniques, carried out in the rotating frame, can lead to significantly larger transition probabilities for the forbidden transitions, leading to larger nuclear polarizations. Examples of pulsed DNP techniques include Nuclear Orientation via Electron Spin Locking (NOVEL) [70], the integrated solid effect [71] and the dressed-state solid effect [72].

For more information on DNP processes, see Refs [60, 63, 69, 73].

2.4 Taking DNP to MRI

Approximately 25 years after the 1940s discovery of NMR [74, 75], Paul Lauterbur introduced the concept of using magnetic field gradients to encode position information by way of an NMR frequency shift and in doing so, took the first ever images with MRI [76]. Extending DNP, first demonstrated only a few years after NMR [54, 66, 67], to MRI took much longer. Despite DNP being applied to enhance sensitivity or yield spectroscopic information in NMR experiments [77], its application to MRI was largely impeded by high electron frequencies. High electron frequencies, typically in the microwave regime, limit the penetration depth of the resonant magnetic field required for DNP and cause heating in liquid environments. In this section, we discuss two methods that overcome these limitations to enable DNP MRI.

2.4.1 Overhauser-enhanced MRI

Overhauser-enhanced MRI (OMRI) [78], also known as Proton-Electron Double Resonance Imaging (PEDRI) [79], leverages polarization transfer, via the Overhauser effect, from an unpaired electron present in a contrast agent molecule to ^1H nuclei in water. The Overhauser effect, driven by EPR saturation and mediated by dipolar cross-relaxation, can lead to an enhancement of the ^1H nuclear spin polarization by up to $-\frac{\gamma_e}{2\gamma_{^1\text{H}}} = -330$, which can then be imaged with conventional MRI techniques. Note that in OMRI, the hyperpolarization occurs *in situ*, with interleaved hyperpolarization and MRI acquisition. To overcome penetration depth and tissue heating issues that result from EPR saturation at high frequencies, OMRI is typically performed at ultra low magnetic field (<10 mT), where the lowering of electron resonance frequencies makes these issues manageable. This reduction in magnetic field strength causes a significant drop in nuclear polarization and thus, MRI sensitivity, which can be addressed through MRI hardware and sequence design, as we discuss in the course of this thesis.

2.4.2 Dissolution-DNP

Dissolution DNP (d-DNP) is a technique that utilizes solid-state DNP effects to achieve near unity hyperpolarization of nuclear spins at cryogenic temperatures (~ 1 K) and magnetic fields of a few Tesla [80]. To perform d-DNP, a radical species is mixed with a biomolecule enriched with a nuclear spin-1/2 isotope (typically ^{13}C), and then frozen inside a high field magnet. Irradiation of the frozen sample with microwaves at $\omega_e + \omega_n$ or $\omega_e - \omega_n$ leads to the buildup of high nuclear spin polarizations. The sample is then rapidly melted and then transferred to the MRI scanner, with the hyperpolarized contrast agent typically injected intravenously [81, 82].

The combination of DNP and the brute force ‘temperature jump’ in d-DNP allows the enhancement of ^{13}C polarization by more than 10 000 times [64]. The availability of such large ^{13}C polarizations in biomolecules has seen the rapid translation of d-DNP applications such as metabolic imaging [82], with the clinical application of d-DNP prostate cancer imaging re-

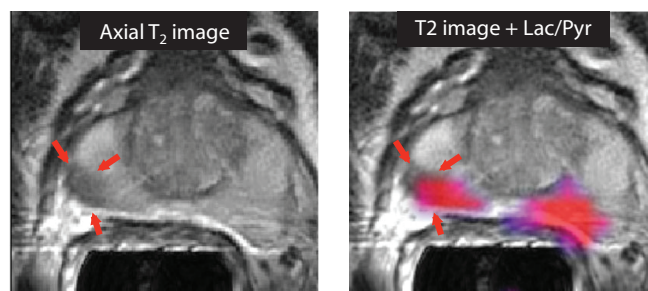


Figure 2.11: **Dissolution DNP images from a patient with prostate cancer.** The T_2 weighted ^1H image (left) shows a region of reduced signal intensity indicated by red arrows. The T_2 weighted image with lactate/pyruvate (right) shows voxels with a heightened concentration of ^{13}C signal from hyperpolarized $[1-^{13}\text{C}]$ lactate/ $[1-^{13}\text{C}]$ pyruvate in pink. Reproduced with permission from Ref. [83]. Copyright AAAS 2013.

cently demonstrated (see Fig. 2.11) [83]. A key limitation of d-DNP is that once in the liquid state, the T_1 lifetime of the hyperpolarized ^{13}C nuclei is a minute at most, after which the nuclear polarization rapidly returns to thermal equilibrium. Thus, the timescale over which metabolites can be imaged is limited to a couple of minutes at most. Further, as hyperpolarization and imaging occur in separate systems, all imaging with d-DNP must be single-shot. Despite these limitations, the release of a commercial polarizer in 2014,² making d-DNP widely available, has led to the discovery of new applications for d-DNP across chemistry, biology and medicine [84].

2.5 DNP MRI with Nanoparticles

Tracking nanoparticles via d-DNP is particularly attractive for theranostic applications, as when made of materials with dilute concentrations of spin-1/2 nuclei, they can have spin-relaxation times of many hours [85]. Such material candidates include nanodiamonds (NDs) [86] with 1.1% ^{13}C and silicon nanoparticles [87] with 4.7% ^{29}Si . Being able to image nanoparticles

²The GE SPINlab MRI Hyperpolarizer, released in 2014, integrates quality control and the ability to hyperpolarize numerous samples simultaneously, enabling the use of d-DNP in clinical applications.

with positive contrast over a time period of hours, using d-DNP, could enable new modalities for drug tracking and delivery.

Extending the success of d-DNP to hyperpolarized nanoparticle imaging has proven challenging as electronic defects must be embedded at concentrations optimized to give large DNP enhancements without shortening the T_1 lifetime of the hyperpolarized state [61]. Unlike d-DNP of liquid molecular compounds, where electron spin concentration can be easily adjusted by addition of a radical solution known as ‘DNP juice’ [88], synthesizing solid nanomaterials with different concentrations of embedded electronic defects is typically nontrivial. Once such materials are synthesized for d-DNP, however, they do carry the significant benefit of not requiring the addition of potentially toxic radicals to carry out the DNP process. However, even when such nanoparticles can be highly spin polarized, sensitive MRI is still difficult due to the short nuclear T_2 of solids. A short T_2 restricts the time available for position encoding with magnetic field gradients during signal acquisition and results in poor MRI resolution [56].

Here, we discuss the progress that has been reported on performing d-DNP with silicon nanoparticles, before we explore nanodiamond in more detail in Section 2.6.

2.5.1 Silicon

Hyperpolarization of silicon has been explored in the context of MRI via brute force [59], DNP [89] and optical techniques [90]. The most promising *in vivo* demonstration has been d-DNP with silicon microparticles, an example of which is shown in Fig. 2.12 [16]. These 2 μm particles can be hyperpolarized using DNP at 4 K and 2.9 T, with polarization being transferred via spin diffusion from intrinsic electronic defects at the particle surface to ^{29}Si nuclei with long T_1 times in the core. Rapid dissolution and injection of the particles in the MRI scanner enables imaging of the silicon microparticles for up to 30 minutes. Transfer of the silicon particles between the polarizer and imager is aided by the field independent T_1 of ^{29}Si in high purity silicon particles [91]. Further, fast spin refocusing techniques were shown to be useful for extending

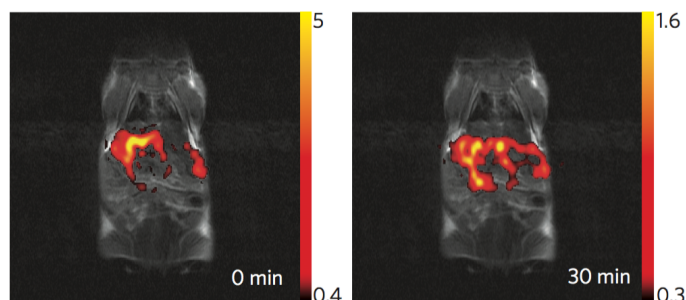


Figure 2.12: *In vivo* co-registered $^1\text{H}:$ ^{29}Si MRI of hyperpolarized silicon particles administered intragastrically to a mouse. ^{29}Si signal is shown as a false color overlay. Reproduced with permission from Macmillan Publishers Ltd: Nature Nanotechnology, Ref. [16], copyright 2013.

the nuclear T_2 lifetimes into a regime that was useful for imaging [92].

A key challenge to further development of this silicon platform is that reducing the particles to biologically relevant sizes shortens the T_1 of the ^{29}Si nuclei, presumably because relaxation of nuclei in the core via surface impurities becomes more efficient. Whilst blocking this relaxation process via passivation of surface defects has enabled the synthesis of 10 nm silicon particles with ^{29}Si lifetimes of 10 minutes, without surface defects, achieving large polarizations via DNP becomes unlikely [93]. As the quest for the perfectly synthesized silicon nanoparticle continues [94], applications in catheter tracking [95] and targeting [96] are also emerging.

2.6 Diamond

Having provided background on modalities for nanoparticle imaging in biomedicine and on emerging hyperpolarized MRI techniques, in this section we turn our attention to a particular material system - diamond. Nanodiamonds (NDs), nanoparticles formed from sp^3 hybridized carbon, are currently of much interest in biomedicine. In this section, we explain reasons for this biomedical interest and discuss techniques for nanodiamond imaging, laying foundations for the new nanodiamond imaging techniques we introduce in later sections of this thesis.

2.6.1 NDs in Biomedicine

Diamond has attracted much attention in biomedicine as a carbon-based material with properties that are tailorable on demand [97, 98]. This versatility has enabled the fabrication of NDs with surfaces that are readily functionalizable with targeting ligands [99] and therapeutic cargo [100]. In combination with the extremely high *in vivo* stability [101] and demonstrated non-toxicity [102–105], surface modification has seen ND find such applications as chemotherapeutic delivery to tumors [106–108], tissue engineering and regenerative medicine [109, 110].

Over the last decade, the optical tracking of nanodiamonds synthesized with fluorescent nitrogen-vacancy (NV) centers, defects embedded in the diamond lattice, has become an effective technique for subcellular imaging [111, 112], an example of which is shown in Fig. 2.13. Unlike fluorescent dyes, these NV centers do not photobleach, and thus allow long-term, high-resolution nanoparticle tracking. The applications unlocked by NV tracking are vast, including study of intraneuronal transport [113], determining the regenerative capabilities of stem cells [114] and finding quiescent cancer cells [115]. Beyond simple fluorescent tracking, resonant driving of spin-states in the NV centers with microwaves is enabling particle orientation readout [112] and magnetic field sensing [116].

Whilst fluorescence techniques have proven excellent for ND tracking in optically accessible environments, the development of corresponding methods for whole body, noninvasive ND tracking has been limited. Whole-body imaging approaches have predominantly been based on MRI of NDs with conventional T_1 or T_2 contrast agents, such as gadolinium and manganese, grafted to their surfaces [117–121], an example of which is shown in Fig. 2.14. Similar methods have also been used to graft radioisotopes to ND surfaces for PET imaging [122]. Whilst such grafting techniques can be effective for imaging purposes, they compromise the versatility of the ND surface and suffer from the drawbacks of a large background signal (MRI T_1/T_2 contrast) and ionizing radiation (PET). Hence, the development of a noninvasive imaging modality, free of ionizing radiation, that does not affect

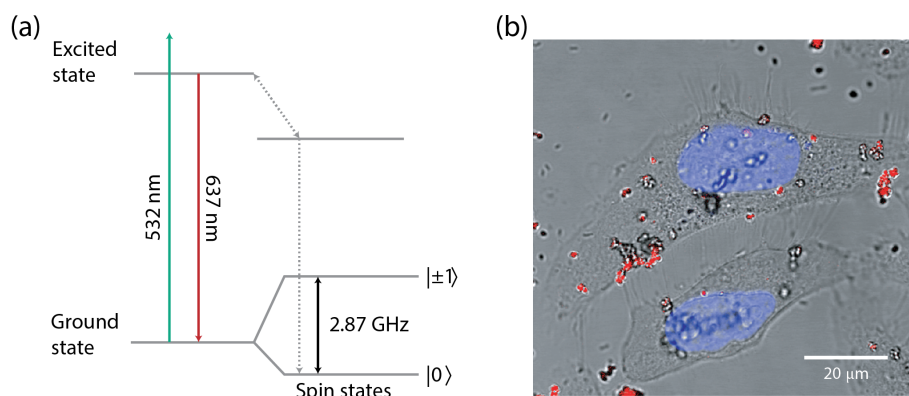


Figure 2.13: **Optical Tracking of Nanodiamonds.** (a) Energy levels of the nitrogen-vacancy defect in diamond. Pumping nanodiamonds with a green laser (532 nm) leads to red fluorescence (637 nm). (b) Overlay of bright-field and confocal fluorescence images of cells, showing uptake of nanodiamonds. NV fluorescence is shown in red and the nucleus is stained blue. Adapted by permission from Macmillan Publishers Ltd. from Reference [112].

the ND surface would be highly valued. Dissolution-DNP meets all of these demands—in the next section we turn to address the properties of ND that make it a DNP candidate.

2.6.2 Diamond DNP

Diamond presents itself as an excellent material for DNP due to the predominance of electronic defects through the crystal structure (see Fig. 2.15). These defects have been used extensively to perform solid state hyperpolarization of the 1.1% abundant ^{13}C in bulk diamond samples, through both DNP [123–125] and optical hyperpolarization techniques [126, 127]. Recent efforts have seen large ^{13}C polarizations achieved in nanodiamond samples via DNP experiments that exploit P1-centers and carbon dangling bonds, spin-1/2 defects that are commonly found in diamond (see Fig. 2.15) [128–131]. Given the exceptionally long ^{13}C T_1 times of diamond [132], the successful demonstration of ^{13}C DNP in nanodiamond raises the possibility of a new nanodiamond imaging modality based on hyperpolarized MRI.

Over the following chapters we will explore the material properties of

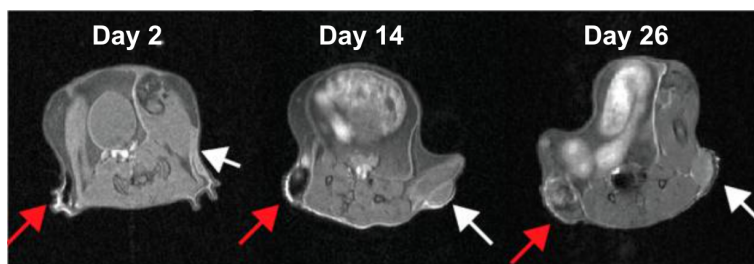


Figure 2.14: **MR imaging of ND labeled with gadolinium.** The mouse being imaged bears a ND-Gadolinium labeled tumor (red arrows) and an unlabeled tumor (white arrows). Images are shown 2, 14 and 26 days after engraftment. ND-Gadolinium tumor shows a darker signal than healthy tissue due to T_2 shortening. The unlabeled tumor has similar brightness to healthy tissue. Reprinted (adapted) with permission from [118]. Copyright 2016 ACS.

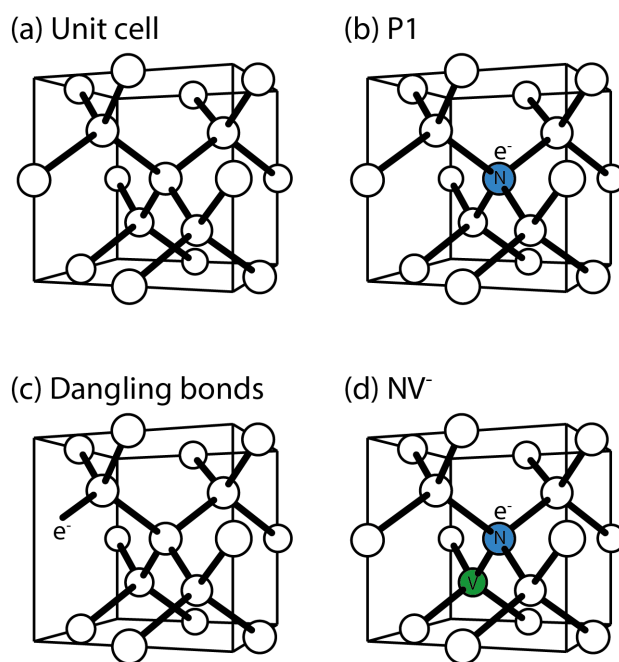


Figure 2.15: **The diamond unit cell and common defects.** Carbon atoms (white), nitrogen atoms (blue) and vacancy site (green) are shown. (a) The diamond unit cell. (b) P1 center. P1 centers occur when a carbon atom in the lattice is substituted by a nitrogen atom. The additional spin-1/2 electron, that is bound to the nitrogen atom, is a source of polarization for DNP. (c) Dangling bonds lead to unpaired spin-1/2 electrons. (d) NV centers occur when a lattice vacancy and a substitutional nitrogen atom pair up. NV centers are spin-1 electronic defects.

nanodiamond in detail and explain our new approaches to imaging nanodiamond with MRI. In particular, we will show how the electronic and nuclear spin properties of nanodiamond are linked to size and defect concentration, finding that synthetic nanodiamond is a promising candidate for d-DNP applications in biomedicine. We also detail our surprise finding that synthetic nanodiamond can act as a contrast agent in Overhauser-enhanced MRI as a result its surface properties. Time is also spent explaining the hardware developments that were necessary to enable these two new nanodiamond imaging modalities. Come join us as we outline how nanodiamond imaging with hyperpolarized MRI has become a reality.

Chapter 3

Hyperpolarized Nanodiamond with Long Spin-Relaxation Times

3.1 Abstract

The use of hyperpolarized agents in magnetic resonance (MR), such as ^{13}C -labeled compounds, enables powerful new imaging and detection modalities that stem from a 10,000-fold boost in signal. A major challenge for the future of the hyperpolarization techniques is the inherently short spin-relaxation times, typically less than 60 seconds for ^{13}C liquid-state compounds, which limit the time that the signal remains boosted. Here, we demonstrate that 1.1% natural abundance ^{13}C spins in synthetic nanodiamond (ND) can be hyperpolarized at cryogenic and room temperature without the use of free-radicals, and, owing to their solid-state environment, exhibit relaxation times exceeding 1 hour. Combined with the already established applications of NDs in the life-sciences as inexpensive fluorescent markers and non-cytotoxic substrates for gene and drug delivery, these results extend the theranostic capabilities of nanoscale diamonds into the domain of hyperpolarized MR.¹

¹This chapter is adapted from E. Rej, T. Gaebel, T. Boele, D. E. J. Waddington and D. J. Reilly, Hyperpolarized nanodiamond with long spin-relaxation times. *Nat. Commun.*, **6**, 9459 (2015).

3.2 Introduction

Nanoparticles, having found use in the treatment of cancers [133], the study of autoimmune diseases [134], and cardiovascular affections [135], are currently of interest as theranostic agents needed for the advent of personalized medicine [136]. These nanoscale systems are expected to integrate imaging, tracking, and monitoring capabilities with targeted delivery of compounds to tumors, cellular functions and processes, or specific organs. Especially powerful is the modality established by combining high-resolution magnetic resonance imaging (MRI) with nanoparticles that have been hyperpolarized to act as contrast agents, as has been achieved recently using silicon compounds [16, 137].

Nanodiamonds (ND) are well-suited to act as theranostic platforms, having demonstrated an innate compatibility with biological environments and low toxicity in comparison to other nanoscale structures [138, 139]. The readily modifiable surface, which is easily functionalized [140], has enabled NDs to be conjugated to specific molecules [141], opening a plethora of biomedical applications that include pharmaceutical delivery [106, 139, 142, 143] and intracellular tracking [112] based on the unique optical properties of defects in the diamond lattice [141]. A particular defect, the nitrogen-vacancy (NV) color center, has also established a sensitive means of detecting minute magnetic fields on the nanoscale using methods pioneered in controlling quantum devices [116, 144–148]. Beyond luminescence-based techniques however, approaches to non-invasively detect and image diamond nanoparticles *in vivo* have to date, been lacking.

Standard MRI modalities (operating at magnetic fields of up to a few Tesla) are not well suited to resolving weak concentrations of ND *in vivo* since diamond is a dilute spin system (1.1% ^{13}C) and carbon has a small gyromagnetic ratio. This limitation can, in principle, be overcome using hyperpolarization techniques [149] which can result in a 10,000-fold boost in signal over that from typical thermal polarization conditions [80, 82]. Hyperpolarized molecular compounds such as $[1-^{13}\text{C}]$ pyruvate, for example, have recently been used to study tumor metabolism in humans by first transferring

electron spin polarization to ^{13}C nuclei at cryogenic temperatures [83].

In these liquid-state compounds, hyperpolarized ^{13}C spins typically relax to thermal equilibrium on timescales T_1 less than 60 seconds [149]. In contrast, bulk, high-purity diamond can exhibit ^{13}C T_1 times of many hours [132], and recent work using optical techniques to manipulate NV centers [127, 150–152] has produced significant polarization in large single-crystal samples. The challenge therefore is to maintain these long spin lifetimes even when diamond is produced in nanoparticle form and in sufficient quantities to be of clinical relevance. Addressing this challenge requires a detailed understanding of particle size effects, the structure of internal crystal defects, contaminants, and spin-relaxation channels that arise from the nanoparticle surface [128, 129, 153, 154]. Balancing these constraints, the hyperpolarization mechanism also requires the presence of unpaired electrons which, in the case of liquid ^{13}C compounds, are typically added to the agent in the form of organic free-radicals.

In this chapter we extend the opportunity for deploying nanodiamond in life-science applications by demonstrating its suitability as a MR marker and contrast agent for MRI. Using electron spin resonance (ESR) we observe that inexpensive commercially available NDs, produced via the high pressure high temperature (HPHT) process, exhibit a suitable balance of paramagnetic centers from defects and surface dangling bonds to allow both hyperpolarization and the preservation of long spin relaxation times. In comparison to previous results on detonation ND [153, 154], the ^{13}C relaxation data reported here exhibits a 1,000-fold extension in T_1 together with signal enhancements that compare favorably with hyperpolarized ^{13}C liquid-state compounds. Particle size is found to significantly affect both the relaxation time and amount of achievable hyperpolarization, opening the possibility of selectively detecting NDs of a particular size distribution.

In addition to showing significant hyperpolarization at $T = 4$ K, we demonstrate that a sizable signal enhancement is also possible at liquid nitrogen (77 K) and room temperature using dynamic nuclear polarization (DNP), alleviating the need for expensive liquid helium and potentially enabling new *in vivo* modalities. Finally, we examine the spin dynamics of the ND core and

its surface using hyperpolarized states to resolve new phenomena associated with defects in this versatile material system.

3.3 Results

3.3.1 ESR spectra and nuclear spin relaxation

Turning to the experimental results, SEM images (see Fig. 3.1a-d) and the ESR spectrum and simulation results (see Fig. 3.1e) for a representative ND sample are shown. The ESR spectrum, which indicates the predominant types of defects available for use in hyperpolarization, can be seen to comprise three components that sum to produce the black simulation curve in Fig. 3.1e. These are a broad spin-1/2 Lorentzian component (blue trace) attributed to carbon dangling bonds near the surface of the ND, a narrow spin-1/2 Lorentzian component (yellow trace) attributed to defects within the diamond lattice, and a component associated with P1-color centers (green trace) which constitutes a substitutional nitrogen atom with the extra electron hyperfine coupled to the ^{14}N spin-1 nucleus. The number of P1-center impurities, which lead to central ($m_I = 0$) and hyperfine transitions ($m_I = \pm 1$), increases as ND size increases, while the number of spin-1/2 impurities (broad and narrow spectra) decreases as ND size increases [see Fig. 3.2].

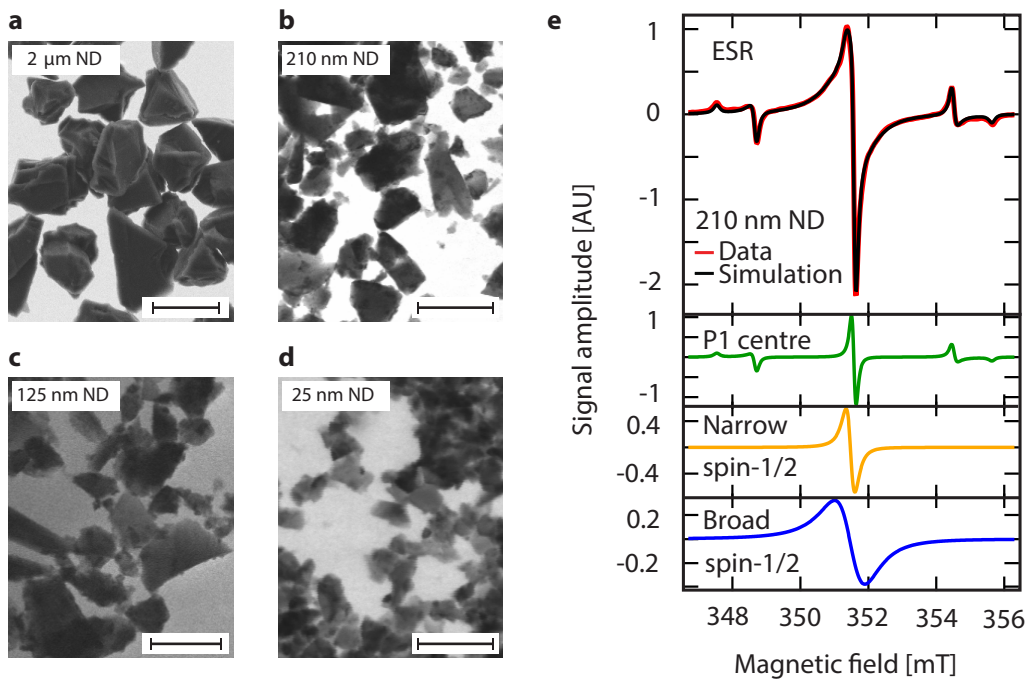


Figure 3.1: **ND characterization.** (a-d) Electron micrographs of various sized NDs used in this work. (a) 2 μm ND, scale bar = 2 μm, (b) 210 nm ND, scale bar = 400 nm, (c) 125 nm ND, scale bar = 200 nm, (d) 25 nm ND, scale bar = 100 nm. (e) ESR spectrum of 210 nm ND (red). The black line is a simulated spectrum consisting of three components: a narrow spin-1/2 component (yellow) a broad spin-1/2 component (blue) and a P1-center component (green). The peaks seen in the P1-center spectrum arise from hyperfine coupling between electrons and ^{14}N spin-1 nuclei.

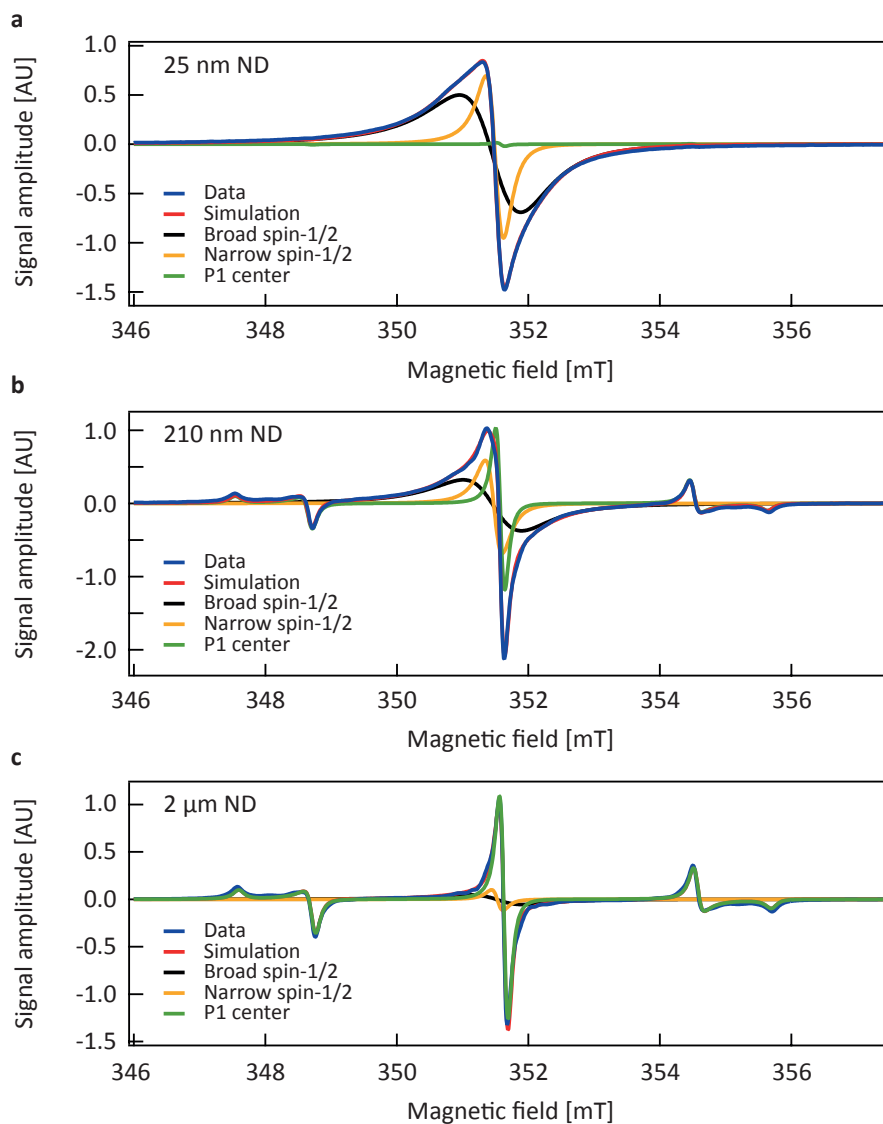


Figure 3.2: **ESR spectra of various NDs.** (a) 25 nm ND (b) 210 nm ND, and (c) 2 μm ND. Data (blue) is simulated (red) with three components: a broad spin-1/2 component (black) a narrow spin-1/2 component (yellow), and a P1-center component (green). Fit parameters are linewidths, relative intensities and g-factors. The g-factors stayed constant over all ND sizes, with $g_{\text{broad}} = 2.0027$, $g_{\text{narrow}} = 2.0027$, and $g_{\text{P1-center}} = 2.0021$. Total number of spins in samples 25 nm:210 nm:2 μm is in the ratio 2.6:1.2:1.

These defect sites also provide the primary mechanism for ^{13}C nuclear spin relaxation in ND. We find that the T_1 relaxation time grows with increasing particle size, as shown in Fig. 3.3. In determining these T_1 times, the spin polarization build-up for smaller diamonds is well described by models [155,156] in which the dipolar interaction of nuclear spins with paramagnetic impurities dominates over nuclear spin diffusion, leading to polarization curves that follow a stretched exponential form. Diamond particles with average diameter approaching $1\ \mu\text{m}$ however, are better characterized by a double exponential in their polarization build-up with time, presumably due to distinct regions within the diamonds of differing spin behavior. For $2\ \mu\text{m}$ diamonds the longer component of the double exponential yields a T_1 time of 63 min [see Fig. 3.4 and methods in Section 3.5].

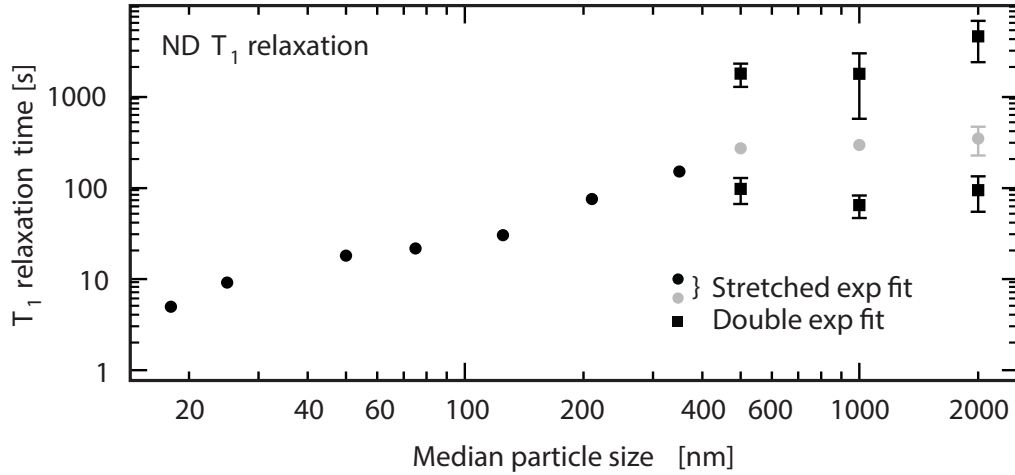


Figure 3.3: **Characterization of the T_1 size dependence in ND.**(a) Room temperature ^{13}C relaxation times, T_1 , as a function of diamond particle size at $B = 7$ T. Relaxation times were measured using the saturation recovery method with build-up time of magnetization M determined by fitting a stretched exponential $M = M_0(1 - \exp(-(t/T_1)^\alpha))$ or double exponential. Small NDs exhibit a buildup with $\alpha = 2/3$ (black circles), with larger NDs better fitted by a stretched exponential with $\alpha = 1/2$ (gray circles) or double exponential fits with a long and short component shown as black squares. Such stretched exponential behavior is expected in solids where spin-lattice relaxation is governed by the presence of paramagnetic centers [155]. The error bars indicate the standard deviation of the three measurements that were taken, and are shown when the error exceeds the size of the marker.

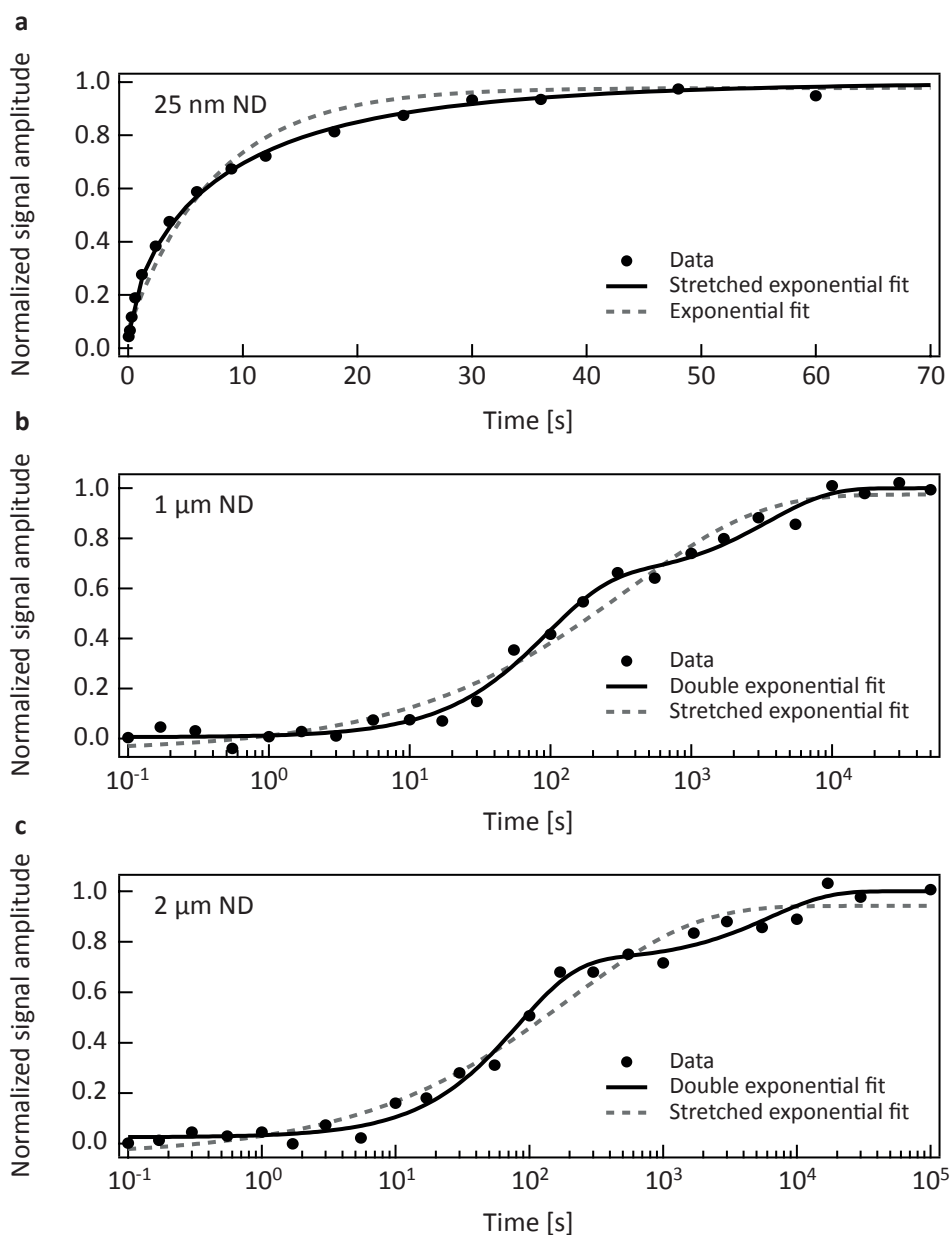


Figure 3.4: T_1 magnetization build up in ND measured at $B=7$ T. (a) Comparison between a stretched exponential fit (solid black line) and exponential fit (gray dashed line) to the saturation recovery build up data (black dots) of 25 nm ND. The stretched exponential is a better fit for small NDs. (b, c) Comparison between a double exponential fit (solid black line) and a stretched exponential fit (gray dashed line) for (b) 1 μm ND and (c) 2 μm . For larger ND particles the double exponential fit has a smaller variation from the data than a stretched exponential fit, presumably due to the presence of distinct regions within larger diamonds that have different spin behavior.

3.3.2 Brute-force hyperpolarization

The simplest method of increasing the MR signal from ND is to first cool the system to low temperatures in a high magnetic field to increase the Boltzmann population difference in the nuclear spins, a process termed brute-force polarization. If the NDs are subsequently moved to a different magnetic field and temperature, the spin system can be considered hyperpolarized until it thermalizes on timescale T_1 . Using the brute force method we hyperpolarize 2 μm ND at $T = 35$ mK and $B = 4$ T in a dilution refrigerator fitted with a rapid sample exchange system that allows fast (< 1 min) transfer of the ND sample to a room temperature $B = 7$ T spectrometer for detection. A $\pi/2$ pulse applied immediately after transfer produces a signal (see inset Fig. 3.5) that is enhanced by an order of magnitude when compared to the signal from 2 μm ND at thermal equilibrium and $B = 7$ T. To measure the relaxation time a series of small tip-angles is used to probe the polarization over 0.5 hours, as indicated by the decaying signal in Fig. 3.5. The decay is a combination of the T_1 relaxation of spins in the ND (~ 53 min) and polarization lost from the tipping pulses [see methods in Section 3.5 for details].

3.3.3 Hyperpolarization via the solid effect

To achieve even higher polarizations and larger signals, DNP [54] can be used to transfer electron polarization to the ^{13}C nuclear spins in the diamond [132]. As described above, the source of these unpaired electrons in ND are paramagnetic centers in the lattice, dipolar coupled to a surrounding nuclear spin bath. Application of a microwave magnetic field slightly below the electron spin resonance frequency can drive spin flip-flops between nuclear and electron spins associated with centers, leading to a net transfer of spin polarization from the electrons to the nuclei near the impurities in a process known as the Solid Effect (see Fig. 3.6a,b).

Turning to the main result of this chapter, we demonstrate that DNP can be used to hyperpolarize commercially available NDs, which, as was shown above, also exhibit long relaxation times. In the case of the largest diameter diamonds (2 μm) a $T = 4$ K signal enhancement of ~ 400 is achieved

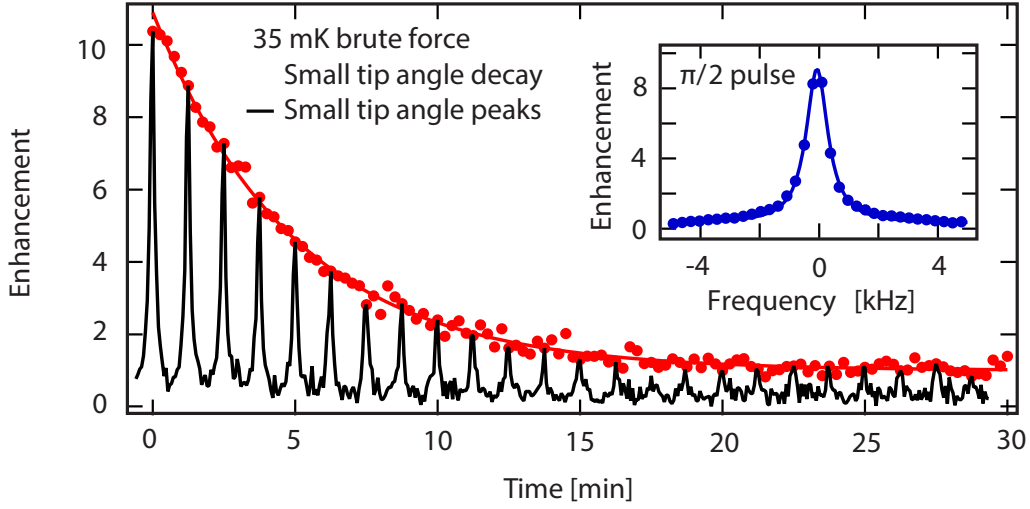


Figure 3.5: **Brute force hyperpolarization.** Enhanced signal following brute-force hyperpolarization of $2\ \mu\text{m}$ ND at $T = 35\ \text{mK}$ and $B = 4\ \text{T}$ for 3 days in a dilution refrigerator. Following a 40 s transfer in a field of 630 mT, detection is at $B = 7\ \text{T}$, via a $\pi/2$ -pulse (inset) with decay ($T_1 \sim 53\ \text{min}$) measured via a sequence of small tip angles (main panel).

over thermal equilibrium, corresponding to a nuclear polarization of $\sim 8\ \%$, as shown in Fig. 3.6c,d,e. Comparing this 4 K hyperpolarized signal to the thermal signal at room temperature gives an enhancement of 13,500; similar to what has been demonstrated with isotopically labeled ^{13}C liquid compounds [149]. We estimate that for a ND concentration of $1\ \text{mg mL}^{-1}$, this amount of hyperpolarization leads to a spatial resolution better than $2\ \text{mm} \times 2\ \text{mm}$ in a preclinical MRI scanner [see calculation in Section 3.6 for details]. Note that ND exceeding this concentration has already been used for therapeutic delivery *in vivo* [106].

It is possible that by hyperpolarizing the nuclear spin system using DNP, new relaxation channels are created that shorten the relaxation time. We test this possibility by first polarizing $2\ \mu\text{m}$ ND for 1 hr and then allowing it to decay for 1 hr at field. The resulting signal, shown in Fig. 3.7a, indicates a T_1 comparable to measurements performed at thermal equilibrium. As a further demonstration of the potential for hyperpolarized ND, we show in Fig. 3.7b that the enhanced polarization can be maintained during transfer

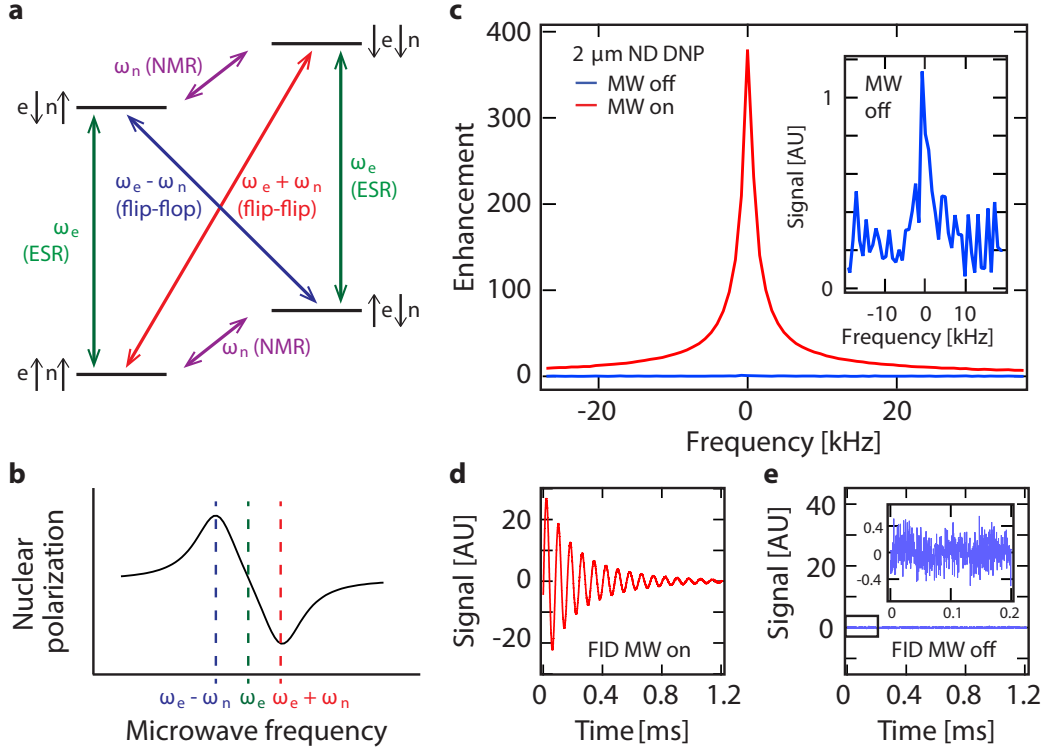


Figure 3.6: **Dynamic nuclear polarization of ND.** (a,b) DNP via the Solid Effect is used to hyperpolarize ND. (a) Energy level diagram for a dipolar coupled electron spin-1/2 (e) and a nuclear spin-1/2 (n) system in a magnetic field. The ESR at frequency ω_e (green), NMR at frequency ω_n (purple), flip-flop at frequency $\omega_e - \omega_n$ (blue), and flip-flip at frequency $\omega_e + \omega_n$ (red) transitions are shown. Driven flip-flop transitions involve a mutual electron flip and a nuclear flop resulting in a positive nuclear polarization. Driven flip-flip transitions result in a negative nuclear polarization. (b) Schematic showing positive and negative nuclear polarization when driving flip-flop and flip-flip transitions, respectively. (c) Hyperpolarized signal enhancement of 380 times for 2 μm ND at $T = 4$ K. Inset: Zoom of NMR signal taken at thermal equilibrium ($T = 4$ K) with no microwaves. (d,e) NMR free induction decay of 2 μm ND after a $\pi/2$ -pulse at $T = 4$ K. (d) Signal after hyperpolarization. (e) Thermal polarization signal. Zoom of the thermally polarized signal is shown in the inset of e.

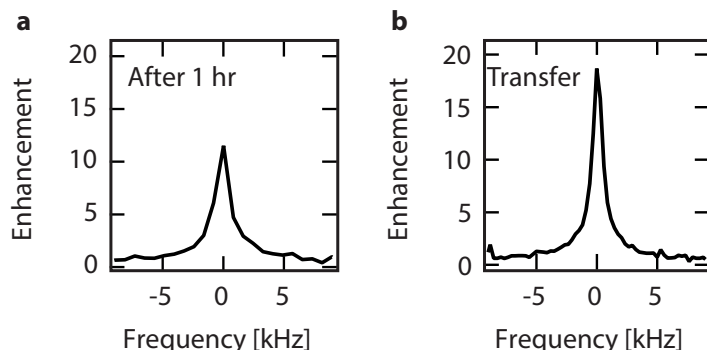


Figure 3.7: **Polarization Decay of Hyperpolarized ND.** (a) Signal enhancement of 2 μm ND that was polarized for 1 hr and then allowed to decay at field in the polarizer ($T = 4$ K, $B = 3$ T) for 1 hr. The signal decay is comparable to that measured at $B = 7$ T and room temperature. (b) 2 μm ND signal enhancement after transfer from the polarizer to a $B = 7$ T magnet for detection at room temperature. The signal is enhanced over that measured for a sample thermally polarized at room temperature. The 2 μm ND was polarized for 15 min at $T = 4$ K. The transfer took place in a field of 730 mT and took approx. 15 s.

of the sample from a lower field polarizer to a high field MR detection system [see methods in Section 3.5 for details].

Unlike hyperpolarized molecular compounds, the use of nanoparticles opens a new modality that links MR signal strength (and relaxation time) to particle size. For hyperpolarized ND, we determine a significant size dependence to the signal enhancement, as shown in Fig. 3.8. This dependence is most prominent for particle sizes below ~ 300 nm, where the larger rate of spin relaxation competes with the rate at which hyperpolarization from DNP occurs. We suggest that this dependence on the diameter of NDs opens a means of selectively tracking particles based on their size distribution, which is potentially of use in determining the integrity of permeable barriers and epithelium membranes.

For potential clinical use of hyperpolarized MRI, a major drawback of the technique is the need for liquid helium to cool sample agents during the polarization phase. This drawback is particularly significant for applications that require MR in remote locations, for instance in battlefield MRI using

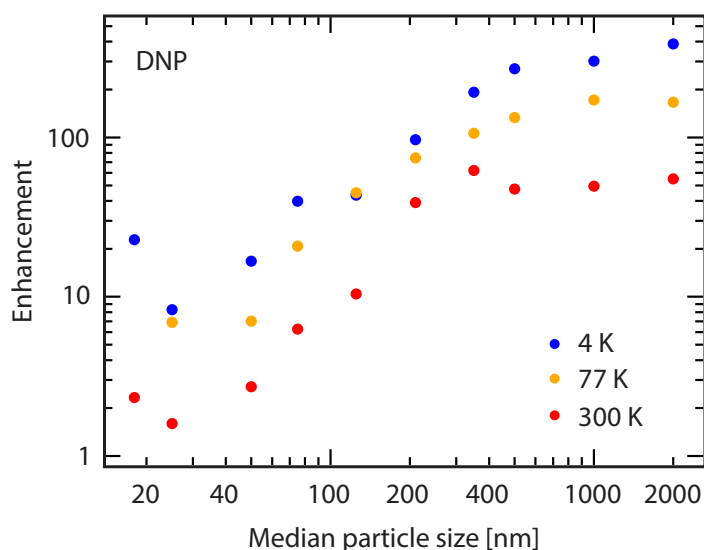


Figure 3.8: **Size dependent enhancement of ND.** Signal enhancement as a function of particle size and temperature at $T = 4$ K (blue), 77 K (yellow) and 300 K (red). The enhancement is given by the hyperpolarized signal divided by the thermal signal at each temperature.

ultra-low magnetic fields. In the case of hyperpolarized ND however, we find that sizable enhancements are possible at liquid nitrogen temperatures (77 K) (see Fig. 3.8), where cryogenics are readily available. Extending this idea, Fig. 3.8 also shows that hyperpolarization is possible at room temperature, doing away with cryogenics altogether.

3.3.4 Hyperpolarization in the presence of water

Room temperature hyperpolarization, even for modest enhancements, opens the prospect of new modalities that polarize and detect compounds *in vivo*. The significant barrier to this technique is the heating of water and surrounding tissue during the application of microwaves needed to perform DNP. Polarizing at low magnetic field and microwave frequency however, can significantly reduce heating but requires sufficiently long T_1 times to enable magnetic field ramping between polarization and high-field detection conditions [157]. Hyperpolarized nanodiamonds appear well suited to explore this modality, since for example, the signal from 350 nm ND (as a dry powder)

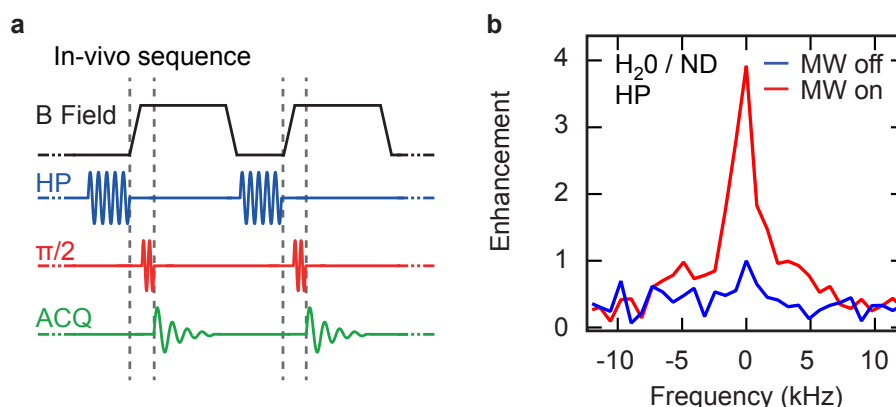


Figure 3.9: **ND hyperpolarization in the presence of water.** (a) The combination of room temperature signal enhancement and long relaxation times opens the possibility of *in vivo* hyperpolarization using a magnetic field shuttling technique. With the ND agents already administered to the bio-system, hyperpolarization (HP) is performed at low-field where microwave heating is reduced. The field is then ramped on a timescale much shorter than T_1 to enable imaging and detection of the hyperpolarized ND without sample shuttling. Schematic shows a repeated sequence with radio frequency $\pi/2$ -pulses and acquisition window (ACQ). (b) Hyperpolarization in the presence of water. Even at the high microwave frequency of 80 GHz, we observe an enhanced signal (red) of ~ 4 times compared to the thermal polarization (blue).

can be enhanced by a factor of 40 at room temperature and exhibits a T_1 of several minutes (long enough for field ramping). Since the polarize and detect sequence can be cycled many times *in vivo* (see Fig. 3.9a), background noise can be averaged well below the limits imposed by one-shot polarize and detect methods.

To test this modality we hyperpolarize a slurry of 125 nm ND and water (200 μ L water with ~ 50 mg ND) at room temperature. Even in the presence of ~ 80 GHz microwaves, we observe a 4-fold enhancement of ^{13}C MR signal from the diamond with little discernible heating of the water when 2 W of microwave power is incident on the DNP probe (see Fig. 3.9b). This enhancement, which corresponds to a halving of the signal relative to the case without water, suggests that such modalities may be possible for small animals.

3.3.5 ND impurity selection and surface modification

The results presented so far are for ND samples readily obtained commercially, without further treatment or surface modification. We now turn to examine the role that surface impurities play in both hyperpolarization and relaxation, noting that there is significant scope to tailor the surface chemistry via passivation and treatment [158]. Our approach is to effectively perform ESR spectroscopy at the magnetic field used for DNP ($B \sim 3$ T), by monitoring the NMR signal enhancement as a function of microwave frequency [see Fig. 3.10a]. At room temperature we observe enhancement spectra consisting of four peaks that are in agreement with the low-field ESR data shown in Fig. 3.1e. The position of these peaks correspond to DNP processes at $\omega_e \pm \omega_n$. As the temperature is lowered, these distinct peaks become dipolar broadened. The high field DNP spectra are similarly broadened as the particle size is increased, as shown in Fig. 3.10b.

Modifying the defects or the types of defects within the nanodiamonds can change the DNP spectra, leading to enhanced polarization and longer relaxation times. We find that burning off the outer layer of ND using air oxidation (AO) processes [159] removes some of the broad spin-1/2 component associated with impurities near the surface of the ND. This can be seen in Fig. 3.10c where we compare the hyperpolarization spectra of 25 nm AO ND (black) with standard 25 nm ND (gray). The oxidation process leads to a suppression of the two central lines (f_2, f_3) in the spectrum, consistent with removing some of the surface impurities that would otherwise contribute to the signal.

By adjusting the microwave frequency for DNP, we can select different impurity sites for use in hyperpolarization. Polarization via the P1-centers, for instance, can be selected by irradiating at the frequencies corresponding to the outer peaks (f_1, f_4) in Fig. 3.10a. This is in contrast to irradiating at the inner peaks (f_2, f_3) which also comprise both narrow and broad components from spin-1/2 sites (see discussion of Fig. 3.1e). We find that hyperpolarization due to microwave driving at the inner peaks takes longer to build up and is retained longer than when driving at the outer peaks as-

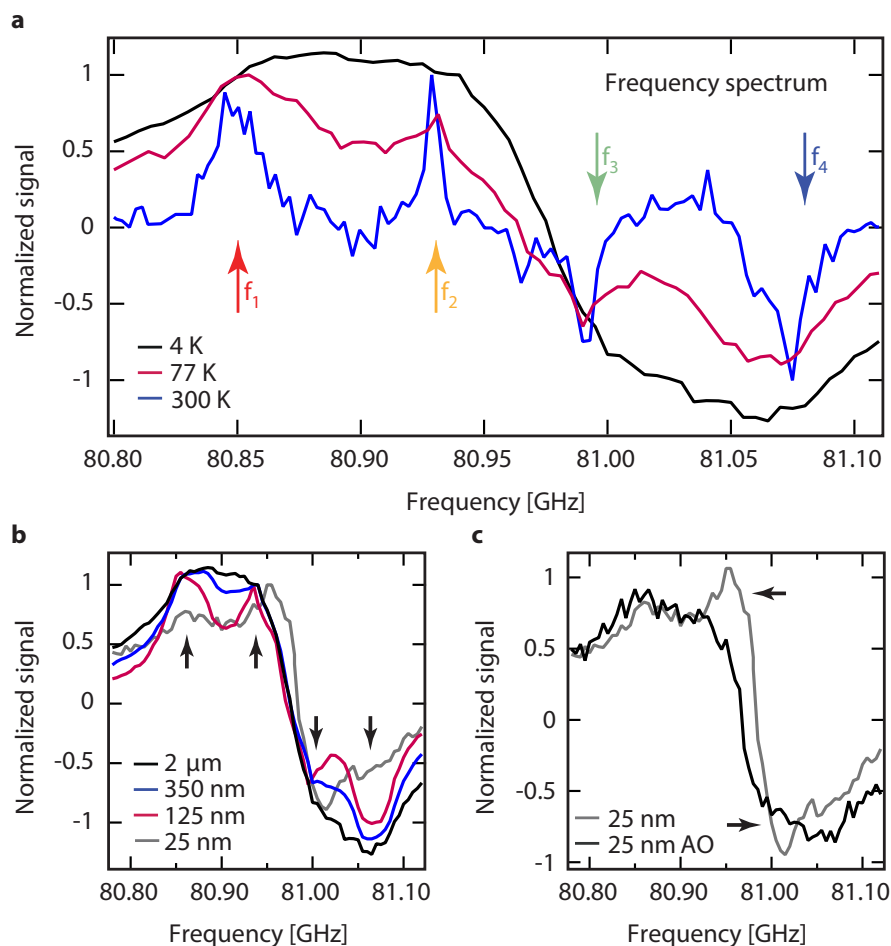


Figure 3.10: **ND impurity selection and surface modification.** (a) Hyperpolarized signal of 2 μm ND as a function of polarization frequency at $T = 4$ K (black), 77 K (purple) and 300 K (blue). The arrows indicate the four frequencies at which polarization build up and decay are examined: **red** ($f_1 = 80.870$ GHz, **yellow** ($f_2 = 80.925$ GHz, **green** ($f_3 = 80.990$ GHz, and **blue** ($f_4 = 81.050$ GHz). The traces were normalized to 1. Note the features broaden as temperature decreases. (b) Normalized hyperpolarized signal of 2 μm ND (black), 350 nm ND (blue), 125 nm ND (purple), and 25 nm ND (gray) at $T = 4$ K as a function of microwave frequency. More features are visible as the particle size decreases. (c) Comparison of the hyperpolarized signal amplitude as a function of frequency for 25 nm ND and 25 nm air oxidized ND.

sociated with the P1-centers. This behavior is seen in Fig. 3.11b, where for 350 nm ND, we compare the decay of hyperpolarization established by driving at peak f_1 or peak f_2 in Fig. 3.10a. These results suggest that nuclear spin diffusion is somewhat suppressed in these systems, since relaxation appears dominated by the particular impurities selected for polarization via the choice of microwave frequency.

Beyond examining the spin dynamics of ND, these results are of practical interest in optimizing conditions for maximum signal enhancement with minimal relaxation. As an example, we compare the signal from 350 nm ND, initially irradiated with microwaves at the four distinct frequencies indicated in Fig. 3.10a and then subsequently transferred to a $B = 7$ T system for detection. Following sample transfer, the relaxation data in Fig. 3.11c show that a larger polarization is maintained if the nuclei were polarized using the two central spectra peaks (f_2 and f_3), in comparison to the outer peaks associated with the P1-centers (f_1 and f_4).

3.4 Discussion

There is significant scope to further enhance the degree of hyperpolarization in ND. In particular, by adding microwave capability to our brute force hyperpolarizer at mK temperature (based on a dilution refrigerator), much larger polarizations appear possible. Eliminating isolated defects via surface passivation techniques [158] will also likely result in longer relaxation times. Another direction is to work with isotopically enriched ^{13}C NDs to increase the number of spins that contribute to the signal and enhance spin diffusion from polarization sites on the surface to the spins in the core. Finally, we mention the possibility of using NDs for long time storage of nuclear polarization that is transferred to the hydrogen nuclei in an aqueous environment using cross-polarization sequences [160, 161]. Although the efficiency for polarization transfer is yet to be experimentally explored, this modality may enable life-science applications in which nanodiamond is tracked and imaged using standard MRI technology [161].

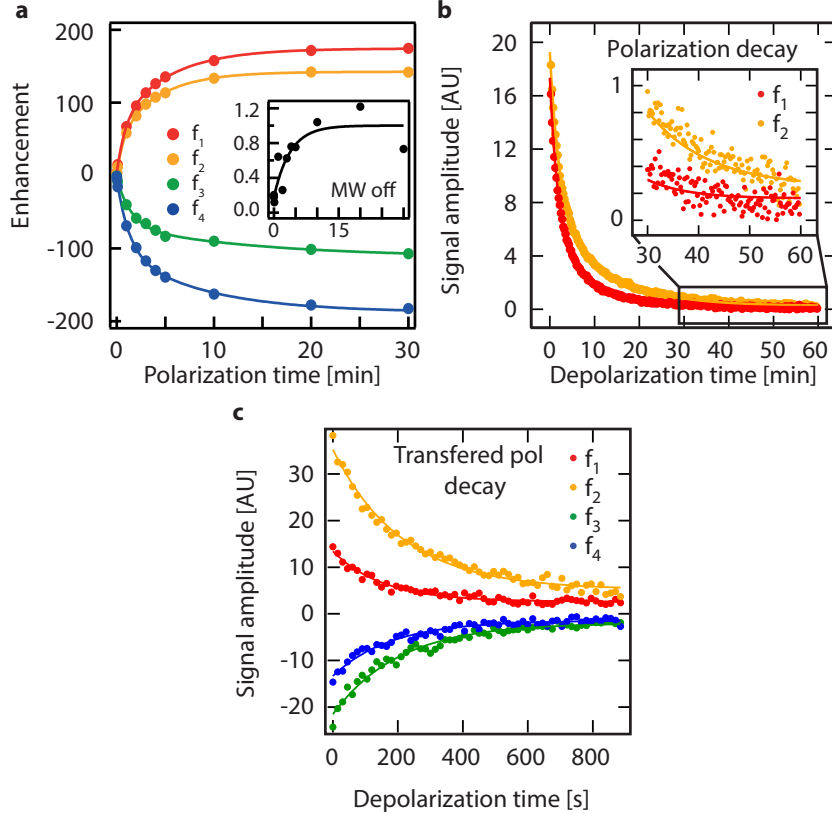


Figure 3.11: **Hyperpolarization and depolarization of NDs.** (a) Hyperpolarization build up in 350 nm ND at $T = 4$ K. Enhancement as a function of polarization time, normalized to the saturated magnetization taken with no microwave power (inset) in ND. We see a difference in the buildup times of the **red** (f_1 , $T_1 = 0.8$ min, 5.2 min), **yellow** (f_2 , $T_1 = 0.7$ min, 4.2 min), **green** (f_3 , $T_1 = 1.4$ min, 14 min), **blue** (f_4 , 1.0 min, 6.0 min) and **black** (microwaves off, $T_1 = 4$ min). (b) Depolarization of the hyperpolarized signal of 350 nm ND at $T = 4$ K using a small tip angle pulse sequence ($\theta = 3.5^\circ$, $TR = 15$ s). The ND was hyperpolarized for 180 minutes before the depolarization measurement. Fits to the data (solid lines) are double-exponential decay curves. We see a difference in the decay times of the red trace (f_1 , $T_1 = 12$ s, 2.1 s) and the yellow trace (f_2 , $T_1 = 16$ s, 2.5 s). (c) Depolarization of the signal from 350 nm ND after hyperpolarization for 15 min at $T = 4$ K and transfer to a $T = 7$ T magnet for detection. The decay was examined using a small tip angle sequence ($\theta = 8^\circ$, $TR = 15$ s). Data is shown in **red** (f_1 , $T_1 = 157$ s), **yellow** (f_2 , $T_1 = 250$ s), **green** (f_3 , $T_1 = 190$ s) and **blue** (f_4 , $T_1 = 157$ s). Microwaves for DNP were at $f_1 = 80.870$ GHz (red), $f_2 = 80.925$ GHz (yellow), $f_3 = 80.990$ GHz (green), and $f_4 = 81.050$ GHz (blue).

3.5 Methods

Nanodiamonds. The nanodiamonds used in these experiments were purchased from Microdiamant. The diamonds are synthesized using the HPHT technique. The sizes of the NDs are given as a distribution and a median size. We refer to the diamonds by their median size. Measurements were made on MSY 0-0.030, (0-30 nm, median 18), MSY 0-0.05 (0-50 nm, median 25 nm), MSY 0-0.1 (0-100 nm, median 50 nm), MSY 0-0.15 (0-150 nm, median 75 nm), MSY 0-0.25 (0-250 nm, median 125 nm), MSY 0-500 (0-500 nm, median 210 nm), MSY 0.25-0.5 (250 nm-500 nm, median 350 nm), MSY 0.25-0.75 (250 nm-750 nm, median 500 nm), MSY 0.75-1.25 (750-1250 nm, median 1000 nm), and MSY 1.5-2.5 (1500 nm-2500 nm, median 2000 nm).

SEM images. SEM measurements were made using a Zeiss Ultra Plus Gemini SEM spectrometer working in transmission mode. Suspensions were made of these NDs in water and a small amount of the suspension was placed upon a TEM grid. The ND size distributions measured were consistent with those provided by the manufacturer.

ESR measurements. ESR measurements were made using a Bruker EMX-plus X-Band ESR Spectrometer. The cavity Q ranged between 5,000 for small ND particles and 10,000 for large ND particles. ESR spectra were taken at 0.25 μ W, (within the linear regime of the saturation curves of the impurities) at a modulation amplitude of 1 Gs and a modulation frequency of 100 kHz. Each of the three components were simulated separately using Easyspin [162] and added together to make the final spectrum. Linewidth, signal amplitude and g-factor were varied. The best fit to the data was performed using a least squares analysis.

T_1 relaxation. NMR measurements to determine the T_1 relaxation times at $B = 7$ T were made using a saturation recovery pulse sequence that involved $64 \times \pi/2$ saturation pulses to null any initial polarization followed by a varied time for polarization to build up, and then a $\pi/2$ detection pulse. Time domain signals were acquired using a Redstone Tecmag system. Either a stretched exponential (smaller particles) $M = M_0(1 - \exp(-(t/T_1)^\alpha))$ or a double exponential (larger particles) was fitted to the curve [see Fig. 3.4].

Each ND size was measured 3 times and the average of the T_1 times is plotted.

Brute force T_1 measurements. The decay of brute force hyperpolarization in Fig. 3.5 (red dots) was measured using a small tip angle detection sequence ($\theta = 17^\circ$, $TR = 15$ s). The solid red line is a fit to $M = M_0 \cos(\theta)^{n-1} e^{-(n-1)TR/T_1}$ resulting in a T_1 of 53 min. The decay is a combination of the T_1 decay of the particles and the signal lost due to rf induced polarization loss with tip angle θ where n is the n th pulse and TR is the repetition time. Every fifth peak is shown in black.

Hyperpolarization measurements. Measurements were made at a field of 2.88 T with a Redstone Tecmag system and a in-house constructed NMR probe (design details can be found in Ref [163]) inside an Oxford Instruments flow cryostat. The microwave source was a tunable Gunn Oscillator (80.5 - 81.5 GHz) combined with a power amplifier. Microwaves were coupled to the sample using a waveguide. Polarization transfer measurements were determined using an in-house constructed NMR spectrometer based upon a National Instruments system and an NMR probe at a field of 7 T. Before polarization the signal was saturated with $64 \times \pi/2$ pulses to null any signal. Enhancement measurements were made by hyperpolarizing the ND at $f = 80.855$ GHz (4 K, 77 K) and 80.85 GHz (300 K) and then detecting the signal with a $\pi/2$ pulse. The hyperpolarized signal was compared to the NMR signal with no microwaves and the same polarization build up time. Frequency sweeps: The frequency was swept between 80.78 and 81.12 GHz in discrete steps of 5 MHz and polarization was measured at every point. The 2 μ m ND was polarized for 30 s, 3 min and 3 min at $T = 4$ K, 77 K, and 300 K, respectively. The spectra have been normalized to 1 for ease of comparison.

Depolarization. Measurements at $B = 7$ T: the ND was polarized for 15 minutes at four frequencies ($f = 80.87$, 80.925, 80.99 and 81.05 GHz in successive experiments) and then transferred to a $B = 7$ T magnet for detection. The transfer was performed in a field of $B \sim 0.7$ T, created from rare-earth permanent magnets and took ~ 20 s. A small tip angle pulse sequence with 8° pulses was used to detect the signal. Enhancement is compared to ND at thermal equilibrium at $B = 7$ T. Measurements at $B = 2.88$ T: The ND was

polarized for 180 minutes at two frequencies and the decay was monitored with small tip angle pulses (every 15 s). Depolarization data was multiplied by $\cos(\alpha)^{(n-1)}$ to take into account rf induced depolarization. The resulting data was fitted with a double exponential.

3.6 Feasibility of imaging with hyperpolarized nanodiamonds

We expect to perform hyperpolarized ND imaging with a small tip angle 2D Fast Spin Echo (FSE) sequence, with ^1H - ^{13}C co-registration. Overlaying ^{13}C images of functionalized nanodiamonds on high resolution ^1H anatomical images would provide information in a similar format to those seen in PET/MRI [164]. Here, we present calculations estimating a pixel signal-to-noise ratio (SNR) of ~ 11 for a nanodiamond concentration of 1 mg mL^{-1} . This SNR value is for $2 \text{ mm} \times 2 \text{ mm}$ sized pixels in a 5 mm slice assuming significant polarization loss during transfer from polarizing cryostat to imager. We note that nanodiamond concentrations of 2 mg mL^{-1} have previously been used *in vivo* [106].

First, we consider the fundamental limit to MRI resolution set by the observed transverse coherence time T_2^* , which is reached when the frequency line-width of the signal is approximately equal to the frequency separation between each pixel [165]:

$$dz \sim \frac{1}{\gamma G \pi T_2^*}, \quad (3.1)$$

where dz is the pixel length, γ the nuclear gyromagnetic ratio and G is the peak gradient strength. Our nanodiamond samples have $T_2^* \sim 250 \mu\text{s}$, which corresponds to a fundamental resolution limit of 0.25 mm in a preclinical scanner or 2.5 mm in a whole body MRI scanner (assuming typical peak gradient strengths for these systems of $G = 500 \text{ mT m}^{-1}$ and $G = 50 \text{ mT m}^{-1}$, respectively).

Next, we consider the pixel SNR that would be possible from our hyper-

polarized nanodiamond samples in an imaging experiment. Our 2 μm ND samples have a polarization after DNP at 4 K, P_{DNP} , of $\sim 8\%$. The thermal polarization, P_{thermal} , at $B_0 = 7$ T and $T = 300$ K, is 0.0006%, as given by the Boltzmann distribution:

$$P = \frac{h\gamma B_0}{2k_{\text{B}}T}, \quad (3.2)$$

where γ is the gyromagnetic ratio and k_{B} is Boltzmann's constant. The free induction decay (FID), after a $\pi/2$ pulse, from a 0.1 g, thermally polarized, 2 μm ND sample was acquired in our 7 T spectroscopic probe under the matched filter condition, $t_{\text{acq}}/T_2^* = \pi/2$, where t_{acq} is the acquisition time. The Fourier transform of this FID has $\text{SNR}_{\pi/2\text{-thermal}} = 35$. Preliminary transfer measurements between the hyperpolarizer and 7 T detection magnet have shown a sample transfer efficiency, η , of 10%. Hence, we predict that, after sample transfer of a hyperpolarized sample to our 7 T spectrometer, we will have an SNR post transfer, $\text{SNR}_{\pi/2\text{-PT}}$, of 45 000, as given by:

$$\text{SNR}_{\pi/2\text{-PT}} = \eta \text{SNR}_{\pi/2\text{-thermal}} P_{\text{DNP}}/P_{\text{thermal}}. \quad (3.3)$$

Scaling this SNR value to give an expected sensitivity in an imaging experiment is inherently nontrivial due to the difficulty of estimating noise associated with coil resistance and losses arising from the sample [166–168]. Here we make an SNR estimate for a preclinical scanner on the assumption that our SNR is limited primarily by coil resistance, which is generally true at $B = 7$ T for mouse coils [169].

The SNR of a pickup coil scales as:

$$\text{SNR} \propto \frac{B_{\text{r}}}{I_{\text{r}}} \frac{1}{\sqrt{4k_{\text{B}}TR_{\text{c}}}}, \quad (3.4)$$

where $\frac{B_{\text{r}}}{I_{\text{r}}}$ is the magnetic field strength of the pickup coil per unit current, T is the coil temperature and R_{c} is the coil resistance. $\frac{B_{\text{r}}}{I_{\text{r}}}$ at the center of an

optimized saddle coil is given by:

$$\frac{B_r}{I_r} = \frac{\sqrt{3}\mu_0 N}{\pi d} \frac{l}{\sqrt{l^2 + d^2}}, \quad (3.5)$$

where N is the number of turns in the coil, μ_0 is the permeability of free space, l is the coil length and d is its diameter [170]. If all power dissipation occurs in the coil, then we can estimate the coil resistance from:

$$Q = \frac{\omega_0 L_c}{R_c}, \quad (3.6)$$

where L_c is the coil inductance and ω_0 is the resonance frequency. Typically Q is ~ 100 at 75 MHz for preclinical imaging and spectroscopic NMR probes. Assuming a homogeneous field across the saddle coil, we estimate from Faraday's law that the coil's inductance scales approximately as [170, 171]:

$$I_c \sim \frac{Nl^2}{\sqrt{l^2 + d^2}}. \quad (3.7)$$

Assuming a 1 turn 40 mm diameter, 60 mm long saddle coil is used for mouse imaging, the ratio $\frac{B_r}{I_r}$ is reduced by 95% compared to the 2 turn 6 mm diameter, 13 mm long coil in our spectroscopic NMR probe. Therefore, the expected SNR after DNP and transfer to the imager is $\text{SNR}_{\pi/2\text{-imager}} = 2100$. This result is very similar to that obtained when the resistance is simply scaled by the ratio of the wire lengths in the coils.

We envision using a small tip angle 2D FSE sequence, similar to that used in Ref. [16], to image ^{13}C . When using a CPMG sequence, our nanodiamond samples have demonstrated T_2 values of approximately 100 ms, which would then allow for many echoes, making a FSE sequence feasible. Based on previous calculations for a 2D gradient-recalled echo (GRE) sequence, we estimate the pixel SNR of a 2D FSE imaging sequence to be [172, 173]:

$$\text{SNR}_{\text{pixel}} = \frac{N}{N_0^2} (\text{SNR}_{\pi/2\text{-imager}}) \sin \theta. \quad (3.8)$$

Where N is the number of pixels across an $N \times N$ image, N_0 is the num-

ber of pixels across the object, θ is the tip angle (setting the acquisition time $t_{\text{acq}} \sim T_2^*$). If the 0.1 g of nanodiamond powder in our sample is uniformly distributed through a 40 mm \times 40 mm \times 5 mm phantom there is a nanodiamond concentration of 16 mg mL⁻¹. For a 32 \times 32 pixel image with 2 mm \times 2 mm resolution and 5 mm slice thickness, $N = 32$, $N_0 = 20$. For tip angles 10° and 90°, this gives $\text{SNR}_{\text{pixel}} = 30$ and $\text{SNR}_{\text{pixel}} = 170$, respectively. Normalizing this value, we predict $\text{SNR}_{\text{pixel}} = 11$ at 1 mg mL⁻¹ for a 90° tip angle.

Hence, we estimate that there will be sufficient SNR for hyperpolarized nanodiamond imaging. In practice, the measured SNR will deviate from these values depending on the actual sensitivity of the detection coil and polarization lost during sample transfer. We have also not considered the loss of spin coherence due to T_2 effects during the acquisition sequence. These effects will cause some degradation of the SNR at higher spatial frequencies. A range of linewidth narrowing sequences developed for solid imaging may also help to improve image quality [165].

Chapter 4

Phase-Encoded Hyperpolarized Nanodiamond for MRI

4.1 Abstract

Surface-functionalized nanomaterials can act as theranostic agents that detect disease and track biological processes using hyperpolarized magnetic resonance imaging (MRI). Candidate materials are sparse however, requiring spinful nuclei with long spin-lattice relaxation (T_1) and spin-dephasing times (T_2), together with a reservoir of electrons to impart hyperpolarization. Here, we demonstrate the versatility of the nanodiamond material system for hyperpolarized ^{13}C MRI, making use of its intrinsic paramagnetic defect centers, hours-long nuclear T_1 times, and T_2 times suitable for spatially resolving millimeter-scale structures. Combining these properties, we enable a new imaging modality that exploits the phase-contrast between spins encoded with a hyperpolarization that is aligned or anti-aligned with the external magnetic field. The use of phase-encoded hyperpolarization allows nanodiamonds to be tagged and distinguished in an MRI based on their spin-orientation alone, and could permit the action of specific bio-functionalized complexes to be directly compared and imaged.¹

¹This chapter is adapted from the preprint D. E. J. Waddington *et al.*, Phase-Encoded Hyperpolarized Nanodiamond for Magnetic Resonance Imaging. *arXiv*, 1709.0185 (2017).

4.2 Introduction

Diamond is a remarkable material with outstanding thermal, mechanical, optical, and electrical properties, which have given rise to a diverse array of technologies since it was found to be readily synthesizable in the 1950s. In the context of nanomedicine, synthetic nanodiamond can act as a bright, fluorescent marker [174] of use in sub-cellular tracking of biological processes [175], *in vivo* sequestering of migratory cell populations [134] or as a non-toxic substrate for the delivery of chemotherapeutic payloads [9, 176–178]. Further, the extremely weak nuclear magnetism in diamond makes the material interesting for hosting quantum information [179] and for constructing quantum sensors that exploit its long-lived nuclear [180] or electron [181] spin-states.

The long lifetime of these spin-states has recently motivated the development of new nanodiamond-based theranostic agents that are detectable with magnetic resonance imaging (MRI) by acquiring signal from their ^{13}C nuclei [130, 182]. In natural abundance carbon however, spin-1/2 ^{13}C nuclei comprise only 1.1% of the diamond lattice, rendering their signal undetectable using conventional MRI. The presence of paramagnetic centers in diamond offers a means of boosting the weak signal from ^{13}C using hyperpolarization to transfer the much larger thermal polarization of the centers to the ^{13}C nuclei, by driving spin transitions optically [152], or with microwaves at cryogenic temperatures [128–131]. Conversely, the presence of paramagnetic centers also shortens the nuclear spin relaxation time (T_1), limiting the timescale over which hyperpolarized nuclei can be put to use [16, 93]. Beyond simply detecting the boosted signal from ^{13}C , constructing spatially-resolved images requires that the nuclear dephasing time (T_2) is sufficiently-long relative to the timescale set by the strength of practical magnetic field gradients. For this reason, solid-state compounds with short T_2 times have always presented a major challenge for imaging.

Here we address these challenges by demonstrating the use of nanodiamond for hyperpolarized- ^{13}C MRI. Via electron paramagnetic resonance (EPR) measurements, we first show that synthetic nanodiamond contains a concentration of impurities and dangling-bonds that is well suited to hyper-

polarization (see Fig. 4.1a), without significantly degrading the long nuclear T_1 time. In a major advance over previous work [130], we highlight how hyperpolarization via paramagnetic centers in nanodiamond opens up new avenues for preparing spin-populations with unique MRI contrast signatures. Reasoning that spatially-resolved imaging requires suitably long spin coherence, data characterizing the dephasing times for ^{13}C nuclei is presented, demonstrating the use of dynamical decoupling pulse sequences that preserve coherence and offer a means of improving image resolution. Testing the viability of hyperpolarized nanodiamond for MRI, we first acquire image data as a function of time, nanoparticle concentration, and size, before deploying the technique in a setting relevant to preclinical applications, acquiring a co-registered ^{13}C - ^1H image in a mouse *post mortem*.

Taken in combination, the properties of the nanodiamond spin-system enable a new, phase-encoded imaging modality not possible using hyperpolarized liquid compounds with short T_1 relaxation times [183]. Extending the repertoire of nanodiamond for MRI [118, 184, 185], we show how this method provides an *in situ* control, such that nominally identical nanoparticles can be tagged and distinguished in an MRI by the direction of their nuclear hyperpolarization alone. Finally, we speculate on the use of phase-encoded hyperpolarized MRI for addressing common challenges faced with targeted nanoparticle theranostics.

4.3 Intrinsic Defects as a Source of Polarized Spins

Turning to the details of our experiments, we begin by comparing synthetic nanodiamond produced via the high-pressure high-temperature method (HPHT), to natural nanodiamond (NAT) samples, highlighting the suitability of each for hyperpolarized MRI. Both kinds of nanodiamond exhibit a series of intrinsic electronic defects, immediately apparent in their X-band EPR spectra, shown in Fig. 4.1b. The generic features in the spectra can be attributed to a convolution of a hyperfine-split P1 center associated

with substitutional nitrogen atoms [186], a narrow single-line component from vacancy sites, and a broad single-line that stems from dangling carbon bonds [187, 188]. We find that P1 center concentration in the HPHT diamonds (95 ppm) is more than an order of magnitude higher than the P1 center concentration in the NAT nanodiamonds (4 ppm) [see Section 4.10.1 for details of particle size dependent effects].

In the presence of an external magnetic field ($B = 2.88$ T), these paramagnetic defects provide a platform for nuclear hyperpolarization via microwave driving of the manifold of hyperfine transitions, shown in Fig. 4.1c. Although room temperature hyperpolarization is possible [130], the most significant enhancements occur when microwaves are applied at cryogenic temperatures (4 K or below), transferring the large Boltzmann polarization of the electronic defects to closely coupled ^{13}C nuclei. For spins in nanodiamond, hyperpolarization occurs via a mixture of the solid-effect and cross-effect and leads to a polarized nuclear population of order 8% at saturation [see Section 4.10.1 for discussion of polarization mechanism]. Detuning the microwave frequency below or above the central EPR line drives hyperfine transitions that build a positive or negative enhancement in the ^{13}C signal (see Fig. 4.1c,d). The sign of the signal indicates nuclear hyperpolarization that is aligned or anti-aligned with the external magnetic field. Hyperpolarizing HPHT and NAT nanodiamond yields the ^{13}C signal enhancements shown in Fig. 4.2a and 4.2b, for a mean particle diameter $d = 2$ μm and $d = 210$ nm, respectively. We draw attention to the variation in signal enhancement with particle size and when using nanodiamonds with different concentrations of paramagnetic defects (HPHT versus NAT).

4.4 Spin Relaxation and Spin Dephasing

The concentration and configuration of paramagnetic centers in nanodiamond carry-over into the characteristic times for (electron-mediated) nuclear spin relaxation, limiting the time for which hyperpolarization can be usefully deployed. In their readily available synthetic form, HPHT nanodiamonds are well-optimized for hyperpolarization applications, retaining up to 11 %

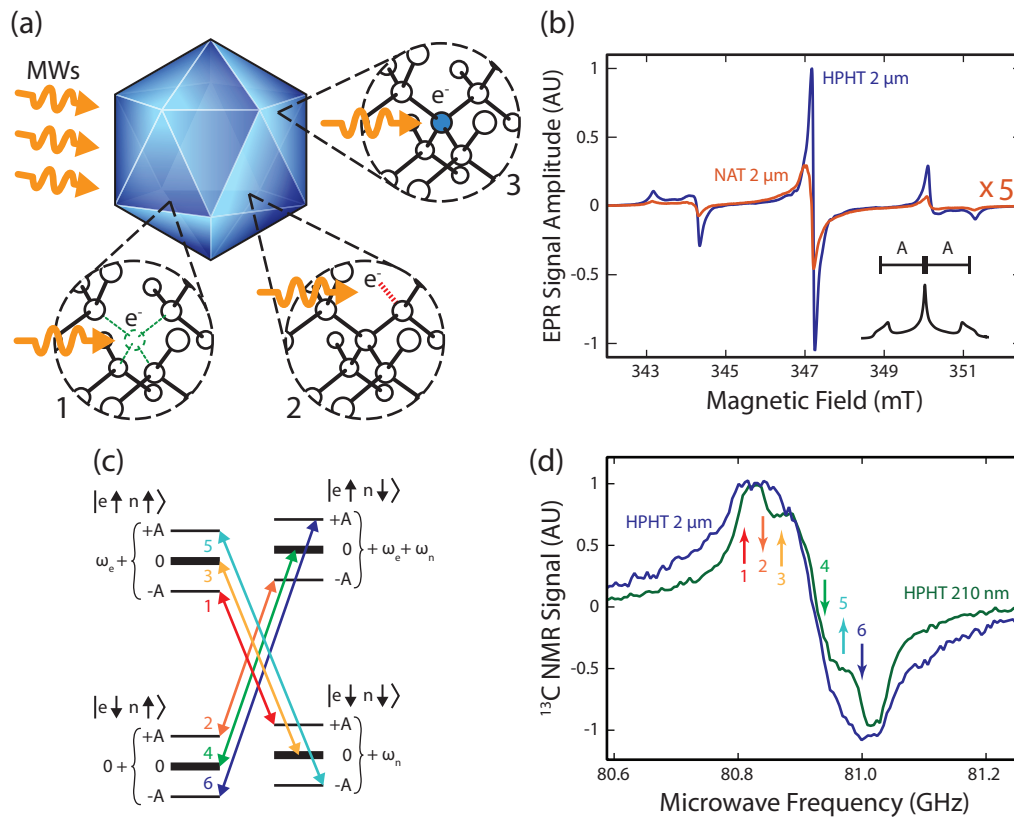


Figure 4.1: **Hyperpolarization of diamond via intrinsic defects.** (a) Diamond particles (blue) are host to spin-1/2 defects such as charged vacancy sites (1), dangling bonds (2) and substitutional nitrogen atoms (3). Resonant microwaves can be used to drive spin polarization from these defects to ^{13}C nuclei in the lattice. (b) X-band EPR spectra of 2 μm HPHT (blue) and 2 μm NAT (orange) diamonds. The HPHT and NAT nanodiamonds have substitutional nitrogen impurities present at 95 ppm and 4 ppm, respectively. Other spin-1/2 defects are present at concentrations of 115 ppm in the HPHT nanodiamonds and 28 ppm in the NAT nanodiamonds. A representative EPR absorption signal is also shown (inset, bottom right). Hyperfine splitting (A) of the EPR line results from nitrogen impurities. (c) Energy level schematic of Zeeman split electrons (e) and nuclei (n), showing possible flip-flip and flip-flop transitions in diamond. Transitions are numbered in order of increasing energy (1-6). (d) Hyperpolarization spectra of ^{13}C as a function of microwave frequency for HPHT 210 nm (green) and HPHT 2 μm (blue) diamond particles. Signals are normalized to 1. Transitions shown in c are indicated by arrows (1 - 80.81 GHz; 2 - 80.84 GHz; 3 - 80.87 GHz; 4 - 80.94 GHz; 5 - 80.97 GHz; 6 - 81.0 GHz).

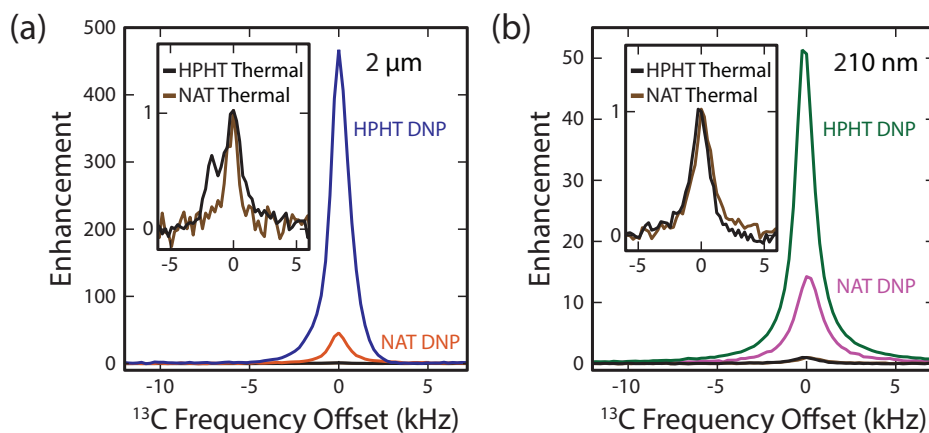


Figure 4.2: **Hyperpolarization of different nanodiamond types.** (a) ^{13}C NMR spectra of HPHT (blue) and NAT (orange) 2 μm diamonds after 20 minutes of hyperpolarization, normalized to the NMR signal from thermal polarization (HPHT - black; NAT - brown). (b) ^{13}C NMR spectra of HPHT (green) and NAT (purple) 210 nm nanodiamonds after 20 minutes of hyperpolarization, normalized to the NMR signal from thermal polarization (HPHT - black; NAT - brown).

of their polarization two hours after being transferred to an imaging platform see Fig. 4.3a. Decay rates for the smaller 210 nm particles are faster but still sufficient for imaging applications, with 10 % of hyperpolarization remaining after a period of 20 minutes [see Fig. 4.3b].

Comparing the relaxation data to the hyperpolarization spectra reveals that driving at select microwave frequencies leads to polarization that relaxes with a distinct nuclear T_1 (colored arrows in Fig. 4.1d correspond to colored curves in Fig. 4.3a). This dependence likely arises due to the microwave frequency selecting particular paramagnetic centers to act as hyperpolarization lattice sites for their surrounding nuclei. The same centers then dominate nuclear spin relaxation, such that different types of centers and their concentration will lead to different relaxation rates in presumably distinct magnetic micro-environments.

Examining the decay of the hyperpolarized state shows that the data is bi-exponential, containing short and long characteristic relaxation time components. Further, as a function of magnetic field, both components vary

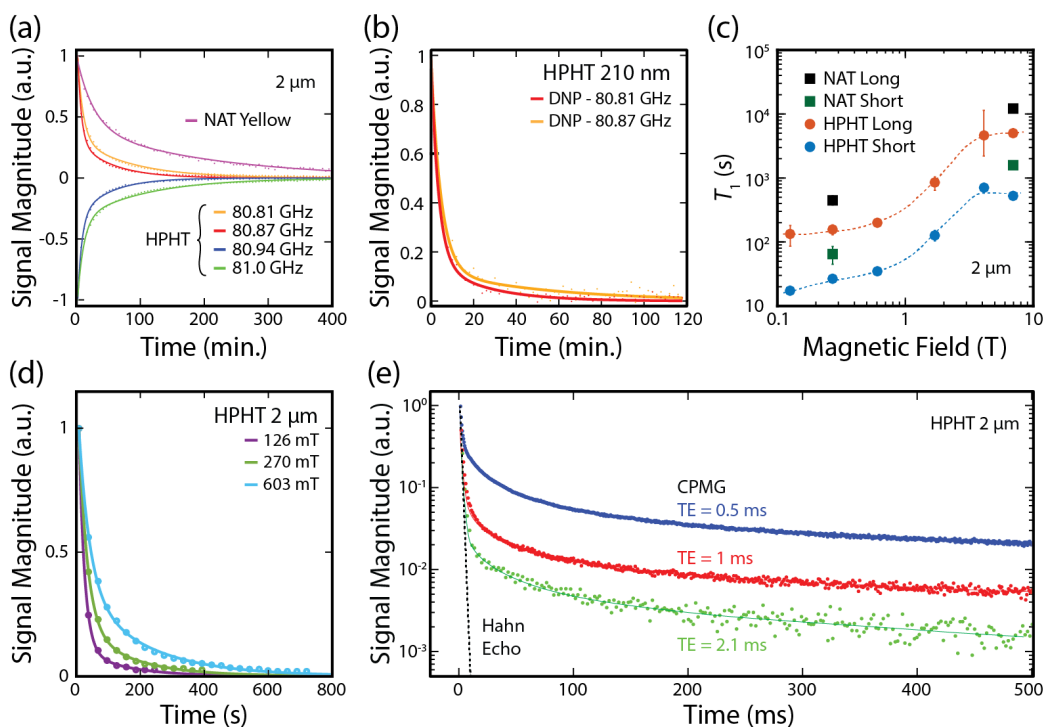


Figure 4.3: **Slow decay of nuclear polarization post-transfer.** (a) Signal decay of hyperpolarized 2 μm diamond particles at $T = 293$ K and $B_0 = 7$ T. Decay curves are shown for NAT 2 μm diamonds hyperpolarized at 80.87 GHz (purple) and HPHT 2 μm diamonds hyperpolarized at various frequencies (red - 80.81 , yellow - 80.87 GHz, green - 80.94 GHz and blue - 81.0 GHz). Lines are double exponential fits to the data (see Table 4.1 for fit values). (b) Signal decay of hyperpolarized 210 nm HPHT ND at $T = 293$ K and $B_0 = 7$ T. Decay curves are shown for hyperpolarization at 80.87 GHz (yellow) and 80.81 GHz (red). Lines are double exponential fits (see Table 4.1 for fit parameters). (c) T_1 versus magnetic field for 2 μm diamond particles. Circular markers show the HPHT long (red), NAT long (black), HPHT short (blue) and NAT short (green) components of a double exponential fit to the hyperpolarized decay curve. Lines are a guide to the eye. (d) Signal decay of hyperpolarized 2 μm HPHT ND at $T = 293$ K and 126 mT (purple), 270 mT (green) and 603 mT (blue). Decay curves are shown for ND hyperpolarized at 80.87 GHz. Double exponential fits to the curves are shown (Fit values are the markers in b). (e) Magnitude of echoes in a hyperpolarized 2 μm diamond sample. CPMG traces are shown with various echo spacings (Echo time (TE) = 0.5 ms - blue; TE = 1 ms - red; TE = 2.1 ms - green). The fit to a Hahn echo experiment performed with thermally polarized 2 μm diamond is also shown (black dotted line; data is shown in Section 4.10.2).

Diamond	Freq. (GHz)	a	$T_{1,\text{short}}$ (s)	$T_{1,\text{long}}$ (s)
HPHT 2 μm	80.81	0.69 ± 0.03	349 ± 28	3253 ± 248
HPHT 2 μm	80.87	0.66 ± 0.03	521 ± 46	5058 ± 358
HPHT 2 μm	80.94	-0.63 ± 0.02	589 ± 45	6330 ± 327
HPHT 2 μm	81.0	-0.67 ± 0.02	394 ± 26	2966 ± 181
NAT 2 μm	80.87	0.54 ± 0.03	1570 ± 145	12282 ± 618
HPHT 210 nm	80.81	0.85 ± 0.06	207 ± 21	1426 ± 332
HPHT 210 nm	80.87	0.82 ± 0.05	278 ± 38	3150 ± 1188

Table 4.1: **Fit parameters for hyperpolarized decays curves.** Hyperpolarized decay curves were fit with a two-component model: $M_z = ae^{-t/T_{1,\text{short}}} + (1 - a)e^{-t/T_{1,\text{long}}}$, where M_z is the measured signal (proportional to the z -component of ^{13}C magnetization), $T_{1,\text{short}}$ is the relaxation time of the short component, $T_{1,\text{long}}$ is the relaxation time of the long component and a is a ratio accounting for the relative contributions of the different relaxation-time components. Fit parameters shown here are for the decay curves in Fig. 4.3a,b of different ND types hyperpolarized at various DNP frequencies.

by nearly two orders of magnitude as the field is increased from $B = 130$ mT to 7 T, as shown in Fig. 4.3c. We attribute this field dependence to the presence of electron and three-spin mediated processes [189], characteristic of nitrogen impurities. Rapid decay of hyperpolarization at low-field presents a practical challenge to the implementation of hyperpolarized nanodiamond imaging, requiring the use of magnetized sample shuttles [190] [see Section 4.10.3 for details].

Moving from detecting hyperpolarized nanodiamond to imaging clinically-relevant concentrations of the material brings new challenges. In particular, since the short T_2 dephasing times of solids can limit the spatial resolution that is possible using typical scanner gradient magnetic field strengths. However, we find the ^{13}C nuclear spins in HPHT nanodiamond fortuitously possess T_2 times already suitable for demonstrating the technique, with substantial scope for improving spatial resolution using dynamical decoupling sequences [191]. To see this, in Fig. 4.3e we compare the signal decay from a standard Hahn-echo sequence (dotted-line) to the signal produced by the use of a Carr-Purcell-Meiboom-Gill (CPMG) decoupling sequence, after the

sample has been transferred from the polarizer to a 7 T imaging platform. Although the T_2 seen with Hahn-echo is already suitable for sub-millimetre imaging (see Section 4.10.4 for discussion of resolution limits), we find that spin-coherence is preserved for a significantly longer time by decreasing the inter-pulse spacing in the CPMG sequence. This enhancement in spin coherence is likely due to nulling of the dipolar term in the internal spin Hamiltonian by the repeated π -pulses [192]. This significant line-narrowing achieved with this technique could improve the imaging resolution of hyperpolarized nanodiamond [193].

4.5 MRI with Hyperpolarized Nanodiamond

Having established nanodiamond as a viable material for hyperpolarization applications, we now turn to the main result of our work, the demonstration of nanodiamond imaging with hyperpolarized ^{13}C MRI. We restrict our imaging experiments to the HPHT diamonds due to their larger signal enhancement. We begin our study by preparing the “half-moon” phantom shown in Fig. 4.4a, which consists of one chamber filled with water and one with an aqueous mixture of 2 μm diamond particles that have been hyperpolarized for 2 hours. The magnetic field that the diamond particles were exposed to was maximized at all times during the transfer and dissolution process in order to retain hyperpolarization [see methods in Section 4.9]. Once transfer of the phantom to the MRI system is complete, ^{13}C imaging is performed immediately with a centric-ordered, ultrafast gradient echo (GRE) sequence operating at $B = 7$ T. Sequences such as GRE allow for very short echo times with small tip angles, making them well suited to imaging hyperpolarized dipolar systems such as diamond, where T_2 is short and polarization is nonrenewable between phase encoding steps.

Immediately following the acquisition of the ^{13}C signal we perform conventional ^1H MRI in order to generate a co-registered water-nanodiamond image, shown in Fig. 4.4b. The ^1H component (gray-scale) of the co-registered image clearly shows the location of water and structure of the phantom, with the ^{13}C component (red-orange) indicating the location of the hyperpolarized

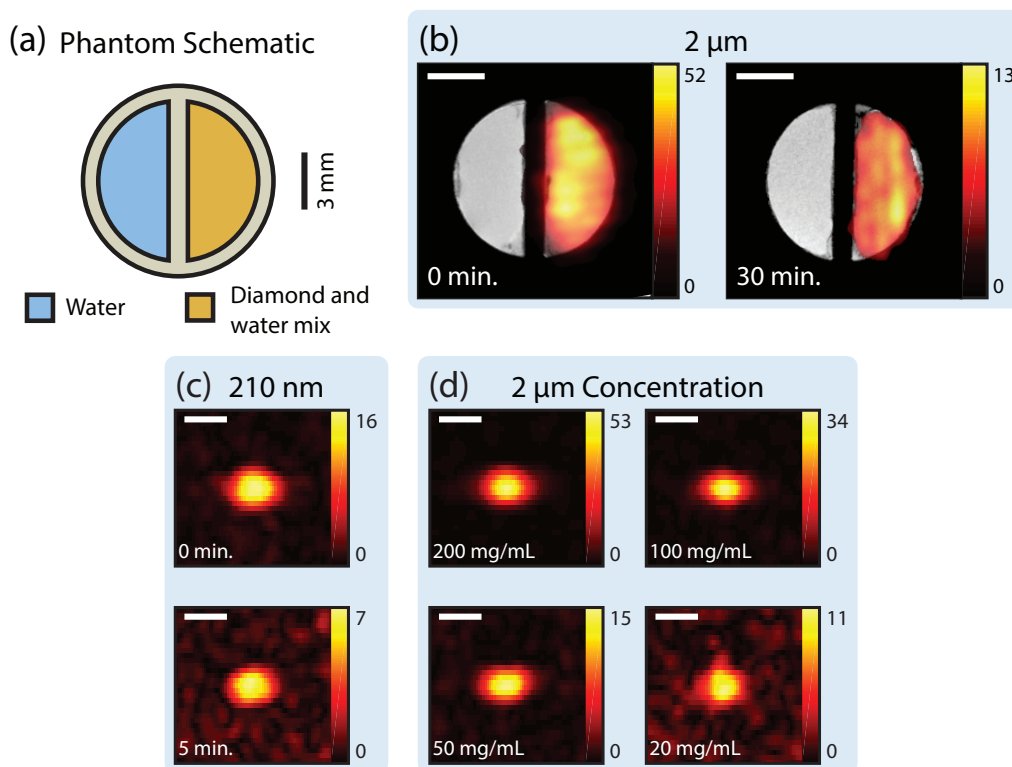


Figure 4.4: **Hyperpolarized Diamond Imaging.** (a) Phantom schematic. One side of the “half-moon” phantom was filled with a mixture of hyperpolarized diamond and water (orange). The other half of the phantom is filled with water (blue). (b) Hyperpolarized $2\ \mu\text{m}$ microdiamonds were imaged after dissolution in a $120\ \text{mg/mL}$ water mixture, using the phantom described in a after 0 minutes and 30 minutes in the scanner. (c) Hyperpolarized $210\ \text{nm}$ nanodiamonds in a teflon tube at $200\ \text{mg/mL}$ concentration were imaged after transfer from the polarizer after 0 minutes and 5 minutes in the MRI scanner. (d) Images of hyperpolarized $2\ \mu\text{m}$ microdiamonds in a teflon tube immediately after transfer from the polarizer at various concentrations. The colorscale in all images indicates ^{13}C signal magnitude in units of the noise floor. All scale bars are $3\ \text{mm}$ in length.

nanodiamond solution. We repeat the experiment, now with a delay of 30 minutes between transfer of the phantom to the MRI system and subsequent imaging. Although the image taken after 30 min shows a significant reduction in ^{13}C signal (down to $\sim 25\%$, of the image that was acquired with no delay), we note that it still contains sufficient contrast to be able to identify the presence of nanodiamond. Switching to the smaller 210 nm nanodiamonds yields images with a reduced signal-to-noise (SNR) (comparable to 30% of the 2 μm solution), with the images decaying more rapidly in keeping with the size dependence of T_1 [see Fig. 4.4c].

Evaluating the sensitivity of ^{13}C MRI in our current setup, we acquire images for aqueous solutions of hyperpolarized nanodiamonds in a range of concentrations from 20 - 200 mg mL^{-1} , as shown in Fig. 4.4d. For the larger 2 μm particles, concentrations as low as 20 mg mL^{-1} continue to yield an acceptable SNR ~ 11 , corresponding to 57 μg of diamond per pixel. This particle mass sensitivity is similar to other particle imaging techniques based on hyperpolarization [16, 185].

4.6 Animal Imaging

Aware that MRI phantoms can artificially enhance image quality, we demonstrate hyperpolarized nanodiamond imaging in a setting that is more realistic to the clinic by acquiring a co-registered $^{13}\text{C}:^1\text{H}$ MRI of a *post mortem* three-week old laboratory mouse (*mus musculus*). Using 2 μm HPHT nanodiamond, the sample was hyperpolarized for 2 hours before rapid dispersion into a syringe incorporating a 450 mT Halbach array to retain hyperpolarization. The mouse was positioned on a stage within an open-access permanent magnet and the hyperpolarized bolus then injected into the thoracic cavity. Transfer of the mouse to the 7 T MRI system again made use of a custom Halbach array. The total time between removal of the sample from the hyperpolarizer and insertion of the mouse in the MRI system was ~ 60 seconds.

Co-registered $^1\text{H}:^{13}\text{C}$ images of nanodiamond in the mouse are shown in Fig. 4.5. The ^1H image reveals anatomical features within the chest at sub-millimeter resolution. The ^{13}C diamond image then clearly shows

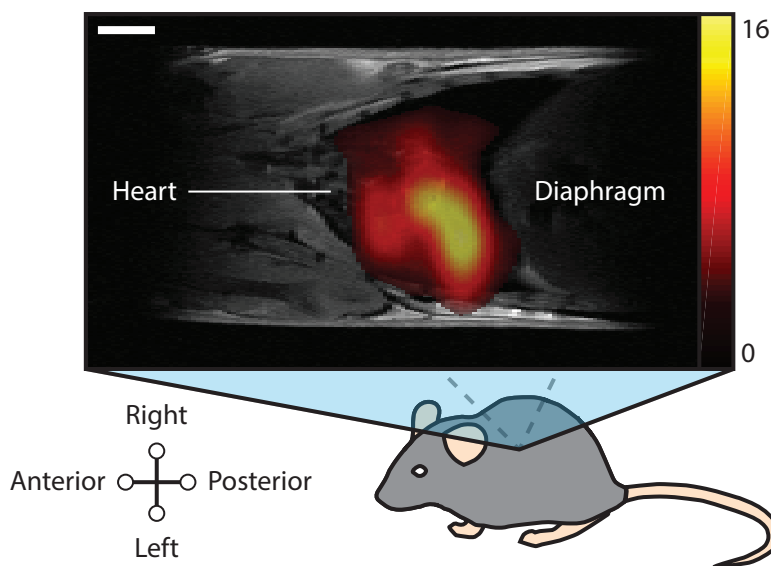


Figure 4.5: **Animal Imaging.** Co-registered $^1\text{H}:$ ^{13}C MRI of a mouse thorax following intrathoracic injection of hyperpolarized $2\ \mu\text{m}$ diamond particles. The colorscale indicates ^{13}C signal magnitude in units of the noise floor. Scale bars is 3 mm in length.

that the nanodiamond is confined to a region around the lungs. We would expect this localization to occur after injection into the thoracic cavity as the $2\ \mu\text{m}$ particles are too large to cross membranes into other regions of the mouse [16, 96].

4.7 Phase-Encoded Hyperpolarization

The use of nanoparticles for future theranostic applications hinges on the effectiveness of their functionalized surfaces, which, for instance, can enable targeted up-take of particles by binding to specific cells and localizing at specific disease foci. Accompanying these active targeting mechanisms are passive biological responses to nanoparticles based on their size, morphology, or particle composition [194–197]. Having demonstrated hyperpolarized nanodiamond MRI, we now look to the future and present a new imaging modality enabled by the material properties of nanodiamond and which aims

to directly address the challenge of resolving passive response mechanisms from the active targeted delivery of nanoparticles. The goal of distinguishing actively targeted vectors from a passive uptake is illustrated in Fig. 4.6, where the yellow particles feature surfaces with receptor molecules in contrast to the bare nanoparticles shown in green. The challenge then is to establish an imaging modality that enables contrast between nominally identical nanoparticles, based on a labeling mechanism that does not require a difference in particle size, composition, morphology, or physical state.

A means of tagging nanodiamond populations is evident in the data presented in Fig. 4.7a [reproduced from Fig. 4.1d], which shows the preparation of hyperpolarized states with equal magnitude, both aligned, or anti-aligned, with the external magnetic field by selecting the frequency of microwave driving. In each case the populations of ^{13}C spins are prepared predominantly in their ground or excited state, relaxing back to thermal equilibrium on a timescale T_1 , as indicated in Fig. 4.7a.

Imaging contrast between the ground and excited state populations is thus encoded in the opposing phases, rather than in the amplitudes of nuclear magnetization. Demonstrating this modality, we hyperpolarize two identical samples of 2 μm nanodiamond, the first at frequency $f = \omega_e - \omega_n$ and the second at $f = \omega_e + \omega_n$, flipping the phase of the magnetization as indicated in the phantom shown in Fig. 4.7b. Following adiabatic transfer to the imaging platform, we acquire co-registered $^1\text{H}:^{13}\text{C}$ magnitude and ^{13}C phase images, as shown in Fig. 4.7c. Conventional images constructed from the magnitude of the ^{13}C signal clearly show the location in the phantom of the hyperpolarized nanodiamond samples, but without appreciable contrast between them. Alternatively, significant contrast is apparent in the phase response of the ^{13}C signal, reflecting the phase-labeling of the hyperpolarized states and enabling the nominally identical nanodiamond populations to be readily distinguished.

Simultaneous administration of positively-polarized nanodiamonds, functionalized with active targeting ligands, and negatively-polarized, untargeted diamonds, opens the prospect of tracking and imaging nanodiamonds accompanied by an *in vivo* control. Such a control would also be useful for identify-

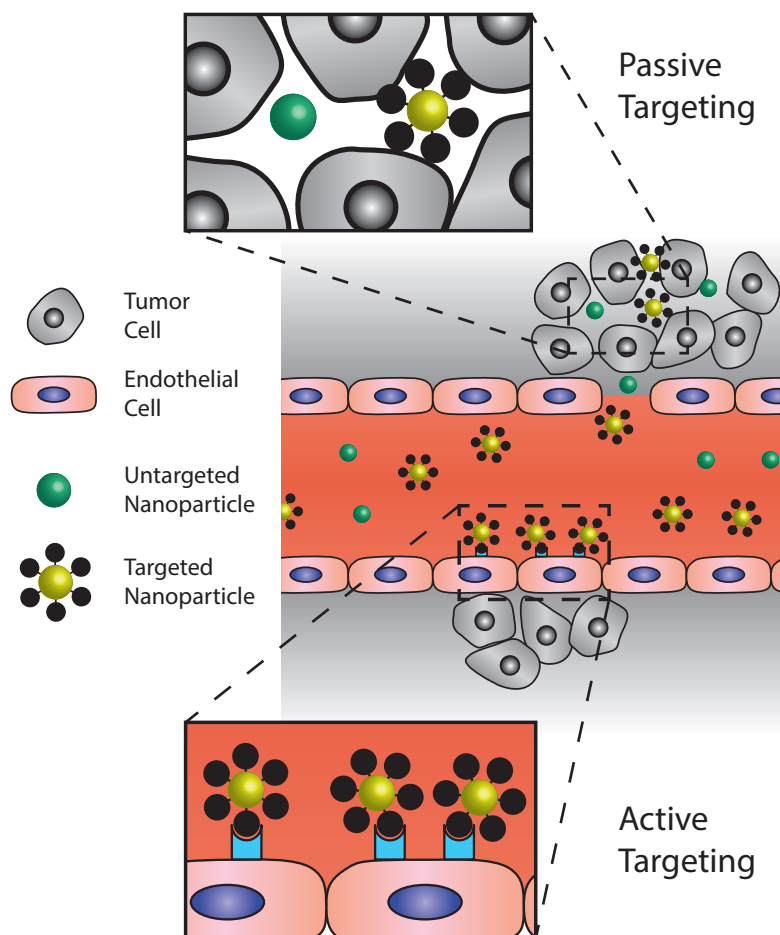


Figure 4.6: **Active targeting versus passive targeting.** Schematic representation of functionalized nanoparticles targeting tumors both actively and passively. Active targeting in the vasculature relies on specific interactions between ligands on the nanoparticle surface and receptors expressed on the surface of endothelial cells adjacent to tumors. Passive targeting is nonspecific to nanoparticle functionalization and can occur via the enhanced permeability and retention effect in regions of leaky vasculature at tumor sites. Potentially, phase-contrast imaging could distinguish between these two regimes.

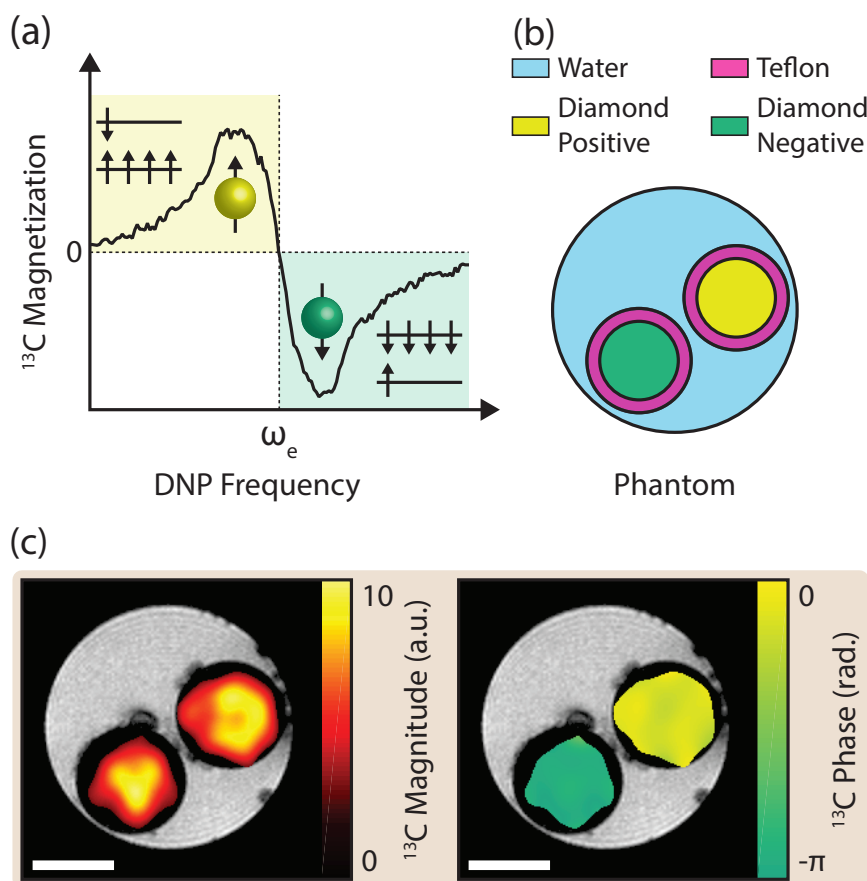


Figure 4.7: **Distinguishing identical particles with phase contrast.** (a) Direction of hyperpolarized ^{13}C magnetization versus the pump frequency. (b) Phantom schematic showing two $2\ \mu\text{m}$ diamond samples (yellow and green) in a tube of water (blue). Teflon walls of the tubes containing diamond are also shown (pink). The sample shown in yellow was hyperpolarized at $80.87\ \text{GHz}$ ($f = \omega_e - \omega_n$) for 20 minutes before transfer to the imager. The diamond sample shown in green was subsequently hyperpolarized at $80.94\ \text{GHz}$ ($f = \omega_e + \omega_n$) for 4 minutes before transfer to the hyperpolarizer. (c) Imaging of the phantom described in b. Overlaid ^{13}C magnitude (left) and phase (right) colormaps are shown with masks applied to regions with less than 8 times the root mean square value of the background signal. Small black spots in gray-scale ^1H magnitude image are bubbles adhered to surfaces in the phantom. Scale bar is 3 mm in length.

ing cases where targeting agents bind in undesired locations. As the targeting ability of functionalized nanoparticles can often disappear when placed in a biological environment [198,199], the ability to non-invasively verify, via MRI phase, that nanoparticle accumulations are due to active targeting appears useful.

4.8 Discussion

Opportunities exist to significantly improve the concentration sensitivity of nanodiamond MRI reported here. At present, transfer of the sample from hyperpolarizer to imaging platform results in a substantial loss of polarization, stemming from the rapid relaxation that occurs in a low-field (< 380 mT) environment. The use of high-field sample-shuttles during transfer can likely increase the signal by a factor of 10 or more [see Section 4.10.3 for discussion]. Further, we draw attention to the use of dynamical decoupling pulse sequences in preserving coherence in dilute spin systems such as diamond, as shown in Fig. 4.3c. Whilst CPMG based imaging sequences have displayed similar sensitivity in our scanner, they offer strong potential for improving spatial resolution and sensitivity when used in conjunction with appropriate gradient-field protocols [see Section 4.10.2 for details]. Developing a single-shot sequence based on quadratic echo imaging [193], for instance, would allow rapid pulsing and high-resolution imaging via the long echo tails observed in the hyperpolarized nanodiamond system.

Perhaps the most impactful opportunity for improving the performance of nanodiamond MRI is in isotopic engineering of the precursor carbon. Enriching the ^{13}C content, from the 1.1% that occurs in natural abundance, to a few percent will lead to a proportional increase in MRI sensitivity [182,200] with limited impact on relaxation times [see Section 4.10.5 for discussion]. A further avenue for improvement is in optimizing the type and concentration of paramagnetic centers in an effort to lengthen spin dephasing times [201] and suppress low-field relaxation [91,189]. This will be particularly important in extending the applications for smaller nanodiamonds. The use of photo-excited radicals, such as those that persist at low temperatures but

recombine on warming the sample [202], may further provide a means of achieving long-lived hyperpolarization.

In conclusion, we have demonstrated ^{13}C magnetic resonance imaging using nanodiamonds, including the introduction of a new imaging modality based on phase-encoded hyperpolarization, exploiting the long relaxation times inherent to the diamond material system. Future improvements in materials, hardware, and sequence design will likely see the nanodiamond platform emerge as a valuable theranostic tool for multimodal imaging, combining MRI and optical fluorescence to span sub-cellular to whole-body scales.

4.9 Methods

Diamond Particles: The nanodiamonds used in this work were purchased from Microdiamant (Switzerland). Specific nanodiamond types were monocrystalline, synthetic HPHT and NAT particles. Both types were used in sizes of 210 nm (0-500 nm, median diameter 210 nm) and 2 μm (1.5-2.5 μm , median diameter 2 μm). The 2 μm HPHT diamonds used here are well suited to injection as they have a zeta potential of -38 ± 7 mV in water. This zeta potential shows that they are aggregation-resistant, a characteristic important to benefiting fully from the surface of nanodiamond in biological applications [99]. The 2 μm particles display sedimentation on the timescale of hours, as is to be expected for diamond particles larger than 500 nm, which is the point at which gravitational forces overcome Brownian motion. 210 nm HPHT nanodiamonds have a near identical zeta potential of -39 ± 8 mV with limited sedimentation observed over a period of weeks. For details of dynamic light scattering measurements and calculation of particle stability, see Section 4.10.6.

EPR Characterization: EPR spectra were measured using a Bruker EMX EPR Spectrometer operating at 9.735 GHz and room temperature. Resulting spectra were fit using Easyspin to a three spin component model [130,162]. Defect concentrations were calculated relative to the signal from an irradiated quartz EPR standard [203].

Hyperpolarization of diamond: Hyperpolarization is performed in a

2.88 T superconducting NMR magnet with a homebuilt DNP probe [163]. 80-82 GHz microwaves are generated via a frequency multiplier (Virginia Diodes) and 2 W power amplifier (Quinstar) before being directed to the sample via a slotted waveguide antenna. A helium flow cryostat (Janis) was used to cool the sample to 4.5 K. NMR measurements in the polarizer were taken with a custom saddle coil tuned to the ^{13}C Larmor frequency of 30.912 MHz. All hyperpolarization events begin with a ^{13}C NMR saturation sequence ($64 \times \pi/2$ pulses) to zero the initial polarization. Individual points in the frequency sweeps of Fig. 4.1d correspond to unique hyperpolarization events, showing the ^{13}C NMR signal from a $\pi/2$ pulse after 60 s of microwave saturation at a constant frequency. NMR enhancement plots in Fig. 4.2e,f show the ^{13}C signal magnitude after 20 minutes of microwave saturation compared with the signal seen after an identical period of thermal polarization. Absolute polarization values are calculated from the thermally polarized ^{13}C signal at equilibrium and the expected Boltzmann polarization [130]. Diamond samples were hyperpolarized in teflon tubes, chosen for their transparency to microwaves and robustness to thermal cycling.

Transfer and dissolution: All post-transfer NMR signals were acquired in the same 7 T superconducting NMR magnet used for imaging. Adiabatic sample transfer between the DNP probe and the MRI scanner occurs via a series of “magnetic shields” based on permanent magnets and Halbach arrays (see Sections 4.10.3 and 4.10.7 for further detail). Halbach arrays are especially useful for transferring samples between superconducting magnets as they experience no net translational force in external magnetic fields.

Depolarization at 7 T was measured via small tip angle for 2 μm and 210 nm samples hyperpolarized for 2 hours and 1 hour, respectively. Data were divided by $(\cos \alpha)^{n-1}$, where α is the tip angle and n the pulse number, to account for RF-induced signal decay.

T_1 versus magnetic field strength was measured in the stray field of the imaging magnet with samples hyperpolarized for 20 minutes. Small tip angle measurements of the ^{13}C signal magnitude were taken at 7 T before and after shuttling the sample to a lower field region for repeated periods of 30 s.

The phantom in Fig. 4.4a was prepared in an approximately 200 mT

permanent magnet by rapid thawing of a ^{13}C hyperpolarized 2:1 mixture of nanodiamond and water. The hyperpolarized mixture was then mixed with additional water to give a 120 mg mL^{-1} concentration. Transfer to the MRI system occurred via a 110 mT Halbach array.

MRI Experiments: All MRI was performed in a 7 T widebore, microimaging system with ^1H and ^{13}C Larmor frequencies of 299.97 MHz and 75.381 MHz, respectively. The microimaging gradient set produces gradient fields up to 250 mT m^{-1} . Phantoms were imaged using a 10 mm, dual resonance $^1\text{H}:$ ^{13}C NMR probe. ^1H phantom images were acquired with a GRE sequence with $60\text{ }\mu\text{m} \times 60\text{ }\mu\text{m}$ pixel size and 6 mm slice thickness. ^{13}C slice thickness was restricted to 20 mm by the active region of the detection coil. Concentration phantoms contained 140 μL of diamond and water mixture.

^{13}C GRE image data in Fig. 4.4b-d and 4.7c were acquired with a 64×32 matrix and pixel resolution of $0.7\text{ mm} \times 0.6\text{ mm}$. The refocusing time (TE) of 1.22 ms was minimized by ramping gradients to full strength and using short, 60 μs , excitation pulses (see Fig. 4.8 for complete timing parameters). Centrally-ordered phase encoding with a constant flip angle of 20° was used to increase SNR by 1.96 times at the expense of limited blurring in the phase encode direction [204].

All images displaying ^{13}C data only were interpolated to 128×128 resolution by zero-filling and Gaussian filtering in k -space. Co-registered ^{13}C images were interpolated to the resolution of the accompanying ^1H image and values smaller than 3 times (Fig. 4.4b) or 5 times (Fig. 4.5, Fig. 4.7c) the SNR made transparent to reveal the underlying structure in the ^1H image.

Animal Imaging: A 150 mg sample of 2 μm nanodiamonds was hyperpolarized for 2.5 hours in a 1:1 mixture with water with 0.2 mL of hot water added during dissolution. Small tip angle characterization showed that hyperpolarizing in water or ethanol gave the same ^{13}C enhancement seen for dry samples. The resulting 0.5 mL bolus was injected into the thoracic cavity of a three-week old female mouse *post mortem* (11 g, *mus musculus*) with a 21G needle and syringe before transfer to the MRI system. Hyperpolarized nanodiamonds were magnetically shielded with custom magnets when not in the polarizer or imager (further details in Section 4.10.3). The total time for

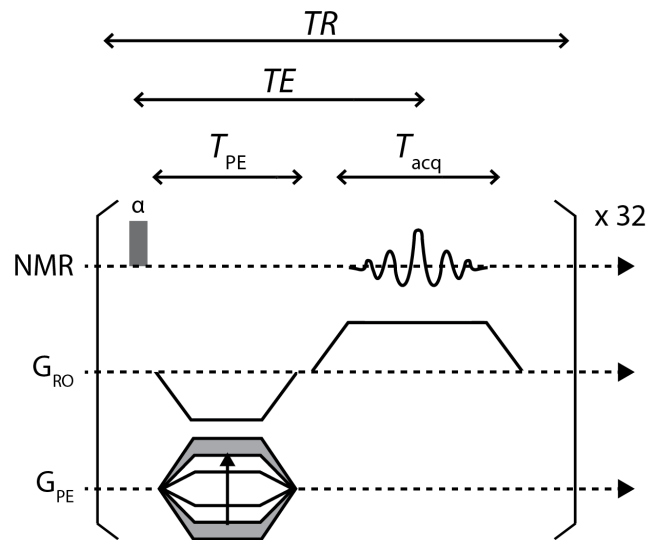


Figure 4.8: **Pulse timing diagram for GRE sequences.** (a) Gradient Refocused Echo (GRE) sequence used for ^{13}C imaging. Relative timing of NMR pulses, readout gradient (G_{RO}) and phase encode gradient (G_{PE}) are shown. Imaging parameters were: repetition time (TR) = 100 ms, echo time (TE) = 1.2 ms, acquisition time (T_{acq}) = 0.64 ms, phase encode time (T_{PE}) = 0.4 ms and $\alpha = 20^\circ$. No crusher gradients were required as the 100 ms repetition time is sufficient to spin dephasing with negligible spin-lattice relaxation. TE and T_{PE} were adjusted to 0.9 ms and 0.12 ms, respectively for mouse experiments.

dissolution, injection and transfer to the imager was approximately 60 s.

A $^1\text{H}:$ ^{13}C double resonance microimaging probe with 18 mm bore size was used for imaging the mouse torso. ^{13}C SNR of this probe was measured to be one third of the 10 mm probe used for phantom imaging. A conventional ^1H spin-echo sequence was used for high-contrast anatomical imaging. ^1H images were acquired with 1 mm slice thickness with a 256×256 matrix and pixel resolution of $230 \mu\text{m} \times 176 \mu\text{m}$. The same ^{13}C GRE sequence was used as in Fig. 4.4b-d but with a gradient echo time of 0.90 ms and pixel size of $2.1 \text{ mm} \times 1.9 \text{ mm}$. Slice thickness was limited to less than 18 mm by the sensitive region of the probe.

Phase-contrast Imaging: To demonstrate phase-contrast imaging, a $2 \mu\text{m}$ HPHT sample was positively polarized with 80.87 GHz microwaves for 20 minutes and transferred to the MRI scanner. A second, nominally identical sample was then negatively polarized with 80.94 GHz microwaves for 4 minutes and transferred to the MRI scanner.

4.10 Additional Results

4.10.1 Hyperpolarization Mechanism and Nanodiamond Characterization

Establishing the precise mechanism of ^{13}C hyperpolarization in diamond particles at $B_0 = 2.88 \text{ T}$ is complicated by the very similar g -factors of the electronic defects and the spin-1 ^{14}N nucleus induced hyperfine splitting of substitutional nitrogen defects (for defect concentrations and EPR spectra of all diamond samples used in this chapter, see Table 4.2 and Fig. 4.9, respectively). The similarity of g -factors means that the ^{13}C hyperpolarization we observe at 80.87 GHz and 80.94 GHz results from unresolved, overlapping positive and negative DNP peaks from multiple EPR lines. For example, at 80.87 GHz we are observing positive hyperpolarization at $\omega_e - \omega_n$ from the broad component, narrow component and $m_I = 0$ line of the P1 centers plus negative hyperpolarization at $\omega_e + \omega_n$ resulting from the $m_I = -1$ line of the P1 centers. The hyperpolarization behaviour at the outer two frequencies of

Diamond	Defect Concentration (ppm)			
	Total	P1	Broad	Narrow
HPHT 2 μm	210 \pm 10	95 \pm 5	108 \pm 5	7 \pm 1
HPHT 210 nm	380 \pm 20	35 \pm 2	300 \pm 20	41 \pm 2
NAT 2 μm	32 \pm 2	4.3 \pm 0.2	25 \pm 1	3.3 \pm 0.2
NAT 210 nm	190 \pm 10	6.8 \pm 0.3	169 \pm 9	14 \pm 1

Table 4.2: **Defect concentrations.** Concentrations of defects extracted from the fits shown in Fig. 4.9. The defect concentration was calculated relative to an irradiated quartz standard [203, 207].

80.81 GHz and 81.0 GHz is simpler, each being dominated by only one line of the P1 centers.

At 2.88 T, the ^{13}C nuclear frequency ω_n is 31 MHz, approximately twice the 0.6 mT (17 MHz) inhomogeneous linewidth Δ of P1 centres we expect at such field strengths [205]. These values are significantly larger than the homogeneous linewidth δ of the electronic defects, which for P1 centers is on the order of 600 kHz [206]. Hence, given that δ and ω_n are smaller than Δ , we expect that hyperpolarization via P1 centres, and the component of our EPR spectra with similar linewidth, occurs via the solid effect [63]. As the solid effect occurs via the interaction of one electron and one nucleus, this would also explain the roughly linear scaling of DNP enhancement with defect concentration that we observe between HPHT and NAT samples. However, we also note that the broad component of our EPR spectra is expected to have an inhomogeneous linewidth of 2.0 mT (56 MHz) at 2.88 T, larger than the nuclear Larmor frequency, raising the possibility of ^{13}C hyperpolarization via the cross effect. Other studies of diamond hyperpolarization have suggested there could also be a very small contribution to hyperpolarization from the Overhauser effect [131]. Synthesis of diamond with carefully controlled defect composition will help reveal the details of these complex DNP mechanisms and the variation in spin-relaxation properties shown in Table 4.3.

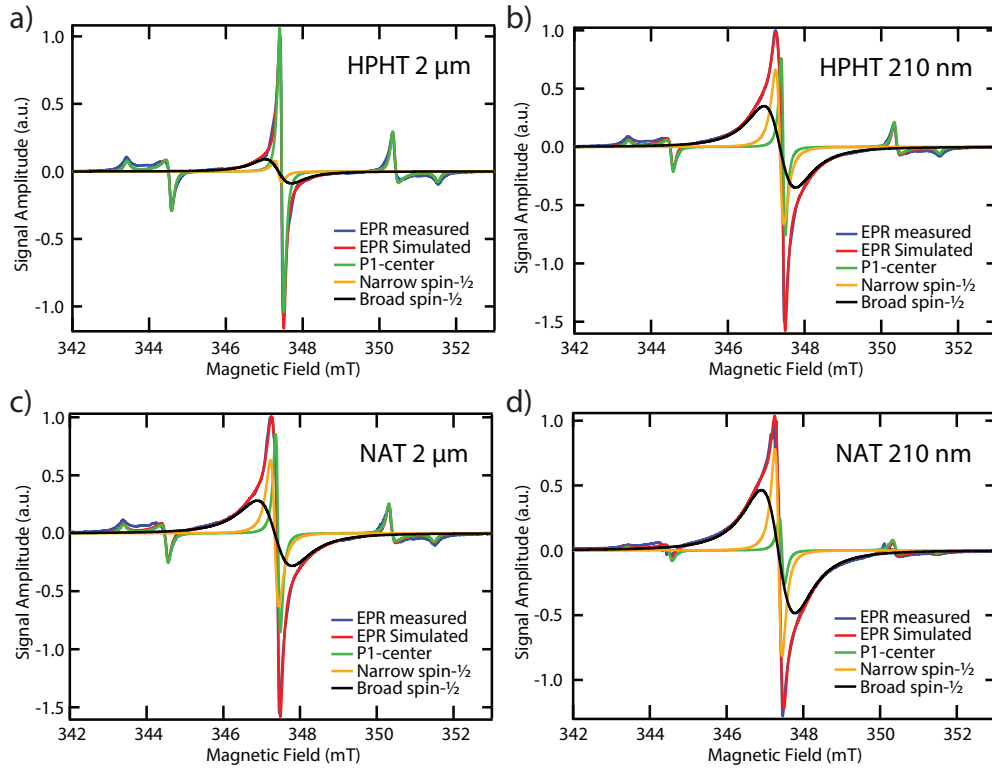


Figure 4.9: **Fitting EPR spectra.** EPR spectra of HPHT 2 μm (a), HPHT 210 nm (b), NAT 2 μm (c) and NAT 210 nm (d) diamond particles. Spectra are fit by a spin-1/2 model comprising three components: a broad single-line, a narrow single-line and a hyperfine split P1 center. Narrow single-line (linewidth 0.2 mT) and broad single-line (linewidth approximately 0.8 mT) components likely correspond to vacancy sites and dangling bonds in the diamond lattice, respectively [187, 188]. The hyperfine-split component is attributed to P1 centers (linewidth 0.1 mT), substitutional nitrogen atoms in the diamond lattice [186].

Diamond	$T_{1,\text{short}}$ (s)	$T_{1,\text{long}}$ (s)	a	T_2 (ms)
HPHT 210 nm	12 ± 5	152 ± 40	0.42 ± 0.09	2.1 ± 0.1
HPHT 2 μm	77 ± 18	6441 ± 2220	0.59 ± 0.05	1.2 ± 0.1
NAT 210 nm	23 ± 7	359 ± 67	0.33 ± 0.06	2.7 ± 0.1
NAT 2 μm	491 ± 202	9672 ± 1607	0.29 ± 0.06	3.1 ± 0.1

Table 4.3: **T_1 and T_2 relaxation times of thermally polarized diamond particles.** The ^{13}C T_1 relaxation times of the various diamond particles were measured using saturation recovery at $T = 293$ K and $B_0 = 7$ T. The resulting data were fit with a two component model: $M_z = 1 - ae^{-t/T_{1,\text{short}}} - (1 - a)e^{-t/T_{1,\text{long}}}$, where M_z is the measured signal (proportional to the z -component of ^{13}C magnetization), $T_{1,\text{short}}$ is the relaxation time of the short component, $T_{1,\text{long}}$ is the relaxation time of the long component and a is a ratio accounting for the relative sizes of the two components. The ^{13}C T_2 relaxation times of the various diamond particles were measured at $T = 293$ K and $B_0 = 7$ T via a Hahn-echo experiment. The normalized data at various echo times were fit to an exponential model: $M_x = e^{-t/T_2}$, where T_2 is the spin-spin relaxation time.

4.10.2 RARE Imaging

CPMG sequences can be used to extend the T_2 coherence times of ^{13}C nuclei in nanodiamond, as measured via Hahn echo techniques [see Fig. 4.10a,b]. To leverage these extended coherence times for imaging we use a custom imaging sequence based on Rapid Acquisition with Refocused Echoes (RARE) MRI [16, 208], which integrates phase encode steps and readout between π pulses. Such RARE sequences are popular for their high sensitivity but require accurate calibration to prevent artifacts. In Fig. 4.10c,d we show RARE images of 2 μm and 210 nm hyperpolarized samples. A short pulse width of 40 μs and 2.1 ms echo time was used to acquire these images with a resolution similar to that used in GRE images in Fig. 4.4. Complete RARE timing parameters are provided in the caption of Fig. 4.11. To prevent artifacts due to rapid initial signal decay, centricly ordered phase encoding begins with the third CPMG echo and post-processing was used to weight the amplitude of phase encodes by the gradient-free long tails acquired in 4.10b.

The SNR of the RARE images shown here should be multiplied by $2.5\times$

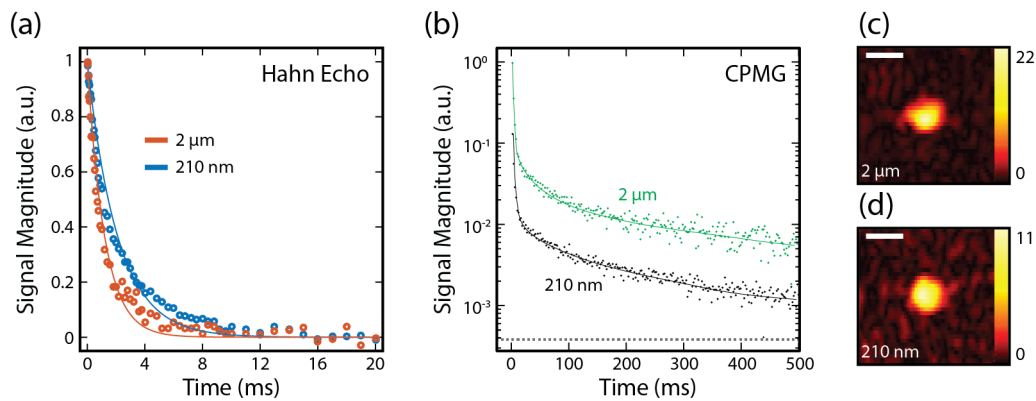


Figure 4.10: **Spin-echoes in diamond.** (a) ^{13}C T_2 characterization of HPHT diamonds in a Hahn-echo experiment at $B = 7$ T and $T = 293$ K. Data is shown for $2\ \mu\text{m}$ (red) and $210\ \text{nm}$ (blue) samples. Solid lines are a fit to the experimental data with fit parameters shown in Table 4.3. The $2\ \mu\text{m}$ fit is shown in Fig. 4.3. (b) Signal magnitude of hyperpolarized echoes in a CPMG experiment with $2.1\ \text{ms}$ echo spacing. Traces for hyperpolarized $2\ \mu\text{m}$ (green) and $210\ \text{nm}$ (black) HPHT samples are shown. (c) Rapid Acquisition with Refocused Echoes (RARE) acquired image of hyperpolarized HPHT $2\ \mu\text{m}$ diamonds at $200\ \text{mg/mL}$. (d) RARE acquired image of hyperpolarized HPHT $210\ \text{nm}$ diamonds at $200\ \text{mg/mL}$. All RARE data were acquired with a 64×32 matrix and pixel resolution of $0.7\ \text{mm} \times 0.5\ \text{mm}$ resolution. Scale bars are $3\ \text{mm}$ in length. The colorscale in all images indicates signal magnitude in units of the noise floor.

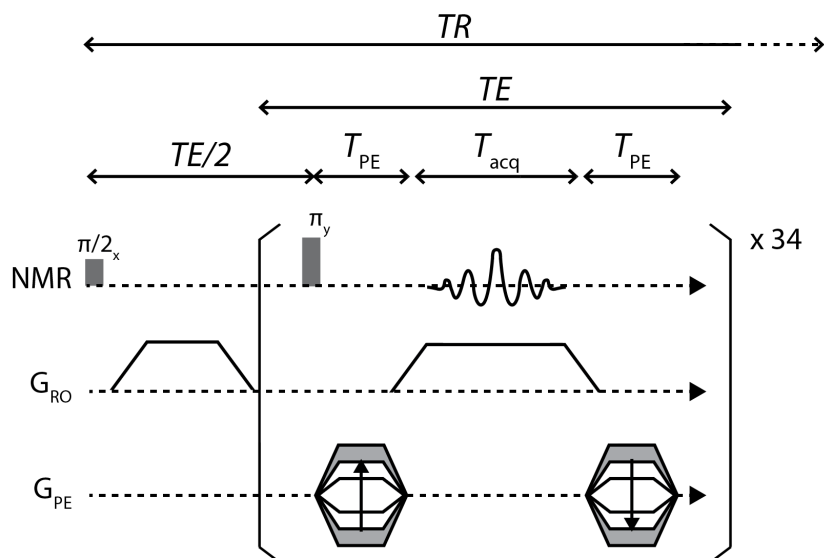


Figure 4.11: **Imaging sequence with refocused echoes.** Rapid acquisition with refocused echoes (RARE) sequence used for ^{13}C imaging. Relative timing of NMR pulses, readout gradient (G_{RO}) and phase encode gradient (G_{PE}) are shown. Imaging parameters were: repetition time (TR) = 75 ms, echo time (TE) = 2.1 ms, acquisition time (T_{acq}) = 0.8 ms and phase encode time (T_{PE}) = 0.4 ms. Gradient amplitude was set to zero for the first 2 signal acquisition steps so that imaging began after the long tail echo was established.

for a fair sensitivity comparison with GRE images shown in Fig. 4.4 (to take account of variations in pixel size and the expected SNR with a variable flip angle GRE sequence). After this SNR correction, we find that the RARE and GRE sequences have near equivalent sensitivity for 2 μm particles, whilst RARE is approximately 70 % higher sensitivity when imaging 210 nm particles. As RARE has optimal sensitivity for long spin-coherence times, we expect this difference is due to the intrinsically longer T_2 of ^{13}C nuclei in the 210 nm NDs [see Supp. Table 4.3 for T_2 values].

Whilst the sensitivity of GRE and RARE sequences, as applied here, are nearly equivalent, with higher strength gradients it should be possible to shorten the 2.1 ms echo time used for RARE imaging. This would allow us to leverage the significantly larger ^{13}C signal tail that appears for a 0.5 ms echo time in Fig. 4.3c for significantly higher SNR in RARE imaging.

4.10.3 Retaining Polarization with Magnetic Shielding

The hyperpolarized T_1 of nanodiamond drops by orders of magnitude as the external magnetic field becomes small, as was shown previously in Fig. 4.3. Hence, for spectroscopic experiments, we have developed magnetic tunnels and sample shuttles for sample transfer between the hyperpolarizer and MRI scanner, as shown in Fig. 4.12a-c. These tunnels and shuttles keep the hyperpolarized samples at magnetic fields above 300 mT for the majority of the transfer path, as is shown in Fig. 4.12d. However, there is one extreme point where the magnetic field strength drops below 5 mT. This point corresponds to the neck on the cryostat we use to achieve low hyperpolarization temperatures.

The hyperpolarized signal post-transfer is enhanced by a factor of nearly 200 compared with room temperature values, as shown in Fig. 4.13a, corresponding to a post-transfer ^{13}C polarization of $\sim 0.1\%$. This means that the post-transfer ^{13}C polarization is reduced by nearly 99% from the pre-transfer ^{13}C polarization. We attribute this reduction to the low-field region the sample passes through on exiting the cryostat. This low-field relaxation may be arising from a three-spin relaxation process being favored when the nuclear Larmor frequency is of a similar magnitude to the hyperfine splitting in P1-centers. Such a scenario occurs at magnetic fields below a few hundred mT.

To determine the characteristic magnetic field that we need to retain polarization during transfer, we shuttled the hyperpolarized sample between the detection coil at 7 T and lower field regions for 30 second periods, collecting the retained polarization data shown in Fig. 4.13b. The retained polarization curve implies that construction of a polarizer that keeps the sample at a field strength of above 300 mT at all times would enable transfer of hyperpolarized nanodiamond samples, whilst retaining more than 50% of the ^{13}C polarization. The construction of such polarizers is a subject of active research [190] and could see an improvement in MRI sensitivity of 50 times that seen in Fig. 4.4.

Aware of the added complexity of performing *in vivo* experiments with

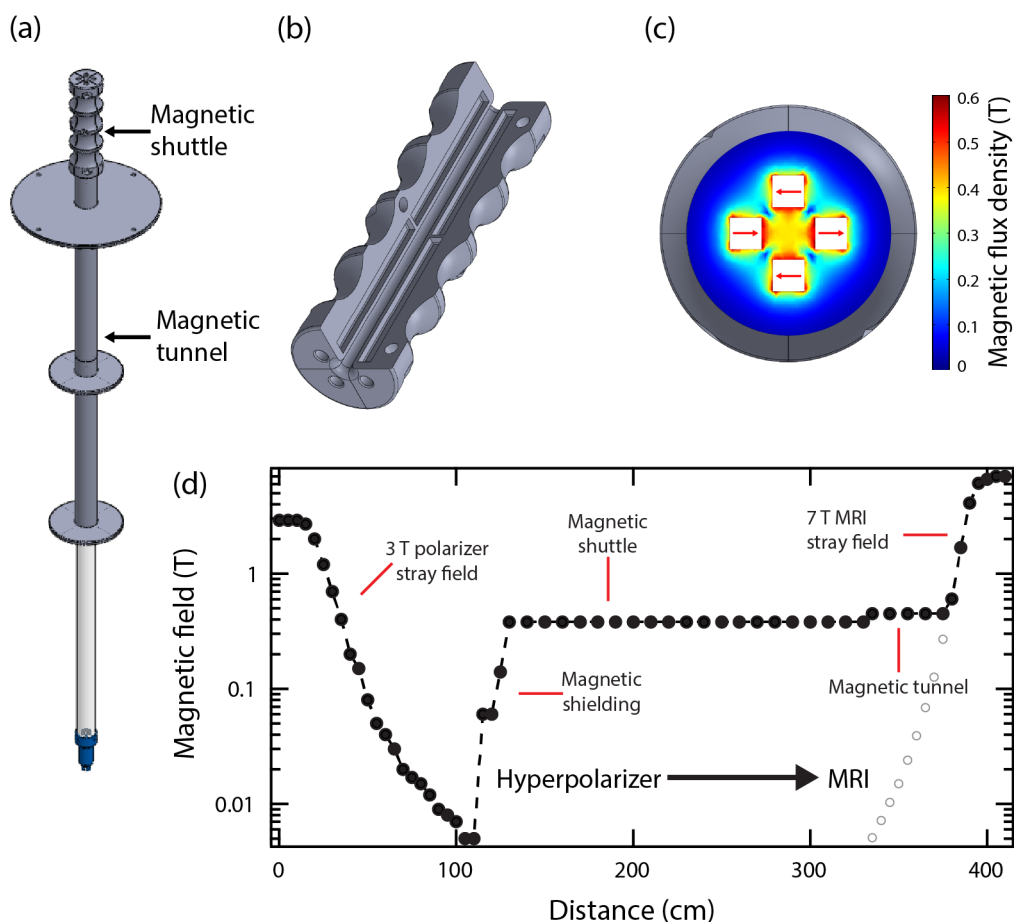


Figure 4.12: **Magnetic transfer apparatus and field profile** (a) A magnetic tunnel is used to keep the sample at high magnetic field when entering the bore of the 7 T MRI. The tunnel is lined with neodymium magnets in a simplified Halbach arrangement. (b) Magnetic shuttle. Cutout shows slots for 5 mm x 5 mm x 60 mm neodymium magnets. (c) Magnetic field simulations of the magnetic field in a cross-section of the sample shuttle. Simulations were performed with Comsol Multiphysics for N38 grade neodymium magnets. Red arrows indicate orientation of magnets. (d) Magnetic field strength at the diamond sample during direct transfer between the hyperpolarizer and MRI. Solid circles indicate field strength with the magnetic tunnel in place. Open circles indicate the stray field from the MRI magnet when the magnetic tunnel is not in place.

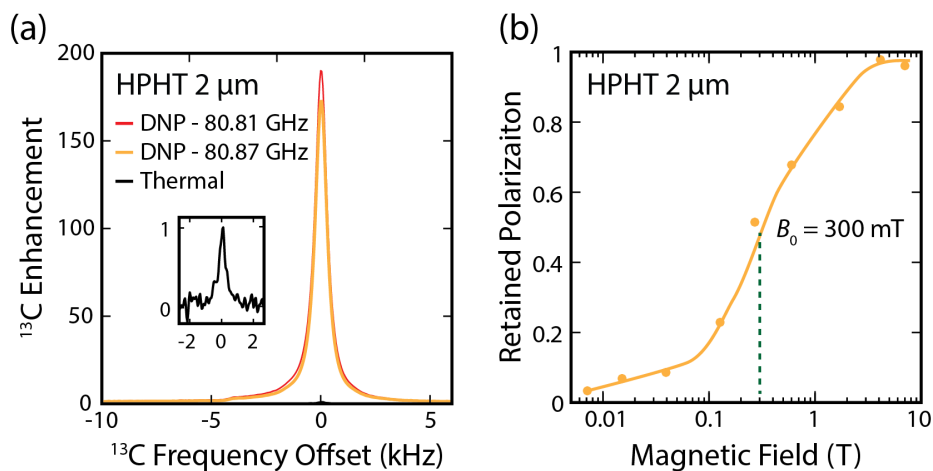


Figure 4.13: **Polarization loss at low magnetic field.** (a) Hyperpolarized NMR spectra in the 7 T imager at room temperature after transfer of 2 μm diamond particles hyperpolarized for 20 minutes at 80.81 GHz (red) and 80.87 GHz (yellow). Magnitude is normalized to the thermal signal after 5 hours buildup at 293 K and 7 T (black). Average hyperpolarized signal magnitudes were 192 ± 63 and 176 ± 38 for samples hyperpolarized at 80.81 GHz and 80.87 GHz, respectively. Magnitude values quoted are the average of 3 consecutive transfers with errors. (b) ^{13}C magnetization retained after 30 seconds at various field strengths for 2 μm HPHT diamond hyperpolarized at 80.87 GHz. Solid line is intended as a guide to the eye.

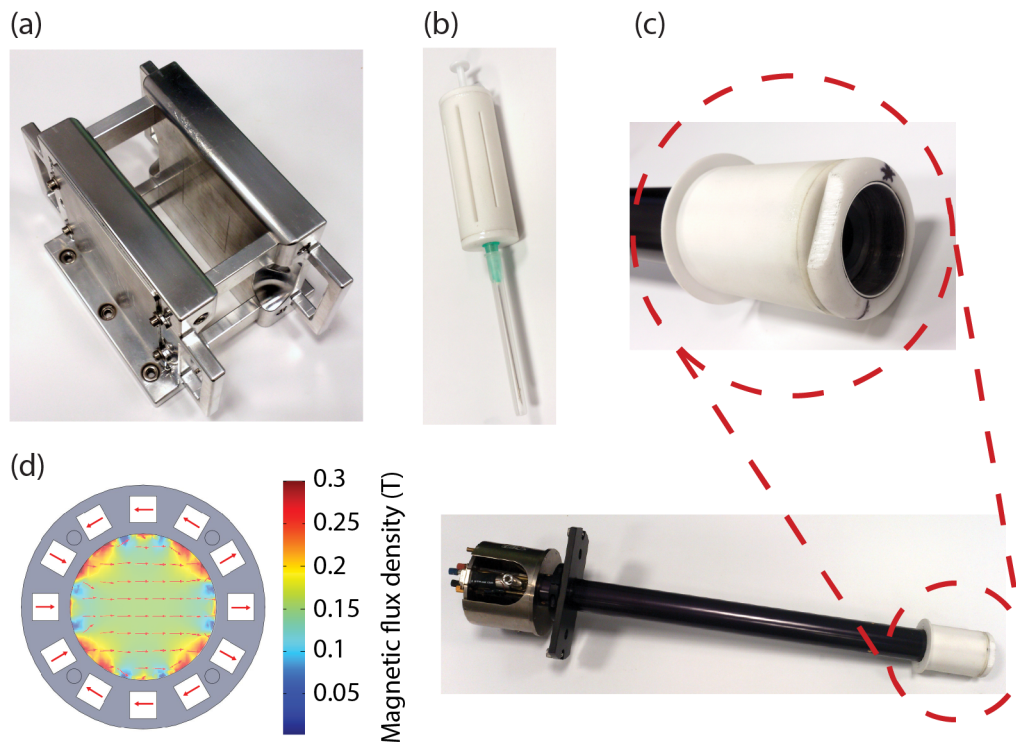


Figure 4.14: **Transfer hardware for animal imaging.** Various magnet assemblies used to maximize the magnetic field at hyperpolarized samples. (a) Two 100 mm \times 100 mm neodymium magnets create a 50 mm \times 50 mm \times 50 mm working space with a magnetic field greater than 200 mT. (b) Syringe with simplified Halbach array for injection of hyperpolarized diamonds. (c) Microimaging probe with a sliding collar that integrates a Halbach array. (d) Simulations (Comsol Multiphysics) of the magnetic field strength inside simplified Halbach array with an inner diameter of 30 mm.

constraints on minimum magnetic fields, we developed the hardware shown in Fig. 4.14 for our animal experiments. The permanent magnet shown in Fig. 4.14a is integrated with a mouse bed, allowing injection of hyperpolarized NDs from the shielded syringe shown in Fig. 4.14b. The mouse is then loaded into a microimaging probe. The hyperpolarized NDs in the mouse are magnetically shielded on transfer to the MRI scanner by the sliding Halbach array shown in Fig. 4.14c.

4.10.4 Effect of T_2 relaxation times on resolution.

Even in cases of high polarization, short spin-spin coherence times limit the time available for position encoding with magnetic field gradients, limiting the achievable MRI resolution. For conventional MRI sequences, the fundamental MRI resolution limit is reached when the NMR linewidth is approximately equal to the frequency separation between each pixel [165]:

$$dz \sim \frac{1}{\gamma G \pi T_2^*}, \quad (4.1)$$

where dz is the pixel length, γ the nuclear gyromagnetic ratio, G is the peak gradient strength, and T_2^* is the transverse coherence time. Our nanodiamond samples have $T_2^* \sim 1$ ms, which corresponds to a resolution limit of 0.4 mm in our microimager (250 mT/m peak gradient strength). Increasing the resolution beyond this point will require the use of more complex MRI sequences incorporating such features as multipulse line narrowing [193].

4.10.5 ^{13}C Enrichment

Isotopic enrichment of the concentration n of spin-1/2 nuclei in nanoparticles is attractive for the proportional increase in MRI signal. Whilst increased MRI signal alone is valuable, if electron lifetimes are sufficiently short, the increase of the spin diffusion rate [189, 209] in enriched samples may also reduce the duration of DNP required to reach high nuclear polarizations. These improved properties may be achieved whilst maintaining long nuclear T_1 times, with studies of 99% ^{13}C enriched bulk diamond having shown spin-lattice relaxation times of several hours [209]. However, in enriched samples, the dipolar coupling strength between spins increases due to decreased interspin spacing, giving an NMR linewidth $\delta_{1/2}$ that is proportional to n . Thus, increasing n carries an inversely proportional reduction in T_2^* and corresponding reductions in imaging sensitivity. In light of these considerations, we believe isotopic enrichment of spin-1/2 nuclei up to 10% abundance will reveal the ideal compromise between high magnetizations and long spin-spin

relaxation times.

4.10.6 Stability of nanodiamond solutions

Dynamic light scattering (DLS) measurements showed that the 2 μm HPHT diamonds used in this work have a zeta potential of -38 ± 7 mV in water. The 210 nm HPHT NDs have a near identical zeta potential of -39 ± 8 mV. DLS measurements of particle size and zeta potential were performed in a Zetasizer Nano ZS. Nanoparticle dispersions were prepared by sonication. DLS size measurements agreed with specifications provided by the manufacturer. Such a large, negative zeta potential means that these HPHT diamonds are highly aggregation-resistant in aqueous solution, making them well suited to injection and biological applications that require surface functionalization [99]. The 2 μm particles display sedimentation from aqueous solution on the timescale of hours, whilst little sedimentation was observed in solutions of 210 nm HPHT NDs over a period of weeks. This difference in sedimentation phenomena occurs due to the relative size of gravitational forces and Brownian motion as we show through a calculation of the Péclet number P_e . The Péclet number is a dimensionless measure of the relative effects of flow and thermal diffusion [210] and, for a particle in suspension, is given by:

$$P_e = m_R g a / k_B T, \quad (4.2)$$

where m_R is the buoyant mass of the particle (mass of particle minus mass of displaced solvent), g is acceleration due to gravity, a is the particle radius, k_B is the Boltzmann constant and T is the temperature. For $P_e \gg 1$, gravity dominates over Brownian forces, leading to sedimentation in the absence of other hydrodynamic forces.

We can calculate a P_e of 0.003 for our 210 nm particles if we assume spherical particles, diamond density of 3510 kg m^{-3} and water density of 1000 kg/m^3 . Similarly, we can calculate a P_e of 25 for the larger 2 μm diamond particles. Of interest is the critical diamond size of 504 nm where $P_e = 1$, such that Brownian forces and gravitational forces are balanced.

These values explain the sedimentation of the 2 μm diamond particles.

4.10.7 Conditions for adiabatic transfer

Moving hyperpolarized samples through changing magnetic fields during sample transfer from the polarizer to MRI system results in fluctuation of the Zeeman energy between spin-up and spin-down states. If the rate of change of the magnetic field is comparable to the Larmor frequency the polarization state may change. To ensure this does not occur, the adiabatic parameter A must be much less than one at all times during the transfer process. We can calculate the adiabatic parameter from [190]:

$$A = \frac{1}{\gamma_n |\vec{B}|^3} \left| \vec{B} \times \frac{d\vec{B}}{dt} \right|, \quad (4.3)$$

Where γ_n is the nuclear gyromagnetic ratio, \vec{B} is the magnetic field and $\frac{d\vec{B}}{dt}$ the rate of change of the magnetic field. When $\frac{d\vec{B}}{dt}$ and \vec{B} are parallel, as is the case when the sample enters and exits a superconducting magnet, the cross-product in Eq. 1 is zero and adiabaticity is maintained. This means that transfer is adiabatic when the sample exits the hyperpolarizer and enters the MRI system. However, we must also consider the situation where the sample enters the 380 mT Halbach array used for sample transfer, as the magnetic field in this array is perpendicular to B_0 of the superconducting NMR magnets. From an analysis of our transfer process, we estimate a minimum $|\vec{B}| = 5 \text{ mT}$ perpendicular to a maximum $\frac{d\vec{B}}{dt} = 4 \text{ T s}^{-1}$. For a ^{13}C nucleus, these values give $A = 0.09$, confirming the adiabatic nature of our transfer process.

Chapter 5

Hyperpolarized Nanodiamond Surfaces

The widespread use of nanodiamonds as a biomedical platform for drug-delivery, imaging, and sub-cellular tracking applications stems from their non-toxicity and unique quantum mechanical properties. Here, we extend this functionality to the domain of magnetic resonance, by demonstrating that the intrinsic electron spins on the nanodiamond surface can be used to hyperpolarize adsorbed liquid compounds at low fields and room temperature. By combining relaxation measurements with hyperpolarization, spins on the surface of the nanodiamond can be distinguished from those in the bulk liquid. These results are likely of use in signaling the controlled release of pharmaceutical payloads.¹

5.1 Introduction

Bio-functionalized nanoparticles are emerging as highly versatile platforms upon which to develop the new theranostic and tailored imaging modalities needed in the era of personalized medicine [136, 211]. These nanoscale agents, smaller than most subcellular structures, open the prospect of detect-

¹This chapter is adapted from E. Rej, T. Gaebel, D. E. J. Waddington and D. J. Reilly, Hyperpolarized Nanodiamond Surfaces. *J. Am. Chem. Soc.*, **139**, 193-199 (2017).

ing and imaging a spectrum of diseases with enhanced sensitivity, and offer a means of targeting the delivery and controlled release of pharmaceutical payloads [133, 177]. Enabling such advanced applications will require a detailed understanding of the chemical interface of a nanoparticle *in vivo*, configuring its complex interaction with, for instance, the extracellular matrix, disease processes, or the tumor microenvironment.

Magnetic resonance (MR) techniques are well-suited for probing biochemical reactions involving nanoparticles *in vivo*, but challenging in the limit of small concentrations, where interactions at the nanoparticle interfacial surface lead to only fractional changes in the dominant signal arising from the surrounding fluid [212, 213]. The difficulty in isolating signals that are derived specifically from the nanoparticle surface has led to new techniques based on hyperpolarization to enhance the sensitivity of MR spectroscopy, mostly via the use of surface-bound radicals [214–219]. These techniques have been extended to dynamic nuclear polarization (DNP) of liquids using both extrinsic [220–224] and intrinsic [137] nanoparticle defects. In the case of nanodiamond (ND), a biocompatible nanoscale allotrope of carbon [138, 139, 225], the rich surface chemistry [140] is ideally suited to binding small molecules such as proteins, ligands, antibodies, or therapeutics, making it a promising substrate for loading and targeted delivery applications [100, 106, 142, 143, 226]. Further, cellular imaging and tracking of NDs is also possible using fluorescent color centers [112, 141], and future developments may combine imaging with nanoscale magnetic and electric fields sensing capabilities [116, 144]. Complementing these attributes, the detection of hyperpolarized ^{13}C nuclei in the ND core [128–130, 227] has recently opened the prospect of new MRI modalities based on ND.

Here, we demonstrate that ^1H nuclear spins from liquid-state compounds including water, oil, acetic acid, and glycerol mixtures can be hyperpolarized using X-band microwaves at room temperature via contact with free-electron impurities on the surface of ND. Rather than the Overhauser mechanism usually seen in the polarization of liquids, we observe a DNP frequency spectrum that is indicative of the solid-effect, in which the polarized ^1H spins are those that are adsorbed on the ND surface. Further, by combining low field ($B <$

1 T) spin relaxation measurements and hyperpolarization, we demonstrate that it is possible to determine the extent to which the ND surface is saturated by its liquid environment. In combination with modalities based on hyperpolarized ^{13}C in the ND core [130], these results are likely of use in enabling *in vivo* approaches to monitor the binding and release of biochemicals from the functionalized ND surface.

5.2 Results

5.2.1 Nanodiamond Surfaces

The NDs used in these experiments are manufactured using the high pressure high temperature (HPHT) technique [228] and purchased from Microdiamant. A micrograph showing NDs with an average size of 125 nm is shown in Fig. 5.1a. Measurements were made on diamonds in a size range between 18 nm and 2 μm . Adsorption of the compounds onto the ND surface occurs passively when diamonds are mixed and sonicated with various liquids.

Using Raman spectroscopy, we observe that our NDs comprise two phases of carbon, sp^2 hybridized, attributed to carbon on the surface of the ND, at wavenumber $\nu = 1580 \text{ cm}^{-1}$, and sp^3 hybridized, attributed to carbon in the core of the ND, at $\nu = 1332 \text{ cm}^{-1}$, as shown in Fig. 5.1b. The sp^2 carbon phase results in free electrons and provides a surface for liquid adsorption. We observe more sp^2 hybridized carbon in smaller NDs than larger NDs, due to the much higher surface to volume ratio. Air oxidation [159] of the NDs etches away some of the surface, removing sp^2 hybridized carbon and surface electrons.

Much of the functionality of ND, including its fluorescence, magnetic field sensitivity, and use as an MRI contrast agent stems from the presence of impurities and unbound electrons in the crystal lattice or nanoparticle surface. For DNP applications these intrinsic free-radicals provide a means of hyperpolarizing nuclear spins [130], but also open pathways for spin relaxation [155, 229]. For the smaller NDs, the dominant electronic defects are carbon dangling bonds on the surface, contributing a broad spin-1/2 compo-

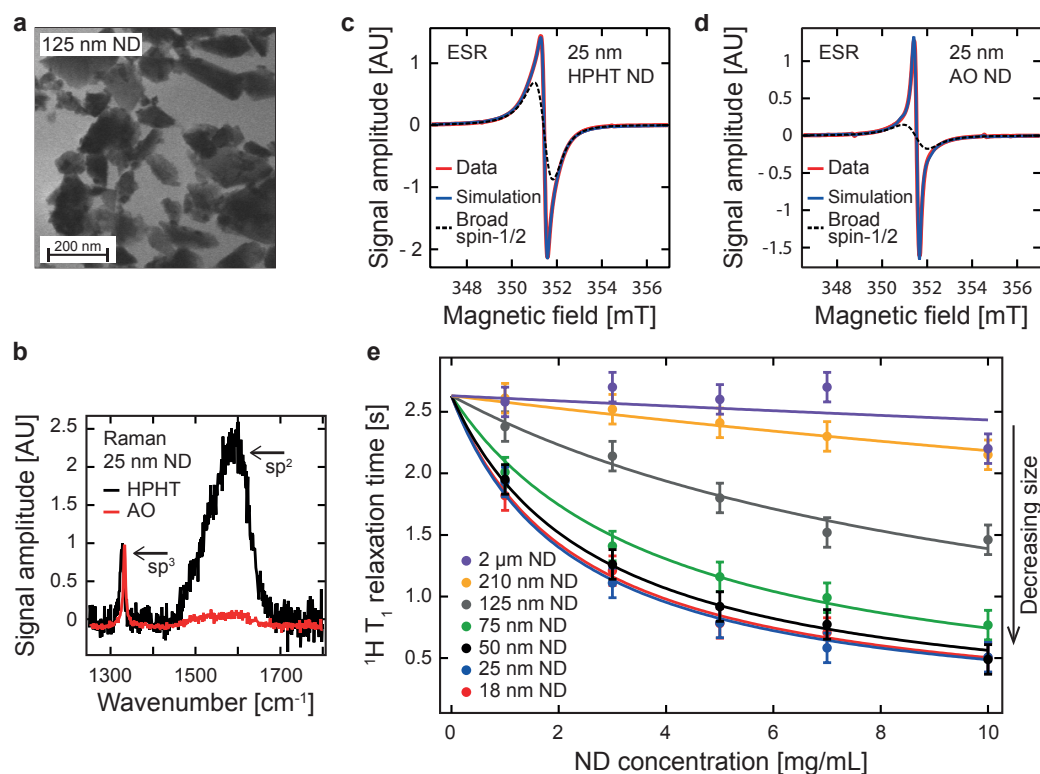


Figure 5.1: **Characterizing ND surfaces.** **a)** Electron micrograph of 125 nm ND. **b)** Comparison of Raman spectra for HPHT ND (black) and air oxidized (AO) ND (red). Raman spectra show sp^2 hybridized carbon from the surface of the diamond and sp^3 hybridized carbon from the core of the diamond. The sp^2 Raman cross section is ~ 150 times larger than the sp^3 Raman cross section leading to a comparatively larger peak. The fluorescence of the diamond has been subtracted using a baseline correction, and spectra have been normalized to the sp^3 hybridized peak. **c,d)** Comparison of the ESR spectrum of 25 nm HPHT ND and 25 nm AO ND. The data (red), simulation (blue), and broad spin-1/2 Lorentzian component (black) are shown. **e)** The 1H T_1 relaxation time of water in water-ND mixtures as a function of ND size and concentration at $B = 330$ mT. Data points are fits to the 1H T_1 build up performed using an inversion recovery sequence, and error bars represent the uncertainty in the fit. The solid lines are fits to the relaxivity equation [see methods in Section 5.4]. Smaller NDs (25 nm ND, blue dots, relaxivity: $R = 0.17$ $mg^{-1} mL s^{-1}$) have a larger effect upon the T_1 relaxation time of water than larger NDs (2 μm ND, purple dots, relaxivity: $R = 0.003$ $mg^{-1} mL s^{-1}$).

ment in an electron spin resonance (ESR) spectrum, (see black dashed trace in Fig. 5.1c). Air oxidation of the NDs removes some of these surface electrons, resulting in a decrease in the broad spin-1/2 component in the spectrum, as shown in Fig. 5.1d. Other components of the ESR spectrum include a narrow spin-1/2 component, attributed to defects in the core of the ND, and a P1 center component which results from a substitutional nitrogen atom with the electron hyperfine coupled to the ^{14}N spin [187, 205]. Increasing the diameter of the NDs shrinks the surface to volume ratio and reduces the relative amplitude of the broad and narrow spin-1/2 components. At the same time, the larger NDs have more P1-centers in the core. Typical defect concentrations are 10^{18} - 10^{19} spins/cm³ in HPHT ND [129, 205]. This equates to an average distance of 5 - 15 nm between defects on the particle surface (assuming spherical particles, equally distributed spins, and taking into account the relative number of spins in the broad component of the ESR trace).

We first examine whether the presence of these free electron spins on the diamond surface can be identified by mixing the nanoparticles with various liquids containing ^1H spins at $B \sim 330$ mT. In this configuration, the presence of free electrons on the ND surface enhances the spin relaxation (with characteristic time T_1) of the surrounding ^1H from the liquid, as shown for the case of water in Fig. 5.1e. Consistent with the ESR measurements, we find that this relaxivity effect is more prominent for small NDs, which have a larger surface to volume ratio, and a higher number of surface spins. We note that although the relaxivity effect is small when compared to commonly used contrast agents based on metal conjugates [117], it is significant enough to enable T_1 -weighted imaging when using concentrations of order 1 mg/mL, as is demonstrated in Appendix B.

5.2.2 Nanodiamond as a Hyperpolarizing Agent

Turning now to a key result of the paper, we make use of room temperature hyperpolarization as a means of further probing and identifying the spins at the liquid-ND interface. In contrast to high-field hyperpolarization modali-

ties [63] that aim to increase the MR signal for enhanced contrast, our focus here is the hyperpolarization spectrum, which enables different hyperpolarization methods to be distinguished. The Overhauser effect, for instance, is commonly observed when polarizing liquid compounds comprising molecules that undergo rapid translational or rotational diffusion. This mechanism relies on scalar and dipolar relaxation pathways to build up a nuclear polarization when driving at the electron Larmor frequency, $f = \omega_e$, resulting in positive or negative enhancement depending on the electron-nuclear coupling. In contrast, in a system with static dipolar interactions, where the nuclear and electron spins are bound such that the primary mode of nuclear spin relaxation in the adsorbed liquid is via the same electrons used for polarizing [230–232], hyperpolarization can occur via the solid-effect, cross-effect, or thermal-mixing mechanism, see Fig. 5.2a and 5.2b.

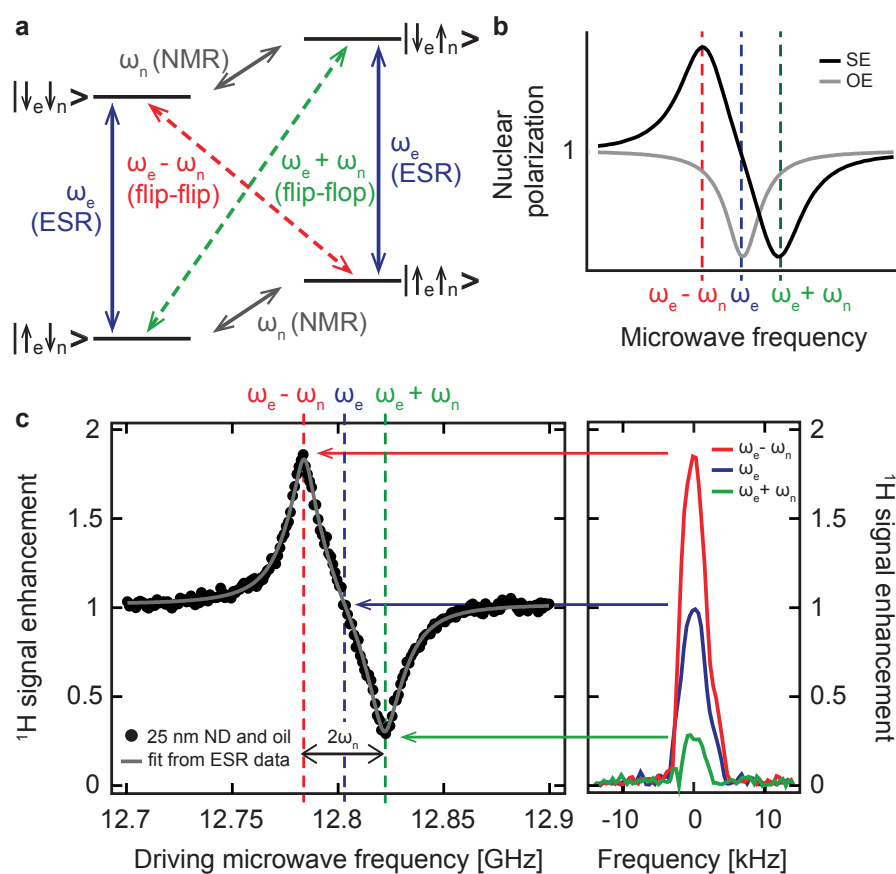


Figure 5.2: **Solid effect enhancement of adsorbed liquids on NDs.** **a)** Energy level diagram for a dipolar coupled electron and nuclear spin-1/2 system in a magnetic field. The ESR (blue), NMR (grey), flip-flop (green) and flip-flip (red) transitions are shown. For the solid effect, driven flip-flip transitions (red) at a frequency $f = \omega_e - \omega_n$ involve a mutual electron and nuclear flip resulting in a positive nuclear polarization, shown in **b**. Driven flip-flop transitions (green) result in a negative nuclear polarization. For Overhauser effect hyperpolarization, saturating the ESR transition can lead to positive or negative enhancement (shown in **b**), through relaxation via the zero quantum (green) or double quantum (red) transitions, respectively. **b)** Theoretical enhancement spectra for the solid effect (black) and Overhauser effect (grey) hyperpolarization mechanisms. **c)** ^1H signal enhancement as a function of driving microwave frequency at $B = 458$ mT (black dots). The fit to the data (grey line) is based on the ESR trace linewidths for the broad and narrow spin-1/2 impurities in the ND. The hyperpolarization spectrum is consistent with that given by the solid effect. Enhancement is given by the hyperpolarized signal divided by the signal with microwaves off.

Using the naturally occurring electrons on the surface of NDs, we are able to hyperpolarize the ^1H spins in a range of liquid-ND compounds including water, oil, acetic acid, and glycerol mixtures, despite their variation in chemical polarity. The data presented in Fig. 5.2c is representative of the effect, showing in this case ^1H hyperpolarization from oil (Sigma O1514) mixed with 25 nm ND. The data clearly exhibits the signature of hyperpolarization via the solid-effect, with a positive signal enhancement when driving at $f = \omega_e - \omega_n$ and a negative signal enhancement at $f = \omega_e + \omega_n$. No enhancement is seen at $f = \omega_e$, as would be expected if the Overhauser effect was contributing to the hyperpolarization, and there is no enhancement in liquid solutions without NDs. The presence of the solid-effect provides a strong indication that the signal enhancement stems from hydrogen spins that are adsorbed at the ND surface. A contribution from thermal mixing and the cross effect is also expected given the ESR spectrum contains a broad spin-1/2 component that is wider than the nuclear Larmor frequency. Similar behavior is observed when hyperpolarizing other liquid-ND mixtures (see Fig. 5.3). We also note that the highest enhancements occur for small nanoparticles (see Fig. 5.4), a further indication that DNP is mediated via spins on the ND surface and consistent with the relaxivity measurements presented in Fig. 5.1e. We believe the absolute enhancements currently achieved are limited by heating effects, see Fig. 5.5.

We further examine the hyperpolarization spectrum as a function of magnetic field over the range $B = 300 \text{ mT} - 500 \text{ mT}$, as shown in Fig. 5.6a. The position of the enhancement peaks follow $f = \omega_e - \omega_n$ and $f = \omega_e + \omega_n$ with a peak splitting of $f = 2\omega_n$ (black dashed lines) at low magnetic fields, see Fig. 5.6b. Surprisingly, we also observe that the ^1H signal enhancement increases with magnetic field, as shown in Fig. 5.6c. This dependence with field is currently not understood, given that the solid- and cross-effect enhancements are expected to scale in proportion to $1/B^2$ and $1/B$, respectively [63]. Field-dependent spin relaxation of electrons and nuclear spins, as well as a narrowing of the ESR line with increasing field, may lead however, to more efficient hyperpolarization as both the solid effect and cross effect/thermal mixing mechanism scale with the nuclear relaxation time T_{1n} and the inverse

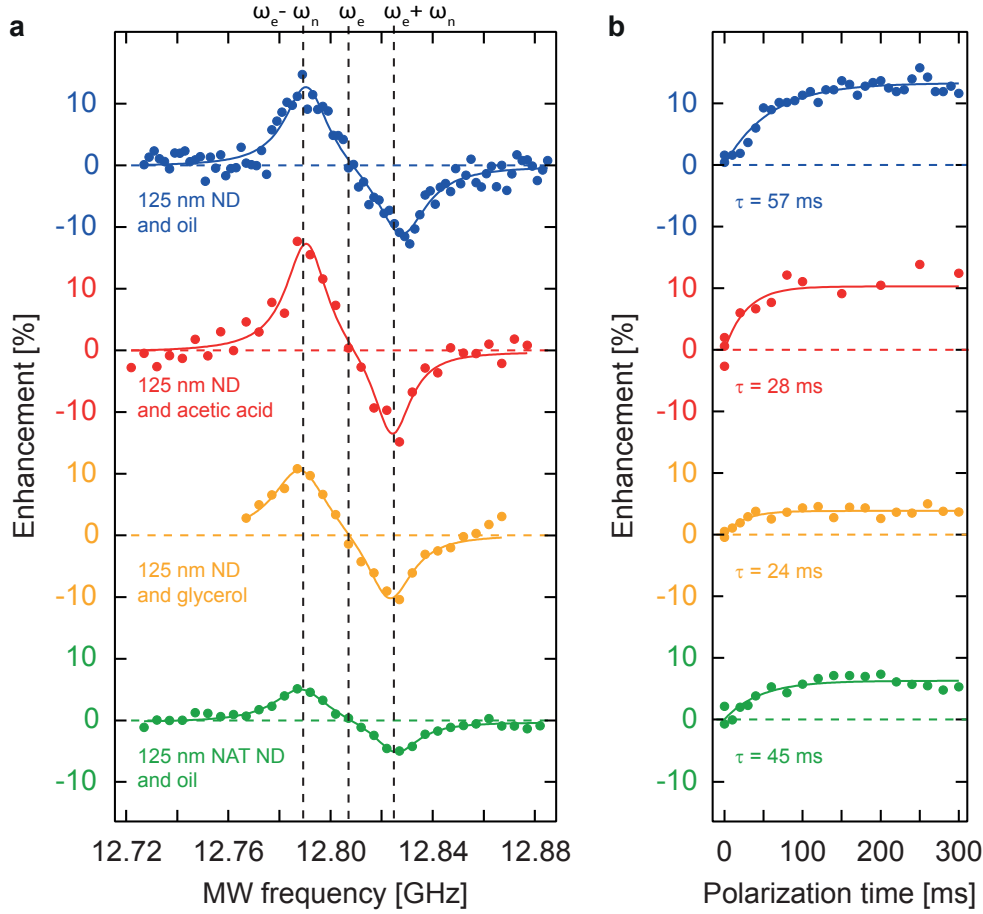


Figure 5.3: **Solid effect enhancement in liquid-ND mixtures.** **a)** ^1H signal enhancement as a function of driving microwave frequency and **b)** polarization build up at $B = 458$ mT for 125 nm HPHT ND mixed with oil (blue), acetic acid (red), and glycerol (yellow), and for 125 nm natural ND mixed with oil (green). 50 mg of ND was mixed with $30 \mu\text{L}$ of liquid. All hyperpolarization spectra follows a solid effect trend with a positive enhancement when driving at $f = \omega_e - \omega_n$, a negative enhancement when driving at $f = \omega_e + \omega_n$, and no enhancement at $f = \omega_e$. Data points are the enhancement after 300 ms of microwave radiation and solid lines are double Lorentzian fits. Polarization build up was measured when driving at $f = \omega_e - \omega_n$ and is fitted with a single exponential (solid lines), with τ as the fit parameter.

of the ESR line width δ . To obtain an increasing enhancement over the range $B = 300$ mT - 500 mT, T_{1n} and δ would have to collectively increase

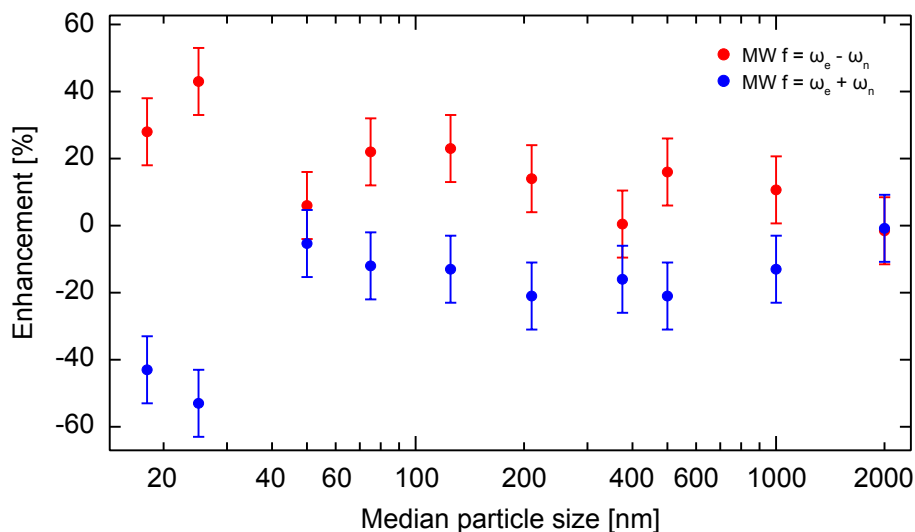


Figure 5.4: **^1H enhancement in oil-ND solutions.** The ^1H NMR enhancement as a function of particle size from an oil-ND mixture (50 mg ND, 60 μL oil) at $B = 500$ mT when polarized for 300 ms at $f = \omega_e - \omega_n$ (red), and at $f = \omega_e + \omega_n$ (blue). Enhancement is given as a percentage by comparing to the NMR signal with off-resonant driving microwaves, that is, as a fraction of the NMR signal at thermal equilibrium (which is normalized to 1). Error bars represent the error in the signal amplitude. We see the largest enhancement for the two smallest NDs used, moderate enhancement for NDs in the range 50 nm - 1000 nm, and no enhancement for 2 μm ND.

by a factor of 3. The T_{1n} of protons can increase with magnetic field [54] and we observe an increase in T_{2e} of NDs with field. We also note that as the magnetic field increases we move from the differential solid effect hyperpolarization spectrum to the well-resolved solid effect hyperpolarization spectrum. The underlying mechanism for the increase in enhancement is likely a combination of all these factors.

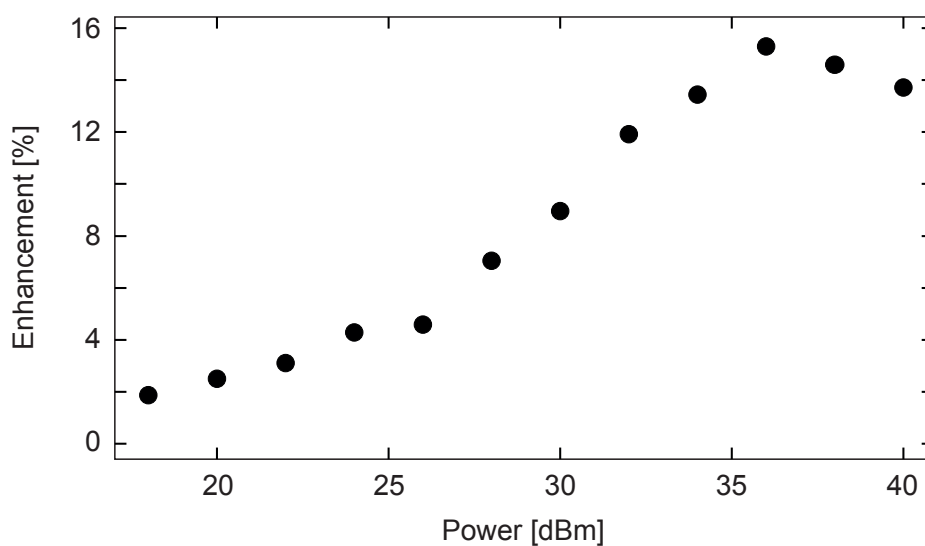


Figure 5.5: **Enhancement as a function of microwave power.** Enhancement of an acetic-acid ND mixture with 70 mg of 125 nm ND mixed with 30 μL of acetic acid for a range of microwave powers at $B = 458 \text{ mT}$. The system was driven at $f = \omega_e - \omega_n$ for positive polarization enhancement. The enhancement is given by the saturated value (at 300 ms) divided by the signal with no microwaves. The power stated is the power at the output of the power amplifier. We expect some loss from propagation through the waveguide and coupling from the horn antenna. We observe a drop in the enhancement after 35 dBm of power. We attribute this to heating effects, rather than electron-nuclear spin properties.

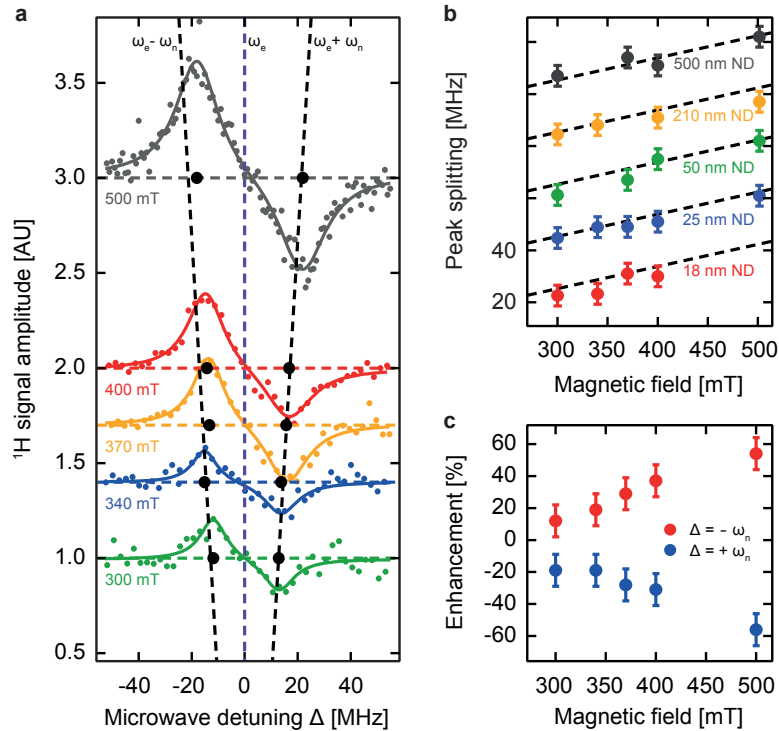


Figure 5.6: **Hyperpolarization behavior at various magnetic fields.** **a)** The hyperpolarized ^1H NMR signal in oil adsorbed onto 25 nm ND as a function of driving microwave frequency at magnetic fields between $B = 300$ mT and $B = 500$ mT ($B = 300$ mT in green, 340 mT in blue, 370 mT in yellow, 400 mT in red, and 500 mT in grey). The solid lines are bi-Lorentzian fits to the data [see methods in Section 5.4]. The positions of the peaks (black dots) follow the lines $f = \omega_e - \omega_n$ and $f = \omega_e + \omega_n$ (black dashed lines). We see no hyperpolarization at $f = \omega_e$ (blue dashed line). The microwave detuning is given by $\Delta = f - \omega_e$. The traces have been offset by the magnetic field scaling for clarity. **b)** The frequency splitting between the maximum and minimum ^1H signal from oil adsorbed on the ND surface for 18 nm ND (red), 25 nm ND (blue), 50 nm ND (green), 210 nm ND (yellow), and 500 nm ND (grey). The splitting follows the predicted value for the solid effect of $f = 2\omega_n$ (dashed lines). Errors are extracted from the peak positions of the Lorentzian fit, which results in a 10% error in the peak splitting. Traces are offset for clarity. **c)** The ^1H signal enhancement as a percentage of the non-polarized signal at magnetic fields between $B = 300$ mT - 500 mT for a 25 nm ND and oil mixture. Positive enhancement at $f = \omega_e - \omega_n$ is shown in red and negative enhancement at $f = \omega_e + \omega_n$ is shown in blue. Data points are the signal after 1 s of polarization divided by the signal with detuned microwaves. Error bars are the noise in the signal amplitude.

5.2.3 Hyperpolarization at the Nanodiamond Surface

Mixing ND with a significant amount of liquid leads to behavior indicative of a system with two independent spin baths. In our ND-water illustration shown in Fig. 5.7a, the ^1H spins in the bulk of the liquid comprise one bath, with the other being those spins that are adsorbed on the surface of the ND, in contact with free electrons. We isolate the independent contribution to the signal from each bath by comparing spin relaxation as a function of water concentration and in the presence of hyperpolarization using the pulse sequences shown in Fig. 5.7b and Fig. 5.7c. Consistent with the behavior expected for two spin baths, the relaxation decay exhibits a bi-exponential dependence with a short T_1 and long T_1 , as shown by the black curve in Fig. 5.7d. We attribute the short T_1 (green shading) to spins adsorbed on the ND surface, where the presence of electrons can rapidly relax nuclear spins in close proximity. When the ND-water mixture is sufficiently diluted ($> 60 \mu\text{L}$, or a ND concentration $< 1.16 \text{ mg}/\mu\text{L}$), a longer tail in the decay appears (blue shading) that likely stems from spins in the bulk liquid, decoupled from the ND surface. Reducing the amount of water, Fig. 5.7e shows that the long time component is suppressed since all spins can then be rapidly relaxed by the ND surface. The ND concentration $\sim 1.2 \text{ mg}/\mu\text{L}$ corresponds to a solution where all the space between loosely packed ND has been filled with liquid. At lower concentrations, the ND is dispersed in the liquid, and at higher concentrations, the liquid wets the ND surface. We note that the ND concentrations used here are much higher than the concentrations in Fig. 5.1e.

Inserting a microwave pulse (for hyperpolarization) in place of the usual inversion recovery sequence leads to a small enhancement of the signal that rapidly decays, irrespective of the concentration of water in the system. This behavior, taken together with the relaxation measurements, suggests that hyperpolarization is again limited only to those nuclear spins adsorbed on the ND surface, consistent with DNP occurring via the solid-effect. Further, this data puts a bound on the extent to which diffusion can transport hyperpolarized spins from the ND surface to the bulk of the liquid. Since

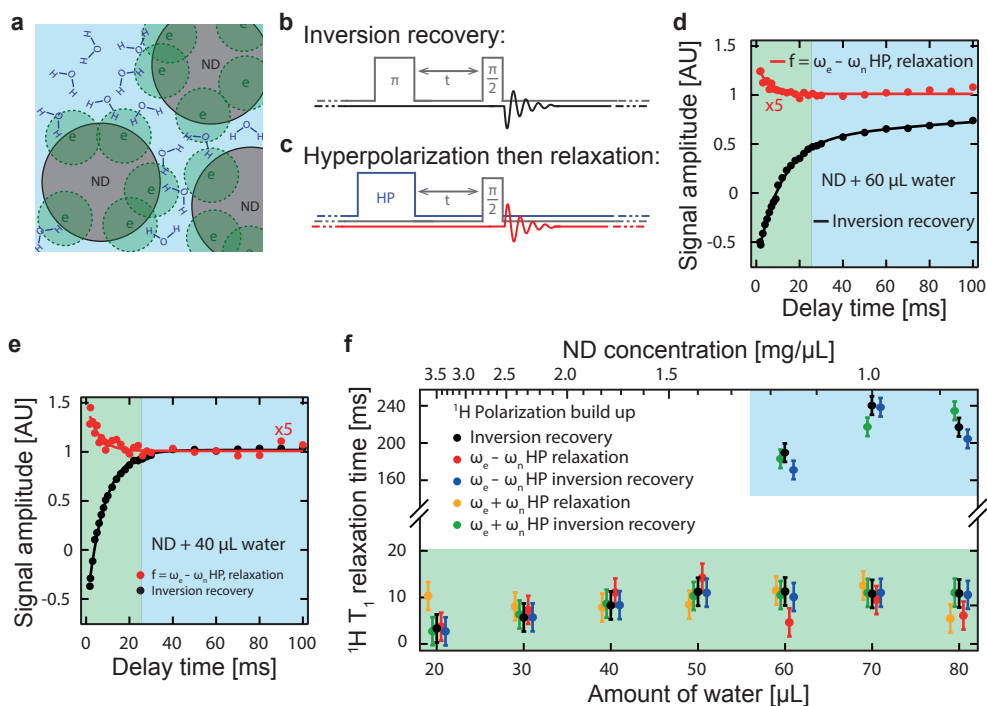


Figure 5.7: T_1 relaxation in hyperpolarized liquids. **a)** Schematic of a ND-water mixture. NDs (grey), with surface electrons (e), are suspended in water (blue). Green circles indicate regions in which hyperpolarization occurs. **b), c)** Pulse sequences used to measure ^1H spin relaxation. **b)** Inversion recovery sequences probing both spins in the bulk and adsorbed water. **c)** Hyperpolarization (HP) for 300 ms followed by a $\pi/2$ pulse probes the relaxation of spins close to the ND surface. **d), e)** Relaxation of a water-ND mixture (18 nm ND) at $B_0 = 460$ mT, measured by the pulse sequences outlined in **b), c)**. Lines are exponential and double exponential fits. **d)** We observe a double exponential behavior in the inversion recovery experiment (black) at low ND concentration (< 1.16 mg/ μL), whilst the HP relaxation (red) shows only single exponential decay. **e)** At high ND concentration (> 1.75 mg/ μL), we observe fast single exponential decay in both the hyperpolarization (red) and inversion recovery (black) experiments. **f)** ^1H T_1 relaxation times in water-ND mixtures as a function of water concentration. Short (green - ~ 10 ms) and long component (blue - ~ 200 ms) regions are shaded. Data points are exponential and double exponential fit parameters to relaxation experiments: inversion recovery (black), positive enhancement then relaxation (red), negative enhancement then relaxation (yellow), positive enhancement then inversion recovery (blue), and negative enhancement then inversion recovery (green). Error bars are the fit uncertainties. Data points are separated horizontally for clarity.

no signal enhancement is ever observed in the long-time component of the relaxation, we conclude that the hyperpolarized spins that are bound to the surface are unable to diffuse into the bulk before relaxing. In further support of this picture, Fig. 5.7f shows that relaxation (without hyperpolarization), switches from a single exponential to bi-exponential decay when the amount of water exceeds 60 μL (ND concentration $< 1.16 \text{ mg}/\mu\text{L}$) (black dots). This behavior is symptomatic of any sequence that contains an inversion recovery pulse (black, green, or blue dots), since the pulse acts on both the spins on the surface and those in the bulk. Hyperpolarization without inversion recovery however, acts only on ND-surface spins and always leads to fast, single-exponential decay independent of the amount of water.

A complementary picture emerges when ND is mixed with oil. We again conclude that the system comprises two distinct baths with different spin dynamics, in this instance by examining how the signal is enhanced by hyperpolarization beyond the thermal contribution, $\Delta S = S_{\text{HP}} - S_{\text{Th}}$, shown in red in Fig. 5.8a. In the limit of no oil, Fig. 5.8b shows that there is no enhancement in the signal since the electrons on the ND surface cannot hyperpolarize ^1H spins elsewhere in the system. Increasing the amount of oil has two effects. Firstly, more oil leads to a steady increase in the number of spins in contact with electrons on the ND surface, thus increasing the hyperpolarized signal and ΔS . Secondly, the additional oil in the mixture also increases the signal from spins in thermal equilibrium S_{Th} , either at the surface or in the bulk of the liquid. To account for both the hyperpolarized and thermal contributions to the signal, Fig. 5.8b also shows the enhancement $\epsilon = \Delta S/S_{\text{Th}}$ as a function of the amount of oil (blue). Similar to the case of the ND-water mixture, we observe a transition in behavior, around a ND concentration of 1.25 $\text{mg}/\mu\text{L}$, where the contribution from hyperpolarization begins to saturate and adding further liquid simply leads to dilution. We speculate that the liquid concentration at which this transition occurs provides information about the packing density of ND, viscosity, and extent of diffusion present in the mixture. Future efforts may exploit such identifiers to signal the adsorption and desorption of ND payloads such as chemotherapeutics.

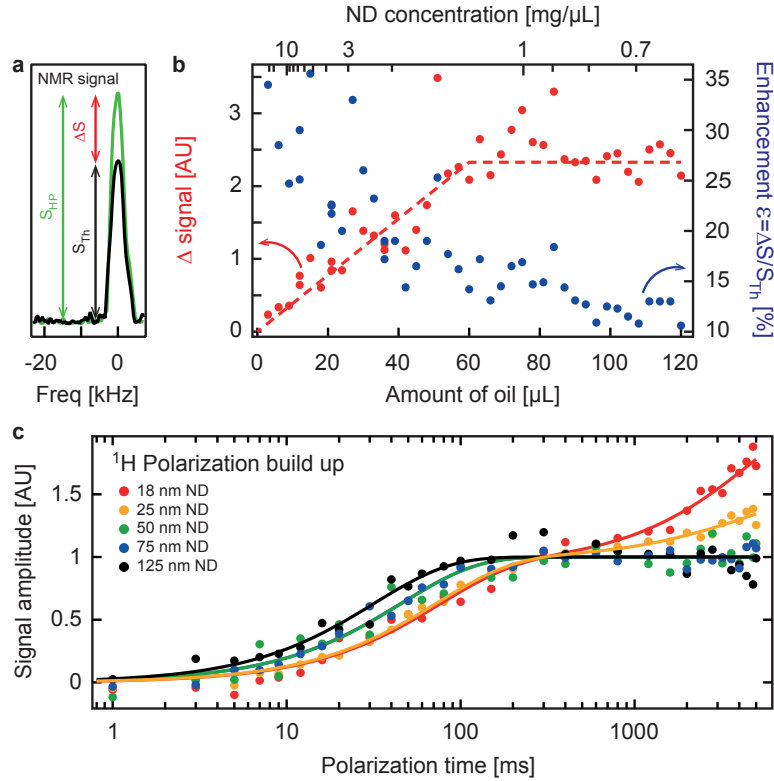


Figure 5.8: **Hyperpolarization dynamics of adsorbed liquids.**

a) Schematic showing the thermal NMR signal (S_{Th}), the hyperpolarized NMR signal (S_{HP}), and the amplitude difference between them (ΔS). **b)** Enhancement (blue) and the change in the 1H NMR signal with hyperpolarization (ΔS , red) for a ND-oil mixture (125 nm ND) as a function of oil concentration at $B = 460$ mT. Saturation of the ND surface occurs after 60 μ L of oil is added (ND concentration 1.25 mg/ μ L). The data points are the saturation values of polarization build up curves (at $f = \omega_e - \omega_n$). The dashed red line is a guide to the eye. **c)** 1H Polarization build up at $f = \omega_e - \omega_n$ in an oil-ND mixture for 18 nm ND (red), 25 nm ND (yellow), 50 nm ND (green), 75 nm ND (blue), and 125 nm ND (black) at $B = 460$ mT. Solid lines are either exponential fits (50 nm, 75 nm and 125 nm ND) or double exponential fits (18 nm and 25 nm ND) to the data. The data has been corrected for heating effects [see methods in Section 5.4], and normalized such that 0 corresponds to the signal with no microwaves, and 1 corresponds to saturation of the fast component of the polarization build-up. The polarization build up times and maximum enhancements (ϵ) achieved after 5 s of polarization are: 18 nm ND: $\tau_1 = 72$ ms, $\tau_2 = 4.7$ s, $\epsilon = 40$ %; 25 nm ND: $\tau_1 = 72$ ms, $\tau_2 = 4.4$ s, $\epsilon = 82$ %; 50 nm ND: $\tau = 46$ ms, $\epsilon = 17$ %; 75 nm ND: $\tau = 45$ ms, $\epsilon = 22$ %; 125 nm ND: $\tau = 32$ ms, $\epsilon = 25$ %.

The combined data-sets for water and oil ND mixtures suggest that hydrogen spins become attached to the ND surface and remain there for times that are long compared with hyperpolarization and relaxation processes. To test this picture further, we examine lastly how the signal enhancement depends on the time over which microwaves are applied to produce hyperpolarization. The signal is observed to grow mostly between 10 and 100 ms of hyperpolarization, saturating for longer times, as shown in Fig. 5.8c. This saturation is consistent with the surface adsorbed ^1H spins undergoing little diffusion into the bulk liquid and thus blocking the surface from being further replenished with new, unpolarized spins. In this regime, the surface bound spins will reach a steady-state enhancement that is determined by the rates of hyperpolarization and relaxation. NDs below 50 nm in size exhibit this saturation in signal, but then undergo a slight further enhancement for hyperpolarization times longer than 1 second. This surprising behavior could be partially explained by diffusion in the oil-ND mixture that becomes enhanced for small diamonds. A further possibility is that the timescale over which ^1H spins remain adsorbed on the surface is reduced for NDs below a certain size. This proton exchange in ND solutions is likely to be pH dependent [233, 234], which may provide a means of linking the MR properties of ND to pH changes in surrounding solutions.

5.3 Discussion and Conclusion

The use of NDs in a biological context is now widespread [141], given they are essentially non-toxic, exhibit a readily functionalized surface as well as attributes that enable new imaging and tracking modalities. Here, we have focused on the spin interactions of the ND surface and liquid interface at room temperature, making strong use of nuclear hyperpolarization to uncover aspects of the dynamics that are otherwise challenging to observe. Beyond a new means of characterization, the use of such hyperpolarization techniques offer a means of detecting the presence or absence of adsorbed compounds, of use in targeted delivery and release of chemotherapeutics. Extending this approach into the high field spectroscopic domain, where limitations set by

signal to noise and resolving chemical shifts are easier to overcome, would enable the possibility of distinguishing local environments and compounds interacting with the ND surface.

Given the long relaxation times and significant ^{13}C hyperpolarization that is possible with ND [130], the surface spin interactions investigated here open the prospect of transferring polarization from the ND-core to the surface. In this mode, intrinsic surface electrons can act to mediate polarization transfer between ^{13}C storage and ^1H spins for detection. Such an approach is amenable to techniques based on microfluidics [235].

In conclusion, we have examined the use of ND and its surface in establishing polarized states of various liquids at low fields and room temperature. The presence of ND leads to enhanced relaxation of ^1H spins in solution, opening a means of generating ND-specific contrast for MRI. The application of microwaves near the resonance frequency of the surface electrons leads to hyperpolarization of ^1H spins, consistent with dynamic nuclear polarization via the solid-effect and cross-effect. Finally, the combined use of hyperpolarization and relaxation measurements allow for spins on the ND surface to be distinguished from those in the bulk liquid, opening a means to probe the local environment of ND *in vivo*.

5.4 Methods

Nanodiamonds. In these experiments HPHT NDs purchased from Microdiamant were used. We refer to the diamonds by their median size. Measurements were made on MSY 0-0.030, (0-30 nm, median 18 nm), MSY 0-0.05 (0-50 nm, median 25 nm), MSY 0-0.1 (0-100 nm, median 50 nm), MSY 0-0.15 (0-150 nm, median 75 nm), MSY 0-0.25 (0-250 nm, median 125 nm), MSY 0-500 (0-500 nm, median 210 nm), MSY 0.25-0.75 (250 nm-500 nm, median 350 nm), MSY 0.25-0.75 (250 nm-750 nm, median 500 nm), MSY 0.75-1.25 (750 nm-1250 nm, median 1000 nm) and MSY 1.5-2.5 (1500 nm-2500 nm, median 2000 nm). All experiments were performed on HPHT ND unless otherwise stated.

Air Oxidation. HPHT NDs were spread in a thin layer and placed in

a furnace at 550°C for 1 hr (with 1 hr of heating to reach 550°C and 20 min to return to room temperature).

Adsorption. Initially NDs were heated on a hot plate to remove any adsorbed water. Loosely packed NDs were mixed with various liquids and ultrasonicated. Adsorption occurred passively. The ND remained suspended in solution for the duration of the experiments. We estimate a ND packing density of ~ 0.3 based on volume measurements.

Experimental setup. Signals were acquired with a single spaced solenoid coil in a home built NMR probe in a magnetic field range of $B = 300$ mT - 500 mT provided by either a permanent magnet ($B = 460$ mT) or an electromagnet. X-band microwave irradiation was amplified to a power of 10 W and coupled to the sample using a homebuilt horn antenna and reflector that we describe the details of in Appendix A. NMR signals were measured by initially polarizing the sample, then detecting the polarized signal using either a $\pi/2$ pulse or an echo ($\pi/2 - \tau - \pi$) sequence, and finally waiting for the polarization to return to thermal equilibrium. Data was acquired using either a Redstone NMR system (Tecmag) or a Spincore NMR system. Feedback control in the microwave hyperpolarization frequency was used to compensate for magnetic field drifts caused by temperature variations and inhomogeneity in both the permanent magnet and electromagnet.

SEM images. SEM images were taken on a Zeiss Ultra Plus Gemini SEM spectrometer working in transmission mode.

Raman spectra. Raman spectra were acquired with a Renishaw inVia Raman Microscope at $\lambda = 488$ nm and $P = 50$ μ W.

ESR measurements. ESR measurements were made using a Bruker EMX-plus X-Band ESR Spectrometer. The cavity (Bruker ER4102ST rectangular cavity) Q-factor ranged between $Q = 5\ 000$ - 10 000 for small and large ND particles, respectively. ESR power was $P = 0.25$ μ W, modulation amplitude was $B_{mod} = 0.1$ mT, the modulation frequency was $f_{mod} = 100$ kHz, the conversion time was $ct = 15.06$ ms, and the time constant was $tc = 0.01$ ms. Simulations of the ESR spectra were performed in Easyspin [162]. Fit parameters were linewidth, signal amplitude and g-factor for each spin species.

Relaxivity Measurements. The T_1 polarization build up curves were fitted with an exponential fit $M/M_0 = 1 - 2e^{-t/T_1}$, where M is the magnetization, M_0 is the equilibrium magnetization, T_1 is the spin lattice relaxation time and t is the polarization build up time. Relaxivity data was fitted with $T_1 = 1/(1/T_{01} + RC)$ where C is the concentration of ND, T_{01} is the T_1 relaxation time of pure (undoped) water and R is the relaxivity. The water had a T_1 relaxation time of $T_{01} = 2.6$ s measured at $B = 300$ mT.

Hyperpolarization spectra of ND-liquid mixtures. For the ND-oil mixtures, approximately 50 mg of ND was mixed with 60 μ L of oil. The mixtures were polarized for 300 ms, at $B = 458$ mT and for 1 s at other fields in the range $B = 300$ mT - 500 mT. Solid lines are double Lorentzian fits to $y = y_0 + \frac{a_1}{(x-x_1)^2+B_1} + \frac{a_2}{(x-x_2)^2+B_2}$.

Enhancement as a function of oil concentration. 75 mg of 125 nm ND was mixed incrementally with oil. Polarization build up was measured out to 1 second and fitted with an exponential curve. All the curves reached saturation.

Polarization build up. 70 mg of ND was mixed with 40 μ L of oil. With off-resonant microwaves, a signal decrease of 6% due to heating effects was seen after 1 second of polarization. Data with on-resonant microwaves was corrected to account for this heating effect.

Chapter 6

Nanodiamond-enhanced MRI via *in situ* Hyperpolarization

6.1 Abstract

Nanodiamonds are of interest as nontoxic substrates for targeted drug delivery and as highly biostable fluorescent markers for cellular tracking. Beyond optical techniques however, options for noninvasive imaging of nanodiamonds *in vivo* are severely limited. Here, we demonstrate that the Overhauser effect, a proton-electron double resonance technique, can enable high contrast magnetic resonance imaging (MRI) of nanodiamonds in water at room temperature and ultra-low magnetic field. The dynamic nuclear polarization (DNP) technique transfers spin polarization from paramagnetic impurities at nanodiamond surfaces to ^1H spins in the surrounding water solution, creating MRI contrast on-demand. We examine the conditions required for maximum enhancement as well as the ultimate sensitivity of the technique. The ability to perform continuous *in situ* hyperpolarization via the Overhauser mechanism, in combination with the excellent *in vivo* stability of nanodiamond, raises the possibility of performing noninvasive *in vivo* tracking of nanodiamond over indefinitely long periods of time.¹

¹This chapter is adapted from D. E. J. Waddington *et al.*, Nanodiamond-enhanced MRI via *in situ* Hyperpolarization. *Nat. Commun.*, **8**, 15118 (2017).

6.2 Introduction

Nanoparticles are rapidly emerging as powerful theranostic substrates [236] for the targeted delivery of vaccines [237], chemotherapy agents [238], immunotherapeutics [176] and as a means of tracking tumor distribution on whole-body scales [239, 240]. Biocompatible nanodiamonds (NDs) are ideal examples, featuring surfaces that are readily functionalized to enable tissue growth and their selective uptake by disease processes [106, 107, 241, 242]. Imaging NDs *in vivo*, however, has been to date, mostly limited to sub-cellular environments that are optically accessible [105, 112]. Without imaging modalities beyond optical fluorescence, realization of the full theranostic potential of ND to track and investigate complex disease processes, such as metastatic disease, is unlikely.

Magnetic resonance imaging (MRI) is the gold standard for noninvasive high-contrast imaging of disease in radiology, but has proven ineffective for directly detecting NDs *in vivo* due to the low abundance and small gyromagnetic ratio of spin-active ^{13}C nuclei that comprise the carbon lattice. Dynamic nuclear polarization (DNP) of the ^{13}C nuclei at cryogenic temperatures can, in principle, overcome the inherently weak signal from diamond by boosting it some 10,000 times to enable MRI contrast from nanoparticle compounds [128–131]. Despite these prospects, hyperpolarized nuclei always relax to their thermal polarization in a time that, for the smaller sub-micron particles, is currently short enough to limit the usefulness of the method in an imaging context [16, 130].

An alternative approach to tracking ND relies on functionalizing the ND surface with paramagnetic Gd(III)-chelates to create complexes for imaging with conventional T_1 -weighted MRI [117]. However, this approach faces the challenges of a large background signal, and concern for the long-term toxicity of gadolinium-based compounds [243].

Here, we demonstrate a different means of imaging and tracking water-ND solutions using Overhauser magnetic resonance imaging (OMRI) [244–247]. Operation at ultra-low magnetic field (ULF) enables efficient Overhauser polarization transfer between electronic and nuclear spins in an RF regime

compatible with *in vivo* use. RF pulsing of the electron paramagnetic resonance (EPR) transition between MRI signal acquisitions continually transfers spin polarization from the paramagnetic centers at the surface of ND to ^1H nuclei in the surrounding water [248]. The presence of ND in the solution thus leads to an enhancement in the ^1H MRI signal that can readily produce images with contrast sensitive to ND concentrations. The ability to perform *in situ* hyperpolarization overcomes the limitations imposed by short spin relaxation times of smaller particles and enables switchable tracking of ND solutions with no polarization transport losses over indefinite timescales. In addition to producing images to demonstrate this new approach, we investigate the conditions that lead to maximum sensitivity to the presence of ND, presenting data characterizing the efficiency of the Overhauser mechanism as a function of particle concentration and size. These results significantly enhance the theranostic capabilities of non-toxic, bio-functionalized ND, opening the possibility that MRI can be used to monitor and track ND-compounds *in vivo*.

6.3 Results

6.3.1 The Overhauser effect in nanodiamond solutions

Various types of ND were used in this study, including high-pressure high-temperature (HPHT), natural (NAT) and detonation (DET) NDs in sizes from 4 nm - 125 nm. We focus on results obtained from HPHT 18 nm and HPHT 125 nm NDs as typical representatives of the general behaviour observed. An air oxidization process, known to etch the ND surface, produces additional variants of NDs for comparison with the commercially sourced varieties [159]. Aqueous solutions of ND in deionized (DI) water were prepared using high power probe sonication, with HPHT NDs exhibiting the most stability in solution. HPHT 125 nm solutions show no aggregation over a period of months and a zeta potential of -55 mV [see methods in Section 6.5 for further details on ND preparation and additional results in Section 6.6.1 for zeta potential measurements].

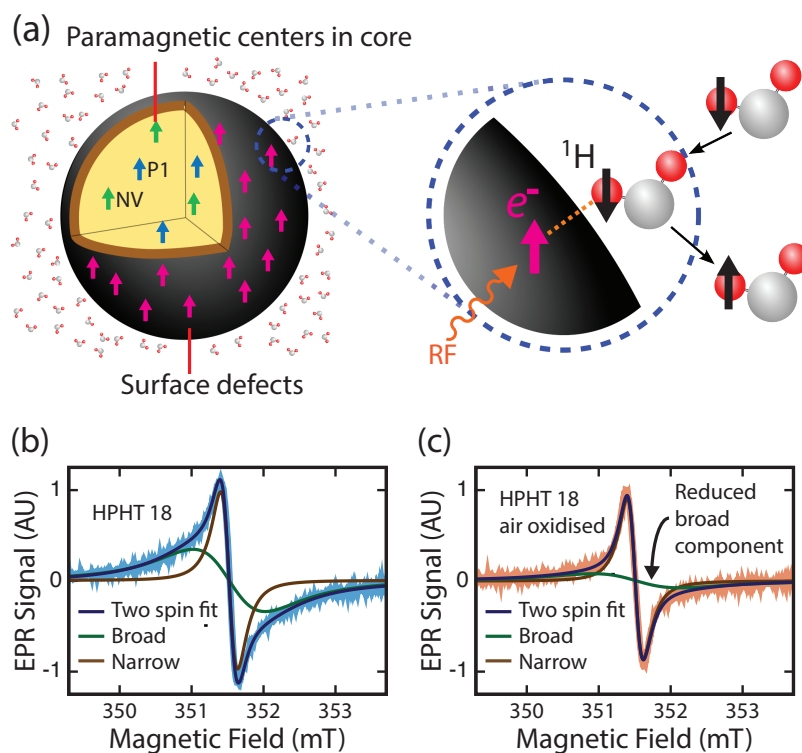


Figure 6.1: **Hyperpolarizing solutions via the Overhauser effect.** (a) Schematic of the Overhauser effect at the nanodiamond-water interface. (b) X-band electron paramagnetic resonance (EPR) spectra of high-pressure high-temperature (HPHT) 18 nm nanodiamonds (NDs) in 100 mg mL^{-1} solutions of deionized water (blue). Two-spin model fit (dark blue) is the sum of a broad spin-1/2 component (green) and a narrow spin-1/2 component (brown). (c) X-band EPR spectra of air oxidized HPHT 18 nm NDs in 100 mg mL^{-1} solutions of deionized water (orange). Two-spin model fit (dark blue) is the sum of a broad spin-1/2 component (green) and a narrow spin-1/2 component (brown). The broad component is reduced by air oxidation.

The basis for detecting and imaging ND in solution is shown in Fig. 6.1(a). Image contrast arises from the Overhauser effect, which as a starting point, requires a reservoir of partially polarized electron spins [65]. Driving these electrons with a resonant AC magnetic field transfers spin polarization to the interacting ^1H nuclei in the surrounding solution [249, 250]. NDs provide such a reservoir in the form of paramagnetic impurities such as nitrogen vacancy centers, substitutional nitrogen (P1) centers, and unpaired electrons at the nanoparticle surface [229, 251]. We first characterize our NDs using EPR spectroscopy, determining their impurity content and suitability for Overhauser imaging.

The EPR spectra of our HPHT 18 nm ND solution is shown in Fig. 6.1(b) and fits a two-component spin-1/2 model comprising a broad (1.2 mT) component and a narrow (0.2 mT) component (solid lines in figure) [162]. Air oxidation of NDs reduces the amplitude of the broad component in the spectra, as shown in Fig. 6.1(c), presumably by removing the paramagnetic centers at the surface. Our results are consistent with previous studies suggesting that the broad component is due to disordered dangling bonds at the surface of the ND with the narrow component arising from lattice defects in the crystalline core [205]. Other types of ND studied here demonstrate similar spectral components [see Section 6.6.2 for EPR data from solutions of all nanodiamond types used in this chapter].

Having established that ND provides a paramagnetic reservoir suitable for the Overhauser effect, we turn now to address the additional conditions that must be satisfied to enable imaging. In Fig. 6.2(a) we show the energy level diagram of a system comprising an electron coupled to a ^1H nucleus in an external magnetic field. When the EPR transition is pumped, the relative sizes of the cross relaxation transitions w_0 and w_2 will cause nuclei to accumulate in spin up or down states. This accumulation gives a nuclear enhancement ϵ , defined as the ensemble average of the z -component of the nuclear magnetization M_z over the nuclear magnetization under thermal equilibrium conditions M_0 , that is $\epsilon = \langle M_z \rangle / M_0$. The enhancement generated by the Overhauser mechanism is a function of four parameters [62]:

$$\epsilon = 1 - \rho f s \frac{|\gamma_e|}{\gamma_n} \quad (6.1)$$

where ρ is the coupling factor between electron and nuclear spins, f the leakage factor, s the saturation factor, and γ_e and γ_n are the electron and nuclear gyromagnetic ratios. Addressing first the coupling factor ρ , we note that, when there is dipolar coupling but no hyperfine contact interaction between spins, ρ takes a positive value determined by the correlation time of the two spins, diffusion coefficients and the EPR frequency. Relatively long correlation times are expected at ND surfaces due to the formation of a nanophase of water with 1 nm thickness at the ND-water interface [252]. Assuming free diffusion of water at a distance of 1 nm from the ND surface, we follow refs. [22, 223, 253, 254] and plot the field dependence of ρ for a calculated correlation time of 430 ns, as shown in Fig. 6.2(b) [see Section 6.6.3 for details of calculation]. Not surprisingly, given the long correlation time between spins, increasing the magnetic field above a few milli-Tesla rapidly suppresses the mutual flip-flip of dipolar coupled electron and nuclear spins and thus the nuclear enhancement possible via the Overhauser effect. Our choice of magnetic field for Overhauser imaging is thus constrained to the ULF regime, where serendipitously, the frequency of the EPR field produces minimal heating from dielectric loss associated with water at 20°C [255]. Fig. 6.2(b) also explains why previous DNP studies of ND solutions at 340 mT did not show Overhauser enhancement of freely diffusing water molecules in the bulk solution [184]. Instead they showed solid effect DNP of ^1H nuclei adsorbed to the ND surface.

To demonstrate that NDs can be detected via the Overhauser effect at ULF, we set $B_0 = 6.5$ mT and apply an RF magnetic field at the EPR frequency of 190 MHz to a HPHT 125 nm, 100 mg mL⁻¹ sample. The ^1H signal from the water surrounding the ND is then detected through standard inductive NMR techniques after the ^1H system has reached equilibrium [see methods]. Under these conditions we observe an enhancement of -4.0 in the ^1H spin polarization when EPR power is applied, as shown in Fig. 6.3(a).

Examining the enhancement produced by different types of ND, Fig.

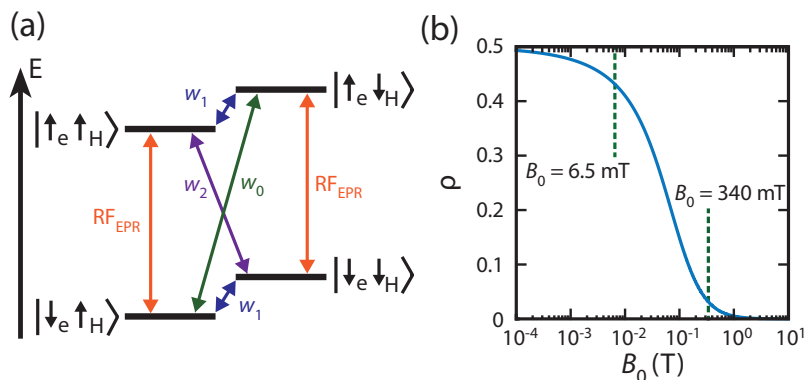


Figure 6.2: **Transition probabilities in the Overhauser effect.** (a) Zeeman split electron and nuclear spin levels in a magnetic field. Zero-quantum (w_0), single-quantum (w_1) and double-quantum transitions (w_2) are shown. If the w_2 transition dominates, when the EPR transition is pumped with a radiofrequency (RF) field, there is a net movement to the $|\downarrow_e\downarrow_H\rangle$ state. (b) Coupling factor ρ as a function of magnetic field (B_0) for a translational correlation time (τ_c) of 430 ns.

6.3(b) shows the sensitivity of the Overhauser technique to nanoparticle concentration. We draw attention to the data for the HPHT 18 nm NDs, which indicates that at concentrations of 1 mg mL^{-1} , a 33 % change in ^1H polarization of the solution can be observed. Natural NDs produce a small enhancement relative to HPHT NDs, probably due to a relatively low concentration of paramagnetic defects, as seen in their EPR spectra [spectra of these NDs are included in Section 6.6.2].

Having demonstrated that Overhauser enhancement is possible with ND, we return to Eq. 6.1 to further consider the conditions needed for optimal imaging. The saturation factor s describes the proportion of the EPR linewidth that is driven and takes a maximum value of 1 when the electron transitions are completely saturated at high RF power. To measure the EPR linewidth at ULF we sweep B_0 while driving electron transitions at 140 MHz. As shown in Fig. 6.4(a), HPHT 18 nm and HPHT 125 nm solutions show a linewidth for the enhancement of approximately 0.3 mT at a frequency consistent with the gyromagnetic ratio of a free electron. This result indicates that the paramagnetic centers responsible for the Overhauser effect can be

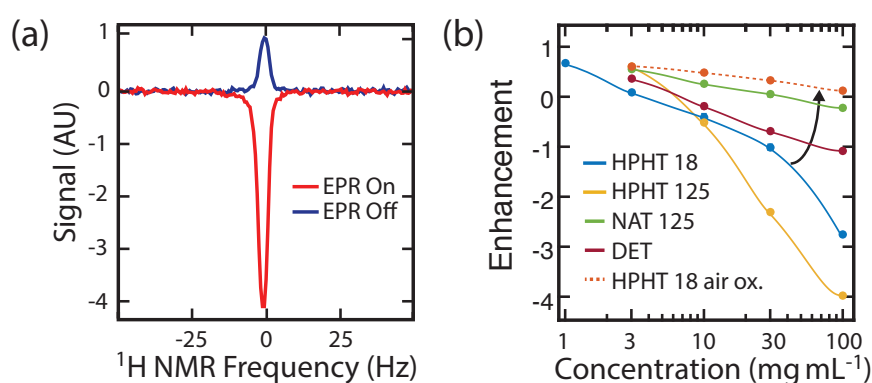


Figure 6.3: **Overhauser effect in nanodiamond solutions.** (a) Overhauser enhancement of ^1H polarization in a high-pressure high-temperature (HPHT) 125 nm 100 mg mL^{-1} nanodiamond (ND) solution. The hyperpolarized ^1H spectrum (red) is enhanced by -4.0 over the thermal ^1H spectrum (blue). The enhanced spectrum was acquired after the electron paramagnetic resonance (EPR) transition had been driven for 1.5 s with 49 W of RF power at 190 MHz. (b) ^1H saturation enhancement versus concentration for ND solutions at 49 W, 6.5 mT and 190 MHz. The Overhauser effect was observed for HPHT (blue - 18 nm, yellow - 125 nm), natural (NAT) 125 nm (green), detonation (DET) (red) and air oxidized HPHT 18 nm NDs (orange). Solid lines are included as a guide to the eye. Arrow indicates the change in enhancement after air oxidation.

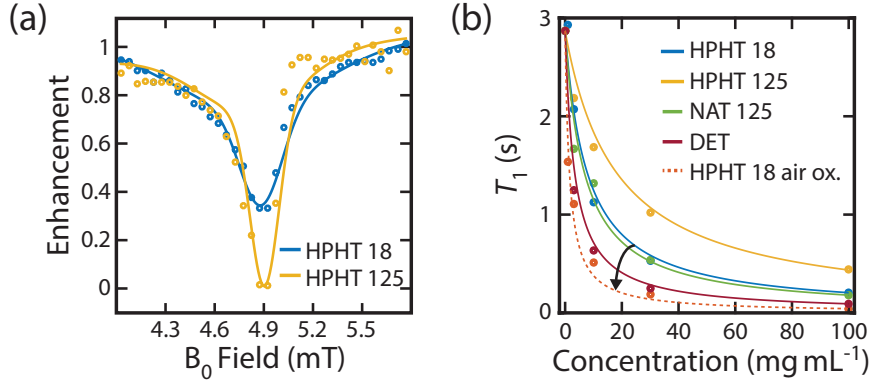


Figure 6.4: **Overhauser linewidth and spin-lattice relaxation rates.** (a) ^1H enhancement versus B_0 with EPR pumping at a constant frequency of 140 MHz with 24 W of power. ^1H NMR detection was performed on resonance. Aqueous solutions of HPHT 18 nm (blue) and HPHT 125 nm (yellow) at 50 mg mL^{-1} concentration were used. Solid lines are included as a guide to the eye. (b) T_1 relaxation times of ND solutions at 6.5 mT. Solid lines are a fit to the concentration dependent relaxivity equation. The fit error on individual T_1 measurements is smaller than the marker size. Arrow indicates the change in relaxivity after air oxidation. The T_1 relaxivity coefficients are $4.5 \pm 0.2 \times 10^{-2} \text{ mL s}^{-1} \text{ mg}^{-1}$ for HPHT 18 nm (blue), $1.9 \pm 0.2 \times 10^{-2} \text{ mL s}^{-1} \text{ mg}^{-1}$ for HPHT 125 nm (yellow), $5.2 \pm 0.2 \times 10^{-2} \text{ mL s}^{-1} \text{ mg}^{-1}$ for NAT 125 nm (green), $1.0 \pm 0.1 \times 10^{-1} \text{ mL s}^{-1} \text{ mg}^{-1}$ for DET (red) and $2.3 \pm 0.2 \times 10^{-1} \text{ mL s}^{-1} \text{ mg}^{-1}$ for air oxidized HPHT 18 nm (orange).

fully saturated with a resonant AC magnetic field of magnitude 1 mT, which is easily achieved in our spectroscopic probe [170]. Accordingly, we observe that, for EPR powers above 30 W, the Overhauser enhancement saturates [data is shown with further details of enhancement buildup in Section 6.6.1], and the maximal saturation factor is reached.

The remaining parameter in Eq. 6.1 is the leakage factor f which describes how effectively electrons relax the nuclear spin environment, taking a maximum value of 1 when all nuclear spin relaxation is via the paramagnetic solute. The leakage factor of a given solution can be calculated from [65]:

$$f = 1 - \frac{T_1}{T_{01}} \quad (6.2)$$

where T_1 is the spin-lattice relaxation time of ^1H spins in ND solution, shown in Fig. 6.4(b), and T_{01} is the spin-lattice relaxation time of the undoped solvent. We note that ND solutions with shorter T_1 , and hence larger f , do not necessarily give a higher Overhauser enhancement as Eq. 6.1 would predict. For example, NAT 125 nm NDs show a T_1 relaxivity more than double that of HPHT 125 nm NDs, despite showing a much smaller enhancement in Fig. 6.3(b). Presumably, ρ is suppressed in the quasistatic nanophase by slow diffusion of water molecules and the increased paramagnetic nuclear relaxation rate [184]. ^1H nuclei ‘trapped’ in the nanophase will experience rapid spin-lattice relaxation, giving the f we observe and an overall enhancement that depends on the specifics of each ND surface. A detailed understanding of dynamics in the nanophase compared to freely diffusing bulk water is thus crucial to calculation of the factors in Eq 6.1 [see Section 6.6.4 for further discussion].

Solutions prepared with air oxidized ND consistently exhibit reduced enhancements and higher T_1 relaxivity, as shown for 18 nm HPHT air oxidized NDs in Figs. 2(b) and 2(d). The increased nuclear spin-lattice relaxation rate will contribute to a reduction in Overhauser enhancement and we speculate that the enhancement is further reduced due to a lower concentration of paramagnetic centers after removal of surface impurities by air oxidation.

6.3.2 Overhauser-enhanced MRI with Nanodiamond

With conditions that lead to a significant Overhauser enhancement now established, we demonstrate this approach as the basis for detecting ND solutions using ultra-low field MRI. Imaging is performed using a custom proton-electron, double resonant probe in an open-access, low-field, human MRI scanner operating at a B_0 of 6.5 mT [256]. To display the MRI contrast possible between a ND solution and water we make use of the phantom illustrated in Fig. 6.5(a), which consists of glass vials filled with 500 μL of either DI water or aqueous solutions of HPHT 125 nm ND at 100 mg mL^{-1} and is organized in a diamond-shaped pattern.

MRI at ultra-low field of the phantom was performed using a high-

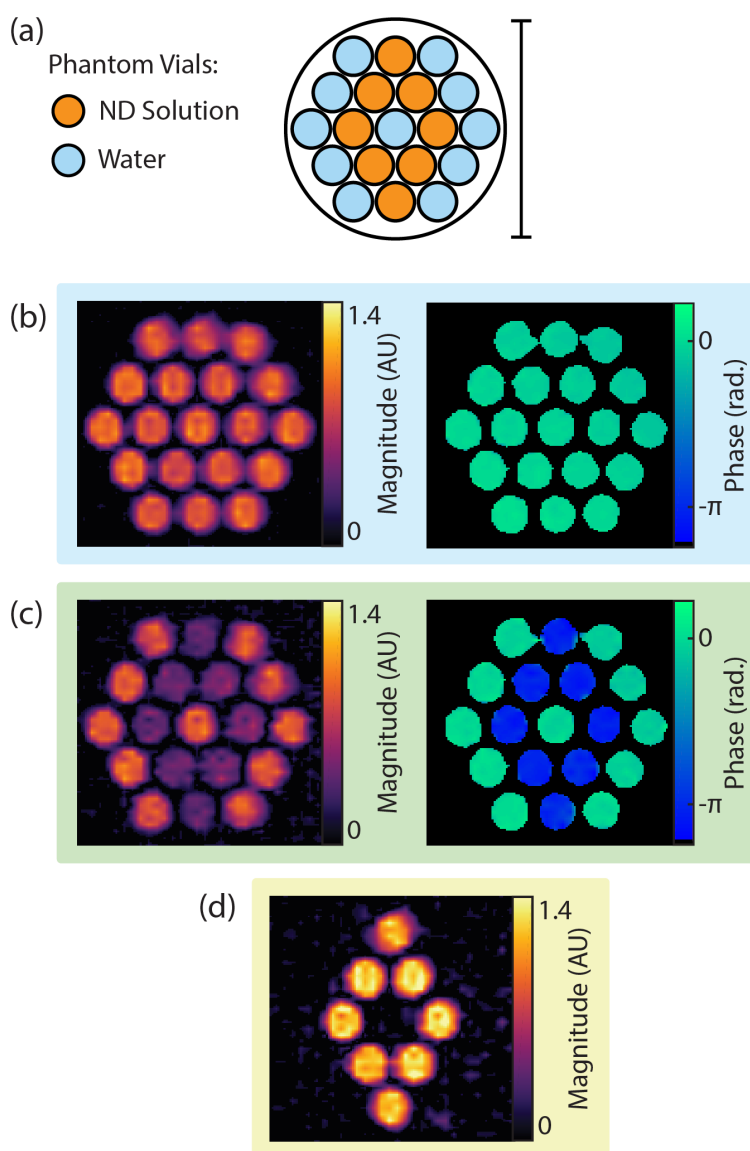


Figure 6.5: **ND imaging with Overhauser-enhanced MRI at 6.5 mT.** (a) Imaging phantom. Vials of deionized water (blue) and vials of high-pressure high-temperature (HPHT) 125 nm nanodiamond (ND) at 100 mg mL^{-1} (orange) were arranged in the pattern shown. Scale bar is 30 mm in length. (b) Standard balanced steady-state free precession (bSSFP) MRI of the phantom shown in a. (c) Overhauser-enhanced MRI (OMRI) bSSFP image of the same phantom. The Overhauser effect generates contrast between ND solution and water. The phase of the acquired signal is inverted in the ND solution. (d) The difference of MRI and OMRI acquisitions. The background signal is suppressed, showing signal only where ND is present.

efficiency balanced steady-state free precession (bSSFP) MRI sequence in which 1/3 of the imaging time is spent acquiring signal [see methods for details] [257]. Although good spatial resolution is achieved, no discernible contrast is evident between ND solution vials and water vials, as shown in Fig. 6.5(b). This is not surprising given that contrast using the bSSFP sequence is produced via ^1H concentration weighted by the ratio T_2/T_1 , which is approximately equal for all vials in the phantom [see Fig. 6.4(b) for T_1 and Fig. 6.7(c) for T_2]. We note that obtaining relaxation-contrast with bSSFP at ULF is usually challenging, as when $B_0 \rightarrow 0$, it is a general result that $T_2/T_1 \rightarrow 1$ [258]. Such changes in T_1 and T_2 times may, however, be useful for ND imaging with conventional spin echo sequences at high magnetic field, a possibility that we investigate in Appendix B.

After the MRI scan, the phantom was then imaged with an OMRI bSSFP sequence, as shown in Fig. 6.5(c). The OMRI bSSFP sequence is equivalent to the regular bSSFP sequence except the EPR transition of the ND solution is driven during the phase encode period [248]. The maximum time period without Overhauser saturation in our OMRI bSSFP sequence is 28 ms. As this is much shorter than the T_1 and T_2 of the ND solution, the polarization approaches a steady state during OMRI bSSFP, ensuring that hyperpolarized signal is continually present for acquisition. The appearance of water vials in the OMRI bSSFP image is unchanged from the regular bSSFP image. However, the ND solutions demonstrate significant relative contrast, with a change in magnitude and inversion of signal phase, as a result of the negative enhancement from the Overhauser effect. The switchable nature of the Overhauser contrast allows us to take the difference of the signal in MRI and OMRI images to generate the image in Fig. 6.5(d). Such a difference image suppresses the background signal, clearly showing the spatial distribution of NDs.

Having demonstrated ND imaging with OMRI, we now consider the sensitivity of the technique in our current Overhauser setup. We calculate the signal to noise ratio (SNR) as the magnitude of the MRI signal in a region of interest divided by the average root mean square value of the background signal. In Fig. 6.6(a) we show the schematic of a phantom containing vials

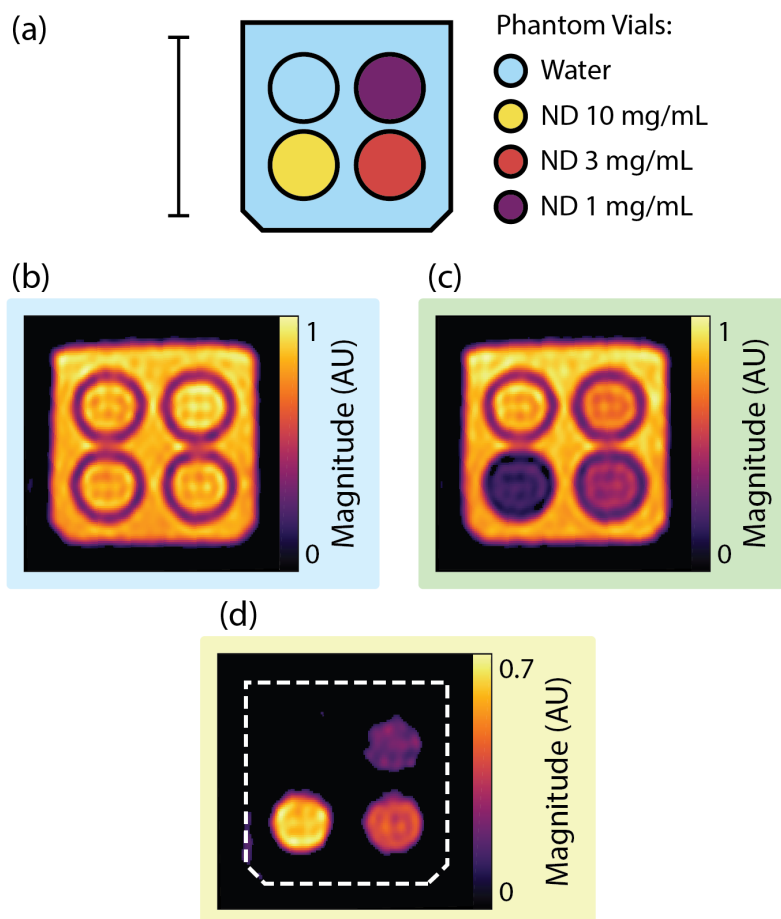


Figure 6.6: **Sensitivity of Nanodiamond Imaging.** (a) Phantom schematic. A vial of deionized water (blue) and vials of high-pressure high-temperature (HPHT) 18 nm nanodiamond (ND) at concentrations of 10 mg mL^{-1} (yellow), 3 mg mL^{-1} (red) and 1 mg mL^{-1} (purple) were mounted in the phantom as shown. The surrounding volume was then filled with water (blue). Scale bar is 20 mm in length. (b) Standard balanced steady-state free precession (bSSFP) MRI of the phantom shown in a. (c) Overhauser-enhanced MRI (OMRI) bSSFP image of the same phantom. The phase of the MRI signal is uniformly positive across the image. (d) The difference of MRI and OMRI acquisitions. The water signal is suppressed and all ND vials clearly visible.

with various concentrations of HPHT 18 nm ND in a container of water. This phantom is imaged with bSSFP, as shown in Fig. 6.6(b). The vials in this image have an SNR of 43, with the glass vial walls clearly outlining their positions. Next we define the contrast to noise ratio (CNR) as the difference in signal between MRI and OMRI scans in a region of interest divided by the average root mean square value of the background signal. Taking the subsequent Overhauser scan, shown in Fig. 6.6(c) and resulting difference image, shown in Fig. 6.6(d), clearly shows the presence of ND at concentrations of 10 mg mL^{-1} , 3 mg mL^{-1} and 1 mg mL^{-1} with CNR values of 27, 18 and 9, respectively.

Images of the 1 mg mL^{-1} vial in Fig. 6.6 were acquired with $23 \text{ }\mu\text{g}$ of ND per pixel, or a particle molar sensitivity of 150 nM for 18 nm particles. We note that this particle mass sensitivity is equivalent to that reported for other hyperpolarized MRI particle imaging modalities [16].

6.4 Discussion

NDs are non-toxic at high concentrations and resist *in vivo* degradation for periods of over a month [101]. Thus, the results presented here illustrate the potential of nanodiamond OMRI as a practical methodology for long-term biological imaging providing new types of contrast and functionality. All imaging was performed on systems designed for *in vivo* OMRI with RF powers acceptable for use *in vivo* [259], raising the possibility of biological applications. In particular, NDs may be of diagnostic use for diseased organs where nanoparticle accumulation can be an effective marker of pathology, such as the brain [260], liver [261] and lymph nodes [237]. Current diagnostic methodologies, using the T_2^* properties of iron oxide nanoparticles [3], suffer from the long biodistribution times of nanoparticles as the precomparison scan is taken before nanoparticle administration. In the resulting interval before a postcomparison scan various types of biological noise are introduced that make difference imaging infeasible [17]. The ability to perform interleaved MRI and OMRI scans with ND could overcome this limitation.

We have demonstrated sensitivity to ND at concentrations as low as

1 mg mL⁻¹. An upgraded version of our scanner with higher strength imaging gradients will enable slice selection without compromise to the bSSFP acquisition protocol. Hence, we now anticipate sensitivity changes from the implementation of slice selection. The SNR in a slice selected image is given by $\text{SNR} = \kappa V_{\text{voxel}} \sqrt{t_{\text{acq}}}$, where V_{voxel} is the volume of a voxel, t_{acq} is the total acquisition time and κ is a constant that depends on the magnetic field strength, hardware sensitivity, imaging sequence, acquisition parameters as well as the composition and spin-relaxation properties of the material being imaged [56]. Hence, based on the measurements in Fig. 6.6, for the same acquisition time and slice selection in a 5 mm slab with 1 mm × 1 mm pixel size, we calculate that HPHT 18 nm ND at 1 mg mL⁻¹ will be on the threshold of detectability with a CNR of 2. For higher nanoparticle concentrations, imaging times could be significantly accelerated. For example, HPHT 18 nm ND at 10 mg mL⁻¹ will have a CNR of 2 with 5 mm³ voxels and a total MRI and OMRI acquisition time of 2.5 minutes.

The long term clearance of nanoparticles is of interest for assessing biocompatibility. Studying the retention of nanodiamonds in the liver at present requires organ harvesting, which limits long term studies [101,102]. We estimate that for NDs to be present at 1 mg mL⁻¹ in a 3 mL mouse liver [262] would require injection of 5 mg of ND into a 20 g mouse, assuming 60% accumulation in the liver [262,263]. This dose is significant as it is a factor of 30 lower than that used in a recent *in vivo* demonstration of hyperpolarized silicon microparticle imaging [16]. Nanoparticle accumulation could be noninvasively imaged at this concentration with 5 mm³ voxels in the 3000 mm³ liver. This would provide a long term probe of the fate of nanoparticles in the liver, with significant scope for increasing the voxel size or acquisition time if increased sensitivity is required.

Given that nanoparticles about 25 nm in size are known to preferentially accumulate only in healthy lymphatic tissue [237], the ability to detect and image ND with OMRI may also enable isolation of disease in swollen lymph glands, avoiding the need for biopsy [264–266]. Such a technique could prove useful for the diagnosis of lymph node tumors, which is vital to the treatment of metastatic prostate cancer [240].

The ^1H enhancement we observe with the Overhauser effect is approximately two orders of magnitude larger, when accounting for ND concentration, than seen with solid effect hyperpolarization of water molecules adsorbed to ND surfaces [184]. Further, there is potential to increase the Overhauser enhancement towards the theoretical maximum of -330 [65], over 80 times larger than seen here, by modification of the ND surface. Tailored NDs with impurities selected to remove alternate spin-lattice relaxation mechanisms could be surface treated to increase diffusion of water at the nanosolid-liquid interface [99, 267], maximizing the coupling and leakage factors in Eq. 6.1. Likely, other nanoparticles that display the Overhauser effect in solution also exist. However, identification of these nanoparticles is nontrivial due to significant variation in the surface defects and the hydrophilicity of nanoparticles.

As Overhauser contrast arises via interactions at the nanoparticle surface, we recognize that surface functionalization for targeted molecular imaging must complement the observed enhancement. In this way therapeutic agents attached to the surface could suppress the Overhauser effect by increasing the distance between radicals at their surface and free water, leaving them ‘dark’ in OMRI scans [268]. After targeted drug release, the Overhauser effect could return to normal, showing up ‘bright’ with OMRI and enabling effective tracking of the site of drug delivery. The dependence of Overhauser enhancement on diffusion may also allow the technique to be used as a probe of localized hydration dynamics [223]. The OMRI approach may also enable the hyperpolarization of fluids flowing across the surface of diamond nanostructures [221, 235, 269].

In conclusion, we have used recent advances in ULF MRI to extend the usefulness of OMRI to nanoparticle imaging. The ability to noninvasively image biocompatible NDs with switchable contrast at biologically relevant concentrations is promising for a range of diagnostic applications. Switchable contrast allows suppression of the background signal present in other T_1 and T_2 based nanoparticle MRI modalities [111, 117, 270]. Furthermore, the long term biological stability of nanodiamonds *in vivo*, as well as the unlimited repeatability of the hyperpolarization sequence, raises the possibility

of imaging metabolic processes over dramatically longer timescales than is possible with *ex situ* hyperpolarization techniques [16, 130].

6.5 Methods

Nanodiamond Solution Preparation. NDs used in this study were sourced from Microdiamant, Switzerland. Nanodiamond types used were; monocrystalline, synthetic HPHT NDs in 18 nm (0-30 nm, median diameter 18 nm) and 125 nm (0-250 nm, median diameter 125 nm) sizes; monocrystalline, 125 nm NAT NDs (0-250 nm, median diameter 125 nm); and polycrystalline DET ND (cluster size 250-1000 nm, median 500 nm; individual particle size 4-8 nm). Size specifications were provided by the manufacturer. Air oxidized NDs were prepared by placing them in a furnace at standard pressure for one hour at 550 °C after an initial temperature ramp [159]. ND samples were mixed with DI water and sonicated with a Branson probe sonicator at 120 W and 50% duty cycle for 40 minutes to disaggregate ND clusters.

Particle size and zeta potential measurements were performed on ND solutions in a Beckman Coulter Delsa Nano C Particle Analyzer. Particle size measurements confirmed that monocrystalline NDs were well dispersed in water after sonication. Particle sizes of monocrystalline NDs were found to be consistent with manufacturer specifications. DET NDs still displayed some clustering and inconsistent particle size in solution after probe sonication.

EPR Measurements. CW EPR measurements were performed on 100 mg mL⁻¹ ND samples in a Bruker ElexSys E500 EPR system. Modulation frequency was 100 kHz at an amplitude of 0.1 G and incident microwave power of 0.6725 mW. Sample volumes in the cavity were kept consistent to allow comparison of relative peak heights. Individual EPR components were simulated in EasySpin [162] and a least squares analysis was used to find the best fit to the data while varying *g*-factor, linewidth and amplitude.

Spectroscopic measurements at 6.5 mT. The ¹H enhancement of ND solutions was measured by saturating the EPR transition at 190 MHz for a period of 5*T*₁ using 31 W of RF power before a standard NMR FID

acquisition. The enhancement is given as the ratio of the magnitude of the hyperpolarized FID to the magnitude an FID taken at thermal equilibrium with no EPR power. A high filling factor Alderman-Grant Resonator was used for EPR with a solenoid producing orthogonal B_1 used for NMR detection. T_1 relaxation times were measured using a conventional inversion recovery acquisition and fit with a least squares analysis.

DNP Linewidth Measurements. The linewidth of the Overhauser effect was studied by measuring the ^1H enhancement at various magnetic field strengths whilst driving the EPR resonator at a frequency of 140 MHz and 25 W. The EPR frequency was lowered from 190 MHz in order to capture the enhancement profile either side of the peak without exceeding the maximum field accessible in our ULF magnet. ^1H enhancement was measured as the magnetic field was stepped between 4 mT and 7 mT. NMR detection was performed at the ^1H resonance for any given field strength, with a low Q solenoidal coil.

Overhauser-enhanced MRI. Imaging was performed at 6.5 mT in our ultra-low field MRI scanner [256] using a bSSFP Overhauser-enhanced MRI (OMRI) sequence at room temperature [248]. The homebuilt imaging probe consists of an Alderman-Grant resonator (EPR: 190 MHz) and a solenoid (^1H : 276 kHz). The EPR resonator was pulsed on during the phase encode steps, with 69 W delivered to the EPR resonator at a duty cycle of 52%. Gradient strength was a maximum of 1 mT m^{-1} [further details on the imaging sequence and probe used are provided in Section 6.6.5]. Images in Fig. 6.5 and Fig. 6.6 were acquired with a 256×40 matrix size and cropped. Data was acquired in 2D with a pixel size of $1.0 \text{ mm} \times 0.76 \text{ mm}$ over a $30 \text{ mm} \times 30 \text{ mm}$ field of view and interpolated by zero-filling and Gaussian filtering in k -space to give $0.25 \text{ mm} \times 0.19 \text{ mm}$ pixels. The phantom thickness was 20 mm and 30 mm in Fig. 6.5 and Fig. 6.6, respectively. The standard MRI images were acquired with 200 averages (11 minutes 24 seconds). The OMRI images in Fig. 6.5(c) and Fig. 6.6(c) were acquired with 80 averages (4 minutes 14 seconds) and 200 averages (11 minutes 24 seconds), respectively. Image magnitude was scaled for an accurate comparison.

6.6 Additional Data and Information

6.6.1 Additional characterization of Nanodiamond Solutions and the Overhauser Effect

Nanodiamond (ND) solutions were prepared using high power probe sonication and analyzed by dynamic light scattering (DLS). In Fig. 6.7(a) we present the DLS size distribution obtained for a solution of high-pressure, high-temperature (HPHT) 125 nm ND which shows a median particle size of 125 nm. We note that particle sizes measured with DLS were consistent with manufacturer specifications.

To quantify saturation of the electron paramagnetic resonance (EPR) transition, the nuclear magnetic resonance (NMR) signal enhancement of ND solutions was measured as a function of EPR power. As shown for HPHT 18 nm in Fig. 6.7(b), the enhancement begins to saturate at approximately 30 W. Thus, the Overhauser enhancement is maximized in the spectroscopic measurements presented in Fig. 6.3, where 49 W of RF power was applied to the EPR resonator.

The relaxivity of ND in water solutions was measured in terms of the longitudinal relaxivity ($1/T_1$) and the transverse relaxivity ($1/T_2$). The relaxivity of various ND types was measured by fitting to the relaxivity equation:

$$1/T_{1,2} = 1/T_{1,2}^0 + R_{1,2}[\text{ND}], \quad (6.3)$$

where $T_{1,2}$ is the ^1H relaxation time of the solution with ND, $T_{1,2}^0$ is the ^1H relaxation time in the absence of ND, $R_{1,2}$ is the relaxivity coefficient, and $[\text{ND}]$ is the concentration of ND.

In Fig. 6.4(b) we present T_1 relaxation data of ND solutions. In Fig. 6.7(b) we present the corresponding T_2 characterization data, obtained in a conventional Hahn echo experiment. T_1 and T_2 values for our stock deionized (DI) water were 2.87 s and 2.60 s, respectively.

Enhancement measurements on ND solutions were made using the sequence shown in Fig. 6.8(a). The ^1H enhancement in ND solution was observed to saturate when ~ 30 W of power was applied to the EPR res-

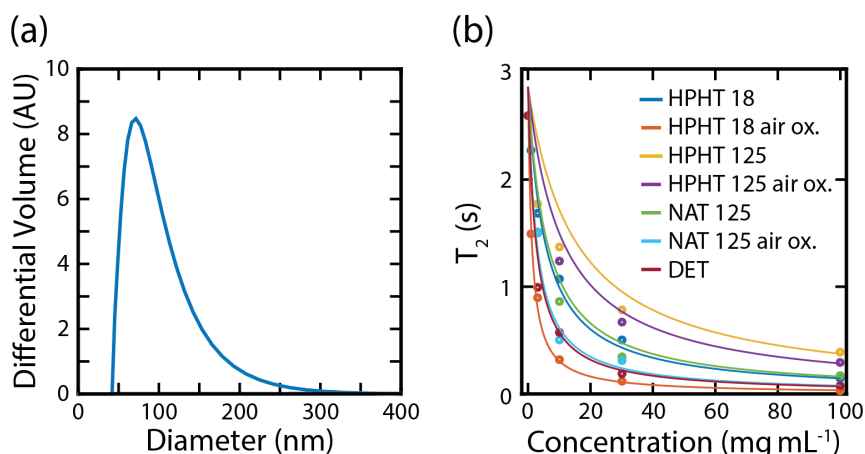


Figure 6.7: **Further characterization of nanodiamond solutions.** (a) Dynamic light scattering characterization of high-pressure, high-temperature (HPHT) 125 nm nanodiamond (ND) sample. The median particle size is 125 nm and the ζ potential in deionized water is -55 mV. (b) T_2 relaxation times of ND solutions. Solid lines are a fit to the concentration dependent relaxivity equation. The fit error on individual T_2 measurements is smaller than the marker size. The T_2 relaxivity coefficients are $6.5 \pm 0.4 \times 10^{-2} \text{ mL s}^{-1} \text{ mg}^{-1}$ for HPHT 18 nm (blue), $2.9 \pm 0.1 \times 10^{-1} \text{ mL s}^{-1} \text{ mg}^{-1}$ for air oxidized HPHT 18 nm (orange), $2.3 \pm 0.4 \times 10^{-2} \text{ mL s}^{-1} \text{ mg}^{-1}$ for HPHT 125 nm (yellow), $3.2 \pm 0.5 \times 10^{-2} \text{ mL s}^{-1} \text{ mg}^{-1}$ for air oxidized HPHT 125 nm (purple), $5.8 \pm 1.1 \times 10^{-2} \text{ mL s}^{-1} \text{ mg}^{-1}$ for natural (NAT) 125 nm (green), $1.3 \pm 0.2 \times 10^{-1} \text{ mL s}^{-1} \text{ mg}^{-1}$ for air oxidized NAT 125 nm (light blue) and $1.4 \pm 0.1 \times 10^{-1} \text{ mL s}^{-1} \text{ mg}^{-1}$ for detonation (DET, red).

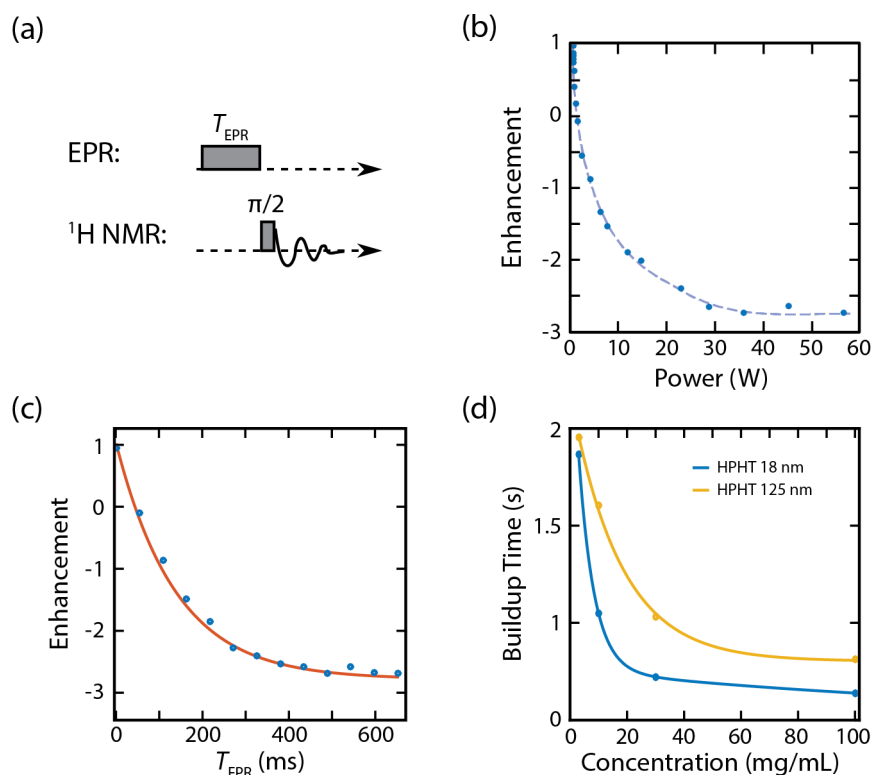


Figure 6.8: **Measuring Overhauser Enhancement.** (a) Spectroscopic sequence used for measuring saturation Overhauser enhancement at 6.5 mT. The resonant EPR transition at 190 MHz was saturated with 31 W of power for a time T_{EPR} before immediate application of a $\pi/2$ pulse to the ^1H NMR channel. The NMR FID is then acquired to measure the ^1H polarization. (b) ^1H enhancement of ND solution as a function of electron paramagnetic resonance (EPR) power. Enhancement is shown for a 100 mg mL $^{-1}$ solution of HPHT 18 nm after a 500 ms EPR pulse at 190 MHz (blue markers). Dotted line is intended as a guide to the eye. (c) ^1H enhancement of an HPHT 18 nm ND sample with concentration of 100 mg mL $^{-1}$. The NMR amplitude was measured for various values of T_{EPR} (blue dots) using the sequence shown in panel **a** and the enhancement calculated by dividing the signal amplitude by the value measured at $T_{\text{EPR}} = 0$. A period of $5T_1$ was allowed to pass between subsequent measurements. The ^1H polarization buildup is well fit by a single exponential curve (red) with a characteristic buildup time of 139 ms. (d) Solutions of HPHT 18 nm (blue) and HPHT 125 nm (yellow) show that the characteristic buildup time, measured as in panel **b**, decreases as ND concentration increased. Solid lines are intended as a guide to the eye.

onator, as shown in Fig. 6.8(b). The buildup time of ^1H enhancement in ND solutions was measured by incrementing the time EPR power was applied for (see Fig. 6.8(c)). As might be expected from the dependence of maximum Overhauser enhancement on T_1 , the enhancement buildup time of ND solutions was longer for ND solutions with longer ^1H T_1 times, as we illustrate in a comparison of HPHT 18 nm and HPHT 125 nm buildup times in Fig. 6.8(d).

6.6.2 EPR Spectra of Nanodiamond Solutions

X-band EPR spectra of all nanodiamond solutions used in this chapter are shown in Fig. 6.9. All spectra can be fit by a model employing broad and narrow spin-1/2 components, with the exception of the HPHT 125 nm sample, which shows an additional component due to P1 centres. These P1 centres are known to be due to substitutional nitrogen atoms in the crystalline core of the ND [205] and we expect that their interaction with water molecules will be much smaller than that of surface defects. We note that detonation ND only shows the broad component from our two spin fit and that natural ND shows a much smaller defect concentration compared to other ND types.

6.6.3 Calculation of the coupling factor

In Fig. 6.2(b) we present calculations of the dipolar coupling between ^1H nuclei in water and paramagnetic impurities, assumed to be at the ND surface. This calculation is based on a translational Brownian diffusion model, which assumes that the spins are on hard, noninteracting spheres (FFHS - force-free hard sphere model) [22, 223, 253, 254].

The dynamics of the ND surface and water molecule can be described by the translational correlation time τ_t , defined as:

$$\tau_t = \frac{d^2}{D_I + D_S}, \quad (6.4)$$

where d is the distance of closest approach and D_I and D_S are the diffusion

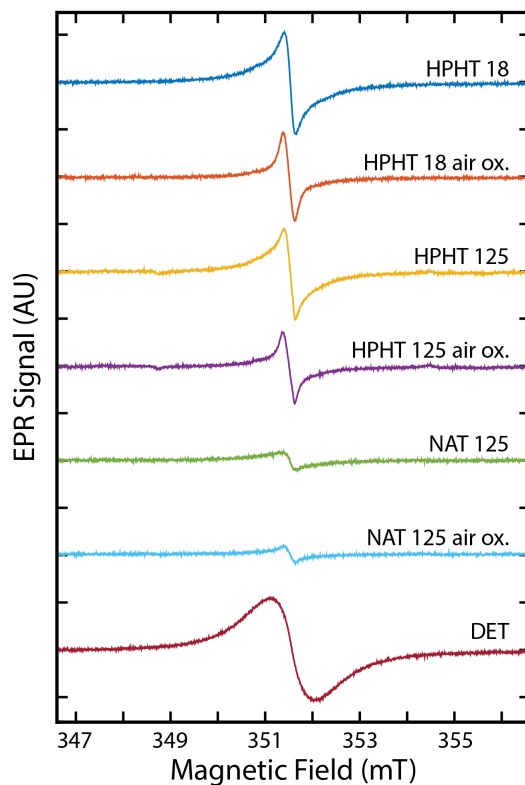


Figure 6.9: **X-band EPR Spectra of Nanodiamond Solutions.** Electron paramagnetic resonance (EPR) spectra of nanodiamonds (NDs) in 100 mg mL^{-1} solutions of deionized water. High-pressure, high-temperature (HPHT) 18 nm (blue), air oxidized HPHT 18 nm (orange), HPHT 125 nm (yellow), air oxidized HPHT 125 nm (purple), natural (NAT) 125 nm (green), air oxidized NAT 125 nm (light blue) and detonation (DET, red). Spectra are offset for clarity.

coefficients for the nuclear spin and electron spin, respectively.

Hydration models of ND in aqueous solution show that free diffusion of water occurs at distances greater than 1 nm from the ND surface for particles of sizes up to 200 nm and that within 1 nm of the surface, water diffusion becomes much slower due to the formation of a nanophase of water [252]. Hence, we assume a distance of closest approach between free water molecules and the ND surface of 1 nm and use the diffusion coefficient (D_1) of water at room temperature $2.3 \times 10^{-9} \text{ m}^2 \text{ s}^{-1}$ [271]. With dynamic light scattering (DLS) we measured D_S of our 125 nm NDs to be $3.4 \times 10^{-12} \text{ m}^2 \text{ s}^{-1}$, consistent with other reported values [272]. These values give a translational diffusion time of $\tau_t = 430 \text{ ps}$.

The coupling factor ρ can be expressed in terms of the reduced spectral density function j , [223, 253]:

$$\rho = \frac{5j(\omega_S, \tau_t)}{7j(\omega_S, \tau_t) + 7j(\omega_I, \tau_t)} \quad (6.5)$$

We use Equation 6.5 to calculate ρ as a function of $\omega_{0S}\tau_t$. We then plot ρ as a function of magnetic field in Fig. 6.2(b), by calculating the electron spin resonance frequency ω_{0S} for $g_e = -2.002$ and using $\tau_t = 430 \text{ ps}$.

This calculation assumes that the dipolar interaction is not limited by the relaxation time of the electron, that is $T_{1e}, T_{2e} \gg \tau_t$. A typical spin-spin relaxation time for electrons in the surface shell of ND is $T_2 = 300 \text{ ns}$ [273], much greater than τ_t .

We have also considered the possibility of the Overhauser effect mediated by rotational diffusion of the nanoparticle. The rotational diffusion coefficient of a spherical particle in solution can be estimated as:

$$\tau_r = \frac{4\pi\eta r^3}{k_B T} \quad (4)$$

Where r is the particle radius, η is the dynamic viscosity of the solution, k_B is the Boltzmann constant and T the temperature. For an 18 nm particle in water this gives $\tau_r = 2.3 \text{ } \mu\text{s}$ for $\eta = 1.002 \times 10^{-3} \text{ kg m}^{-1} \text{ s}^{-1}$ at $T = 293 \text{ K}$ [274]. This timescale, scaling as the cube of radius, suggests that rotational

diffusion will play a much smaller role than translation diffusion in mediating the Overhauser effect in our nanoparticle solutions, however we cannot rule out a contribution, especially for our smaller detonation NDs.

6.6.4 Impact of the nanophase on the Overhauser effect

For HPHT 125 nm ND at 100 mg mL^{-1} we can calculate a leakage factor of $f = 0.87$ from the spin-lattice relaxation measurements in Fig. 6.4(b) and Eq. 6.2. However, if we take $\epsilon = -4.0$ from Fig. 6.3(a), $s = 1$, from Fig. 6.8(b), and $\rho = 0.42$ from Fig. 6.2(b), then we calculate $f = 0.02$ from Eq. 6.1. The difference between these two results is indicative of water molecule exchange between the nanophase at the ND surface and free water outside this layer. We expect that ρ , which we calculated for freely diffusing water in Fig. 6.2(b), is suppressed in the quasistatic nanophase by slow diffusion of water molecules. Meanwhile, ^1H nuclei in the nanophase are rapidly relaxed by proximate paramagnetic centers before exchange out of the nanophase, giving the high leakage factor we observed and suppressing the coupling factor observed in freely diffusing water.

Further, we have assumed that the saturation factor in ND solutions takes a maximal value of 1. We note that in systems with multiple components in the EPR spectrum, such as ND, the saturation factor can take values lower than 1 even at high EPR saturation powers [65, 275].

6.6.5 Probes and Imaging

All dynamic nuclear polarization (DNP) experiments were performed with one of three double resonant probes. All probes are based on orthogonal solenoid (NMR) and Alderman-Grant (EPR) resonators. Spectroscopic probe A is optimized for a large electron drive field (B_{1e}), with a high fill factor Alderman Grant resonator at 190 MHz and external solenoid at 276 kHz and was used for all spectroscopic measurements at 6.5 mT. Spectroscopic probe B, used for field sweeps was optimized for high NMR sensitivity

over a wide range of frequencies, with an Alderman Grant resonator at 140 MHz. An imaging probe with a 33 mm diameter sample region, shown in Fig. 6.10(a) was built for ND Overhauser-enhanced MRI (OMRI) at $B_0 = 6.5$ mT ($f_H = 276$ kHz, $f_{\text{EPR}} = 190$ MHz). A photograph of the phantom used for imaging in Fig. 6.5 is shown in Fig. 6.10(b) All imaging was performed in our 6.5 mT open-access, human imaging scanner [256] with the OMRI balanced steady-state free precession (bSSFP) sequence shown in Fig. 6.10(c) [248].

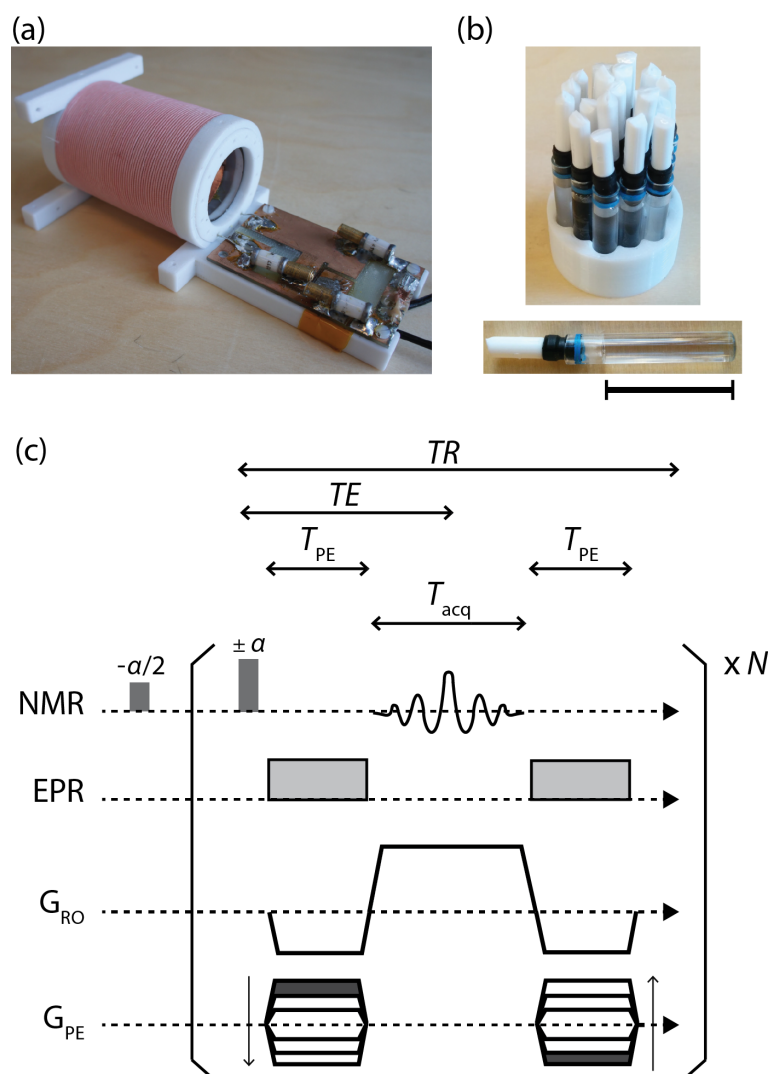


Figure 6.10: **Details of OMRI setup.** (a) Double resonant Overhauser-enhanced MRI (OMRI) imaging probe. The external solenoid was used for nuclear magnetic resonance (NMR) acquisition at 276 kHz. An internal Alderman-Grant resonator was used to saturate the electron paramagnetic resonance (EPR) resonance at 190 MHz. (b) Phantom with vials of ND solution and vials of water, used for imaging in Fig. 6.5. Scale bar is 20 mm in length. (c) Balanced steady-state free precession (bSSFP) OMRI imaging sequence used for imaging. Relative timing of NMR pulses, EPR pulses, readout gradient (G_{RO}) and phase encode gradient (G_{PE}) are shown. Imaging parameters were: repetition time (TR) = 86 ms, echo time (TE) = 43 ms, acquisition time (T_{acq}) = 28 ms, phase encode time (T_{PE}) = 22.5 ms and $\alpha = 70^\circ$.

Chapter 7

A Platform for *in vivo* Overhauser-enhanced MRI

7.1 Abstract

Overhauser-enhanced Magnetic Resonance Imaging (OMRI) is an electron-proton double resonance imaging technique of interest for its ability to non-invasively measure the concentration and distribution of free radicals. *In vivo* OMRI experiments are typically undertaken at ultra-low magnetic field, as both RF power absorption and penetration issues—a consequence of the high resonance frequencies of electron spins—are mitigated. However, working at ultra-low magnetic fields causes a drastic reduction in MRI sensitivity. Here, we report on the design, construction and performance of an OMRI platform optimized for high NMR sensitivity and low RF power absorbance, exploring challenges unique to probe design in the ultra-low magnetic field regime. We use this platform to demonstrate dynamic imaging of TEMPOL in a rat model. The work presented here demonstrates improved speed and sensitivity of *in vivo* OMRI, extending the scope of OMRI to the study of dynamic processes such as metabolism.¹

¹Material in this chapter related to the rat head probe is adapted from D. E. J. Waddington *et. al.*, An Overhauser-enhanced MRI platform for dynamic free radical imaging *in vivo*, *NMR Biomed.*, **31**, e3896 (2018).

7.2 Introduction

Free radicals play crucial roles in the maintenance of tissue health and in the pathogenesis of diseases including diabetes [276], ischemia-reperfusion injuries [277] and cancer [278]. Improvements to accurate diagnosis and appropriate treatment of diseases in which free-radicals play a role require the development of noninvasive methods for mapping the distribution of free radicals *in vivo*. Electron paramagnetic resonance (EPR) is the gold standard of direct free radical detection, enabling unambiguous identification of the unpaired electrons inherent to radical species, but short electronic spin-spin lifetimes (T_{2e}) limit resolution in EPR-based imaging approaches [279, 280]. Overhauser-enhanced MRI (OMRI) overcomes the resolution limits of EPR imaging by indirectly imaging free radicals with high-resolution MRI [78, 79, 281]. In OMRI, the Overhauser effect is used to transfer large spin polarizations from radical electrons to dipolar-coupled ^1H nuclei, with subsequent ^1H MRI used to image the free radical distribution via enhanced ^1H spin polarizations.

While progress in OMRI has seen free radicals used as bioprobes of tissue oxygenation, metabolism and viscosity [250, 282–285], sensitivity limits have prevented widespread use. The sensitivity of OMRI is limited in comparison to clinical MRI, as the high gyromagnetic ratio of electrons (28 GHz/T) means that OMRI is typically performed at ultra-low magnetic fields (ULF, < 10 mT) to reduce the specific absorbance rate (SAR) to safe levels during the application of RF EPR saturation pulses [157, 286]. Overcoming the tradeoff between SAR and nuclear magnetic resonance (NMR) sensitivity has thus been a focus of OMRI development [287]. OMRI probes based on single-loop surface coil resonators minimize SAR by restricting the size of the EPR coil but necessarily result in an inhomogeneous Overhauser enhancement profile due to spatial variation in B_{1e} [288, 289]. Volume resonators built for EPR saturation can yield high B_{1e} homogeneity, but compromises often need to be made to minimize SAR and maintain the quality factor (Q -factor) of the NMR detection coil [289–291]. With another approach, field-cycled OMRI, the applied magnetic field is rapidly ramped to allow EPR saturation

at ULF followed by high efficiency NMR acquisition at near-clinical field strengths [157]. These field-cycled scanners improve OMRI sensitivity at the cost of significantly more complex hardware, but are slowed by the need to refresh the Overhauser-enhanced signal between acquisitions.

Recent advances in balanced steady-state free precession (bSSFP) MRI sequences at ULF have increased the speed and sensitivity of OMRI [246, 248, 256, 292, 293], raising the possibility of *in vivo* radical imaging with high temporal resolution. A stable radical species of interest for dynamic tracking with OMRI is TEMPOL (4-hydroxy-TEMPO). TEMPOL is a neuroprotective antioxidant [294] whose permeability across the blood brain barrier increases in cases of oxidative stress [295, 296]. As TEMPOL reduction has previously been used to monitor redox status in animal models, dynamic tracking of exogenously administered TEMPOL may prove a valuable tool for monitoring neurological diseases in which oxidative stress plays a key role, such as ischemia-reperfusion injury and Alzheimer’s disease [297].

Here we report on an OMRI platform designed for dynamic imaging of TEMPOL in a rat model at ULF. Simulations and experimental results are presented to evaluate the performance of a custom OMRI probe based on a modified Alderman-Grant resonator and designed for high sensitivity, enhancement, homogeneity, and low SAR. Further, we leverage a highly efficient 3D bSSFP OMRI sequence to image TEMPOL *in vitro* at concentrations as low as 10 μM . We conclude this work with an *in vivo* demonstration of our platform, presenting brain images of TEMPOL in a rat model. This platform will enable tracking of exogenously administered radicals to study the role of oxidative stress in neurological diseases.

7.3 Materials and Methods

7.3.1 OMRI Scanner

Experiments were performed in a custom built, ULF MRI scanner consisting of a biplanar 6.5 mT electromagnet with biplanar gradients (Fig. 7.1(a)) [172, 256]. A Redstone NMR Spectrometer (Tecmag Inc., Houston TX, USA)

was used for data acquisition, RF pulse generation and gradient control. A 100 W CW amplifier (BT00100- DeltaB-CW) was used for EPR irradiation at 141 MHz and a 500 W pulsed power amplifier (BT00500-AlphaS) for NMR pulses at 276 kHz (TOMCO Technologies - Stepney SA, Australia). Techtron 7780 gradient amplifiers (Elkhart IN, USA) were used to drive orthogonal gradients to a maximum strength of 1 mT/m.

The custom built OMRI probe shown in Fig. 7.1 was used for all imaging. This probe consists of an internal solenoid used for transmit and receive of the ^1H NMR signal and an external, modified Alderman-Grant (MAG) resonator used for EPR saturation. The design of this probe is now described in detail.

7.3.2 NMR Design

In ULF MRI, noise from the intrinsic resistance of the NMR receive coil dominates over sample noise [298]. Hence, for optimal sensitivity, the Q factor of the NMR coil should be increased to the point that the resonator bandwidth is slightly larger than the required imaging bandwidth [299]. The required bandwidth in our probe is given by $\Delta f_{\text{im}} = \gamma_{\text{H}} G_{\text{max}} \Delta d = 1.9$ kHz, where γ_{H} is the proton Larmor frequency (42.576 MHz/T), G_{max} is the maximum gradient strength (1 mT/m), and Δd is the maximum desired field of view (45 mm).

A 35-mm long solenoidal NMR coil was wound on a 3D-printed 45 mm diameter polycarbonate former using 5/39/42 litz wire (New England Wire Technologies, Lisbon NH, USA), as shown in Fig. 7.1(b). The specifications of this Litz wire were chosen to minimize AC resistance at 276 kHz. An external resonator board was used to parallel-tune and series-match the solenoid to 276 kHz with non-magnetic ceramic chip capacitors (Voltronics, Cazenovia NY, USA). Construction with 85 turns of litz wire in a double layer gave an NMR resonator bandwidth of 2.5 kHz ($Q = 109$). Coil dimensions were chosen to maximize the fill factor when imaging a rat's head. The NMR geometric fill factor, and resulting ^1H receive sensitivity, was prioritized over the EPR fill factor, as lower EPR fill factors can be overcome by using higher EPR transmit power.

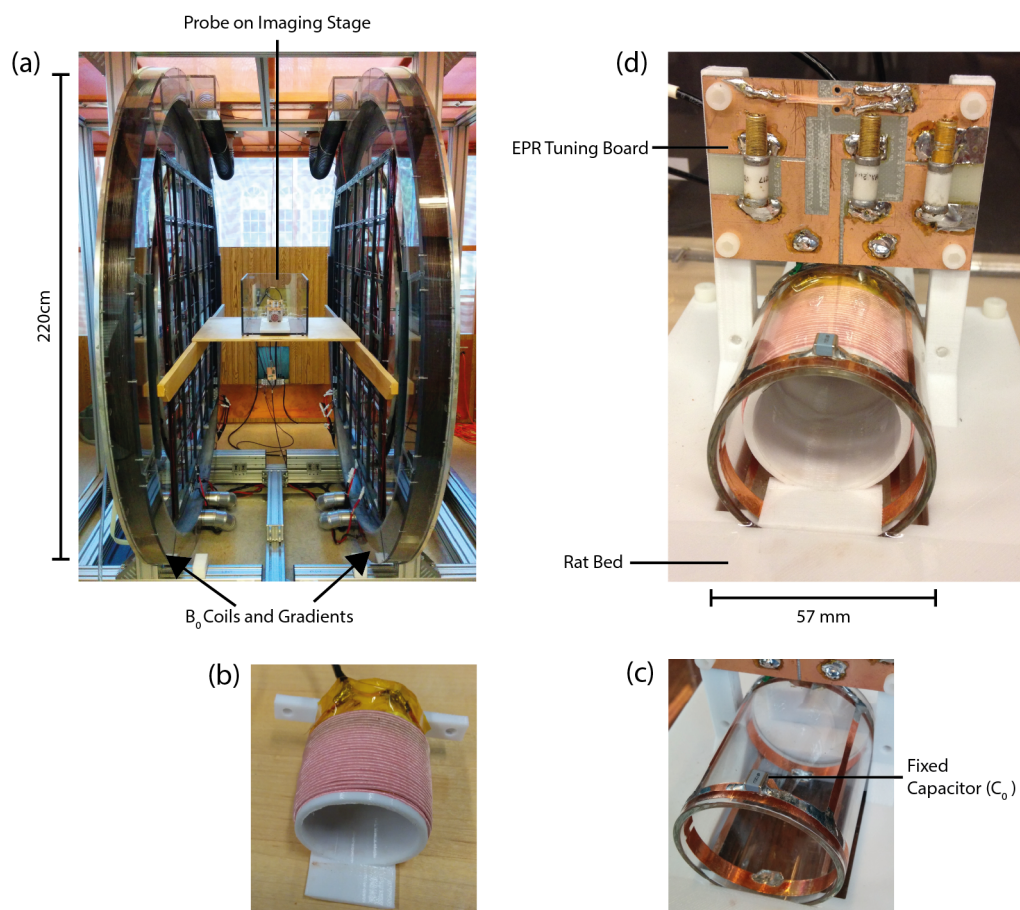


Figure 7.1: **Hardware for OMRI at ULF.** (a) Ultra-low field 6.5 mT MRI scanner with rat probe on the imaging table between electromagnet and gradient coils. (b) NMR solenoid coil wound on a polycarbonate former. The coil is tuned and matched to 276 kHz with an external resonator board (not shown). (c) Modified Alderman-Grant EPR (141 MHz) resonator. (d) NMR/EPR rat head probe assembly. High voltage variable capacitors on EPR tuning board are used for fine-tuning and matching.

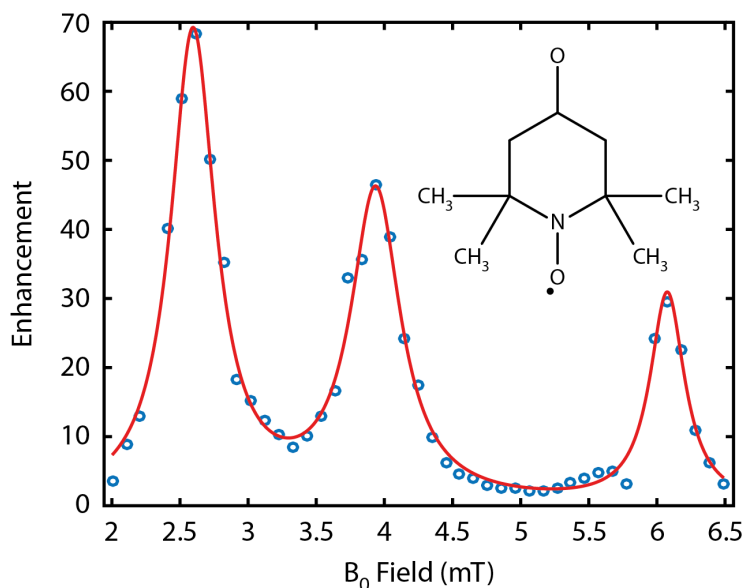


Figure 7.2: **Overhauser NMR spectroscopy of a 2 mM TEMPOL solution.** The MAG resonator was temporarily tuned to 131 MHz to acquire this data. The B_0 field was swept and a conventional NMR FID acquired at data points shown (blue). At each of these points, 15 W of resonant power was applied to the EPR resonator for 0.5 s and then an enhanced NMR FID acquired. Enhancement shown is the ratio of the magnitudes of these two FIDs. Red line is the fit of three Lorentzian profiles to the enhancement data and is intended as a guide to the eye. Inset: Chemical structure of the TEMPOL radical.

7.3.3 EPR Design

Effective OMRI probe design maximizes the B_{1e} field that can be applied while minimizing SAR that arises from inductive and dielectric heating effects during EPR saturation. Inductive power deposition occurs when the alternating B_{1e} field induces currents that dissipate energy in a conductive sample, and is proportional to $\omega_e^2 B_{1e}^2$ [56]. Dielectric power deposition results from a quasi frictional force, as electric dipole moments of molecules in the sample align with the alternating electric field E in the EPR resonator, and is proportional to $\omega_e E^2 \epsilon''(\omega_e)$, where $\epsilon''(\omega_e)$ is the imaginary component of the dielectric constant of the sample.

To reduce both heating effects, the EPR frequency ω_e is minimized by

driving the lowest frequency transition of the TEMPOL spectral triplet, which is at 141 MHz in our ULF scanner (see Fig. 7.2 for Overhauser enhancement spectrum identifying the three resonant lines). We also used a 70 mm length, 57 mm diameter and 2.4 mm thick piece of Pyrex tubing (Chemglass, Vineland NJ, USA) as the EPR former for its close fit around the NMR coil (see Fig. 7.1(c)), as maximizing the EPR fill factor confines E and B_{1e} fields, and resultant heating, to the region of interest.

The Alderman-Grant resonator, originally designed to reduce heating of conductive samples in proton decoupled NMR experiments at high magnetic fields [170,300], is a popular choice for minimizing SAR. Compared to alternatives such as a saddle coil, capacitive segmentation of the AG resonator reduces sample losses caused by the E field as voltage only accumulates over half the inductance before reversal at the segmentation capacitor [169]. Further, quadrupolar symmetry reduces the average value of the E field in the sample.

Here, we construct a modified Alderman-Grant (MAG) resonator by affixing two pieces of 0.07 mm thick adhesive copper tape (3M, Maplewood MN, USA) to the Pyrex EPR former along with four 12 pF bridging capacitors (Fig. 7.1(c)). The MAG resonator assembles around the NMR coil (Fig. 7.1(d)). The copper tape is shaped such that the MAG resonator has the geometry of an AG resonator with additional split guard rings and “windows” in the copper foils that form the sides of the resonator (described in Section 7.4.1). B_{1e} is oriented in the vertical direction (i.e perpendicular to the coronal plane for the rat), orthogonal to the axial B_{1H} of the solenoid. High-voltage variable capacitors (NMAJ40HV - Voltronics, Cazenovia NY, USA), in a balanced series-match, parallel-tune configuration, are used to connect the resonator to the EPR drive amplifier. A conventional AG resonator with the same geometry and internal guard rings made from continuous loops of copper tape was also constructed for comparison.

Finite element analysis simulations of EPR resonators were performed in COMSOL Multiphysics (COMSOL Inc., Burlington MA, USA). Copper foils were simulated as perfect electrical conducting surfaces (a 3D rendered model is included in Fig. 7.3). Simulated resonators were tuned to 141 MHz with

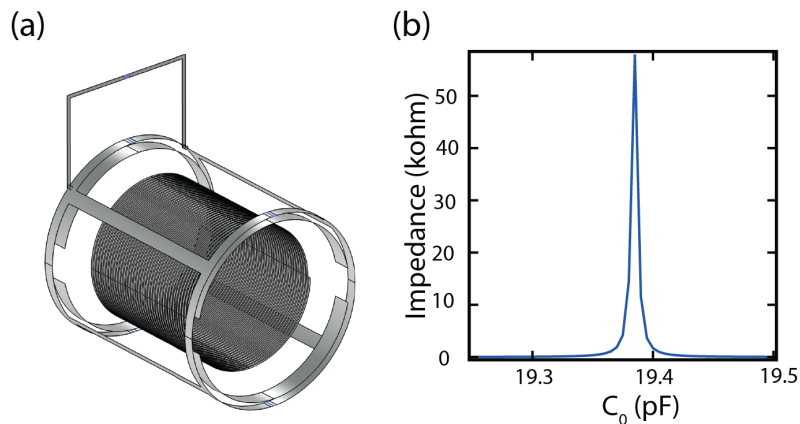


Figure 7.3: (a) The complete NMR/EPR assembly as simulated in COMSOL. (b) Magnitude of the simulated impedance between resonator halves. Simulations were performed at 141 MHz for different values of the fixed capacitance C_0 .

fixed capacitors modeled as lumped elements. Field values were normalized to 1 mT B_{1e} field in the center of each resonator.

7.3.4 Overhauser-enhanced MRI

Imaging was performed with a 3D OMRI bSSFP sequence that has been described previously [248]. The efficiency of this sequence is improved over conventional OMRI sequences by using EPR saturation pulses coincident with phase encoding, allowing steady-state signal acquisition during more than one-third of the imaging time. Images were acquired with

$TE/TR = 25.4/50.7$ ms, $T_{PE} = 16.3$ ms, readout time $T_{RO} = 17.1$ ms, a $128 \times 35 \times 11$ matrix (Readout (RO) \times Phase Encode 1 (PE1) \times Phase Encode 2 (PE2)), and $1.1 \times 1.6 \times 8$ mm³ voxel size. A transmit power of 8 mW was used for NMR pulses 240 μ s in length and a tip angle α of 70°. A sequence timing diagram is provided in Fig. 7.4. Phantom images were fully sampled (sampling factor (SF) = 1). Image reconstruction was performed via conventional Fourier reconstruction in Matlab (Mathworks, Natick MA, USA). The magnitude colorscale in all images is normalized to the signal without Overhauser enhancement.

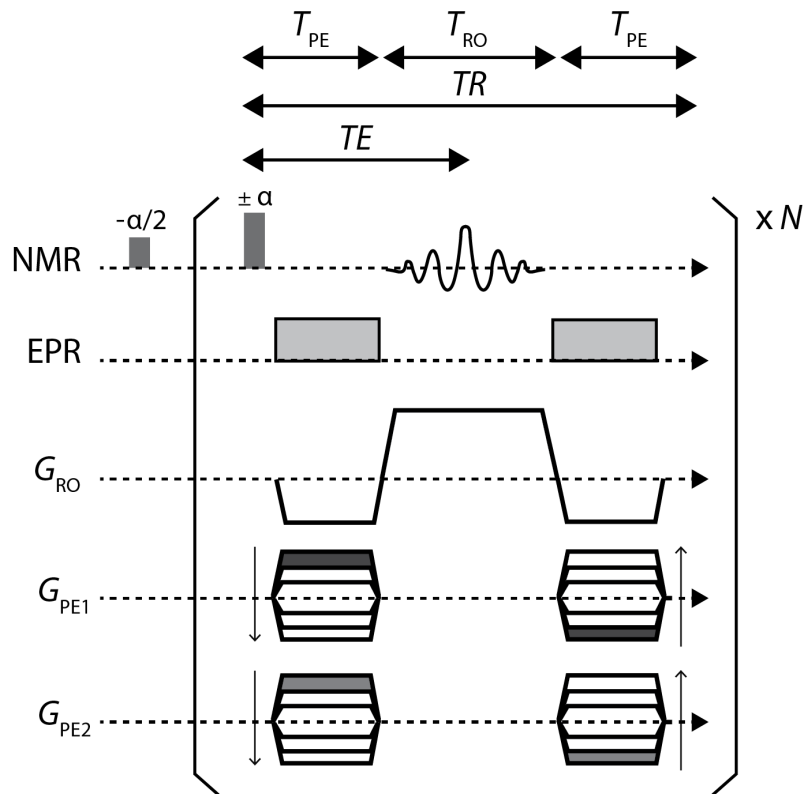


Figure 7.4: **3D OMRI bSSFP imaging sequence with EPR pulses embedded in the phase encode.** Acquisition parameters were $TE/TR = 25.4/50.7$ ms, $T_{PE} = 16.3$ ms and FID acquisition time $T_{RO} = 17.1$ ms. The tip angle α was 70° . Data were acquired in a $128 \times 35 \times 11$ matrix (Readout (RO) \times Phase Encode 1 (PE1) \times Phase Encode 2 (PE2)).

Probe homogeneity was measured with a 60 mL vial of 2 mM TEMPOL solution. TEMPOL sensitivity was tested using vials of various TEMPOL concentrations. Image signal-to-noise ratio (SNR) was measured as the average signal magnitude in a region of interest (ROI) divided by the standard deviation of the signal in a signal-free region at the edge of the field of view. The number of averages (NA), and resulting total acquisition time (AT), was chosen independently for the various images acquired.

7.3.5 Animal Preparation

All experiments were performed in accordance with our Institutional Animal Care and Use Committee guidelines.

Under anesthesia (2%-isoflurane), a 450g Sprague-Dawley male rat was prepared for TEMPOL injection while rectal temperature was continuously monitored. Buprenorphine 0.08 mg/kg was given subcutaneously 30 minutes before surgery. After dissection of the common carotid artery and the carotid bifurcation, ligation of pterygopalatine artery and external carotid artery, a polyethylene catheter (PE10) filled with 0.9% saline and heparin 50 U/mL, connected to a Genie Touch infusion pump (Kent Scientific, Torrington CT, USA), was inserted via the external carotid and advanced into the right carotid artery bifurcation.

After surgery, the animal was transferred to the flat animal bed of the OMRI scanner. The NMR and EPR coils of the OMRI probe sit within a recessed slot in the animal bed. A sliding polycarbonate bite bar with integrated anesthesia nose cone was incorporated into the probe assembly to position the rodent in the isocenter of the scanner and to anesthetize it during imaging. A sealed glass sphere containing 2 mM TEMPOL was located on the contralateral side with respect to the catheter placement and used as a fiducial. An optical fiber temperature sensor (Osensa FTX-301-PWR, Burnaby BC, Canada) was used for continuous rectal temperature measurement while the animal was in the scanner. Cardiac and respiratory rates, as well as pO_2 were continuously monitored with a Model 1025T Monitoring and Gating System (Small Animal Instruments, Inc, Stony Brook, NY).

7.3.6 *In vivo* Overhauser-enhanced MRI

In vivo imaging is performed with the 3D bSSFP sequence described above, additionally accelerated by 50% random Gaussian undersampling in the phase encode direction ($SF = 0.5$) as described in Ref. [248]. A reference image was acquired using $NA = 30$, corresponding to $AT = 4.5$ minutes. Following the reference scan, 1 mL of 150 mM TEMPOL was injected into the internal carotid artery (ICA) over 2 minutes with the infusion pump. A dynamic OMRI sequence, consisting of 16 independent 3D OMRI acquisitions spaced at 15 s intervals, was started at the same time as the injection. Each OMRI scan had $NA = 1$ ($AT = 9$ s) and 24 W of power for EPR saturation pulses. Zero-filling was used for *in vivo* image processing to increase the acquired voxel resolution of $1.1 \times 1.6 \times 8$ mm³ to the interpolated resolution of $0.4 \times 0.4 \times 8$ mm³.

The animal was euthanized at the completion of the experiment.

7.3.7 Specific absorbance rate

To measure the SAR of our OMRI system, the probe was loaded with a 25 mL solution of Phosphate Buffered Saline (PBS-10X) and the dynamic OMRI sequence with 12 dynamics scans, $NA = 1$, $SF = 0.5$ and 18 W EPR power was run. The temperature increase of the solution was measured via optical fiber. The sample was wrapped in insulating closed cell foam to prevent heat transfer to the local environment. PBS-10X was used for its high conductivity, which results in easily measurable temperature changes when subjected to RF power.

7.4 Results

7.4.1 EPR Resonator Design

The NMR coil has a bandwidth of 2.1 kHz which is broadened to 5.1 kHz upon assembly of the NMR coil with a conventional AG resonator with guard rings. This broadening corresponds to a 59% reduction in NMR Q -factor.

Introducing small splits in the guard rings (see Fig. 7.5(a)) reduces mutual inductance between the guard rings and the NMR coil, reducing the NMR bandwidth in the assembly by 0.5 kHz. Further modifying the AG resonator, by removing copper from the center of the resonator walls (see Fig. 7.5(b)), minimizes losses occurring due to the proximity of wires in the NMR solenoid and the conducting planes that form the walls of the AG resonator, reducing the NMR bandwidth in the probe assembly to 2.9 kHz ($Q = 94$). Thus, these modifications give the OMRI probe with MAG resonator a near factor of two increase in NMR Q -factor when compared to the traditional AG resonator. The Q -factor of the EPR resonator is 31 at 141 MHz.

To evaluate the changes in E -field and B -field that occur from resonator modifications, we performed finite element analysis simulations of an AG resonator and a MAG resonator, as shown in Fig. 7.5(c,d). We find that in the center of an AG resonator, there is high B_{1e} homogeneity and exclusion of the E field, properties that have made the AG resonator popular for use in high-field bioimaging. Reduction of B_{1e} homogeneity in the new MAG resonator is minimized by removing the conducting walls of the AG resonator, which are the regions of lowest current density in the AG resonator [170]. We see that in the B_0 direction, the orthogonal B_{1e} component falls to 50% of its maximum value at 26 mm from the center of the AG resonator, and at 20 mm from the center of the MAG resonator. Our simulations indicate that the split guard rings in the MAG resonator are effective at shielding the large electric fields at the ends of the AG resonator. We note that the guard rings were split at the four points furthest from the fixed capacitors, where the E -field is expected to be at a minimum. Additionally, simulations also show that the B_{1e} homogeneity of the MAG resonator is improved by increasing the angle subtended between rungs in the B_{1e} direction. The MAG resonator homogeneity is increased at a subtended angle of 60° , the optimal angle for homogeneity in saddle coils [301], but with much less effective E -field exclusion than seen in the resonator with the 90° subtended angle used here (supporting simulations are provided in Fig. 7.6).

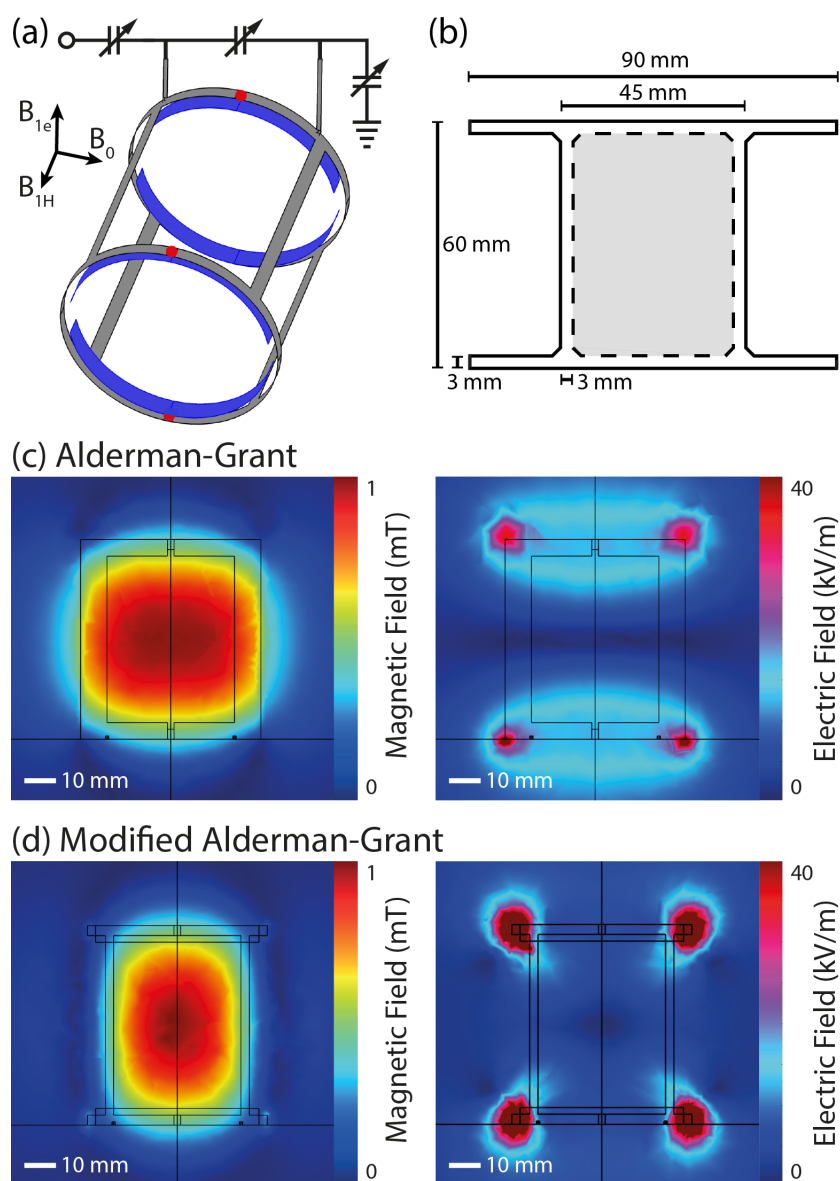


Figure 7.5: **EPR resonator design.** (a) MAG resonator schematic. A traditional AG resonator with guard rings is modified by splitting the guard rings (shown in blue) and cutting windows in the sides of the slotted tube (shown in grey). Directions of mutually orthogonal B_0 , B_{1H} and B_{1e} fields are indicated. The fixed capacitor locations are marked in red (one is hidden from view). (b) Shape and dimensions of copper foil pieces cut for EPR resonator. The region shaded in grey was removed to build the MAG resonator. (c) Field simulations (B_{1e} - left, E - right) of AG resonator. (d) Field simulations (B_{1e} - left, E - right) of MAG resonator.

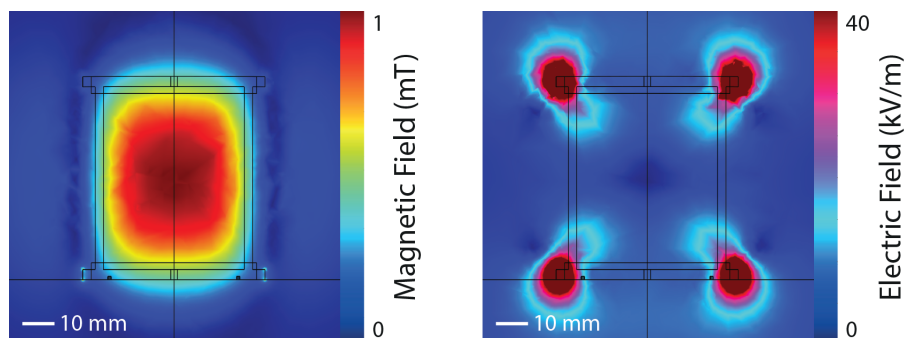


Figure 7.6: Simulations of a MAG resonator with a 60° angle subtended between rungs in the B_{1e} direction. B_{1e} (left) and E field profiles are shown.

7.4.2 Probe performance

Images acquired with no EPR power and $NA = 32$, of a uniform TEMPOL phantom (see Fig. 7.7(a)), show that the NMR coil sensitivity is highly homogeneous across an axial slice, as would be expected from the axial symmetry of the solenoid. OMRI, taken with an EPR power of 15 W and $NA = 8$, of the same phantom (Fig. 7.7(b)) shows uniform inversion of MRI signal phase due to negative enhancement of the ^1H polarization via the Overhauser effect. There is spatial variation of Overhauser enhancement, with a reduction of intensity towards the horizontal edges of the FOV. Simulations of the EPR resonator that include a model of the NMR coil (Fig. 7.8(a)), indicate that these hypointense areas of enhancement correspond to regions of lower B_{1e} . These simulations also show that inclusion of the NMR solenoid has little effect on B_{1e} field, but does result in increased penetration of the E -field into the center of the imaging volume (Fig. 7.8(b)) when compared to the simulations shown in Fig. 7.5. This increased E -field penetration is to be expected, given the proximity of EPR and NMR coils, and close spacing of solenoid turns.

To test for *in vivo* changes in E - and B_{1e} -field profiles, simulations were also performed for the EPR probe when loaded with a 30 mm diameter sphere of the same conductivity and relative permittivity as brain grey matter [302]. These “*in vivo*” simulations showed E - and B_{1e} -field distributions nearly identical to those presented in Fig. 7.8 (supporting data included in Fig. 7.9).

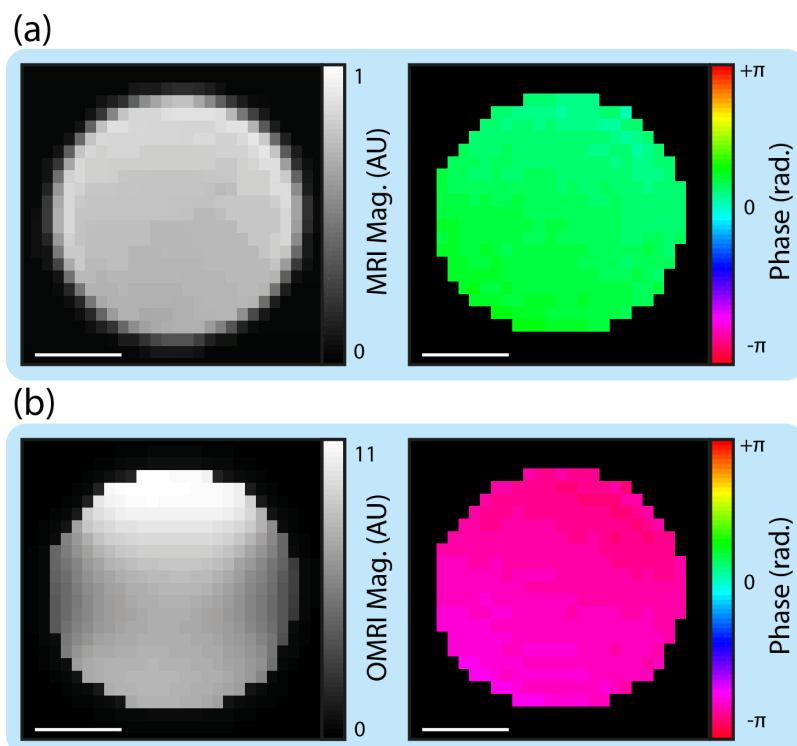


Figure 7.7: **Overhauser enhancement in the complete NMR/EPR probe assembly.** (a) Axial slice of a 2 mM TEMPOL solution acquired with conventional bSSFP MRI. Magnitude (left) and phase (right) images are displayed. (b) Axial slice of a 2 mM TEMPOL solution acquired with bSSFP OMRI. Magnitude (left) and phase (right) are displayed. (c) Simulations of the B_{1e} profile in coronal and axial cross sections of our MAG resonator assembly. (d) Simulated E field profile of the MAG resonator assembly. Scale bars (white) are 10 mm in length. In c,d the NMR coil was modeled as a 40-turn helix with a perfect electrically conducting surface.

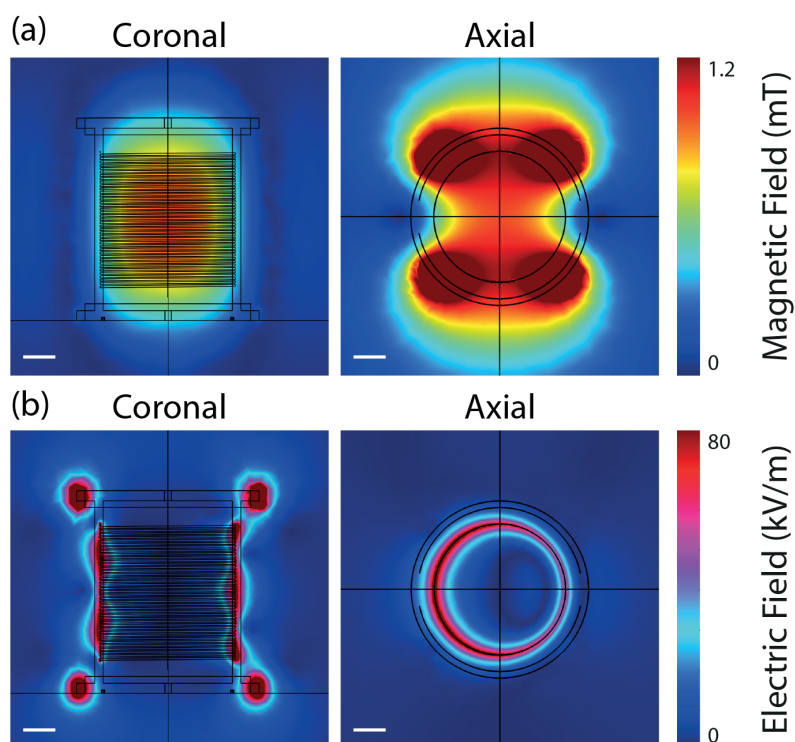


Figure 7.8: **Simulations of the complete NMR/EPR probe assembly.** (a) The B_{1e} profile in coronal and axial cross sections of our MAG resonator assembly. (b) E field profile of the MAG resonator assembly. Scale bars (white) are 10 mm in length. The NMR coil was modeled as a 40-turn helix with a perfect electrically conducting surface.

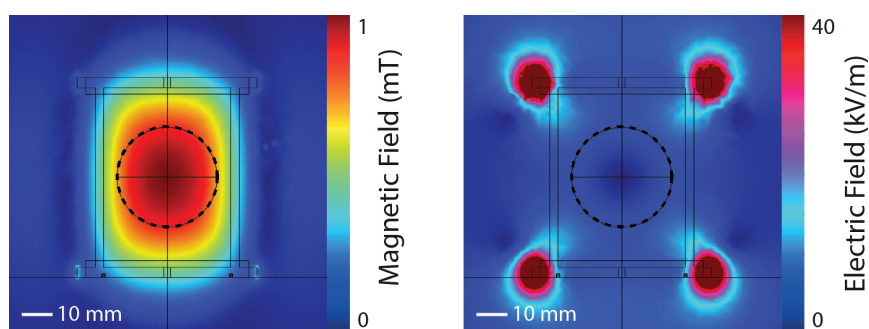


Figure 7.9: **Simulations of a loaded MAG resonator.** The dotted line shows the boundary of a 30 mm diameter sphere with relative permittivity and conductivity values of 100 and 0.8 S/m, respectively. B_{1e} (left) and E (right) field profiles are shown. Relative permittivity and conductivity values were chosen to match values expected in a rat brain.

To assess the sensitivity of our OMRI probe to TEMPOL concentration, a reference image of vials containing high concentrations of TEMPOL (Fig. 7.10(a)) was acquired with EPR off and $NA = 32$ ($AT = 9.5$ min.), as shown in Fig. 7.10(b). No significant contrast is apparent between different vials in this reference image.

Afterwards, images were acquired with EPR pulses enabled (24 W) and $NA = 1$ ($AT = 18$ s), as shown in Fig. 7.10(c). Slices from this OMRI dataset show clear contrast between TEMPOL vials of different concentration, with a maximum image enhancement of -17 observed in the 2 mM TEMPOL solution. OMRI scans were also acquired from low concentration vials of TEMPOL with $NA = 64$ ($AT = 19$ min.) as shown in Fig. 7.10(d). In our system at 24 W EPR power, below TEMPOL concentrations of 0.1 mM, the OMRI signal is no longer inverted by the Overhauser effect but instead is reduced in magnitude compared to the MRI signal. In this low concentration regime, TEMPOL detection can be performed by comparison of the OMRI signal with the unenhanced MRI signal. Voxels of 50 μM , 20 μM , 10 μM and 5 μM TEMPOL have average signal magnitudes of 0.05, 0.65, 0.85 and 0.88, respectively, compared to the unenhanced water value of 1. As the water vial has an SNR of 21 (noise = 0.05), voxels corresponding to 10 μM and 5 μM concentrations are just on the detection threshold with an OMRI signal change of 2-3 times the noise floor.

7.4.3 *In vivo* Overhauser-enhanced MRI

We begin our *in vivo* experiments by acquiring reference bSSFP MRI images of the rat head immediately following surgery (see Fig. 7.11(a)). The 2 minute, 1 mL injection of 150 mM TEMPOL is started and a 3D OMRI scan acquired every 15 s for a total of 4 minutes. These OMRI scans show negative ^1H signal enhancement in the ipsilateral hemisphere of the brain, as well as in the fiducial (see Fig. 7.11(b)). Absolute signal enhancement decreases for the remainder of the scans (see Fig. 7.11(c)) following the end of the injection. The mean signal in regions of interest within ipsilateral and contralateral hemispheres of the brain show that signal changes are predom-

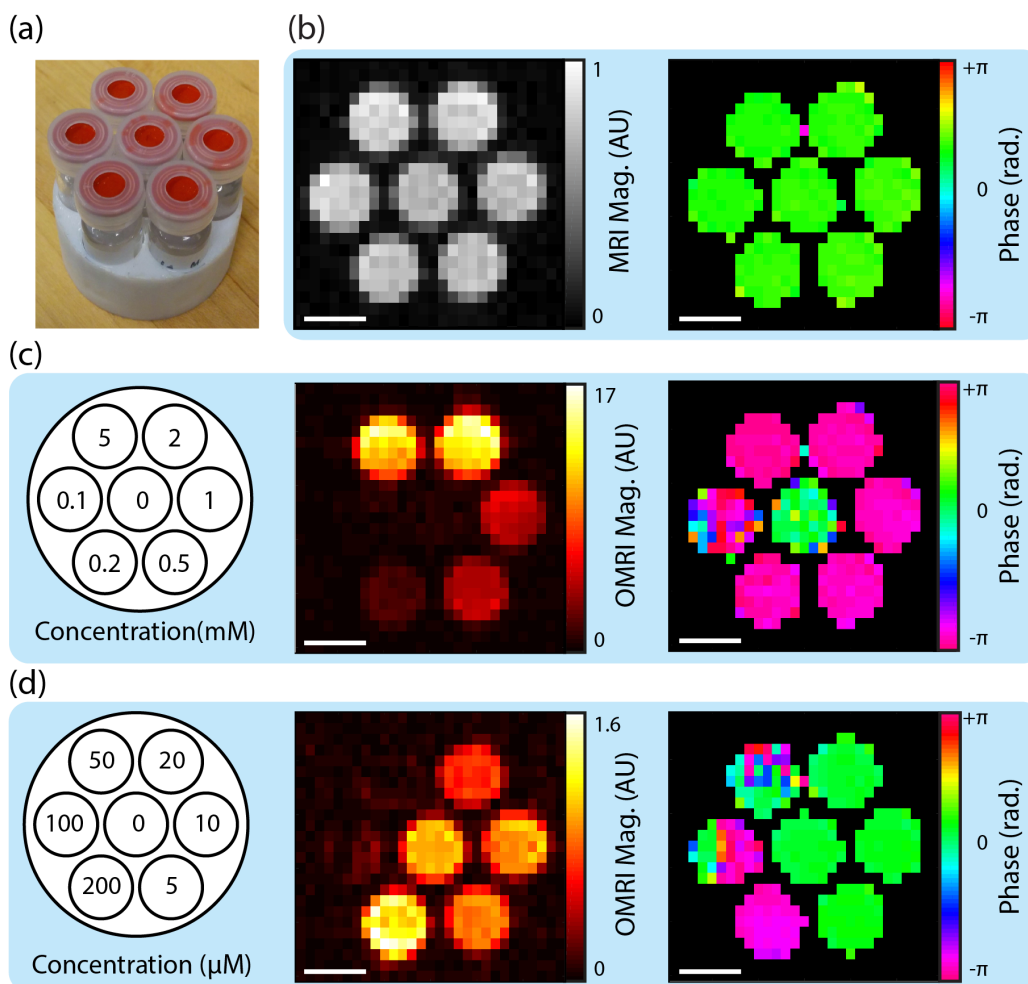


Figure 7.10: **Sensitivity of TEMPOL imaging.** (a) Photograph of phantom containing 2 mL vials of TEMPOL. (b) Magnitude (left) and phase (right) images of a high concentration TEMPOL phantom acquired with conventional bSSFP MRI. Phantom schematic is the same as shown in c. (c) OMRI of a high concentration TEMPOL phantom. Schematic shows vial concentrations. (d) OMRI of a low concentration TEMPOL phantom. Schematic shows vial concentrations. All signal magnitudes are normalized to the unenhanced water value. All images were acquired at 6.5 mT. Scale bars (white) are 10 mm in length.

inantly confined to the ipsilateral cerebral hemisphere (see Fig. 7.11(c,d)). Although, other regions including the eye, and contralateral anterior cerebral artery territory, which is supplied by a single confluent vessel contributed by the ipsilateral internal carotid, also appear to be labeled. Furthermore, the signal magnitude in the ipsilateral hemisphere peaks at the end of the injection with the ^1H enhancement halving in the 2 minutes after injection.

Rectal temperature remained at 37.8 ± 0.2 °C throughout the experiment. The respiration rate remained within 64 ± 6 breaths per minute (bpm) at all times, averaging 60 bpm when the rat was at rest and increasing to a maximum of 70 bpm during TEMPOL injection. The cardiac rate was steady at 310 ± 10 beats per minute (bpm) when the rat was at rest and decreased to a minimum of 118 bpm during TEMPOL injection, likely due to Cushing reflex, which is a physiological nervous system response to increased intracranial pressure [303]. The cardiac rate recovered to 290 bpm by the end of the dynamic imaging sequence. An OMRI sequence run without TEMPOL injection showed no significant change in the monitored physiological parameters.

7.4.4 Specific absorbance rate

Having demonstrated the *in vivo* use of our OMRI platform, we now quantify SAR, which is critical to determining limits on RF power use in future OMRI applications. The RF power absorbed during EPR pulses can be estimated from:

$$P_{\text{abs}} = P_{\text{EPR}} \frac{\Delta Q}{Q_{\text{unloaded}}}, \quad (7.1)$$

where P_{EPR} is the power to the EPR resonator, P_{abs} is the absorbed RF power, Q_{unloaded} is the Q -factor of the unloaded EPR resonator and ΔQ is the change in EPR resonator Q -factor on loading [56]. During *in vivo* experiments, P_{EPR} was 24 W and loading with the rat $\Delta Q = 0.9$, giving $P_{\text{abs}} = 0.8$ W.

To test the accuracy of this SAR estimate, we loaded the OMRI probe

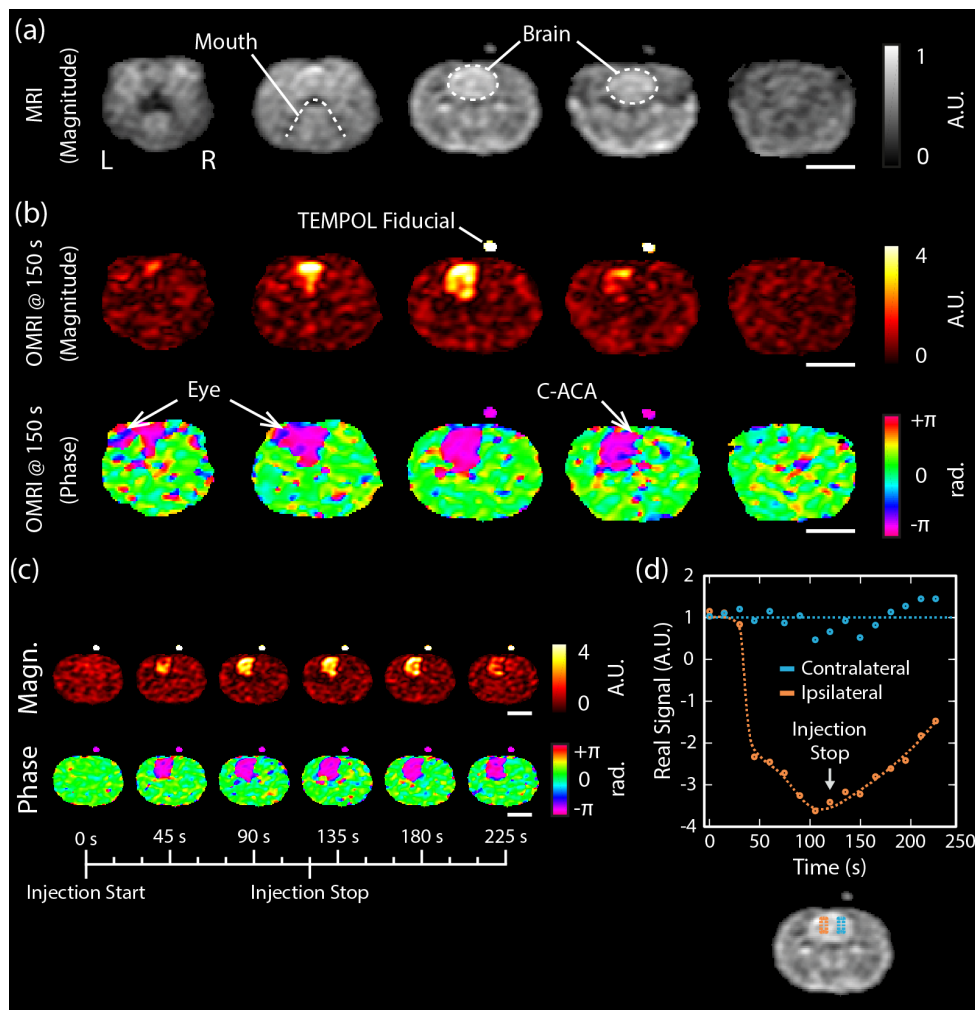


Figure 7.11: **MRI and OMRI dynamics in a rat model.** An anatomy scan was acquired with MRI before injection of 1 mL of 150 mM TEMPOL into the ICA over 2 minutes. The rat head was imaged with OMRI once every 15 s from the beginning of the injection. Each 9 second acquisition captured a full 11 slice dataset. (a) The MRI anatomy scan. The five central slices are shown. (b) OMRI bSSFP images acquired 150 s after the beginning of the TEMPOL injection. The 5 central slices are shown. Arrows indicate regions of the eye and contralateral anterior cerebral artery (C-ACA). (c) Dynamic imaging of TEMPOL with OMRI during the injection. The OMRI signal from the central slice is shown at the indicated time points during and after injection. (d) The average real OMRI signal is plotted over time for regions of interest in the ipsilateral hemisphere (orange) and contralateral hemisphere (blue) of the central slice. Scale bars (bottom right of subfigures, white) are 10 mm in length.

with a 25 mL vial of PBS 10X. An OMRI sequence with 16 dynamic scans and $P_{\text{EPR}} = 18$ W heated the solution by 5.6 °C. This heating corresponds to $P_{\text{abs}} = 6.7$ W, based on a calculation including the EPR duty cycle, specific heat of the solution and assuming no heat loss from the solution. The PBS solution gives a loaded EPR Q -factor of 23.4 corresponding to a Q of 7.1 and an estimated P_{abs} of 4.1 W from Eq. 7.1. Considering that our measured value of RF power absorption in the PBS solution is a factor of 1.6 larger than our estimated value, we calculate a revised upper estimate for *in vivo* RF power absorption during EPR pulses of 1.3 W.

7.5 Discussion - Rat brain imaging

The OMRI platform presented here has enabled dynamic *in vivo* imaging of TEMPOL with $1.1 \times 1.6 \times 8$ mm³ voxel size. Our imaging studies in phantoms demonstrate that the phase inversion of the ¹H MRI signal can be used to detect free radical presence at TEMPOL concentrations above 100 μM. Considering the sensitivity of phantom imaging in Fig. 7.10(d) and, assuming that SNR scales with the number of averages (NA) as \sqrt{NA} , we calculate that signal reduction from 50 μM TEMPOL is more than double the noise floor in our $NA = 1$ dynamic OMRI sequence. Hence, 50 μM is the minimum TEMPOL concentration detectable in our dynamic *in vivo* images. Comparing the *in vivo* enhancement 150 s after the beginning of the injection (see Fig. 7.11(b)) to that observed in our concentration phantoms, we estimate the maximum TEMPOL concentration in the ipsilateral hemisphere to be 300 μM. We note that this value will differ from the actual TEMPOL concentration due to sample specific spin relaxation times. The long lifetime of enhancement in the ipsilateral hemisphere post-injection suggests that TEMPOL may have entered the brain parenchyma. We believe that temporally resolved OMRI with our system will be useful for tracking redox status via the rate of appearance and disappearance of TEMPOL, especially in cases of oxidative stress where brain tissue may be permeable [296].

Increasing B_{1e} , voxel size and acquisition time are straightforward approaches to improving the concentration sensitivity of our platform. How-

ever, significantly increasing *in vivo* acquisition times would require the use of radicals with longer term *in vivo* stability [185]. Alternatively, enhancement would be increased with use of a narrower linewidth radical [250, 304]. However, we note that as EPR saturation occurs during the phase encode step in our bSSFP OMRI sequence, the magnitude of the phase encode gradient is restricted by the radical linewidth. NMR sensitivity would be further improved by reducing coil noise, either by implementing a cryocooled coil [305] or active feedback [306].

Our custom OMRI probe has been designed for a high Q -factor in the NMR resonator and low SAR from the EPR resonator. While the homogeneity of our volume EPR resonator is highly favorable for imaging, as inductive heating scales as the fifth power of sample radius [166], the use of surface EPR coils for B_{1e} confinement will be necessary for samples much larger than a rat's head [288, 307, 308].

In addition to the low-SAR design considerations of our EPR resonator, we have in this study restricted ourselves to 24 W of EPR power to further minimize SAR concerns. An EPR power of 24 W in our resonator corresponds to a peak SAR in the rat model of 2.9 W/kg when averaged over the mass of the entire rat or 52 W/kg when averaged over the mass of the head (approximately 25 g). The EPR duty cycle over the entire dynamic imaging sequence is 40%, resulting in an even lower SAR value when averaged. OMRI studies report incident EPR powers as high as 90 W and SAR values as high as 300 W/kg averaged over the whole body [259, 309, 310]. Therefore, in future *in vivo* studies there is significant scope to increase B_{1e} in our OMRI probe, via increased EPR power, without concern for animal safety.

7.6 Conclusion - Rat brain imaging

We have detailed the design of an optimized OMRI platform that significantly mitigates the sensitivity challenges of ULF MRI and restricts RF power absorbance to levels that are safe for preclinical application. We have routinely used this apparatus to make repeated measurements on more than 50 animals. This platform for TEMPOL imaging in the rat brain will motivate

further use of OMRI to study the role of radicals in ischemic stroke.

7.7 A Probe For Whole Body OMRI in a Rat Model

In this chapter, the development of an OMRI probe for rat head imaging has been described in detail. In this section, we describe the development of another OMRI probe built to image TEMPOL throughout the rat body. Whilst the ultimate experimental goal of our OMRI platform is to probe the redox status of the rat brain, study of the spatial distribution of the exogenous radicals used in our studies is of scientific interest. Whole body imaging studies with OMRI have largely been confined to mice [311], as their small size significantly reduces inductive heating effects, mitigating SAR. OMRI in the abdomen of larger animals, such as rats, is typically performed using surface coils [288]. Localization of B_{1e} with surface coils is effective at reducing SAR, OMRI scans taken with surface coils do not allow imaging of free radicals on whole body length scales. The body probe we present here is designed to mitigate SAR issues while producing a homogeneous B_{1e} through the rat body during OMRI scans, thus enabling noninvasive measurement of TEMPOL distribution on whole body scales.

7.7.1 Body Probe Design

For whole body imaging, a combination of an Alderman-Grant based EPR resonator and orthogonal solenoidal NMR coil that we found so effective for imaging with the OMRI rat head probe is used. A photograph of the assembled whole body probe is shown in Fig. 7.12(a). A 90 mm outer diameter, 200 mm long, Pyrex tube was used as a former for the EPR resonator. A conventional AG resonator, 130 mm in length, was constructed on the former with copper tape.² The angle subtended by the ‘windows’ in the EPR resonator was chosen to be 90° for maximal B_{1e} homogeneity over the large

²The whole body probe described here was constructed before we discovered the sensitivity advantages of using the modified Alderman-Grant resonator described earlier.

imaging volume. Segmentation capacitors (C_0) with a fixed value of 8.2 pF each were used with an external resonator board to resonate the EPR coil at 140 MHz, with a Q of 86.³ The external resonator circuit consists of three 1-20 pF variable capacitors in a balanced “series-match, parallel-tune” configuration.

A 75 mm outer diameter length of Pyrex tubing was used as a former for the internal NMR solenoid. The AG resonator and NMR former of the body probe have an imaging volume suitable for OMRI that is 65 mm in diameter and 110 mm in length. Given this imaging volume, the target bandwidth of the NMR solenoid in the body probe is 4.7 kHz, per the calculation described in Section 7.3.2. A 45 turn solenoid, 110 mm in length, was thus wound on the NMR former with AWG 15 enameled-copper wire. When resonated to 276 kHz in the OMRI assembly (with capacitors in series-match, parallel-tune configuration), this NMR solenoid had a bandwidth of 7.4 kHz ($Q = 35$). To reduce SAR at the ends of the EPR resonator, guard rings made of copper tape were added to AG coil [170]. This modification increased the NMR bandwidth to 55 kHz ($Q = 5$), presumably due to mutual inductance between the solenoid and continuous loops of the guard rings. Splitting the guard rings, as was described in Section 7.3.3, reduced the NMR bandwidth to its final value of 9.0 kHz ($Q = 30$). While this NMR bandwidth is increased from the value without guard rings, the modification was deemed an acceptable tradeoff for the reduction in SAR.⁴

7.7.2 Imaging Performance of the Body Probe

To evaluate the performance our OMRI body probe in realistic conditions, it was loaded with a 60 mm diameter, 120 mm long, bottle of 2 mM TEMPOL.

³When selecting the segmentation capacitance (C_0), care should be taken to ensure that the probe does not resonate in the ‘end ring’ mode, which occurs at slightly higher frequency than the desired mode (30 MHz higher for the geometry and capacitance presented here). The end ring mode is characterized by a B_{1e} node in the center of the resonator and hence, will quickly show up in phantom imaging tests due to no Overhauser enhancement in the center of the probe.

⁴After the measurements described in this thesis, the NMR coil in this body probe was rewound with a single layer of 5/39/42 Litz wire, which reduced the NMR bandwidth to 5.9 kHz.

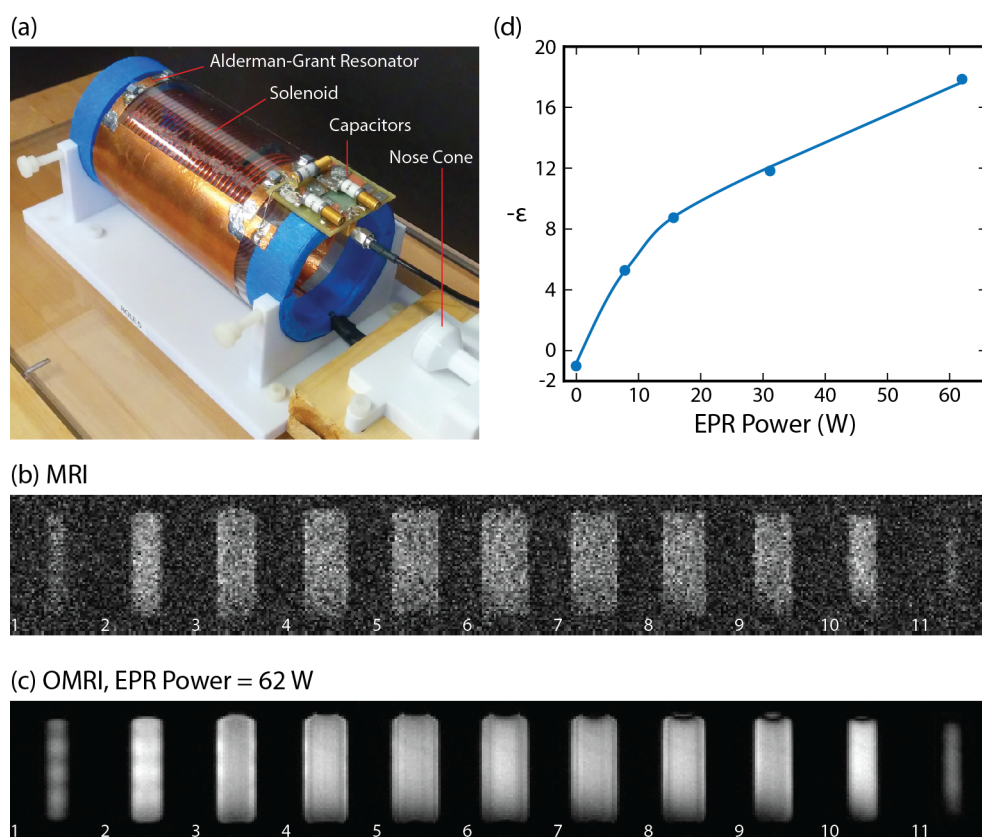


Figure 7.12: **OMRI Body Probe.** (a) Photograph of the assembled probe. The external Alderman-Grant resonator for EPR and internal solenoid for NMR are visible. EPR tuning is performed via the variable capacitors affixed to the top of the probe. A nose cone is used to administer anesthesia for *in vivo* studies. (b) Image enhancement in the center of a 2 mM TEMPOL phantom when imaged with a 3D OMRI bSSFP sequence and various EPR powers. Blue line is intended as a guide to the eye. (c) Conventional bSSFP MRI of a bottle of 2 mM TEMPOL. (d) bSSFP OMRI of a bottle of 2 mM TEMPOL with 62 W of RF power applied during EPR pulses. The bottle phantom used in c and d is 60 mm in diameter and 120 mm in length. Image slice thickness is 6 mm. Acquisition time for each image dataset was approximately 80 s.

A modified version of the 3D OMRI bSSFP sequence described in Section 7.3.4 was used to image the bottle. Data in the modified sequence were acquired with a $64 \times 64 \times 11$ matrix and $NA = 2$ such that the total acquisition time was approximately 40 seconds and voxel sizes were $2 \text{ mm} \times 2 \text{ mm} \times 6 \text{ mm}$.

A sagittal image dataset, taken with conventional bSSFP MRI and shown in Fig. 7.12(b), reveals the shape of the bottle phantom but has a relatively low SNR of 3.3. Acquiring the same image dataset with OMRI and 62 W of EPR power (see Fig. 7.12(c)), boosts the image SNR to 56, corresponding to an image enhancement of -17. The OMRI data shows enhancement throughout the bottle and the improved images reveal features such as the cap. Increased enhancement is seen in slices 2 and 10, likely because these slices lie in the same plane as the segmentation capacitors in the AG resonator, where B_{1e} is maximal (see Fig. 7.8(a) for a similar B_{1e} field profile). Reduced brightness is also seen at the bottom of slices 9 and 10, which is likely a banding artifact, common in bSSFP MRI [312], occurring due to lower magnetic field homogeneity at the edge of the FOV. OMRI scans taken with varying EPR power showed that absolute image enhancement fell with the use of lower EPR powers (see Fig. 7.12(d)).

7.7.3 Cretaceous OMRI

Having established the homogeneity of our body probe, in this section a more complex phantom is used to demonstrate the strength of our platform in revealing anatomical detail. For this purpose, a plastic triceratops toy was sourced from Amazon.com with free 2-day delivery, see Fig. 7.13(a,b). As one of the most widely recognized dinosaurs, triceratops are attractive for increasing the appeal of science to a broad audience.

As is the case for its fossilized cousins, direct MRI of the plastic triceratops is impractical due to the absence of liquid-state ^1H nuclei. To overcome the solid nature of plastic, the triceratops was placed in a sealed container filled with a 2 mM TEMPOL solution rich in ^1H nuclei. This container enables triceratops imaging to occur via negative contrast OMRI (see Fig. 7.13(c)),

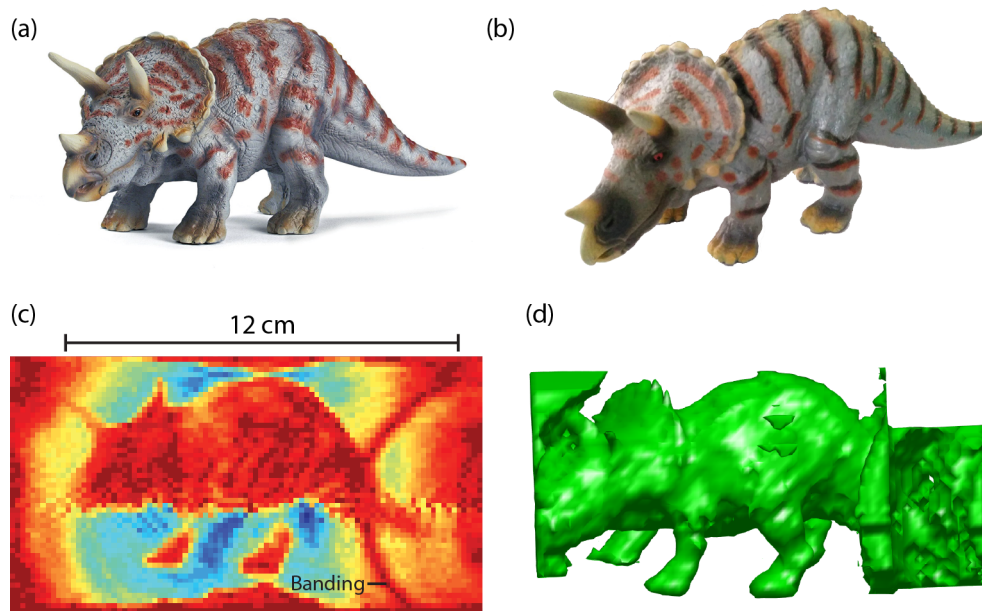


Figure 7.13: **Cretaceous OMRI.** (a) Stock image of the plastic triceratops figurine sourced from Amazon.com Inc. (b) Photograph of the triceratops toy. (c) Coronal slice from a $64 \times 64 \times 99$ (Readout \times Phase Encode 1 \times Phase Encode 2) negative contrast 3D OMRI bSSFP dataset. (d) 3D surface rendering of the triceratops figurine generated in MATLAB from negative contrast OMRI data. Rendering was constructed from the same $64 \times 64 \times 99$ dataset used in c.

in which the colorscale is inverted such that bright voxels (e.g. TEMPOL solution) are dark and dark voxels (e.g. triceratops) are bright. Masking and thresholding of the negative contrast images enable rendering of the 3D triceratops model shown in Fig. 7.13(d). The images and rendering show the characteristic horns, frill and quadrupedal form of the triceratops. Posterior and anterior ends of the triceratops extend beyond the sensitive region of the NMR solenoid, giving rise to artifacts at the far left and right of the images. Magnetic field inhomogeneities caused by iron oxides in the figurine paint likely give rise to the banding artifact indicated in Fig. 7.13(c). Other ‘zipper’ like artifacts appear at the extreme horizontal edges of the images due to low SNR in these regions.

7.7.4 *In vivo* Whole Body OMRI

To demonstrate *in vivo* OMRI, a 310 g male Sprague-Dawley was anesthetised (2% isoflurane) and a tail vein catheter placed. The rat was connected to the animal monitoring and injection systems described in Section 7.3.5 and then placed in the body probe alongside a fiducial containing 2 mM TEMPOL.

The anatomy scan shown in Fig. 7.14(a) contains coronal slices through the abdomen of the rat. In these anatomy images, regions of low proton density, such as the bladder and stomach, are readily visible. However, contrast between other organs is limited to proton density as voxel brightness in bSSFP MRI is weighted by the ratio T_1/T_2 [257] and $T_2 \rightarrow T_1$ at ULF [258].

A 1.5 mL tail vein injection of 150 mM TEMPOL was started, and then an OMRI acquisition with 31 W of EPR power begun. The 80 s OMRI acquisition and 90 s injection finished at the same time. The OMRI magnitude and phase data (Fig. 7.14(b) and Fig. 7.14(c), respectively) shows a negatively enhanced signal in the location of kidneys, indicating that TEMPOL clearance is occurring via the renal system. To increase the sensitivity of the OMRI data, we create a difference image (see Fig. 7.14(d)) by subtracting the real part of the OMRI data from the real part of the MRI anatomy data. This difference image shows a wider region of signal enhancement in

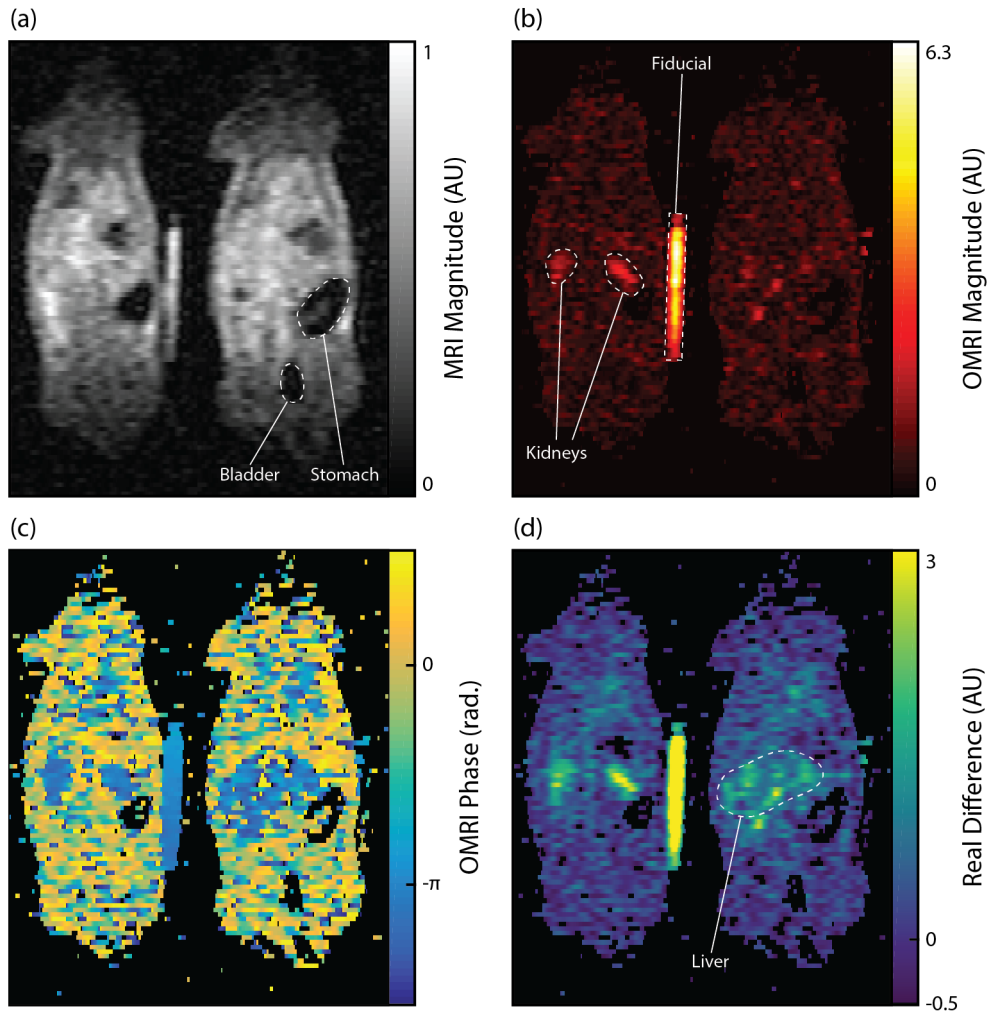


Figure 7.14: In vivo whole body OMRI. (a) bSSFP MRI magnitude images, $NA = 160$, showing the anatomy of a rat. (b) bSSFP OMRI magnitude images, $NA = 4$, of the rat following tail vein injection of TEMPOL. (c) bSSFP OMRI phase images for the magnitude data shown in **b**. (d) Difference image showing the change in real valued signal between MRI and OMRI scans. All images were acquired in a $128 \times 35 \times 11$ matrix with $SF = 0.5$ and FOV $130 \text{ mm} \times 70 \text{ mm} \times 70 \text{ mm}$ for a voxel resolution of $1 \text{ mm} \times 2 \text{ mm} \times 6 \text{ mm}$. The two central slices of the eleven slice datasets, interpolated to 128×128 resolution, are shown in this figure. 1 average takes approximately 20 seconds. Hence, total acquisition time of a given scan is given by $NA \times 20 \text{ s}$.

the vicinity of the kidneys, suggesting that TEMPOL is also present in the liver.

In addition to the *in vivo* results, we note that the OMRI image enhancement of the 2 mM TEMPOL fiducial is -6 in Fig. 7.14(b). This enhancement is only 50 % of what would be expected with 31 W of applied EPR power when compared to body probe characterization data in Fig. 7.12(d). This reduction in TEMPOL enhancement is likely due to the drop in B_{1e} that occurs when the EPR coil is loaded with the rat. Loading with the rat causes the Q of the EPR coil to drop from 86 to 13. As the EPR coil loading effect is so large, we can also assume that nearly all of the applied EPR power is absorbed by the rat. By further assuming that EPR power is absorbed uniformly across the rat body, we calculate a peak SAR of 100 W/kg and an average SAR of 67 W/kg when allowing for the EPR duty cycle.⁵

Before the TEMPOL injection, the rat had a respiratory rate of 45 breaths per minute, a pulse rate of 339 beats per minute and a temperature of 38.1 °C. After the scan, the rat's temperature had increased to 39.2 °C, indicating that SAR in this body probe is much higher than in the rat head probe described previously. After the injection, the pulse rate decreased to 70 beats per minute and continued to decline afterwards, with the rat dying a few minutes later. We note that this TEMPOL injection was the third that the rat had received in the space of an hour, as part of separate OMRI scans. Physiological parameters recovered to normal values shortly after the first two scans of the rat.

7.7.5 Conclusion - Whole body imaging

The rat body probe we have presented in this section complements the rat head coil shown in earlier sections of this chapter. Combined, these two

⁵Consideration was also given to using pulsed DNP to reduce average SAR, as has been proposed in References [313–315]. We were, however, unable to reduce SAR via this technique, and would draw the reader's attention to subsequent work published in Ref. [316] that states for excitation of a single-line of a radical: “*cw*-pumping always gives a higher [Overhauser] enhancement”. We suggest that the reason for discrepancies between Ref. [316] and Ref. [315] is that assumptions made in calculating saturation of the EPR linewidth in Ref. [315] were not realistic.

probes will act as a platform for studying the whole body pharmacokinetics of TEMPOL without invasive dissection and histology. Such a platform will prove useful for our studies of ischemic stroke in a rat model and could also enable the *in vivo* imaging of alternative, longer-lived, Overhauser contrast agents such as nanodiamond.

Chapter 8

Conclusion

Biocompatible nanodiamonds are of much interest in biomedicine, having surfaces that are readily functionalized for targeted delivery of therapeutics and fluorescent centers that enable tracking in subcellular environments. The work presented in this thesis outlines the creation of two new modalities for imaging nanodiamonds with hyperpolarized MRI. The creation of these new modalities, based on dissolution DNP (d-DNP) and Overhauser-enhanced MRI (OMRI) extends the capabilities of nanodiamond as a theranostic probe, promising to enable nanodiamond as a vector for targeted drug delivery that can be tracked optically over subcellular lengthscales and noninvasively imaged on whole body scales with MRI. Such biomedical applications of nanodiamond will be determined by the minimum concentrations detectable with MRI, which is currently of order 1 mg mL^{-1} with both our imaging techniques in phantom experiments. Whilst this concentration is relatively high in a medical context, we note that it is also at the threshold of intratumoural concentrations that have been observed *in vivo* with targeted nanoparticles [317] and as such, we believe that, with expected future increases to imaging sensitivity, hyperpolarized MRI with nanodiamond will find applications in theranostics.

To increase the sensitivity of nanodiamond imaging with d-DNP, a new DNP probe is currently being constructed in our laboratory. This new DNP probe minimizes polarization losses by keeping the hyperpolarized nanodi-

amonds at magnetic fields of above 300 mT at all times during transfer between the polarizer and MRI scanner, and is likely to improve imaging sensitivity by more than an order of magnitude. We also believe that the long echo tails we observed in Chapter 4 could be leveraged for another order of magnitude improvement in sensitivity if new single-shot acquisition protocols based on the quadratic echo sequence are created [193]. Currently, there is also significant commercial interest in d-DNP due to its ability to detect tumours via ^{13}C metabolic imaging. This commercial interest saw the release of the SPINLab MRI Hyperpolarizer by GE in 2014 and has coincided with a dramatic expansion of research being conducted into d-DNP. The improvements in hardware and sequences that come from this research expansion are fully applicable to our nanodiamond imaging technique, and are expected to further improve the prospects for nanodiamond imaging with d-DNP.

The use of d-DNP for tracking of targeted nanodiamonds will also benefit from advances in materials science, such that the size of nanodiamonds suitable for hyperpolarized ^{13}C imaging can be reduced. In our work, we have found that the smaller nanodiamonds, most useful for *in vivo* targeting due to their long circulation times, have significantly reduced T_1 relaxation times, presumably due to higher concentrations of surface defects. Recent work on DNP of silicon nanoparticles suggests that the synthesis of small nanodiamonds, with defect concentrations optimized for long T_1 relaxation times, and large DNP enhancements, is possible [93,94]. Any development of materials should also consider the shape of nanodiamonds produced, as growing evidence suggests that spherical nanoparticles are significantly less toxic than those with jagged edges [318–320]. Alternative nanoparticles, beyond diamond and silicon, may also be useful for hyperpolarized MRI. One such nanoparticle candidate, also popular for fluorescence imaging, is nanoruby, with its 100% abundant ^{27}Al nuclei (see Appendix C for further discussion).

The results of hyperpolarization at nanoparticle surfaces we presented in Chapters 5 and 6 were completely unexpected at the beginning of this PhD work but, with the benefit of hindsight, perhaps this should not have been so. Reflecting on my own studies, and others, it seems to be a general result that a student working on spin physics in the core of nanoparticles

will find interesting phenomena at the nanoparticle surface [163, 321]. The reason for this is simple — as nanoparticles become smaller, their surface area to volume ratio increases dramatically and meanwhile, they often also lose the properties of bulk solids. This leads to experiments that are much more sensitive to surface phenomena than effects in the core. Looking for new physics in the core of a nanoparticle is an uphill battle, looking for new physics at a surface is the low hanging fruit.

Discovering these new hyperpolarized surface phenomena allowed us to establish OMRI as a new technique for nanoparticle imaging. A significant appeal of the OMRI technique lies in its simplicity, requiring inexpensive hardware, modest magnetic fields and no cryogenics. Further, unlike d-DNP, we have already demonstrated the efficacy of the OMRI technique for imaging nanodiamonds 18 nm in diameter, which is an ideal size for avoiding detection and clearance by the immune system. As our development of the platform in Chapter 7 suggests, we are looking to perform an *in vivo* demonstration of OMRI with nanodiamond in the near future. The sensitivity of nanodiamond imaging in these *in vivo* experiments will be improved over that seen in Chapter 6 due to our continuing efforts to improve the sensitivity of ultra-low field MRI (see Appendix D for details), with an upcoming scanner upgrade to reduce the gradient noise floor. We are also planning to introduce low noise cryocoils for an improved signal to noise ratio, in addition to undertaking nanodiamond surface modifications to increase the size of the Overhauser enhancement.

Over the timespan of this PhD work, hyperpolarized MRI with ^{13}C compounds has progressed from a preclinical research tool to a modality for cancer imaging in humans. Given continuing interest in nanoparticle tracking, we expect that similar progress will be made in hyperpolarized MRI of nanodiamonds, as improvements to materials, hardware and sequences that we have outlined here enable sensitivity to be increased by orders of magnitude. With such improvements, one day hyperpolarized MRI may be routinely used to see diamonds on the inside.

Appendix A

Home-built apparatus for X-band Hyperpolarization

The availability of DNP at magnetic fields above 1 T is limited by the expense of superconducting magnets, the cost of high-frequency microwave sources and the complexity of performing experiments at cryogenic temperatures. Lowering the magnetic field to below 1 T dramatically reduces the price of the hardware required to perform DNP. Whilst the drop in magnetic field brings a corresponding drop in NMR sensitivity, this can be compensated by the DNP signal enhancement. Further, at low magnetic fields, DNP is typically more efficient [63] and larger resonant magnetic fields can be used due to reduced electromagnetic absorption, potentially offsetting sensitivity reductions altogether. In this section we describe the design and construction of an inexpensive, homebuilt horn-reflector cavity built for DNP at room temperature and X-band microwave frequencies.

A.1 DNP Probe Design

In designing our X-band DNP probe we sought to maximize both the NMR sensitivity and the efficiency of coupling microwave power into the sample being hyperpolarized. We began our design process by considering various microwave cavity options, finding that whilst commercial EPR cavities and

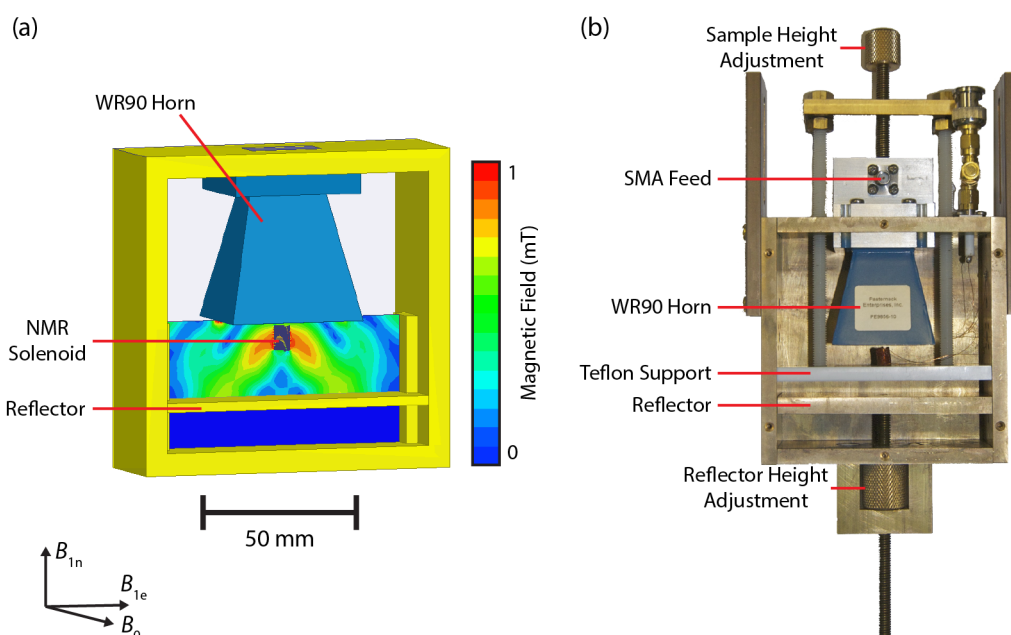


Figure A.1: **X-band Horn-Reflector Cavity.** (a) Simulations of B_{1e} field profile in our horn-reflector cavity with a 12 GHz excitation frequency. The NMR pickup coil profile is modeled as a conductive helix. The cavity was tuned to the mode shown by adjusting the reflector position. (b) Photograph of the horn-reflector cavity. Simulations were performed using Ansys HFSS.

dielectric resonators can generate very high B_{1e} fields, they are also notoriously difficult to tune as sample size increases [322]. Hence, we opted to design our DNP probe as a horn-reflector cavity, which allows DNP to be performed over a wide frequency range and for a variety of sample loadings [323–325]. In such a horn-reflector cavity, the horn antenna, a piece of flared metal waveguide that matches the impedance of the waveguide to that of free space, directs the microwaves into a beam that is reflected back at the sample by a microwave reflector. We designed our horn-reflector probe with an adjustable reflector position to allow movement of the cavity antinode to the sample position, as shown in the simulations in Fig. A.1a. The use of an NMR solenoid 5 mm in diameter, wound with gaps between turns equivalent to the wire width, allows the saturating microwave field (B_{1e}) to penetrate into the sample space. A photograph of the constructed horn-reflector cavity is shown in Fig. A.1b.

For experiments, the horn-reflector cavity was designed to insert between the poles of a watercooled electromagnet ($B_0 = 150\text{-}500$ mT, Model EM4-HVA, Lakeshore). Microwaves were generated with a USB controlled, 8-16 GHz source (Model LMS-163 Lab Brick, Vaunix) and fed through a high power (45 dB gain, 10 W maximum output), X-band microwave amplifier (Model QPJ-06184045, Quinstar Technology). To perform NMR, a Spincore NMR System (ispin-NMR-mini) was used in combination with a TOMCO Power Amplifier (BTM00250-AlphaS) and a homebuilt transmit-receive switch.

A.2 Probe Performance

The readily available, stable free radical TEMPO is commonly used in aqueous solutions to test the efficiency of DNP platforms. In Fig. A.2, we present DNP data acquired in our horn-reflector probe of a 15 mM TEMPO sample in a conventional 5 mm NMR tube. In Fig. A.2a we see that at 40 dBm of applied microwave power, absolute ^1H NMR enhancements of almost 10 times can be achieved in the TEMPO sample. Simulations of our cavity showed an expected B_{1e} field of 50 μT at the sample with the maximum 10 W power from our amplifier. We expect this B_{1e} field to change with sample loading. We also note that our DNP platform was also tested with a commercial Bruker TM₁₁₀ Electron Nuclear Double Resonance (ENDOR) cavity in the place of the horn-reflector probe. This commercial cavity displayed ^1H enhancements of up to 30 times but the sample volume had to be restricted to $\sim 5\%$ of the volume in our horn-reflector probe for matching, reducing NMR sensitivity by 20 times.

Turning to the NMR signals shown in Fig. A.2b, we see that our ^1H linewidth is ~ 10 kHz due to inhomogeneity of the B_0 provided by the electromagnet. This linewidth corresponds to a fractional inhomogeneity in the magnet of 500 ppm (parts per million), orders of magnitude larger than the sub-ppm inhomogeneities observed in superconducting NMR magnets. Whilst such a broad linewidth reduces NMR sensitivity, this is offset by the high fill factor of the solenoidal NMR coil used. Next, we turn to demon-

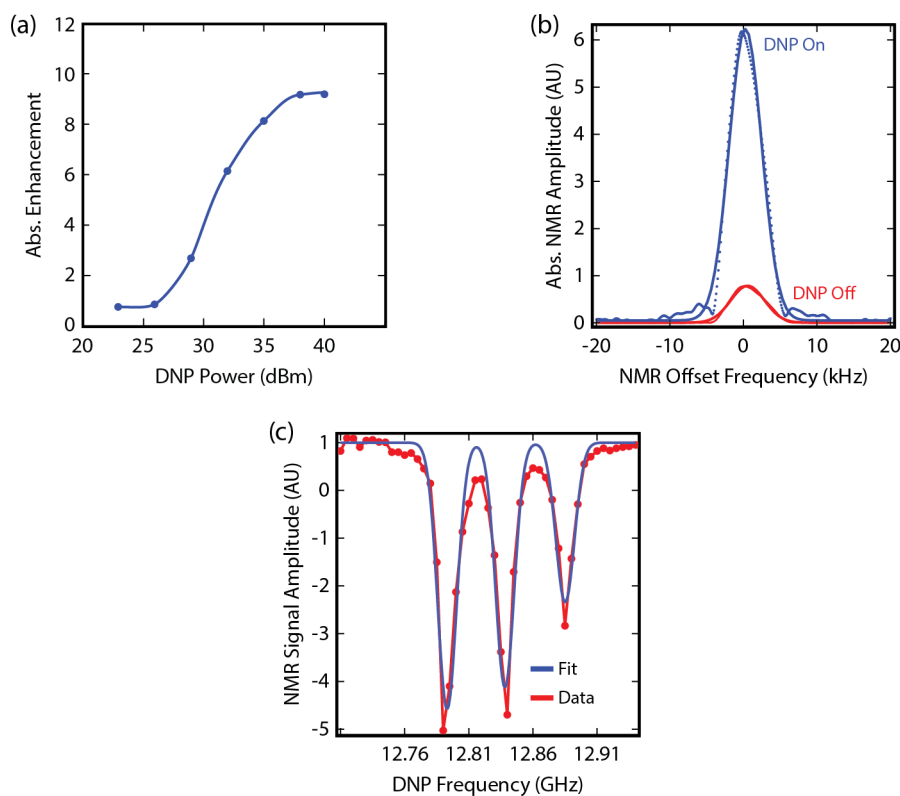


Figure A.2: **Enhancement of TEMPO solution in the horn-reflector cavity.** (a) Enhancement of the ^1H signal for various powers applied to the horn-reflector cavity. Enhancement was calculated by dividing the absolute signal magnitude of an FID acquired after 1 s of DNP at 12.79 GHz by the thermally polarized signal. Solid line is a guide to the eye. DNP was restricted to 1 s as the sample began to boil after this time when microwaves were applied at maximum power. (b) The ^1H NMR signal from a 15 mM aqueous solution of TEMPO was measured with a $\pi/2$ pulse at 450 mT. The ^1H signal from thermal polarization is shown in red. The absolute value of the hyperpolarized ^1H signal acquired after 1.5 W of power was applied at 12.79 GHz to the horn-reflector cavity for 1 s is shown in blue. (c) ^1H NMR signal of a 15 mM TEMPO solution after 1 s of microwave saturation versus DNP frequency. Signals are normalised to a thermally polarized NMR signal. Fit is the sum of three Lorentzian curves separated in frequency by 50 MHz steps.

strate the wide bandwidth of the horn-reflector cavity, showing that all three hyperfine line of the TEMPO radical are readily visible in a microwave frequency sweep across 250 MHz, as shown in Fig. A.2c. We note that as Overhauser enhancement with TEMPO occurs via dipolar coupling, the ^1H signal is enhanced with negative polarization.

A.3 Conclusion

We have developed an inexpensive horn-reflector probe for hyperpolarizing samples at room temperature. This probe was used successfully to acquire all the DNP data shown in Chapter 5. Whilst improvements must be made to the homogeneity of the external magnetic field for this probe to reach its full potential, its robustness to sample loading and wide bandwidth will make it useful for investigation of DNP phenomena into the future.

Appendix B

^1H MRI of of Nanodiamond Solutions at 7 T

Many approaches to nanodiamond (ND) imaging are based on spin-echo ^1H MRI techniques. In these techniques, as was discussed in Section 2.6.1, conventional T_1 or T_2 contrast agents are grafted to the ND surface [118, 120], enabling tracking of the nanodiamond in biological environments via its impact on the spin relaxation times of surrounding ^1H nuclei. Whilst these grafting techniques are effective for nanodiamond imaging, the toxicity of conventional MRI contrast agents such a gadolinium is of concern for future applications in the clinic. In this section we show that, for suitably small nanodiamonds in aqueous solution, the bare ND surface reduces ^1H relaxation times sufficiently to enable imaging of nanodiamond via spin-echo techniques at 7 T without the introduction of additional contrast agents.

Contrast in spin-echo ^1H MRI arises from the differences in proton density and spin-relaxation times between tissues. Assuming other parameters are held constant, tissues with long T_2 will give a relatively large signal in spin-echo MRI, as there is little signal decay during the echo time T_E (see Fig B.1). Meanwhile, for sufficiently short repetition time T_R , tissues with long T_1 will give a relatively small signal, as the ^1H nuclei do not have enough time to fully polarize between acquisition of sequential lines of k -space. Proper adjustment of the spin-echo sequence parameters T_E/T_R thus allows us to

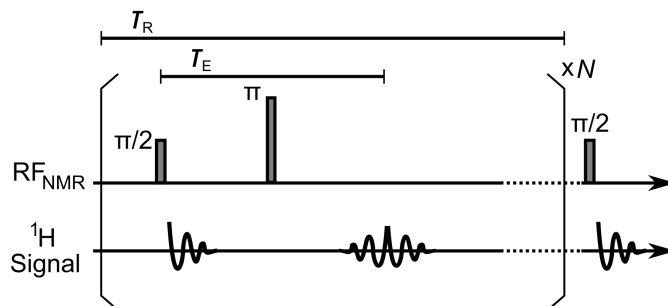


Figure B.1: **Timing Parameters in Spin-Echo Imaging.** During a spin echo MRI acquisition, N lines of k -space must be acquired to reconstruct an $N \times N$ resolution image, each with a different magnitude of phase-encoding gradient. The echo time T_E represents the time between the initial $\pi/2$ NMR pulse and the peak in the refocused signal for each spin-echo acquisition. The repetition time T_R is the delay between subsequent k -space acquisitions and represents the time period over which spin-lattice relaxation mediated recovery of polarization can occur.

take ^1H MRI scans where the signal is T_1 -weighted (long T_1 - dark) or T_2 -weighted (long T_2 - bright) [56].

We find that adding untreated high-pressure, high-temperature (HPHT) NDs to deionized water reduces the spin-lattice relaxation times of ^1H nuclei at 7 T, as shown in Fig. B.2. Presumably, ^1H nuclei in solution are rapidly relaxed when they come in close proximity to electronic defects on the ND surface, as we found to be the case at 6.5 mT in Section 6.3.1. This would also explain why the T_1 shortening effect is more pronounced for the smaller NDs that have a higher surface area to volume ratio and resulting higher effective concentration of surface defects in solution.

Having established that nanodiamond has an effect on the proton T_1 of aqueous solutions, we turn to image the phantom shown in Fig. B.3a in our 7 T microimager. A T_1 -weighted image of the phantom is shown in Fig. B.3b. As expected, the highest concentration 18 nm ND sample, which has the shortest T_1 relaxation time, appears brightest, with a signal intensity approximately 10 times that seen in the deionized water. A T_2 -weighted image of the same phantom is shown in Fig. B.3c. Interpreting the signal intensities in this T_2 -image is complex, as the T_R time of 2 s is insufficiently

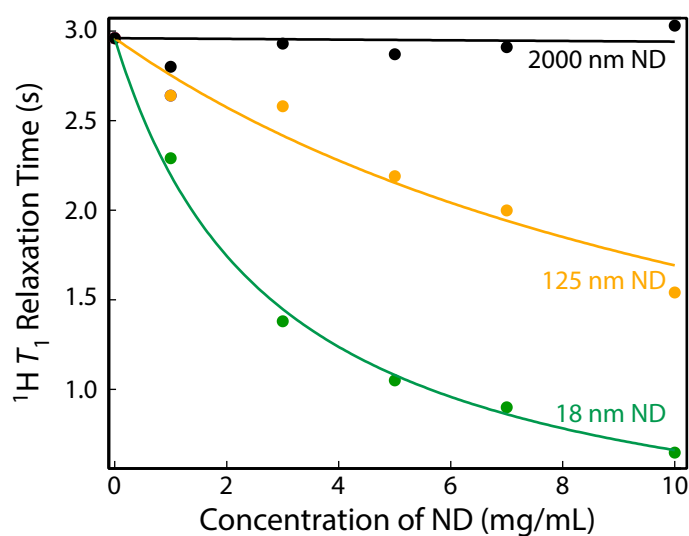


Figure B.2: ^1H spin-lattice relaxation of aqueous nanodiamond solutions. The T_1 of ^1H nuclei in aqueous nanodiamond solutions was measured as a function of concentration at 7 T via inversion recovery techniques. Data is shown for solutions of HPHT 18 nm (green), HPHT 125 nm (yellow) and HPHT 2000 nm (black) nanodiamonds in deionized water. Solid lines are fits to the relaxivity equation (see Eqn. 6.3), with relaxivity values for individual curves being $0.12 \text{ mg}^{-1}\text{mL}^{-1}\text{s}^{-1}$ (18 nm), $0.023 \text{ mg}^{-1}\text{mL}^{-1}\text{s}^{-1}$ (125 nm) and $0.0021 \text{ mg}^{-1}\text{mL}^{-1}\text{s}^{-1}$ (2000 nm). All data in this figure is reproduced from Ref. [321].

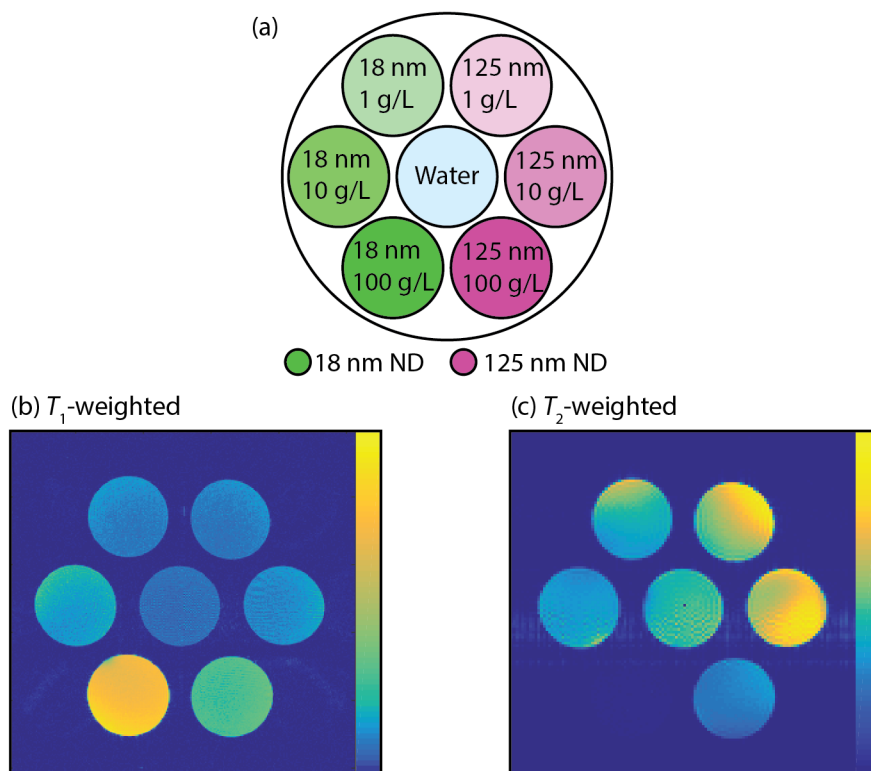


Figure B.3: **Spin-echo imaging of nanodiamond solutions at 7 T.** (a) Phantom Schematic showing the location of 2 mL vials of deionized water (blue), HPHT 18 nm NDs (green) and HPHT 125 nm NDs (pink). (b) T_1 weighted image acquired with $T_E/T_R = 20/100$ ms, 100 averages, a resolution of 256×256 and a slice thickness of 1 mm. (c) T_2 weighted image acquired with $T_E/T_R = 250/2000$ ms, 1 average, a resolution of 128×128 and a slice thickness of 1 mm. The field of view in both images is $40 \text{ mm} \times 40 \text{ mm}$.

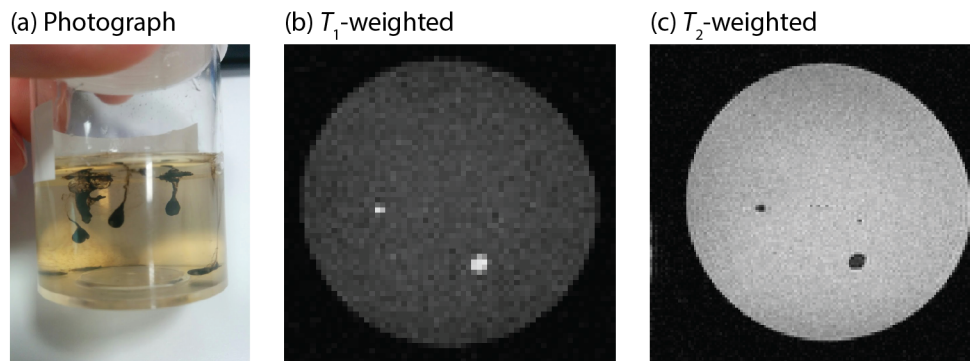


Figure B.4: **Spin-echo imaging of a nanodiamond-gelatine phantom.** (a) Photograph of nanodiamond-gelatine phantom. (b) T_1 weighted image acquired with $T_E/T_R = 13/70$ ms, 20 averages, a resolution of 64×64 and a slice thickness of 0.5 mm. (c) T_2 weighted image acquired with $T_E/T_R = 120/2000$ ms, 1 average, a resolution of 128×128 and a slice thickness of 0.5 mm. The field of view in both images is $45 \text{ mm} \times 45 \text{ mm}$.

long to allow all ^1H nuclei to fully polarize between acquisitions (T_1 in the deionized water sample is ~ 3 s). As such, the highest concentration ND samples, with short T_2 , appear darker than the water sample but the low concentration 125 nm ND solutions appear brighter than the water sample due to their shorter T_1 .

Now that we have shown how spin-echo MRI can be used to create ^1H contrast between ND solutions, we turn to demonstrate the technique in more realistic gelatin-based phantoms. Gelatin is commonly used to simulate soft tissue in MRI phantoms due to its low cost, widespread availability and ease of use. The gelatin phantom shown in Fig. B.4a was made by mixing McKenzie's gelatin powder into hot water at 75 mg/mL. HPHT 18 nm NDs were then mixed into a portion of the gelatin mixture at 50 mg/mL. The 'tadpole' shaped drops of black ND-gelatin-water mixture were dripped into the gelatin-water mixture as it cooled. Subsequent T_1 -weighted and T_2 -weighted imaging of the phantom, as shown in Figs. B.4b and B.4c respectively, demonstrates clear ^1H MRI contrast due to the presence of ND. Next, we repeat this experiment in a setting more relevant to preclinical environments, imaging ND in a rat brain phantom, a 3D rendering of which is shown in Fig. B.5a. This phantom was created by filling a 3D-printed,

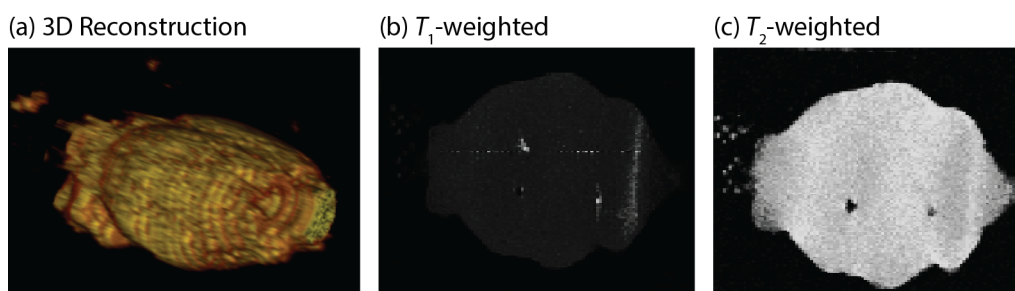


Figure B.5: **Imaging of nanodiamond inside a rat brain phantom.** (a) 3D rendering of the rat brain phantom, as reconstructed from a high-resolution 3D gradient-echo sequence. (b) T_1 weighted image acquired with $T_E/T_R = 13/100$ ms, 40 averages, a resolution of 256×256 and a slice thickness of 1 mm. (c) T_2 weighted image acquired with $T_E/T_R = 100/1000$ ms, 1 average, a resolution of 128×128 and a slice thickness of 1 mm. The field of view in both images is $40 \text{ mm} \times 25 \text{ mm}$. The 3D-printed rat brain phantom was supplied courtesy of Will Ryder.

plastic rat brain cast with ND and gelatin mixture as already described.¹ Again, ND was detected with clear contrast in T_1 -weighted and T_2 -weighted images shown in Figs. B.5b and B.5c respectively.

The results presented in this section demonstrate that ND can be imaged with conventional ^1H MRI techniques. Whilst the relaxivity of ND is relatively low compared to that observed for heavy metal ions such as gadolinium [117], it is likely that the relaxivity at 7 T would be increased by air-oxidation of the NDs, as we observed at 6.5 mT in Section 6.3.1. Such NDs with surfaces treated for high-relaxivity could prove useful for ^1H MRI co-registration of NDs in hyperpolarized ^{13}C imaging studies.

¹Rat brain cast was designed and 3D printed by Will Ryder.

Appendix C

Spin-Relaxation Properties of Ruby Microparticles

Beyond diamond and silicon, another potential nanoparticle candidate for hyperpolarized MRI is ruby ($\text{Al}_2\text{O}_3:\text{Cr}^{3+}$). Ruby's suitability for hyperpolarized MRI stems from its 100% abundant, spin-5/2 ^{27}Al nuclei that can be hyperpolarized via cryogenic DNP with substitutional Cr^{3+} ions [326, 327]. In this section, we present data from our initial NMR investigations into ruby for hyperpolarized MRI applications.

We begin our NMR investigation of ruby by measuring the T_1 of ^{27}Al in 45 μm ruby particles with an inversion recovery experiment (see data in Fig. C.1a). To fit the inversion recovery data, we use a two component double exponential fit given by:

$$\text{Signal} = 1 - ae^{-\frac{t}{T_{1,\text{short}}}} - be^{-\frac{t}{T_{1,\text{long}}}} \quad (\text{C.1})$$

Where $T_{1,\text{short}}$ and $T_{1,\text{long}}$ are the spin-lattice relaxation times of short and long fit components respectively and the parameters a/b reflect the relative magnitudes of the components. From this fit, we find that the ruby microparticles have a long T_1 component of 627 ms, which is similar to T_1 values reported elsewhere for bulk ruby [328].

Next, we turn to investigate the spin-spin relaxation times of our ruby microparticles in a Hahn-echo experiment (see data in Fig. C.1b). To fit the

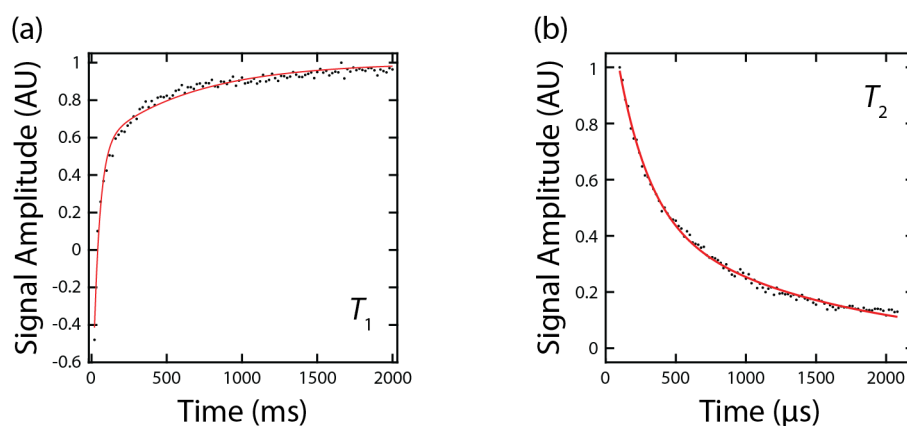


Figure C.1: **Spin relaxation in Ruby particles.** (a) Inversion recovery was used to measure T_1 . Data points (black) are fit by Eq. C.1 (red line). Fit parameters are $a = 1.60 \pm 0.15$, $T_{1,\text{short}} = 41 \pm 5$ ms, $b = 0.45 \pm 0.04$ and $T_{1,\text{long}} = 627 \pm 57$ ms. (b) Hahn-echo was used to measure T_2 . Data points (black) are fit by Eq. C.2 (red line). Fit parameters are $c = 0.81 \pm 0.04$, $T_{2,\text{short}} = 220 \pm 24$ μ s, $d = 0.51 \pm 0.05$ and $T_{2,\text{long}} = 1377 \pm 117$ μ s. Synthetic 45 μ m ruby particles (Cr_2O_3 content: 0.1%) were sourced in powder form from Goodfellow for these experiments. NMR experiments were conducted in a wide bore 2.88 T magnet, where the central ^{27}Al resonance was at 32.0419 MHz, with NMR pulses 10 μ s in length at 293 K.

Hahn-echo data data, we use a two component double exponential fit given by:

$$\text{Signal} = ce^{-\frac{t}{T_{2,\text{short}}}} + de^{-\frac{t}{T_{2,\text{long}}}} \quad (\text{C.2})$$

Where $T_{2,\text{short}}$ and $T_{2,\text{long}}$ are the spin-spin relaxation times of short and long fit components respectively and the parameters c/d reflect the relative magnitudes of the components. From this fit, we find that the ruby microparticles have a long T_2 component of 1.4 ms, which is similar to the ^{13}C T_2 of the NDs we imaged with hyperpolarized ^{13}C MRI in Chapter 4.

The T_1 and T_2 value presented in this section have been measured only for the ^{27}Al : $-\frac{1}{2} \leftrightarrow \frac{1}{2}$ transition, as only the central component of the extremely broad ruby NMR line was accessible in the liquids probe used for the experiment [329]. We further note, that given the spin-5/2 characteristic of ^{27}Al and the powder nature of ruby nanoparticles, it is unlikely that the NMR sensitivity would be high enough to measure signals resulting from transitions between other states with thermal polarization alone at room temperature.

Whilst the T_1 of ^{27}Al in ruby appears too short for imaging with dissolution DNP techniques, the ability to shorten T_1 by increasing Cr^{3+} content raises the prospect of imaging nanoruby with similar techniques to that used for MRI of short- T_1 ^{19}F compounds (described in Section 2.1.1). Further, we have recently gained access to a wideline NMR probe and a microwave source with sufficient bandwidth to saturate the EPR transitions of Cr^{3+} ($g \sim 1.98$) [330]. We look forward to exploring the possibilities for nanoruby in the field of hyperpolarized MRI.

Appendix D

Coil Development for Low-Cost High-Performance MRI

MRI is unparalleled in its ability to visualize soft tissue with high-resolution and high-contrast in a clinical setting. However, access to MRI is limited by its high costs. Contemporary MRI scanners cost in excess of one million dollars per tesla of magnetic field strength and require regular supply of expensive liquid helium to maintain the superconducting magnet. Further, applications of MRI are limited by siting requirements, with reinforced, shielded rooms required to hold scanners weighing many tonnes.

One approach to increasing the availability of MRI is to use ultra low field (ULF, < 10 mT) magnets [331]. Such ULF magnets can be constructed at a fraction of the price and weight of superconducting magnets [172]. However, performing MRI at ULF means accepting a drastic reduction in signal-to-noise ratio (SNR) due to smaller ^1H polarizations and a reduction in the electromotive force induced in detection coils at low frequency. In MRI, as with any imaging technique, there is a minimum quantity of material that is required to generate a signal larger than sources of background noise. Maximizing SNR is thus important to increasing resolution and ultimately, enabling clinically useful information to be acquired in an ULF MRI scan [332].

In this section, we outline our design of a high sensitivity coil for human

head imaging at ULF. We then explain why high efficiency sequences such as balanced steady-state free precession (bSSFP) are well suited to ULF and how they can compensate for reduced SNR. We conclude this section with results from human head imaging experiments at ULF.¹

D.1 Coil Design

Here, we describe how we maximize the SNR of our human head coil. We define the instantaneous signal in an MRI scan as the voltage induced across the end of a pickup coil by precessing nuclear spins. Meanwhile, the noise voltage, measured across the ends of the pickup coil, arises from three fundamental sources: coil noise, body noise and receiver noise [55].

We begin our description of human head coil design by reducing the problem to optimization of two parameters: η the fill factor and the Q -factor.

D.1.1 Noise in ULF MRI

In conventional MRI scanners, which operate at fields above 1 T, the largest contribution to noise is typically body noise [333]. Body noise results from inductive coupling to the detection coil of tiny currents generated by brownian motion of electrolytes in the body [170]. However, as inductive body noise scales as ω_0^2 [56], at ULF we move to a unique regime where the dominant source of noise is from the detection coil itself.

Noise in the pickup coil is Johnson noise, arising from thermal agitation of charge carriers and giving a noise voltage:

$$V_N = \sqrt{4k_B T r \delta f} \quad (\text{D.1})$$

where k_B is the Boltzmann constant, T is the temperature, r is the resistance of the pickup coil and δf is the frequency bandwidth over which the noise is measured.

¹This section contains material adapted from M. Sarracanie, C. D. LaPierre, N. Salameh, D. E. J. Waddington, T. Witzel and M. S. Rosen, Low-Cost High-Performance MRI. *Sci. Rep.*, **5**, 15177 (2015).

To minimize coil resistance r , and hence V_N , at our design frequency of 276 kHz we construct coils with 40/38 Litz wire, which is 1 mm thick wire made of 40 individual 100 μm insulated wire strands. At 276 kHz, copper wire carries electric current down to a skin depth of 124 μm . Hence, at 276 kHz, 40/38 Litz wire has minimal resistance as electric current is carried through the entire width of the conductor's individual strands.

D.1.2 Signal and SNR

The voltage δV_S induced across the ends of a detection coil, immediately after a $\pi/2$ pulse, by ^1H nuclei precessing in an elementary volume of magnetization δV_e is:

$$\delta V_S = \frac{B_1}{I_0} N_0 \frac{\gamma_{\text{H}}^3 \hbar^2}{2k_B T} B_0^2 (\sin \theta) \delta V_e \quad (\text{D.2})$$

Where B_1 is the magnetic field in the rotating frame, I_0 is the current induced in the coil, γ_{H} is the gyromagnetic ratio of ^1H nuclei and N_0 is the number of nuclei per unit volume [170]. Comparing equations D.1 and D.2, we find the following relation for SNR:

$$\text{SNR} \propto \frac{B_1}{I_0 r} \quad (\text{D.3})$$

Which, following Ref. [170], can be replaced by:

$$\text{SNR} \propto \sqrt{\eta Q} \quad (\text{D.4})$$

where η is the filling factor of the coil and Q is the Q -factor. Maximizing these two parameters maximizes the coil SNR.

D.1.3 Coil Geometry

Maximizing η is a coil geometry challenge. For our coil we 3D printed a close fitting former for the head, as shown in Fig. D.1. Grooves were printed to allow easy winding of an archimedean spiral for uniform coverage of the

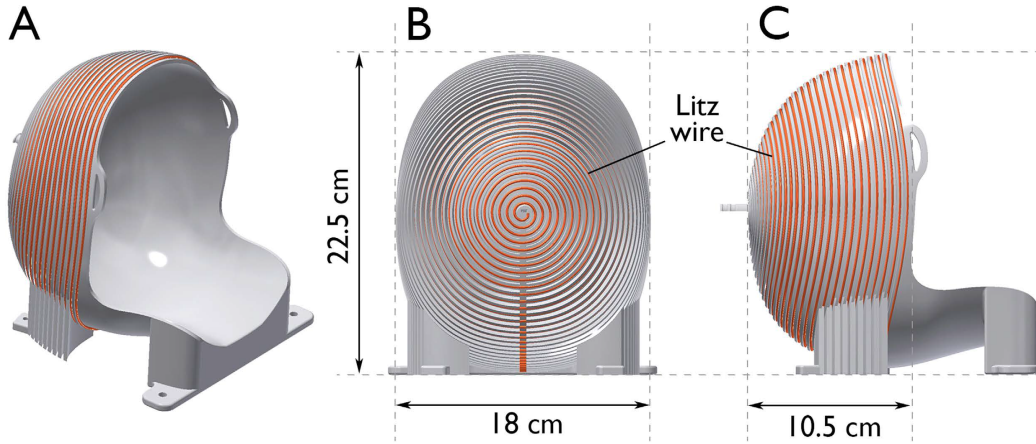


Figure D.1: **3D rendering of the single channel head coil for imaging at ULF.** (a) Isometric, (b) back and (c) side views are shown. Reproduced from [256].

region to be imaged with a single NMR channel.

D.1.4 Q-factor

Increasing the Q -factor of an NMR coil at ULF requires sacrifice of imaging bandwidth, as was described in detail in Section 7.3.2. For the geometry of our ULF head coil, we require Δf (see Fig. D.2a) to be a minimum of 9.5 kHz for sensitivity across the head. This corresponds to a target $Q = f/\Delta f_{\min}$ of 29.

Assuming extremely high quality factors for tuning capacitors, the Q -factor of a loaded radiofrequency probe, coupled to 50Ω via a series-match, parallel-tune, coupling network is given by:

$$Q = \frac{\omega_0 L}{2r} \quad (\text{D.5})$$

where L is the inductance of the coil.

To find the L of our head coil we performed inductance simulations with the Biot Savart application (Ripplon Software Inc). Our head coil was modeled as a spiral of N turns on the surface of half an ellipsoid as shown in Fig. D.2b. Simulations of a 16 turn head coil gave $L = 23 \mu\text{H}$ for a predicted Q

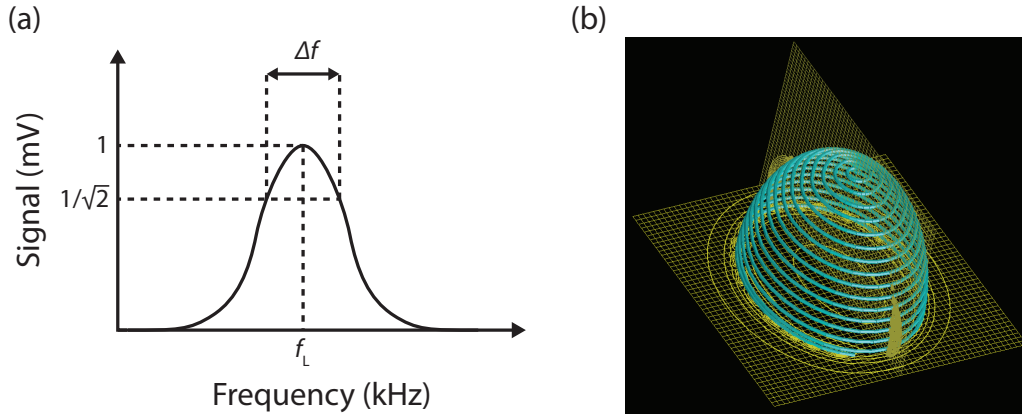


Figure D.2: **Coil design in ULF MRI.** (a) The head coil is tuned to resonate at 276 kHz, which is the Larmor frequency f_L of ^1H at 6.5 mT. The bandwidth Δf of the coil is designed to be approximately equal to the expected frequency spread across the field of view, thus ensuring uniform sensitivity across the head. (b) Biot Savart simulations of the magnetic field and inductance of the archimedean spiral conductor used to simulate the head coil. Turns of copper are shown in blue and magnetic field contours are shown in yellow.

of 58 at 276 kHz, where the resistance of the Litz wire is calculated to be 0.06Ω per metre of wire used.² On construction of an $N = 16$ turn head coil we measured its inductance to be $30 \mu\text{H}$, close to the simulated inductance of $23 \mu\text{H}$. Despite, the accuracy of the inductance simulations, the Q of the constructed 16 turn head coil was only 20, two-thirds of the target. Presumably this difference in Q between simulations and experiment is due to coil resistance being higher than expected as a result of the proximity effect. To compensate for the unexpected resistance, N was increased to 30 in simulations, increasing the predicted L to $75 \mu\text{H}$. The final head coil construction, shown in Fig. D.1 is a 30-turn archimedean spiral and has a Q of ~ 30 .

²Note that the total length of wire used in constructing an NMR coil should be less than $\lambda/20$ to prevent canceling of signal induced at different phases in the pickup coil [55]. Luckily, obeying this condition at 276 kHz, where $\lambda = 1.1 \text{ km}$, is not hard.

D.2 Imaging Sequences at ULF

To acquire images at ULF we use 3D balanced-steady state free precession (bSSFP) techniques. Originally introduced as technique for maximizing SNR in NMR [334], bSSFP dynamically refocuses spins, eliminating the need to wait for T_1 recovery. As a result, bSSFP MRI has the highest SNR per unit time of all imaging sequences [257].

A drawback of bSSFP MRI is its sensitivity to the amount of spin dephasing that occurs, due to magnetic field inhomogeneities, between consecutive RF pulses. However, at ULF, the fractional homogeneity requirement for bSSFP is three orders of magnitude lower than in a conventional MRI scanner, allowing acquisition with a relatively long $T_R = 22.5$ ms.

Given its already high SNR and the requirement of high absolute magnetic field homogeneity, easily satisfied at ULF, bSSFP is well suited to help overcome the low SNR inherent to ULF MRI.

D.3 Human Imaging

After design and construction, the head coil was incorporated into the imaging platform we described in Chapter 7. Images were acquired in humans, as shown in Fig. D.3, with SNR values of 15, 21 and 16 measured in axial, coronal and sagittal orientations respectively. The sinuses, as well as the skull, are easily recognizable as black features in all images. Surrounding the brain, we can identify the dura in bright grey on the coronal and sagittal images (Fig. D.3(b,c)). In the brain, the two hemispheres and the cerebellum are distinct, and cortical tissue can be distinguished from white matter. A slight reduction in signal intensity can be seen at the extreme edges of some images due to the restricted bandwidth of the imaging probe.

D.4 Conclusion

The images presented here were acquired with the highest SNR per unit time achieved in ULF MRI to date. The sensitivity improvements are due

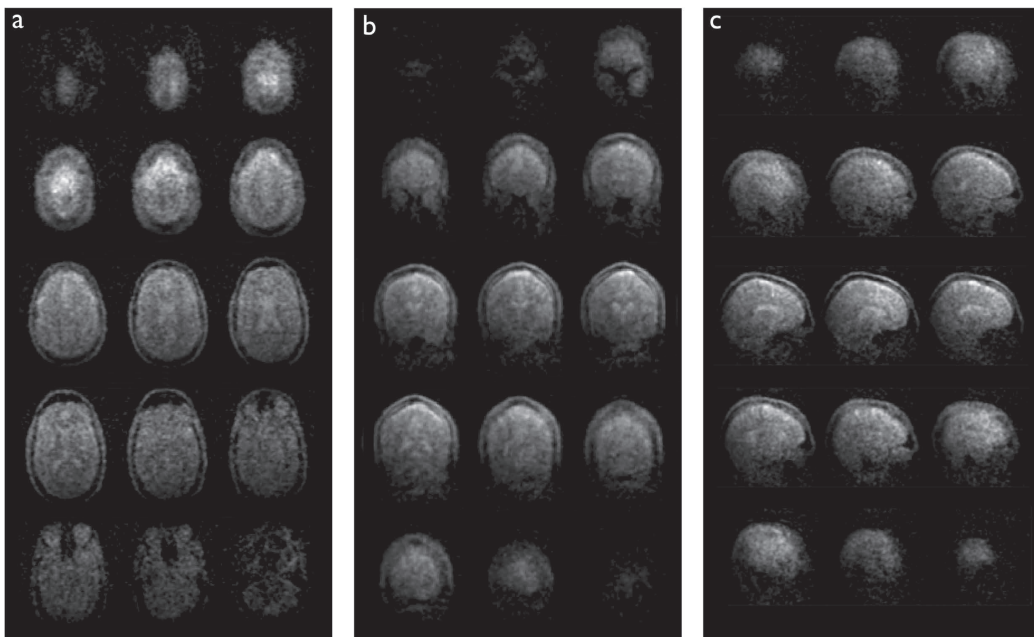


Figure D.3: **3D images of the human head.** Images are shown for (a) axial, (b) coronal and (c) sagittal orientations. Matrix size: $64 \times 75 \times 15$, voxel size: **a** - $2.5 \times 3.5 \times 8.5 \text{ mm}^3$, **b** - $2.5 \times 3.5 \times 11.5 \text{ mm}^3$ and **c** - $2.5 \times 3.5 \times 14.4 \text{ mm}^3$. Each dataset acquired in 6 min. Reproduced from [256].

to the combined application of a custom detection coil and high-efficiency bSSFP acquisition strategies. ULF MRI scanners such as this one could be constructed for \$50k and provide useful clinical information in situations where conventional MRI scanners are impractical or unavailable.

Next steps to increase the sensitivity of the detection coil would be to design a probe with active loading [335] that operates at low temperatures. Conventional low temperature ‘cryocoils’ are not popular in ULF MRI for the added complexity they involve. As a partial solution, we propose that an ultra high- Q coil could be wound for operation at room temperature and then resistively broadened via an external resistor that sits in a cryogenic bath separate to the patient bed. An SNR increase as high as a factor of 9 for liquid helium, or 2 for liquid nitrogen, could be expected in such a scenario.

References

- [1] Xie, J., Lee, S. & Chen, X. Nanoparticle-based theranostic agents. *Adv Drug Deliv Rev* **62**, 1064–1079 (2010).
- [2] Jokerst, J. V., Lobovkina, T., Zare, R. N. & Gambhir, S. S. Nanoparticle PEGylation for imaging and therapy. *Nanomedicine (Lond.)* **6**, 715–728 (2011).
- [3] Rosen, J. E., Chan, L., Shieh, D.-B. & Gu, F. X. Iron oxide nanoparticles for targeted cancer imaging and diagnostics. *Nanomedicine NBM* **8**, 275–90 (2012).
- [4] Couvreur, P. Nanoparticles in drug delivery: Past, present and future. *Adv Drug Deliv Rev* **65**, 21–23 (2013).
- [5] Steichen, S. D., Caldorera-Moore, M. & Peppas, N. A. A review of current nanoparticle and targeting moieties for the delivery of cancer therapeutics. *Eur J Pharm Sci* **48**, 416–427 (2013).
- [6] Smith, B. R. & Gambhir, S. S. Nanomaterials for In Vivo Imaging. *Chem Rev* **117**, 901–986 (2017).
- [7] Pelaz, B. *et al.* Diverse Applications of Nanomedicine. *ACS Nano* **11**, 2313–2381 (2017).
- [8] Chow, E. K.-H. & Ho, D. Cancer Nanomedicine: From Drug Delivery to Imaging. *Sci Transl Med* **5**, 216rv4 (2013).
- [9] Weissleder, R., Nahrendorf, M. & Pittet, M. J. Imaging macrophages with nanoparticles. *Nat Mater* **13**, 125–138 (2014).

- [10] Hahn, M. A., Singh, A. K., Sharma, P., Brown, S. C. & Moudgil, B. M. Nanoparticles as contrast agents for in-vivo bioimaging: Current status and future perspectives. *Anal Bioanal Chem* **399**, 3–27 (2011).
- [11] Le Trequesser, Q., Seznec, H. & Delville, M. H. Functionalized nanomaterials: Their use as contrast agents in bioimaging: Mono-and multimodal approaches. *Nanotechnol Rev* **2**, 125–169 (2013).
- [12] Estelrich, J., Sanchez-Martin, M. J. & Busquets, M. A. Nanoparticles in magnetic resonance imaging: from simple to dual contrast agents. *Int J Nanomedicine* **10**, 1727–1741 (2015).
- [13] Hitchens, T. K. *et al.* ^{19}F MRI detection of acute allograft rejection with in vivo perfluorocarbon labeling of immune cells. *Magn Reson Med* **65**, 1144–1153 (2011).
- [14] Balducci, A. *et al.* A novel probe for the non-invasive detection of tumor-associated inflammation. *Oncoimmunology* **2**, e23034 (2013).
- [15] Kislukhin, A. A. *et al.* Paramagnetic fluorinated nanoemulsions for sensitive cellular fluorine-19 magnetic resonance imaging. *Nat Mater* **15**, 662–668 (2016).
- [16] Cassidy, M. C., Chan, H. R., Ross, B. D., Bhattacharya, P. K. & Marcus, C. M. *In vivo* magnetic resonance imaging of hyperpolarized silicon particles. *Nat Nanotechnol* **8**, 363–368 (2013).
- [17] Zhu, B. *et al.* Selective magnetic resonance imaging of magnetic nanoparticles by acoustically induced rotary saturation. *Magn Reson Med* **75**, 97–106 (2016).
- [18] Xie, J. *et al.* Ultra-Small c(RGDyK)-coated Fe_3O_4 Nanoparticles and Their Specific Targeting to Integrin $\alpha_v\beta_3$ -Rich Tumor Cells. *J Am Chem Soc* 7542–7543 (2008).
- [19] Boiteau, R., Major, J. & Meade, T. Gadolinium-Labeled Nanoparticles for Magnetic Resonance Imaging. *Nanoscape* **5**, 33–39 (2008).
- [20] Ananta, J. S. *et al.* contrast agents in nanoporous particles enhances. *Nat Nanotechnol* **5**, 815–821 (2010).

- [21] Ghaghada, K. B., Ravoori, M., Sabapathy, D., Bankson, J. & Kundra, V. New Dual Mode Gadolinium Nanoparticle Contrast Agent for Magnetic Resonance Imaging. *PLoS One* **4**, e7628 (2009).
- [22] Tóth, É., Helm, L. & Merbach, A. E. Relaxivity of MRI Contrast Agents. *Top Curr Chem* **221**, 61–101 (2002).
- [23] Semelka, R. C., Ramalho, M., AlObaidy, M. & Ramalho, J. Gadolinium in humans: A family of disorders. *Am J Roentgenol* **207**, 229–233 (2016).
- [24] Korkusuz, H. *et al.* Transferrin-coated gadolinium nanoparticles as MRI contrast agent. *Mol Imaging Biol* **15**, 148–154 (2013).
- [25] Evbuomwan, O. M., Merritt, M. E., Kiefer, G. E. & Sherry, A. D. Nanoparticle-based PARACEST agents: the quenching effect of silica nanoparticles on the CEST signal from surface-conjugated chelates. *Contrast Media Mol Imaging* **7**, 19–25 (2012).
- [26] Wu, B. *et al.* An overview of CEST MRI for non-MR physicists. *EJNMMI Phys* **3**, 19 (2016).
- [27] Ali, M. M. *et al.* A nano-sized PARACEST-fluorescence imaging contrast agent facilitates and validates *in vivo* CEST MRI detection of glioma. *Nanomedicine (Lond.)* **7**, 1827–37 (2012).
- [28] Cormode, D. P., Naha, P. C. & Fayad, Z. A. Nanoparticle contrast agents for computed tomography: A focus on micelles. *Contrast Media Mol Imaging* **9**, 37–52 (2014).
- [29] Ashton, J. R., West, J. L., Badea, C. T. & Badea, C. T. In vivo small animal micro-CT using nanoparticle contrast agents. *Front Pharmacol* **6**, 256 (2015).
- [30] Torchilin, V. P., Frank-Kamenetsky, M. D. & Wolf, G. L. CT visualization of blood pool in rats by using long-circulating, iodine-containing micelles. *Acad Radiol* **6**, 61–65 (1999).
- [31] Barnett, B. P. *et al.* Radiopaque alginate microcapsules for X-ray visualization and immunoprotection of cellular therapeutics. *Mol Pharm* **3**, 531–538 (2006).

- [32] Popovtzer, R. *et al.* Targeted Gold Nanoparticles Enable Molecular CT Imaging of Cancer. *Nano Lett* **8**, 4593–4596 (2008).
- [33] Cormode, D. P. *et al.* Atherosclerotic Plaque Composition: Analysis with Multicolor CT and Targeted Gold Nanoparticles. *Radiology* **256**, 774–782 (2010).
- [34] Wolfbeis, O. S. An overview of nanoparticles commonly used in fluorescent bioimaging. *Chem Soc Rev* **44**, 4743–4768 (2015).
- [35] Skajaa, T. *et al.* Quantum dot and Cy5.5 labeled nanoparticles to investigate lipoprotein biointeractions via Förster resonance energy transfer. *Nano Lett* **10**, 5131–5138 (2010).
- [36] Ruedas-Rama, M. J., Walters, J. D., Orte, A. & Hall, E. A. H. Fluorescent nanoparticles for intracellular sensing: A review. *Anal Chim Acta* **751**, 1–23 (2012).
- [37] Tang, R. *et al.* Tunable Ultrasmall Visible-to-Extended Near-Infrared Emitting Silver Sulfide Quantum Dots for Integrin-Targeted Cancer Imaging. *ACS Nano* **9**, 220–230 (2015).
- [38] Santra, S. & Malhotra, A. Fluorescent nanoparticle probes for imaging of cancer. *WIREs Nanomed. Nanobiotechnol.* **3**, 501–510 (2011).
- [39] Gambhir, S. S. Molecular imaging of cancer with positron emission tomography. *Nat Rev Cancer* **2**, 683–693 (2002).
- [40] Welch, M. J., Hawker, C. J. & Wooley, K. L. The Advantages of Nanoparticles for PET. *J Nucl Med* **50**, 1743–1747 (2009).
- [41] Moses, W. W. Fundamental limits of spatial resolution in PET. *Nucl Instr Meth A* **648**, S236–S240 (2011).
- [42] Devaraj, N. K., Keliher, E. J., Thurber, G. M., Nahrendorf, M. & Weissleder, R. ¹⁸F Labeled Nanoparticles for *in vivo* PET-CT Imaging. *Bioconjugate Chem.* **20**, 397–401 (2009).
- [43] Kim, S.-m. *et al.* Biomaterials Hybrid PET / MR imaging of tumors using an oleanolic acid-conjugated nanoparticle. *Biomaterials* **34**, 8114–8121 (2013).

- [44] Huang, B., Law, M. W.-M. & Khong, P.-L. Whole-body PET/CT scanning: estimation of radiation dose and cancer risk. *Radiology* **251**, 166–174 (2009).
- [45] Garcia, J., Tang, T. & Louie, A. Y. Nanoparticle-based multimodal PET/MRI. *Nanomedicine (Lond.)* **10**, 1343–1359 (2015).
- [46] Keliher, E. J. *et al.* ^{89}Zr -labeled dextran nanoparticles allow in vivo macrophage imaging. *Bioconjug Chem* **22**, 2383–2389 (2011).
- [47] Zhang, K. *et al.* Double-scattering/reflection in a Single Nanoparticle for Intensified Ultrasound Imaging. *Sci Rep* **5**, 8766 (2015).
- [48] Pu, K. *et al.* Semiconducting polymer nanoparticles as photoacoustic molecular imaging probes in living mice. *Nat Nanotechnol* **9**, 233–239 (2014).
- [49] Weber, J., Beard, P. C. & Bohndiek, S. E. Contrast agents for molecular photoacoustic imaging. *Nat Methods* **13**, 639–650 (2016).
- [50] Black, K. C. L. *et al.* Dual-radiolabeled nanoparticle SPECT probes for bioimaging. *Nanoscale* **7**, 440–444 (2015).
- [51] Saritas, E. U. *et al.* Magnetic particle imaging (MPI) for NMR and MRI researchers. *J Magn Reson* **229**, 116–126 (2013).
- [52] Panagiotopoulos, N. *et al.* Magnetic particle imaging: Current developments and future directions. *Int J Nanomedicine* **10**, 3097–3114 (2015).
- [53] Kircher, M. *et al.* A brain tumour molecular imaging strategy using a new triple-modality MRI-photoacoustic-Raman nanoparticle. *Nat Med* **18**, 829–835 (2012).
- [54] Abragam, A. *The Principles of Nuclear Magnetism* (Clarendon Press, Oxford, 1961).
- [55] Hoult, D. I. Sensitivity of the NMR Experiment. *eMagRes* 0490 (2007).
- [56] Haacke, E. M., Brown, R. W., Thompson, M. R. & Venkatesan, R. *Magnetic Resonance Imaging: Physical Principles and Sequence Design* (New York; Wiley-Liss, 1999).

- [57] Lilburn, D. M. L., Pavlovskaya, G. E. & Meersmann, T. Perspectives of hyperpolarized noble gas MRI beyond ^3He . *J Magn Reson* **229**, 173–86 (2013).
- [58] Nikolaou, P., Goodson, B. M. & Chekmenev, E. Y. NMR hyperpolarization techniques for biomedicine. *Chem Eur J* **21**, 3156–3166 (2015).
- [59] Aptekar, J. W. *et al.* Silicon nanoparticles as hyperpolarized magnetic resonance imaging agents. *ACS Nano* **3**, 4003–4008 (2009).
- [60] Abragam, A. & Goldman, M. Principles of dynamic nuclear polarisation. *Rep Prog Phys* **41**, 395–467 (1978).
- [61] Wenkebach, T. *Essentials of Dynamic Nuclear Polarization* (Spindrift Publications, Burgh-Haamstede, 2016).
- [62] Günther, U. L. Dynamic Nuclear Hyperpolarization in Liquids. *Top Curr Chem* **335**, 23–69 (2011).
- [63] Maly, T. *et al.* Dynamic nuclear polarization at high magnetic fields. *J Chem Phys* **128**, 052211 (2008).
- [64] Atsarkin, V. A. & Kessenikh, A. V. Dynamic Nuclear Polarization in Solids: The Birth and Development of the Many-Particle Concept. *Appl Magn Reson* **43**, 7–19 (2012).
- [65] Ravera, E., Luchinat, C. & Parigi, G. Basic facts and perspectives of Overhauser DNP NMR. *J Magn Reson* **264**, 78–87 (2016).
- [66] Overhauser, A. W. Polarization of Nuclei in Metals. *Phys Rev* **92**, 411–415 (1953).
- [67] Carver, T. R. & Slichter, C. P. Polarization of Nuclear Spin in Metals. *Phys Rev* **92**, 212–213 (1953).
- [68] Armstrong, B. D. *Overhauser Dynamic Nuclear Polarization to Study Hydration Dynamics*. Ph.D. thesis, University of California Santa Barbara (2010).
- [69] Goldman, M. Overview of Spin Temperature, Thermal Mixing and Dynamic Nuclear Polarization. *Appl Magn Reson* **34**, 219–226 (2008).

- [70] Henstra, A., Ducksen, P., Schmidt, J., Onnes, K. & Laboratories, H. Nuclear Spin Orientation via Electron Spin Locking (NOVEL). *J Magn Reson* **77**, 389–393 (1988).
- [71] Henstra, A., Dirksen, P. & Wenckebach, W. Enhanced dynamic nuclear polarization by the integrated solid effect. *Phys Lett A* **134**, 134–136 (1988).
- [72] Weis, V., Bennati, M., Rosay, M. & Griffin, R. G. Solid effect in the electron spin dressed state: a new approach for dynamic nuclear polarization. *J Chem Phys* **113**, 6795–6802 (2000).
- [73] Goertz, S. The dynamic nuclear polarization process. *Nucl Instr Meth A* **526**, 28–42 (2004).
- [74] Purcell, E. M., Torrey, H. C. & Pound, R. V. Resonance Absorption by Nuclear Magnetic Moments in a Solid. *Phys Rev* **69**, 37 (1946).
- [75] Bloch, F., Hansen, W. W. & Packard, M. The nuclear induction experiment. *Phys Rev* **70**, 474–485 (1946).
- [76] Lauterbur, P. C. Image formation by induced local interactions. Examples employing nuclear magnetic resonance. *Nature* **242**, 190–191 (1973).
- [77] Hall, D. A. Polarization-Enhanced NMR Spectroscopy of Biomolecules in Frozen Solution. *Science* **276**, 930–932 (1997).
- [78] Golman, K. *et al.* Overhauser-enhanced MR Imaging (OMRI). *Acta Radiol* **39**, 10–17 (1998).
- [79] Lurie, D. J., Bussell, D. M., Bell, L. H. & Mallard, J. R. Proton-electron double magnetic resonance imaging of free radical solutions. *J Magn Reson* **76**, 366–370 (1988).
- [80] Ardenkjaer-Larsen, J. H. *et al.* Increase in signal-to-noise ratio of > 10,000 times in liquid-state NMR. *Proc Natl Acad Sci USA* **100**, 10158–10163 (2003).
- [81] Golman, K., Ardenkjaer-Larsen, J. H., Petersson, J. S., Mansson, S. & Leunbach, I. Molecular imaging with endogenous substances. *Proc Natl Acad Sci USA* **100**, 10435–10439 (2003).

- [82] Day, S. E. *et al.* Detecting tumor response to treatment using hyperpolarized ^{13}C magnetic resonance imaging and spectroscopy. *Nat Med* **13**, 1382–1387 (2007).
- [83] Nelson, S. J. *et al.* Metabolic Imaging of Patients with Prostate Cancer Using Hyperpolarized $[1-^{13}\text{C}]$ Pyruvate. *Sci Transl Med* **5**, 198ra108 (2013).
- [84] Ardenkjaer-Larsen, J. H. On the present and future of dissolution-DNP. *J Magn Reson* **264**, 3–12 (2016).
- [85] Terblanche, C. J., Reynhardt, E. C. & van Wyk, J. A. ^{13}C Spin-Lattice Relaxation in natural diamond: Zeeman relaxation at 4.7 T and 300 K due to fixed paramagnetic nitrogen defects. *Solid State Nucl Magn Reson* **20**, 1–22 (2001).
- [86] Raty, J.-Y. & Galli, G. Ultradispersity of diamond at the nanoscale. *Nat Mater* **2**, 792–795 (2003).
- [87] Zywietz, U., Evlyukhin, A. B., Reinhardt, C. & Chichkov, B. N. Laser printing of silicon nanoparticles with resonant optical electric and magnetic responses. *Nat Commun* **5**, 3402 (2014).
- [88] Viger-Gravel, J. *et al.* Frozen Acrylamide Gels as Dynamic Nuclear Polarization Matrices. *Angew Chemie Int Ed* (2017).
- [89] Dementyev, A. E., Cory, D. & Ramanathan, C. Dynamic Nuclear Polarization in Silicon Microparticles. *Phys Rev Lett* **100**, 127601 (2008).
- [90] McCamey, D. R., Van Tol, J., Morley, G. W. & Boehme, C. Fast nuclear spin hyperpolarization of phosphorus in silicon. *Phys Rev Lett* **102**, 027601 (2009).
- [91] Lee, M., Cassidy, M., Ramanathan, C. & Marcus, C. Decay of nuclear hyperpolarization in silicon microparticles. *Phys Rev B* **84**, 035304 (2011).
- [92] Li, D. *et al.* Intrinsic origin of spin echoes in dipolar solids generated by strong π pulses. *Phys Rev B* **77**, 214306 (2008).

- [93] Atkins, T. M. *et al.* Synthesis of Long T1 Silicon Nanoparticles for Hyperpolarized ^{29}Si Magnetic Resonance Imaging. *ACS Nano* **7**, 1609–1617 (2013).
- [94] Kwiatkowski, G. *et al.* Nanometer size silicon particles for hyperpolarized MRI. *Sci Rep* **7**, 7946 (2017).
- [95] Whiting, N. *et al.* Real-Time MRI-Guided Catheter Tracking Using Hyperpolarized Silicon Particles. *Sci Rep* **5**, 12842 (2015).
- [96] Whiting, N. *et al.* Developing hyperpolarized silicon particles for in vivo MRI targeting of ovarian cancer. *J Med Imag* **3**, 036001 (2016).
- [97] Paul, B. Diamond thin films : a 21st-century material. *Philos Trans A Math Phys Eng Sci* **358**, 473–495 (2000).
- [98] Ho, D., Wang, C.-H. K. & Chow, E. K.-H. Nanodiamonds: The intersection of nanotechnology, drug development, and personalized medicine. *Sci Adv* **1**, e1500439 (2015).
- [99] Mochalin, V. N., Shenderova, O., Ho, D. & Gogotsi, Y. The properties and applications of nanodiamonds. *Nat Nanotechnol* **7**, 11–23 (2012).
- [100] Mochalin, V. N. *et al.* Adsorption of Drugs on Nanodiamond : Toward Development of a Drug Delivery Platform. *Mol Pharm* **10**, 3728–3735 (2013).
- [101] Vaijayanthimala, V. *et al.* The long-term stability and biocompatibility of fluorescent nanodiamond as an in vivo contrast agent. *Biomaterials* **33**, 7794–7802 (2012).
- [102] Moore, L. *et al.* Biocompatibility Assessment of Detonation Nanodiamond in Non-Human Primates and Rats Using Histological, Hematologic, and Urine Analysis. *ACS Nano* **10**, 7385–7400 (2016).
- [103] Paget, V. *et al.* Carboxylated nanodiamonds are neither cytotoxic nor genotoxic on liver, kidney, intestine and lung human cell lines. *Nanotoxicology* **8**, 46–56 (2014).

- [104] Brož, A., Bačáková, L., Štenclová, P., Kromka, A. & Potocký, Š. Uptake and intracellular accumulation of diamond nanoparticles - a metabolic and cytotoxic study. *Beilstein J Nanotechnol* **8**, 1649–1657 (2017).
- [105] Schrand, A. M. *et al.* Are diamond nanoparticles cytotoxic? *J Phys Chem B* **111**, 2–7 (2007).
- [106] Chow, E. K. *et al.* Nanodiamond therapeutic delivery agents mediate enhanced chemoresistant tumor treatment. *Sci Transl Med* **3**, 73ra21 (2011).
- [107] Xi, G. *et al.* Convection-enhanced delivery of nanodiamond drug delivery platforms for intracranial tumor treatment. *Nanomed-Nanotechnol.* **10**, 381–91 (2014).
- [108] Lam, R. & Ho, D. Nanodiamonds as vehicles for systemic and localized drug delivery. *Expert Opin Drug Deliv* **6**, 883–895 (2009).
- [109] Kaur, R. & Badea, I. Nanodiamonds as novel nanomaterials for biomedical applications: Drug delivery and imaging systems. *Int J Nanomedicine* **8**, 203–220 (2013).
- [110] Bacakova, L. *et al.* Bone cells in cultures on nanocarbon-based materials for potential bone tissue engineering: A review. *Phys Status Solidi* **211**, 2688–2702 (2014).
- [111] Xing, Y. & Dai, L. Nanodiamonds for nanomedicine. *Nanomedicine (Lond.)* **4**, 207–218 (2009).
- [112] McGuinness, L. P. *et al.* Quantum measurement and orientation tracking of fluorescent nanodiamonds inside living cells. *Nat Nanotechnol* **6**, 358–63 (2011).
- [113] Haziza, S. *et al.* Fluorescent nanodiamond tracking reveals intraneuronal transport abnormalities induced by brain-disease-related genetic risk factors. *Nat Nanotechnol* **12**, 322–328 (2017).
- [114] Wu, T.-J. *et al.* Tracking the engraftment and regenerative capabilities of transplanted lung stem cells using fluorescent nanodiamonds. *Nat Nanotechnol* **8**, 682–9 (2013).

- [115] Lin, H. H. *et al.* Tracking and Finding Slow-Proliferating/Quiescent Cancer Stem Cells with Fluorescent Nanodiamonds. *Small* **11**, 4394–4402 (2015).
- [116] Balasubramanian, G. *et al.* Nanoscale imaging magnetometry with diamond spins under ambient conditions. *Nature* **455**, 648–651 (2008).
- [117] Manus, L. M. *et al.* Gd(III)-nanodiamond conjugates for MRI contrast enhancement. *Nano Lett* **10**, 484–9 (2010).
- [118] Rammohan, N. *et al.* Nanodiamond-Gadolinium(III) Aggregates for Tracking Cancer Growth In Vivo at High Field. *Nano Lett* **16**, 75517564 (2016).
- [119] Osipov, V. Y., Aleksenskiy, A. E., Takai, K. & Vul, A. Y. Magnetic Studies of a Detonation Nanodiamond with the Surface Modified by Gadolinium Ions. *Phys Solid State* **57**, 2314–2319 (2015).
- [120] Hou, W. *et al.* Nanodiamond-Manganese dual mode MRI contrast agents for enhanced liver tumor detection. *Nanomedicine NBM* **13**, 783–793 (2017).
- [121] Chang, I. P., Hwang, K. C. & Chiang, C.-S. Preparation of fluorescent magnetic nanodiamonds and cellular imaging. *J Am Chem Soc* **130**, 15476–15481 (2008).
- [122] Rojas, S. *et al.* Biodistribution of amino-functionalized diamond nanoparticles. *In Vivo* studies based on ^{18}F radionuclide emission. *ACS Nano* **5**, 5552–5559 (2011).
- [123] Duijvestijn, M. *et al.* ^{13}C NMR Spectroscopy in Diamonds Using Dynamic Nuclear Polarization. *Chem Phys Lett* **102**, 25–28 (1983).
- [124] Reynhardt, E. C. & High, G. L. Dynamic nuclear polarization of diamond. I. Solid state and thermal mixing effects. *J Chem Phys* **109**, 4090 (1998).
- [125] Reynhardt, E. C. & High, G. L. Dynamic nuclear polarization of diamond. II. Nuclear orientation via electron spin-locking. *J Chem Phys* **109**, 4100 (1998).
- [126] Jacques, V. *et al.* Dynamic Polarization of Single Nuclear Spins by Optical Pumping of Nitrogen-Vacancy Color Centers in Diamond at Room Temperature. *Phys Rev Lett* **102**, 057403 (2009).

- [127] King, J. P., Coles, P. J. & Reimer, J. A. Optical polarization of ^{13}C nuclei in diamond through nitrogen vacancy centers. *Phys Rev B* **81**, 073201 (2010).
- [128] Dutta, P., Martinez, G. V. & Gillies, R. J. Nanodiamond as a New Hyperpolarizing Agent and Its ^{13}C MRS. *J Phys Chem Lett* **5**, 597–600 (2014).
- [129] Casabianca, L. B., Shames, A. I., Panich, A. M., Shenderova, O. & Frydman, L. Factors Affecting DNP NMR in Polycrystalline Diamond Samples. *J Phys Chem C* **115**, 19041–19048 (2011).
- [130] Rej, E., Gaebel, T., Boele, T., Waddington, D. E. J. & Reilly, D. J. Hyperpolarized nanodiamond with long spin-relaxation times. *Nat Commun* **6**, 8459 (2015).
- [131] Bretschneider, C. O. *et al.* On The Potential of Dynamic Nuclear Polarization Enhanced Diamonds in Solid-State and Dissolution ^{13}C NMR Spectroscopy. *ChemPhysChem* **17**, 2691–2701 (2016).
- [132] Hoch, M. & Reynhardt, E. Nuclear spin-lattice relaxation of dilute spins in semiconducting diamond. *Phys Rev B* **37**, 9222–9226 (1988).
- [133] Wang, M. & Thanou, M. Targeting nanoparticles to cancer. *Pharmacol Res* **62**, 90–99 (2010).
- [134] Getts, D. R. *et al.* Therapeutic inflammatory monocyte modulation using immune-modifying microparticles. *Sci Transl Med* **6**, 219ra7 (2014).
- [135] Gupta, A. S. Nanomedicine approaches in vascular disease: A review. *Nanomedicine Nanotechnology, Biol Med* **7**, 763–779 (2011).
- [136] Mura, S. & Couvreur, P. Nanotheranostics for personalized medicine. *Adv Drug Deliv Rev* **64**, 1394–1416 (2012).
- [137] Cassidy, M. C., Ramanathan, C., Cory, D. G., Ager, J. W. & Marcus, C. M. Radical-free dynamic nuclear polarization using electronic defects in silicon. *Phys Rev B* **87**, 161306 (2013).
- [138] Liu, K.-K., Cheng, C.-L., Chang, C.-C. & Chao, J.-I. Biocompatible and detectable carboxylated nanodiamond on human cell. *Nanotechnology* **18**, 325102 (2007).

- [139] Huang, H., Pierstorff, E., Osawa, E. & Ho, D. Active nanodiamond hydrogels for chemotherapeutic delivery. *Nano Lett* **7**, 3305–3314 (2007).
- [140] Krüger, A., Liang, Y., Jarre, G. & Stegk, J. Surface functionalisation of detonation diamond suitable for biological applications. *J Mater Chem* **16**, 2322–2328 (2006).
- [141] Say, J. M. *et al.* Luminescent nanodiamonds for biomedical applications. *Biophys Rev* **3**, 171–184 (2011).
- [142] Chen, M. *et al.* Nanodiamond-Mediated Delivery of Water-Insoluble Therapeutics. *ACS Nano* **3**, 2016–2022 (2009).
- [143] Zhang, X. Q. *et al.* Polymer-functionalized nanodiamond platforms as vehicles for gene delivery. *ACS Nano* **3**, 2609–2616 (2009).
- [144] Maze, J. R. *et al.* Nanoscale magnetic sensing with an individual electronic spin in diamond. *Nature* **455**, 644–647 (2008).
- [145] Rugar, D. *et al.* Proton magnetic resonance imaging using a nitrogen-vacancy spin sensor. *Nat Nanotechnol* **10**, 120–124 (2015).
- [146] Häberle, T., Schmid-Lorch, D., Reinhard, F. & Wrachtrup, J. Nanoscale nuclear magnetic imaging with chemical contrast. *Nat Nanotechnol* **10**, 125–128 (2015).
- [147] Devience, S. J. *et al.* Nanoscale NMR spectroscopy and imaging of multiple nuclear species. *Nat Nanotechnol* **10**, 129–134 (2015).
- [148] Brenneis, A. *et al.* Ultrafast electronic readout of diamond nitrogenvacancy centres coupled to graphene. *Nat Nanotechnol* **10**, 135–139 (2015).
- [149] Keshari, K. R. & Wilson, D. M. Chemistry and biochemistry of ^{13}C hyperpolarized magnetic resonance using dynamic nuclear polarization. *Chem Soc Rev* **43**, 1627–1659 (2014).
- [150] Fischer, R., Jarmola, A., Kehayias, P. & Budker, D. Optical polarization of nuclear ensembles in diamond. *Phys Rev B* **87**, 125207 (2013).

- [151] Alvarez, G. A. *et al.* Local and bulk ^{13}C hyperpolarization in nitrogen-vacancy-centred diamonds at variable fields and orientations. *Nat Commun* **6**, 8456 (2015).
- [152] King, J. P. *et al.* Room-temperature *in situ* nuclear spin hyperpolarization from optically pumped nitrogen vacancy centres in diamond. *Nat Commun* **6**, 8965 (2015).
- [153] Panich, A. M. *et al.* Nuclear magnetic resonance study of ultrananocrystalline diamonds. *Eur Phys J B* **52**, 397–402 (2006).
- [154] Shames, A. I. *et al.* Defects and impurities in nanodiamonds : EPR , NMR and TEM study. *J Phys Chem Solids* **63**, 1993–2001 (2002).
- [155] Furman, G. B., Kunoff, E. M., Goren, S. D., Pasquier, V. & Tinetti, D. Fractional power time dependence of the nuclear magnetization in the presence of paramagnetic impurities. *Solid State Nucl Magn Reson* **4**, 255–258 (1995).
- [156] Blumberg, W. E. Nuclear Spin-Lattice Relaxation Caused by Paramagnetic Impurities. *Phys Rev* **119**, 79–84 (1960).
- [157] Lurie, D. J., Davies, G. R., Foster, M. A. & Hutchison, J. M. S. Field-cycled PEDRI imaging of free radicals with detection at 450 mT. *Magn Reson Imaging* **23**, 175–181 (2005).
- [158] Baumann, P. & Nemanich, R. Surface cleaning, electronic states and electron affinity of diamond (100), (111) and (110) surfaces. *Surf Sci* **409**, 320–335 (1998).
- [159] Gaebel, T. *et al.* Size-reduction of nanodiamonds via air oxidation. *Diam Rel Mater* **21**, 28–32 (2012).
- [160] Bornet, A., Melzi, R., Jannin, S. & Bodenhausen, G. Cross Polarization for Dissolution Dynamic Nuclear Polarization Experiments at Readily Accessible Temperatures $1.2 < T < 4.2$ K. *Appl Magn Reson* **43**, 107–117 (2012).
- [161] Marco-Rius, I. *et al.* Quantitation of a spin polarization-induced nuclear Overhauser effect (SPINOE) between a hyperpolarized ^{13}C -labeled cell

- metabolite and water protons. *Contrast Media Mol Imaging* **9**, 182–186 (2014).
- [162] Stoll, S. & Schweiger, A. EasySpin, a comprehensive software package for spectral simulation and analysis in EPR. *J Magn Reson* **178**, 42–55 (2006).
- [163] Cassidy, M. C. *Hyperpolarized Silicon Particles as In-vivo Imaging Agents*. Ph.D. thesis, Harvard Univ. (2012).
- [164] Pichler, B. J., Judenhofer, M. S. & Wehrl, H. F. PET/MRI hybrid imaging: Devices and initial results. *Eur Radiol* **18**, 1077–1086 (2008).
- [165] Strange, J. H. & Halse, M. R. Imaging Techniques for Solids and Quasi-Solids. *eMagRes* 1–9 (2007).
- [166] Hoult, D. I. & Lauterbur, P. C. The sensitivity of the zeugmatographic experiment involving human samples. *J Magn Reson* **34**, 425–433 (1979).
- [167] Gadian, D. . G. & Robinson, F. N. H. Radiofrequency losses in NMR experiments on electrically conducting samples. *J Magn Reson* **34**, 449–455 (1979).
- [168] Parra-Robles, J., Cross, A. R. & Santyr, G. E. Theoretical signal-to-noise ratio and spatial resolution dependence on the magnetic field strength for hyperpolarized noble gas magnetic resonance imaging of human lungs. *Med Phys* **32**, 221–229 (2005).
- [169] Doty, F. D., Entzminger, G., Kulkarni, J., Pamarthy, K. & Staab, J. P. Radio frequency coil technology for small-animal MRI. *NMR Biomed* **20**, 304–325 (2007).
- [170] Mispelter, J., Mikaela, L. & Briguet, A. *NMR Probeheads for Biophysical and Biomedical Experiments* (Imperial College Press;, 2006).
- [171] Rainey, J. K., DeVries, J. S. & Sykes, B. D. Estimation and measurement of flat or solenoidal coil inductance for radiofrequency NMR coil design. *J Magn Reson* **187**, 27–37 (2007).

- [172] Tsai, L. L., Mair, R. W., Rosen, M. S., Patz, S. & Walsworth, R. L. An open-access, very-low-field MRI system for posture-dependent ^3He human lung imaging. *J Magn Reson* **193**, 274–285 (2008).
- [173] Callaghan, P. *Principles of Nuclear Magnetic Resonance Microscopy* (Oxford University Press, 1994).
- [174] Fu, C.-C. *et al.* Characterization and application of single fluorescent nanodiamonds as cellular biomarkers. *Proc Natl Acad Sci USA* **104**, 727–732 (2007).
- [175] Kucsko, G. *et al.* Nanometre-scale thermometry in a living cell. *Nature* **500**, 54–58 (2013).
- [176] Almeida, J. P. M., Figueroa, E. R. & Drezeck, R. A. Gold nanoparticle mediated cancer immunotherapy. *Nanomedicine NBM* **10**, 503–514 (2014).
- [177] Li, C. A targeted approach to cancer imaging and therapy. *Nat Mater* **13**, 110–115 (2014).
- [178] Boles, M. A., Ling, D., Hyeon, T. & Talapin, D. V. The surface science of nanocrystals. *Nat Mater* **15**, 141–153 (2016).
- [179] Maurer, P. C. *et al.* Room-Temperature Quantum Bit Memory Exceeding One Second. *Science* **336**, 1283–1286 (2012).
- [180] Waldherr, G. *et al.* High-dynamic-range magnetometry with a single electronic spin in diamond. *Nat Nanotechnol* **7**, 105–108 (2012).
- [181] Grinolds, M. S. *et al.* Nanoscale magnetic imaging of a single electron spin under ambient conditions. *Nat Phys* **9**, 215–219 (2013).
- [182] Parker, A. J. *et al.* Optically-pumped dynamic nuclear hyperpolarization in ^{13}C enriched diamond. *arXiv* 1708.00561 (2017).
- [183] Cunningham, C. H. *et al.* Hyperpolarized ^{13}C Metabolic MRI of the Human Heart: Initial Experience. *Circ Res* **119**, 1177–1182 (2016).
- [184] Rej, E., Gaebel, T., Waddington, D. E. J. & Reilly, D. J. Hyperpolarized Nanodiamond Surfaces. *J Am Chem Soc* **139**, 193–199 (2017).

- [185] Waddington, D. E. J. *et al.* Nanodiamond-enhanced MRI via in situ hyperpolarization. *Nat Commun* **8**, 15118 (2017).
- [186] Barklie, R. C. & Guven, J. ^{13}C hyperfine structure and relaxation times of the P1 centre in diamond. *J Phys C Solid State* **14**, 3621–3631 (1981).
- [187] Loubser, J. H. N. & Wyk, J. A. Electron spin resonance in the study of diamond. *Rep Prog Phys* **41**, 1201–1248 (1978).
- [188] Zaitsev, A. *Optical Properties of Diamond, A Data Handbook* (Springer, 2001).
- [189] Terblanche, C. J., Reynhardt, E. C., Rakitianski, S. A. & Van Wyk, J. A. ^{13}C Spin-Lattice Relaxation in Natural Diamond: Zeeman Relaxation in Fields of 500 to 5000 G at 300 K Due to Fixed Paramagnetic Nitrogen Defects. *Solid State Nucl Magn Reson* **19**, 107–129 (2001).
- [190] Milani, J. *et al.* A magnetic tunnel to shelter hyperpolarized fluids. *Rev Sci Instrum* **86**, 024101 (2015).
- [191] Li, D., Dementyev, A. E., Dong, Y., Ramos, R. G. & Barrett, S. E. Generating unexpected spin echoes in dipolar solids with π pulses. *Phys Rev Lett* **98**, 190401 (2007).
- [192] Dong, Y., Ramos, R. G., Li, D. & Barrett, S. E. Controlling coherence using the internal structure of hard π pulses. *Phys Rev Lett* **100**, 247601 (2008).
- [193] Frey, M. a. *et al.* Phosphorus-31 MRI of hard and soft solids using quadratic echo line-narrowing. *Proc Natl Acad Sci USA* **109**, 5190–5195 (2012).
- [194] Sykes, E. A., Chen, J. & Zheng, G. Investigating the Impact of Nanoparticle Size on Active and Passive Tumor Targeting Efficiency. *ACS Nano* **8**, 5696–5706 (2014).
- [195] Kunjachan, S. *et al.* Passive versus Active Tumor Targeting Using RGD- and NGR-Modified Polymeric Nanomedicines. *Nano Lett* **14**, 972–981 (2014).
- [196] Colombo, M. *et al.* Tumour homing and therapeutic effect of colloidal nanoparticles depend on the number of attached antibodies. *Nat Commun* **7**, 13818 (2016).

- [197] Neri, D. & Bicknell, R. Tumour Vascular Targeting. *Nat Rev Cancer* **5**, 436–446 (2005).
- [198] Salvati, A. *et al.* Transferrin-functionalized nanoparticles lose their targeting capabilities when a biomolecule corona adsorbs on the surface. *Nat Nanotechnol* **8**, 137–143 (2013).
- [199] Kreyling, W. G. *et al.* In vivo integrity of polymer-coated gold nanoparticles. *Nat Nanotechnol* **10**, 619–623 (2015).
- [200] Balasubramanian, G. *et al.* Ultralong spin coherence time in isotopically engineered diamond. *Nat Mater* **8**, 383–387 (2009).
- [201] Knowles, H. S., Kara, D. M. & Atatüre, M. Observing bulk diamond spin coherence in high-purity nanodiamonds. *Nat Mater* **13**, 21–25 (2014).
- [202] Capozzi, A., Cheng, T., Boero, G., Roussel, C. & Comment, A. Thermal annihilation of photo-induced radicals following dynamic nuclear polarization to produce transportable frozen hyperpolarized ^{13}C -substrates. *Nat Commun* **8**, 15757 (2017).
- [203] Eaton, G. R. *et al.* A signal-to-noise standard for pulsed EPR. *J Magn Reson* **205**, 109–113 (2010).
- [204] Zhao, L. *et al.* Gradient-echo imaging considerations for hyperpolarized ^{129}Xe MR. *J Magn Reson B* **113**, 179–183 (1996).
- [205] Yavkin, B. V., Mamin, G. V., Gafurov, M. R. & Orlinskii, S. B. Size-dependent concentration of N^0 paramagnetic centres in HPHT nanodiamonds. *Magn Reson Solids* **17**, 15101 (2015).
- [206] Van Wyk, J. A., Reynhardt, E. C., High, G. L. & Kiflawi, I. The dependences of ESR line widths and spin—spin relaxation times of single nitrogen defects on the concentration of nitrogen defects in diamond. *J Phys D Appl Phys* **30**, 1790–1793 (1997).
- [207] Eaton, G. R., Eaton, S. S., Barr, D. P. & Weber, R. T. *Quantitative EPR* (Springer, 2010).

- [208] Hennig, J., Nauerth, A. & Friedburg, H. RARE Imaging: A Fast Imaging Method for Clinical MR. *Magn Reson Med* **3**, 823–833 (1986).
- [209] Shabanova, E., Schaumburg, K. & Sellschop, J. P. F. ^{13}C NMR Investigations of SpinLattice Relaxation in 99% ^{13}C -Enriched Diamonds. *J Magn Reson* **130**, 8–17 (1998).
- [210] Ramaswamy, S. Issues in the statistical mechanics of steady sedimentation. *Adv Phys* **50**, 297–341 (2001).
- [211] Zhang, L. *et al.* Nanoparticles in medicine: therapeutic applications and developments. *Clin. Pharmacol. Ther.* **83**, 761–769 (2008).
- [212] Hens, Z. & Martins, J. C. A Solution NMR Toolbox for Characterizing the Surface Chemistry of Colloidal Nanocrystals. *Chem Mater* **25**, 1211–1221 (2013).
- [213] Protesescu, L. *et al.* Unraveling the Core—Shell Structure of Ligand-Capped Sn/SnO_x Nanoparticles by Surface-Enhanced Nuclear Magnetic Resonance, Mössbauer, and X-ray Absorption Spectroscopies. *ACS Nano* **8**, 2639–2648 (2014).
- [214] Rossini, A. J. *et al.* Dynamic Nuclear Polarization Surface Enhanced NMR Spectroscopy. *Acc Chem Res* **46**, 1942–1951 (2013).
- [215] Grüning, W. R. *et al.* Molecular-level characterization of the structure and the surface chemistry of periodic mesoporous organosilicates using DNP-surface enhanced NMR spectroscopy. *Phys. Chem. Chem. Phys.* **15**, 13270–13274 (2013).
- [216] Rossini, A. J. *et al.* Dynamic nuclear polarization NMR spectroscopy of microcrystalline solids. *J Am Chem Soc* **134**, 16899–16908 (2012).
- [217] Lelli, M. *et al.* Fast Characterization of Functionalized Silica Materials by Silicon-29. *J Am Chem Soc* **133**, 2104–2107 (2011).
- [218] Lesage, A. *et al.* Surface enhanced NMR spectroscopy by dynamic nuclear polarization. *J Am Chem Soc* **132**, 15459–15461 (2010).

- [219] Piveteau, L. *et al.* Structure of Colloidal Quantum Dots from Dynamic Nuclear Polarization Surface Enhanced NMR Spectroscopy. *J Am Chem Soc* **137**, 13964–71 (2015).
- [220] Gajan, D. *et al.* Hybrid polarizing solids for pure hyperpolarized liquids through dissolution dynamic nuclear polarization. *Proc Natl Acad Sci USA* **111**, 14693–7 (2014).
- [221] Lingwood, M. D., Siaw, T. A., Chan, H. R. & Ross, B. D. Hyperpolarized Water as an MR imaging contrast agent : Feasibility of in Vivo Imaging in a Rat Model. *Radiology* **265**, 418–425 (2012).
- [222] Franck, J. M., Ding, Y., Stone, K., Qin, P. Z. & Han, S. Anomalous Rapid Hydration Water Diffusion Dynamics Near DNA Surfaces. *J Am Chem Soc* **137**, 12013–12023 (2015).
- [223] Armstrong, B. D. & Han, S. Overhauser dynamic nuclear polarization to study local water dynamics. *J Am Chem Soc* **131**, 4641–4647 (2009).
- [224] Franck, J. M., Scott, J. A. & Han, S. Viscosity of Crowded Solutions. *J Am Chem Soc* **135**, 4175–4178 (2013).
- [225] Zhu, Y. *et al.* The biocompatibility of nanodiamonds and their application in drug delivery systems. *Theranostics* **2**, 302–312 (2012).
- [226] Giammarco, J., Mochalin, V. N., Haeckel, J. & Gogotsi, Y. The adsorption of tetracycline and vancomycin onto nanodiamond with controlled release. *J Colloid Interface Sci* **468**, 253–261 (2016).
- [227] Waddington, D. E. J. *et al.* Phase-Encoded Hyperpolarized Nanodiamond for Magnetic Resonance Imaging. *arXiv* 1709.0185v1 (2017).
- [228] Bundy, F. P., Hall, H. T., Strong, H. M. & Wentorf, R. H. Man-made Diamonds. *Nature* **175**, 51–55 (1955).
- [229] Panich, A. M., Sergeev, N. A., Shames, A. I., Osipov, V. Y. & Boudou, J.-P. Size dependence of ^{13}C nuclear spin-lattice relaxation in micro- and nanodiamonds. *J Phys Condens Matter* **27**, 72203 (2015).

- [230] Krebs, J. J. Proton Spin Polarization of Water Adsorbed on Sucrose Chars. *J Chem Phys* **34**, 326–329 (1961).
- [231] Krebs, J. J. & Thompson, J. K. Dynamic Nuclear Polarization Studies of Charred Carbohydrates. *J Chem Phys* **36**, 2509–2514 (1962).
- [232] Uebersfeld, J., Motchane, J. L. & Erb, E. Augmentation de la polarisation nucléaire dans les liquides et gaz adsorbés sur un charbon. Extension aux solides contenant des impuretés paramagnétiques. *J Phys Radium* **19**, 843–844 (1958).
- [233] Williams, O. A. *et al.* Size-Dependent Reactivity of Diamond Nanoparticles. *ACS Nano* **4**, 4824–4830 (2010).
- [234] Kim, H. *et al.* Multiscale Simulation as a Framework for the Enhanced Design of Nanodiamond-Polyethylenimine-Based Gene Delivery. *J Phys Chem Lett* **3**, 3791–3797 (2012).
- [235] Abrams, D., Trusheim, M. E., Englund, D. R., Shattuck, M. D. & Meriles, C. A. Dynamic nuclear spin polarization of liquids and gases in contact with nanostructured diamond. *Nano Lett* **14**, 2471–2478 (2014).
- [236] Min, Y., Caster, J. M., Eblan, M. J. & Wang, A. Z. Clinical Translation of Nanomedicine. *Chem Rev* **115**, 11147–11190 (2015).
- [237] Reddy, S. T. *et al.* Exploiting lymphatic transport and complement activation in nanoparticle vaccines. *Nat Biotechnol* **25**, 1159–1164 (2007).
- [238] Gaur, S. *et al.* Pharmacodynamic and pharmacogenomic study of the nanoparticle conjugate of camptothecin CRLX101 for the treatment of cancer. *Nanomedicine NBM* **10**, 1477–86 (2014).
- [239] Liu, Y. *et al.* Theranostic near-infrared fluorescent nanoplatfrom for imaging and systemic siRNA delivery to metastatic anaplastic thyroid cancer. *Proc Natl Acad Sci USA* **113**, 7750–7755 (2016).
- [240] Harisinghani, M. G. *et al.* Noninvasive Detection of Clinically Occult Lymph-Node Metastases in Prostate Cancer. *New Engl J Med* **348**, 2491–2499 (2003).

- [241] Thalhammer, A., Edgington, R. J., Cingolani, L. A., Schoepfer, R. & Jackman, R. B. The use of nanodiamond monolayer coatings to promote the formation of functional neuronal networks. *Biomaterials* **31**, 2097–2104 (2010).
- [242] Zhang, Q. *et al.* Fluorescent PLLA-nanodiamond composites for bone tissue engineering. *Biomaterials* **32**, 87–94 (2011).
- [243] McDonald, R. J. *et al.* Intracranial Gadolinium Deposition after Contrast-enhanced MR Imaging. *Radiology* **275**, 772–782 (2015).
- [244] Lurie, D. J., Li, H., Petryakov, S. & Zweier, J. L. Development of a PEDRI free-radical imager using a 0.38 T clinical MRI system. *Magn Reson Med* **47**, 181–186 (2002).
- [245] Golman, K., Leunbach, I., Petersson, J. S., Holz, D. & Overweg, J. Overhauser-enhanced MRI. *Acad. Radiol.* **9(suppl 1)**, S104–S108 (2002).
- [246] Koonjoo, N. *et al.* In vivo Overhauser-enhanced MRI of proteolytic activity. *Contrast Media Mol Imaging* **9**, 363–371 (2014).
- [247] Ichikawa, K. & Yasukawa, K. Imaging in vivo redox status in high spatial resolution with OMRI. *Free Radic Res* **46**, 1004–1010 (2012).
- [248] Sarraçanie, M., Armstrong, B. D., Stockmann, J. & Rosen, M. S. High speed 3D overhauser-enhanced MRI using combined b-SSFP and compressed sensing. *Magn Reson Med* **71**, 735–745 (2013).
- [249] Clarkson, R. B. *et al.* Electron paramagnetic resonance and dynamic nuclear polarization of char suspensions: surface science and oximetry. *Phys Med Biol* **43**, 1907–1920 (1998).
- [250] Ardenkjaer-Larsen, J. H. *et al.* EPR and DNP Properties of Certain Novel Single Electron Contrast Agents Intended for Oximetric Imaging. *J Magn Reson* **133**, MN981438 (1998).
- [251] Cui, J.-F., Fang, X.-W. & Schmidt-Rohr, K. Quantification of C=C and C=O Surface Carbons in Detonation Nanodiamond by NMR. *J Phys Chem C* **118**, 9621–9627 (2014).

- [252] Korobov, M., V., A. N., Bogachev, A. G., Rozhkova, N. N. & Osawa, E. Nanophase of water in nano-diamond gel. *J Phys Chem C* **111**, 7330–7334 (2007).
- [253] Hwang, L.-P. & Freed, J. H. Dynamic effects of pair correlation functions on spin relaxation by translational diffusion in liquids. *J Chem Phys* **63**, 4017–4025 (1975).
- [254] Freed, J. Dynamic effects of pair correlation functions on spin relaxation by translational diffusion in liquids. II. Finite jumps and independent T1 processes. *J Chem Phys* **68**, 4034–4037 (1978).
- [255] Gabriel, C., Gabriel, S., Grant, E. H., Halstead, B. S. J. & Mingos, D. M. P. Dielectric Parameters Relevant to Microwave Dielectric Heating. *Chem Soc Rev* **27**, 213–223 (1998).
- [256] Sarraçanie, M. *et al.* Low-Cost High-Performance MRI. *Sci Rep* **5**, 15177 (2015).
- [257] Scheffler, K. & Lehnhardt, S. Principles and applications of balanced SSFP techniques. *Eur Radiol* **13**, 2409–2418 (2003).
- [258] Bottomley, P. A., Foster, T. H., Argersinger, R. E. & Pfeifer, L. M. A review of normal tissue hydrogen NMR relaxation times and relaxation mechanisms from 1100 MHz: Dependence on tissue type, NMR frequency, temperature, species, excision, and age. *Med Phys* **11**, 425–448 (1984).
- [259] Massot, P. *et al.* In vivo high-resolution 3D overhauser-enhanced MRI in mice at 0.2 T. *Contrast Media Mol Imaging* **7**, 45–50 (2012).
- [260] Saraiva, C. *et al.* Nanoparticle-mediated brain drug delivery: Overcoming blood-brain barrier to treat neurodegenerative diseases. *J Control Release* **235**, 34–47 (2016).
- [261] Blanco, E., Shen, H. & Ferrari, M. Principles of nanoparticle design for overcoming biological barriers to drug delivery. *Nat Biotechnol* **33**, 941–951 (2015).
- [262] Yuan, Y., Chen, Y., Liu, J. H., Wang, H. & Liu, Y. Biodistribution and fate of nanodiamonds in vivo. *Diam Rel Mater* **18**, 95–100 (2009).

- [263] Zhang, X. *et al.* Biodistribution and toxicity of nanodiamonds in mice after intratracheal instillation. *Toxicol. Lett.* **198**, 237–243 (2010).
- [264] Liersch, R., Hirakawa, S., Berdel, W. E., Mesters, R. M. & Detmar, M. Induced lymphatic sinus hyperplasia in sentinel lymph nodes by VEGF-C as the earliest premetastatic indicator. *Int J Oncol* **41**, 2073–2078 (2012).
- [265] Zbinden, G. *Fine-Needle Aspiration Biopsy of the Rat Liver: Cytological, Cytochemical and Biochemical Methods* (Elsevier, 2013), 2013 edn.
- [266] Trencsenyi, G. *et al.* Metastatic hepatocarcinoma He/De tumor model in rat. *J Cancer* **5**, 548–558 (2014).
- [267] Duan, X. *et al.* Surface-tailored nanodiamonds as excellent metal-free catalysts for organic oxidation. *Carbon* **103**, 404–411 (2016).
- [268] Mi, P. *et al.* A pH-activatable nanoparticle with signal-amplification capabilities for non-invasive imaging of tumour malignancy. *Nat Nanotechnol* **11**, 724–730 (2016).
- [269] Meriles, C. A. & Doherty, M. W. Generation of spin-polarized currents via cross-relaxation with dynamically pumped paramagnetic impurities. *Appl. Phys. Lett.* **105**, 022403 (2014).
- [270] Bouchard, L.-S. *et al.* Picomolar sensitivity MRI and photoacoustic imaging of cobalt nanoparticles. *Proc Natl Acad Sci USA* **106**, 4085–4089 (2009).
- [271] Holz, M., Heil, S. R. & Sacco, A. Temperature-dependent self-diffusion coefficients of water and six selected molecular liquids for calibration in accurate ^1H NMR PFG measurements. *Phys. Chem. Chem. Phys.* **2**, 4740–4742 (2000).
- [272] Neugart, F. *et al.* Dynamics of diamond nanoparticles in solution and cells. *Nano Lett* **7**, 3588–3591 (2007).
- [273] Yavkin, B. V. *et al.* Defects in Nanodiamonds: Application of High-Frequency cw and Pulse EPR, ODMR. *Appl Magn Reson* **45**, 1035–1049 (2014).

- [274] Kestin, J., Sokolov, M. & Wakeham, W. A. Viscosity of Liquid Water in the Range of -8 °C to 150 °C. *J Phys Chem Ref Data* **7**, 941–948 (1978).
- [275] Armstrong, B. D. *et al.* Portable X-band system for solution state dynamic nuclear polarization. *J Magn Reson* **191**, 273–281 (2008).
- [276] Singh, R., Devi, S. & Gollen, R. Role of free radical in atherosclerosis, diabetes and dyslipidaemia: larger-than-life. *Diabetes Metab Res Rev* **32**, 13–23 (2014).
- [277] Sanderson, T. H., Reynolds, C. A., Kumar, R., Przyklenk, K. & Hüttemann, M. Molecular mechanisms of ischemia-reperfusion injury in brain: Pivotal role of the mitochondrial membrane potential in reactive oxygen species generation. *Mol Neurobiol* **47**, 9–23 (2013).
- [278] Choudhari, S. K., Chaudhary, M., Bagde, S., Gadbail, A. R. & Joshi, V. Nitric oxide and cancer: a review. *World J Surg Oncol* **11**, 118 (2013).
- [279] Epel, B., Redler, G. & Halpern, H. J. How *in vivo* EPR measures and images oxygen. *Adv Exp Med Biol* **812**, 113–119 (2014).
- [280] Danhier, P. & Gallez, B. Electron paramagnetic resonance: a powerful tool to support magnetic resonance imaging research. *Contrast Media Mol Imaging* **10**, 266–281 (2015).
- [281] Utsumi, H. *et al.* Simultaneous molecular imaging of redox reactions monitored by Overhauser-enhanced MRI with ¹⁴N- and ¹⁵N-labeled nitroxyl radicals. *Proc Natl Acad Sci USA* **103**, 1463–1468 (2006).
- [282] Halpern, H. J. *et al.* Diminished aqueous microviscosity of tumors in murine models measured with *in vivo* radiofrequency electron paramagnetic resonance. *Cancer Res* **59**, 5836–5841 (1999).
- [283] He, G., Samouilov, A., Kuppusamy, P. & Zweier, J. L. *In vivo* imaging of free radicals: Applications from mouse to man. *Mol Cell Biochem* **234-235**, 359–367 (2002).
- [284] Kuppusamy, P. & Zweier, J. L. Cardiac applications of EPR imaging. *NMR Biomed* **17**, 226–239 (2004).

- [285] Vikram, D. S., Rivera, B. K. & Kuppusamy, P. In vivo imaging of free radicals and oxygen. In: Uppu RM, Murthy SN, Pryor WA, Parinandi NL (eds.). Free Radicals and Antioxidant Protocols. *Methods Mol Biol* **610**, 3–27 (2010).
- [286] Subramanian, S., Matsumoto, K., Mitchell, J. B. & Krishna, M. C. Radio frequency continuous-wave and time-domain EPR imaging and Overhauser-enhanced magnetic resonance imaging of small animals: instrumental developments and comparison of relative merits for functional imaging. *NMR Biomed* **17**, 263–294 (2004).
- [287] Ahmad, R. & Kuppusamy, P. Theory, instrumentation, and applications of electron paramagnetic resonance oximetry. *Chem Rev* **110**, 3212–3236 (2010).
- [288] Matsumoto, S. *et al.* Advantageous Application of a Surface Coil to EPR Irradiation in Overhauser-Enhanced MRI. *Magn Reson Med* **57**, 806–811 (2007).
- [289] Petryakov, S. *et al.* Dual frequency resonator for 1.2 GHz EPR/16.2 MHz NMR co-imaging. *J Magn Reson* **205**, 1–8 (2010).
- [290] Sundramoorthy, S. V., Epel, B. & Halpern, H. J. Orthogonal resonators for pulse in vivo electron paramagnetic imaging at 250 MHz. *J Magn Reson* **240**, 45–51 (2014).
- [291] Neudert, O., Raich, H. P., Mattea, C., Stapf, S. & Münnemann, K. An Alderman-Grant resonator for S-Band Dynamic Nuclear Polarization. *J Magn Reson* **242**, 79–85 (2014).
- [292] Salameh, N., Sarracanie, M., Armstrong, B. D., Rosen, M. S. & Comment, A. Overhauser-enhanced magnetic resonance elastography. *NMR Biomed* **29**, 607–613 (2016).
- [293] Sun, Z., Li, H., Petryakov, S., Samouilov, A. & Zweier, J. L. In vivo proton electron double resonance imaging of mice with fast spin echo pulse sequence. *J Magn Reson* **35**, 471–475 (2012).

- [294] Deng-Bryant, Y., Singh, I. N., Carrico, K. M. & Hall, E. D. Neuroprotective effects of tempol, a catalytic scavenger of peroxynitrite-derived free radicals, in a mouse traumatic brain injury model. *J Cereb Blood Flow Metab* **28**, 1114–1126 (2008).
- [295] Behringer, W. *et al.* Antioxidant Tempol enhances hypothermic cerebral preservation during prolonged cardiac arrest in dogs. *J Cereb Blood Flow Metab* **22**, 105–117 (2002).
- [296] Lochhead, J. J. *et al.* Oxidative stress increases blood-brain barrier permeability and induces alterations in occludin during hypoxia-reoxygenation. *J Cereb Blood Flow Metab* **30**, 1625–1636 (2010).
- [297] Jin, H. *et al.* Mitochondria-targeted antioxidants for treatment of Parkinson's disease: Preclinical and clinical outcomes. *Biochim Biophys Acta* **1842**, 1282–1294 (2014).
- [298] Gilbert, K. M., Scholl, T. J. & Chronik, B. A. RF Coil Loading Measurements Between 1 and 50 MHz to Guide Field-Cycled MRI System Design. *Concept Magn Res B* **33B**, 177–191 (2008).
- [299] Coffey, A. M. *et al.* High-resolution low-field molecular magnetic resonance imaging of hyperpolarized liquids. *Anal. Chem.* **86**, 9042–9049 (2014).
- [300] Alderman, D. W. & Grant, D. M. An Efficient Decoupler Coil Design which Reduces Heating in Conductive Samples in Superconducting Spectrometers. *J Magn Reson* **36**, 447–451 (1979).
- [301] Li, S., Yang, Q. X. & Smith, M. B. RF coil optimization: Evaluation of B_1 field homogeneity using field histograms and finite element calculations. *Magn Reson Imaging* **12**, 1079–1087 (1994).
- [302] Gabriel, S., Lau, R. W. & Gabriel, C. The dielectric properties of biological tissues: II. Measurements in the frequency range 10 Hz to 20 GHz. *Phys Med Biol* **41**, 2251–2269 (1996).
- [303] Kalmar, A. F., Van Aken, J., Caemaert, J., Mortier, E. P. & Struys, M. M. R. F. Value of Cushing reflex as warning sign for brain ischaemia during neuroendoscopy. *Br J Anaesth* **94**, 791–799 (2005).

- [304] Li, H. *et al.* Proton electron double resonance imaging of the *in vivo* distribution and clearance of a triaryl methyl radical in mice. *Magn Reson Med* **48**, 530–4 (2002).
- [305] Darrasse, L. & Ginefri, J.-C. Perspectives with cryogenic RF probes in biomedical MRI. *Biochimie* **85**, 915–937 (2003).
- [306] Baudin, E., Safiullin, K., Morgan, S. W. & Nacher, P.-J. An active feedback scheme for low field NMR experiments. *J Phys Conf Ser* **294**, 012009 (2011).
- [307] Petryakov, S. *et al.* Segmented surface coil resonator for *in vivo* EPR applications at 1.1 GHz. *J Magn Reson* **198**, 8–14 (2009).
- [308] Enomoto, A., Emoto, M., Fujii, H. & Hirata, H. Four-channel surface coil array for sequential CW-EPR image acquisition. *J Magn Reson* **234**, 21–29 (2013).
- [309] Krishna, M. C. *et al.* Overhauser enhanced magnetic resonance imaging for tumor oximetry: coregistration of tumor anatomy and tissue oxygen concentration. *Proc Natl Acad Sci USA* **99**, 2216–2221 (2002).
- [310] Matsumoto, S. *et al.* Simultaneous imaging of tumor oxygenation and microvascular permeability using Overhauser enhanced MRI. *Proc Natl Acad Sci USA* **106**, 17898–17903 (2009).
- [311] Kosem, N. *et al.* Whole-body kinetic image of a redox probe in mice using Overhauser-enhanced MRI. *Free Radic Biol Med* **53**, 328–336 (2012).
- [312] Ribot, E. J., Wecker, D., Trotier, A. J. & Dallaudi, B. Water Selective Imaging and bSSFP Banding Artifact Correction in Humans and Small Animals at 3T and 7T, Respectively. *PLoS One* 0139249 (2015).
- [313] Un, S. *et al.* Pulsed dynamic nuclear polarization at 5 T. *Chem Phys Lett* **189**, 54 (1992).
- [314] Alecci, M. & Lurie, D. J. Low field (10 mT) pulsed dynamic nuclear polarization. *J Magn Reson* **138**, 313–9 (1999).

- [315] Korchak, S. E. *et al.* Low-Field, Time-Resolved Dynamic Nuclear Polarization with Field Cycling and High-Resolution NMR Detection. *Appl Magn Reson* **37**, 515–537 (2009).
- [316] Nasibulov, E. a., Ivanov, K. L., Yurkovskaya, A. V. & Vieth, H.-M. Theory of the Overhauser effect in the pulsed mode of EPR pumping: exploiting the advantages of coherent electron spin motion. *Phys Chem Chem Phys* **14**, 6459–68 (2012).
- [317] Patra, C. R. *et al.* Targeted Delivery of Gemcitabine to Pancreatic Adenocarcinoma Using Cetuximab as a Targeting Agent. *Cancer Res* **68**, 1970–1978 (2008).
- [318] Yildirim, L., Thanh, N. T., Loizidou, M. & Seifalian, A. M. Toxicological considerations of clinically applicable nanoparticles. *Nano Today* **6**, 585–607 (2011).
- [319] Zakrzewska, K. E. *et al.* Analysis of the cytotoxicity of carbon-based nanoparticles, diamond and graphite, in human glioblastoma and hepatoma cell lines. *PLoS One* **10**, 1–15 (2015).
- [320] Zhang, B. *et al.* Shape dependent cytotoxicity of PLGA-PEG nanoparticles on human cells. *Sci Rep* **7**, 7315 (2017).
- [321] Rej, E. *Hyperpolarized Nanodiamonds for Magnetic Resonance Imaging*. Ph.D. thesis, University of Sydney (2016).
- [322] Ohya-Nishiguchi, H., Sugito, S. & Hirota, N. ESR Spectroeters Using Electromagnetic Horns. *J Magn Reson* **68**, 40–51 (1986).
- [323] Trommel, J. *Molecular Motions and Collisions in Organic Free Radical Solutions as Studied by Dynamic Nuclear Polarization*. Ph.D. thesis, Delft Univ. of Technology (1978).
- [324] Wind, R. *et al.* Experimental setup for enhanced ^{13}C NMR spectroscopy in solids using dynamic nuclear polarization. *J Magn Reson* **52**, 424–434 (1983).
- [325] Han, S. *et al.* Dynamic nuclear polarization enhanced nuclear magnetic resonance of water under ambient conditions (2011).

- [326] Bösigler, P., Brun, E. & Meier, D. Solid-State Nuclear Spin-Flip Maser Pumped by Dynamic Nuclear Polarization. *Phys Rev Lett* **38**, 602–605 (1977).
- [327] Bösigler, P., Brun, E. & Meier, D. Ruby NMR laser: A phenomenon of spontaneous self-organization of a nuclear spin system. *Phys Rev A* **18**, 671–684 (1978).
- [328] Verber, C. M., Mahon, H. P. & Tantilla, W. H. Nuclear Resonance of Aluminium in Synthetic Ruby. *Phys Rev* **125**, 1149–1157 (1962).
- [329] Niebuhr, H. H., Hundt, E. E. & Brun, E. Behavior of the ^{27}Al line shape in ruby under dynamic nuclear polarization. *Phys Rev Lett* **21**, 1735–1738 (1968).
- [330] Terblanche, C. J., Reynhardt, E. C. & Van Wyk, J. A. ^{13}C spin—lattice relaxation in natural type-IIb semiconducting diamond. *Chem Phys Lett* **310**, 97–102 (1999).
- [331] Sepponen, R. E. Low-Field MR Imaging - Development in Finland. *Acta radiol* **37**, 446–454 (1996).
- [332] Hoult, D. I. Sensitivity of Whole Body MRI Experiments. *eMagRes* 0491 (2007).
- [333] Ocali, O. & Atalar, E. Ultimate intrinsic signal-to-noise ratio in MRI. *Magn Reson Med* **39**, 462–473 (1998).
- [334] Carr, H. Steady-State Free Precession in Nuclear Magnetic Resonance. *Phys Rev* **112**, 1693–1701 (1958).
- [335] Baudin, E., Safiullin, K., Morgan, S. W. & Nacher, P, J. An active feedback scheme for low field NMR experiments. *J Phys Conf Ser* **294**, 012009 (2011).